Magnetic Resonance Imaging of the Neonatal Cardiovascular System: Impact of Patent Ductus Arteriosus

Kathryn Mary Broadhouse

A dissertation submitted for the degree of

Doctor of Philosophy

Imperial College London

Imaging Sciences Department, MRC Clinical Sciences Centre

Imperial College London

Abstract

The incidence of premature birth is increasing in absolute number and as a proportion of all births around the world. Many pathologies seen in this cohort are related to abnormal blood supply. Fetal and premature cardiovascular systems differ greatly as to maintain adequate blood flow to the developing organs in the uterine and extra-uterine environments require very different circulations. Subsequently following preterm birth the immature cardiovascular system undergoes abrupt adaptations, often resulting in the prolonged patency of the fetal shunt, ductus arteriosus. The impact of a patent ductus arteriosus (PDA) is poorly understood. However it is thought that large ductal shunt volumes may result in congestive cardiac failure and systemic hypo-perfusion.

Cardiac MRI has contributed greatly to the understanding of many cardiovascular diseases and congenital defects in paediatric and adult patients. Translating these imaging techniques to assess the preterm cardiovascular system requires careful optimization due to their condition, size and significantly increased heart rate. The work presented in this thesis employs multiple functional CMR techniques to investigate the preterm cardiovascular system in the presence and absence of PDA and the resultant cardiac function.

A novel technique utilizing PC MRI to quantify PDA shunt volume and its impact on flow distribution is presented. Despite large shunt volumes, systemic circulation remained within normal range, although slight reduction is detectable when assessed at group level. Subsequently the impact of PDA and associated increased work load on left ventricular dimensions and function was then investigated using SSFP imaging. Results indicated that cardiac function was maintained even in the presence of large shunt volumes. Finally 4D PC sequences were employed to evaluate pulse wave velocity and flow regime within the preterm aorta, demonstrating the feasibility of hemodynamic assessment in this cohort. The findings of these studies provide insight into the impact of PDA. The reliable measurement and assessment of preterm cardiovascular system provides the potential to improve the understanding of the development and effects of certain pathologies seen in this cohort.

This thesis is dedicated to Giovanni Buccoliero

Acknowledgements

I would like to thank everyone in the perinatal imaging department for their support, encouragement and kind words during my PhD. In particular I would like to show my appreciation to my supervisors Jo and Alan for their insight, constant enthusiasm and reassurance throughout. I could not have completed this PhD without them and have gained so much from their supervision.

Thank you to the neonatal cardiac group, Alan, A-Fine, DC, Pricey and G for making even the writing up part of my PhD interesting and above all fun. The memories of the conferences and meetings will stay with/haunt me for the rest of my life.

I would also like to acknowledge Franco P and Ange in room X109 for keeping me going during all the late nights, deadlines and biscuit binges. This was particularly helpful during the final year and you are without a doubt my heroes.

A Giovanni, sempliciamente sei stato il mio supporto per sei anni, durante i periodi piu belli e bruti. Per questo ti rigraziaro' sempre.

Useless otherwise referenced, the work presented in this thesis was conducted by the author at the Imaging Sciences Centre, Hammersmith Hospital, Imperial College London and St Thomas' Hospital between October 2009 and May 2013.

This work has not been submitted for the purpose of another degree

Kathryn M Broadhouse

Contents

List of Figures

Chapter 2

Chapter 3

Chapter 4

4.1.1 PDA treatment rates

4.1.2 SNR phantom test

4.1.3 SNR calculated from PC sequences

4.1.4 Background phase errors

4.1.5 Study design

4.1.6 Brachiocephalic, left common carotid and left subclavian arteries

4.1.7 The azygos system

4.1.8 Bland-Altman analysis

4.1.9 Ductal shunt volume

4.1.10 Normative ranges

4.2.1 The principal veins and arteries that supply the intestine

4.2.2 Study design

4.2.3 Bland-Altman repeatability analysis

4.2.4 Normative ranges

4.3.1 Quantification of cerebral flow

Chapter 5

5.1.1 Frank Starling mechanism

5.3.1 Enlarged heart of the PDA infant

5.3.2 17 segmentation AHA model

5.3.3 Endo and epicardium segmentation

5.3.4 Normative ranges

5.3.5 ED thickness and fractional thickening

5.3.6 Population Frank Starling curve

5.3.7 Visual analysis of impact of hypertrophy

5.3.8 LV myocardial volume vs EDV

5.3.9 Measure of hypertrophy

5.4.1 Pulmonary blood flow

5.5.1 Normative ranges

5.5.2 Postnatal normative ranges

5.5.3 Myocardial wall analysis

5.5.4 Frank Starling curve

5.5.5 Measure of hypertrophy

Chapter 6

6.1.1 Placement of the 4D PC MRI sequence

6.1.2 Visualization of cardio vasculature

6.1.3 Analysis regions along the aorta

6.1.4 4D flow quantification

6.1.5 Agreement between 4D and 2D flow measurements

6.1.6 Aortic blood flow field

6.1.7 Visualization of a ductal shunt

6.1.8a Flow patterns within a healthy preterm infant

6.1.8b Flow patterns within a preterm infant with PDA

6.1.9 Turbulence

6.1.10 Vessel morphology

6.1.11 Chaotic flow within the duct

Chapter 7

7.2.1 Aortic PWV setup

7.2.2 Upslope regions

7.2.3 Least square fit registration

7.2.4 Aortic length

7.2.5 PWV

7.2.6 PWV

7.2.7 Aortic PWV in preterm infants

7.2.8 Normative ranges

7.2.9 Regions along the aorta

7.5.1 Hct and LVO

Chapter 8

8.2.1 Visualization of pulmonary blood flow

Appendix

A.4.1 Multiple linear regression

A.5.1 Linear regression

A.5.2 Linear regression

A.5.3 Multiple linear regression

A.6.1 Velocity vectors

A.7.1 Linear regression

List of Tables

7.2.3 Flow regime

List of Abbreviations

α - Womersley number

A - anterior

AAo -ascending aorta

AMG - Echo observer 1

AR - arrhythmia rejection

BW - birth weight/bandwidth

CAK - Echo observer 2

CBF - cerebral blood flow

cGA - corrected gestational age

CLD - chronic lung disease

CMRI - cardiac magnetic resonance imaging

CO - cardiac output

d - ductal shunt volume

DA - ductus arteriosus

DAo - descending aorta

DV - ductus venosus

ECG - electrocardiogram

ED - end diastole

ED/Max flow – end diastolic ductal blood flow velocity ratio

EDV - end diastolic volume

EF - ejection fraction

ES - end systole

FID - free induction decay

FO - foramen ovale

FOV - field of view

GA - gestation age

GE - gradient echo

Hct - Hematocrit

HR - heart rate

IVC - inferior vena cava

IVRT - isovolumetric relaxation time

L - left

LA - left atrium

LA:Ao – left atrial diameter to root ratio

loa - limits of agreement

LPA - left pulmonary artery

LV - left ventricular/ventricle

LVO - left ventricular output

LVOT - left ventricular outflow tract

MRI - magnetic resonance imaging

MyoV/EDV - LV myocardial volume to LV blood pool ratio

NEC - necrotising enterocolitis

NMR - nuclear magnetic resonance

NSA - number of signal averages

P - posterior

P1 - PDA infant 1

P2 - PDA infant 2

PA - pulmonary artery

PC - phase contrast

PDA - patent ductus arteriosus

PFO - patent foramen ovale

Post - postnatal age

PVR - pulmonary vascular resistance

PWV - pulse wave velocity

PWV-MRI - PWV measures from MRI assessment

PWV-Pres - PWV measurements from invasive pressure and ultrasound assessment

R - right

RA - right atrium

Re - Reynolds number

Rec - critical Reynolds number

RI - repeatability index

ROI - region of interest

RPA - right pulmonary artery

RV - right ventricle

RVO - right ventricular output

SaO2 - saturation level of oxygen

SE - spin echo

SI - units in the international system

SMA - superior mesenteric artery

SNR - signal to noise ratio

SSFP - steady state free precession

St - Strouhal number

SV - stroke volume

SVC - superior vena cava/caval

SVR - systemic vascular resistance

TR - repetition time

TE - echo delay time

VCG - vector cardiac gating

VnonSMA – visceral non SMA

VSD- ventricular septal defect

Chapter 1

Thesis Overview

1.1 Motivation

The incidence of premature birth is increasing in absolute number and as a proportion of all births around the world (Yeaney et al. 2007). Advances in perinatal care mean that survival rates in preterm and furthermore extremely preterm infants are increasing, but these infants are more likely to have long term morbidities and adverse neurodevelopmental outcome compared to their term born peers. 20-25% of infants born <1kg have at least one major disability and a further 50% will have subtle disabilities presenting at school age (Mangham et al. 2009).

The reasons for preterm births are numerous, poorly understood and are outside the scope of this thesis. Despite much research on its prevention, the incidence of premature birth continues to increase. It is therefore widely accepted that a focus to advance the understanding of the pathophysiology of prematurity to improve care and treatment in preterm infants is vital (Goldenberg et al. 1998).

Adverse neurodevelopmental outcome, necrotising enterocolitis (NEC) and pulmonary haemorrhaging are some of the common pathologies seen in preterm infants, all of which are associated with abnormal blood supply (Cheromcha et al. 1988) (Sankar et al. 2008) (Sasi et al. 2011). The immature preterm cardiovascular system has undergone the transformation from fetal to extra uterine life when it is not structurally equipped to do so (Agarwal et al. 2007) (Murphy, 2005) (Wyllie, 2003). The cardiovascular immaturity can result in the prolonged

patency of remnant fetal shunts, the most significant being the patent ductus arteriosus (PDA). Prolonged PDA is thought to cause abnormal pulmonary and systemic flow (Agarwal et al. 1997).

The ability of organs to function largely relies upon an adequate blood supply. It is thought that the immature preterm cardiovascular system, and more specifically the PDA and the resulting haemodynamics, correlate to the presence and development of many pathologies seen in this population (Cheromcha et al. 1988) (Volpe, 1997). The ability to reliably measure and assess preterm cardiac function and blood flow distribution in the presence and absence of PDA provides the potential to improve the understanding of the impact of ductal shunt and development and effects of certain pathologies seen in this cohort.

Magnetic resonance imaging (MRI) is a non-invasive, non ionizing imaging modality that can be used to obtain both anatomical data that provides information of cardiovascular morphology and quantitative data of blood flow and hemodynamics. Cardiac MRI (CMRI) has contributed greatly to the understanding of many cardiovascular diseases and congenital defects in paediatric and adult patients (Fogel, 2000) (Grothues et al. 2002) (Markl et al. 2004). Translating these imaging techniques to assess the preterm cardiovascular system is difficult and requires careful optimization due to their premature condition, size, significantly increased heart rate and lack of patient co-operation.

This work aims to translate the CMRI techniques widely used in adults to quantify ductal shunt volume. Then measure and assess preterm cardiac function, blood flow distribution and flow characteristics in the presence and absence of PDA to better understand the preterm cardiovascular system and impact of PDA.

1.2 Thesis outline

Chapter 2 provides an introduction into preterm and neonatal cardiovascular physiology. It begins by presenting a basic overview of the structural and functional differences of the adult, fetal and neonatal cardiovascular systems. The result of the premature transition from fetal to extra-uterine life is then illustrated. Common congenital defects are then described in more detail, in PDA. This is followed by a short introduction of the pathologies commonly associated with PDA.

In **Chapter 3** ultrasound and MRI are discussed in more detail to provide a background into both techniques and justification for the subsequent studies. A brief description of Ultrasound is given, followed by an introduction to MRI, from the basic concepts of nuclear magnetic resonance to image generation. A brief overview of cardiac MRI is then presented. This is followed by a more in depth description of phase contrast (PC) MRI. The technical aspects of perform MRI in preterm and term infants are then discussed.

In **Chapter 4** a technique to quantify cardiac output and global distribution of systemic blood flow in preterm and term infants using PC MRI is described. The accuracy and repeatability of this technique is then analysed. Blood flow distribution to the upper and lower body in healthy preterm and term infants is then presented as a function of corrected gestational age to establish the normative range. This same technique is then used to quantify ductal shunt volume and its effect on global blood flow distribution in infants with prolonged patency of the

ductus arteriosus. The significance of the presence of PDA on upper and lower body blood flow is then determined. Ductal shunt volumes were also related to echocardiography measures to determine the most robust echo measure of ductal flow.

In addition, investigations into regional blood flow distributions in preterm and term infants are then carried out. PC MRI was used to quantify cerebral blood flow in a preliminary cohort of 5 healthy infants and quantify flow to the abdominal organs in a larger group of healthy and PDA infants. These preliminary studies are presented in the final subsections of this chapter.

In **chapter 5** the left ventricular (LV) function in neonates with and without PDA is assessed using MRI. Firstly a brief overview of the mechanisms and measures of cardiac function and failure are given. This is followed by a brief introduction into a prominent acquisition used in cardiac functional MRI assessment, steady state free precession (SSFP) stack sequences. Morphological and functional cardiac data in healthy preterm and term infants is then presented. Normative ranges for LV parameters such as wall thickness and fractional thickening in healthy preterm and term are determined. The impact of ductal shunt volume on LV dimension and function is determined. Next a preliminary study to first evaluate the pulmonary flow in the presence of a PDA from right ventricular volumetric analysis and secondly to assess the feasibility of RV functional analysis from SSFP stacks is presented. In the concluding section data from treated PDA infants are presented and discussed, highlighting possible future studies to better understand the impact of PDA and treatment approach.

In **Chapter 6** 4D PC MRI is utilized to visualize aortic flow patterns in the presence and absence of a PDA. The flow field is observed by generating particle traces and velocity vectors at specific locations along the aorta in preterm infants with and without PDA. Observed neonatal flow characteristics are then compared to previously reported adult data. The limitations and possible future work are then discussed.

In **chapter 7** the aortic blood flow regime in healthy preterm and term infants is determined. The hemodynamic effect of the ductal shunt and potential presence of turbulence in the aorta is investigated. To begin with the fluid dynamic properties of blood and parameters to quantify them are introduced. A technique to quantify aortic pulse wave velocity is then described in preterm and term infants using 4D PC MRI. Initial normative ranges in this population are established to facilitate comparison with adult data. The calculation of Reynolds number (Re) from 4D PC MRI data is then described and employed to determine the blood flow regime and if turbulence is present within the aorta in infants with and without PDA. Neonatal data is then compared to previously reported adult data.

Chapter 8 summarizes the findings in the previous chapters and considers the contributions of this thesis. Possible areas of future work are then discussed.

1.3 References

Agarwal R, Deorari AK, Paul VK. Patent ductus arteriosus in preterm neonates. AIIMS-NICU protocols. 2007.

Cheromcha D, Hyman PE, Neonatal necrotizing enterocolitis. Inflammatory bowel disease of the newborn. Digestive Diseases and Sciences. 1988; 33(3): 78S-84S.

Fogel MA. Assessment of cardiac function by magnetic resonance imaging. Pediatr Cardiol. 2000; 21:59-69.

Grothues F, Smith GC, Moon JCC, Bellenger NG, Collins P, Klein HU, Pennell DJ. Comparison of interstudy reproducibility of cardiovascular magnetic resonance with two-dimensional echocardiography in normal subjects and in patients with heart failure or left ventricular hypertrophy. Am J Cardiol. 2002; 90:29–34

Goldenberg RL, Rouse DJ. Prevention of premature birth. N Engl J Med. 1998; 339: 313-320.

Mangham LJ, Petrou S, Doyle LW, Draper ES, Marlow N. The Cost of Preterm Birth Throughout Childhood in England and Wales. Pediatrics. 2009; 123: e312-e327.

Markl M, Draney MT, Hope MD, et al. Time-resolved 3-dimensional velocity mapping in the thoracic aorta: visualization of 3- directional blood flow patterns in healthy volunteers and patients. J Comput Assist Tomogr 2004;28:459–468.

Murphy PJ. The fetal circulation. British Journal of Anaesthesia. 2005; 5(4).

Sankar MJ, Agarwal R, Deorari AK, Paul VK. Chronic lung disease in newborns. AIIMS-NICU protocols. 2008

Sasi A, Deorari A. Patent ductus arteriosus in preterm infants. Indian Pediatr. 2011; 48: 301 – 308.

Volpe JJ. Brain injury in the premature infant- from pathogenesis to prevention, brain Dev 1997; 19: 519-534

Wyllie J. Treatment of patent ductus arteriosus. Semin Neonatol. 2003; 8:425-432.

Yeaney NK, Murdoch EM, Lees CC. The extremely premature neonate: anticipating and managing care. BMJ 2009; 338: b2325.

Chapter 2

An Introduction to the Preterm Cardiovascular System

This chapter provides an introduction into preterm and neonatal cardiovascular physiology. It begins by presenting a basic overview of the structural and functional differences of the adult, fetal and neonatal cardiovascular systems. The result of the premature transition from fetal to extra-uterine life is then illustrated. Common congenital defects are then described in more detail, in particular patent ductus arteriosus (PDA). This is followed by a short introduction of the pathologies commonly associated with PDA.

2.1 Cardiovascular Physiology: Adult and Fetal Circulation

Adult and fetal circulatory systems are markedly different due to the different functions and demands they must meet. The following subsections give a brief description of several of these variances.

2.1.1 The Adult Circulatory System

The adult circulatory system can be divided into the low pressure pulmonary and high pressure systemic circulation that are in series with each other (figure2.1.1). The heart consists of 2 synchronous pumps, the right and left ventricles (RV, LV), which are filled via 2 contractile reservoirs, the right or left atrium (RA, LA) (Levick, Fifth Edition, 2010, chpt 1). The RV pumps deoxygenated blood through the pulmonary artery (PA) to the lungs for gas exchange to take place. Oxygenated blood then returns via the pulmonary veins to the left side of the heart completing the short, low pressure pulmonary circulation. The LV pumps the same volume of oxygenated blood through the aorta to the tissues of the body where again gas exchange takes place (in this case delivering oxygen

and extracting carbon dioxide). Deoxygenated blood then returns to the RA via the superior and inferior vena cava (SVC, IVC), completing the long, high pressure systemic circulation. This high pressure systemic circulation causes the left ventricle wall to be around 3 times thicker than the right ventricle, so as to generate the contractile force and pressure needed for ejection (Levick, Fifth Edition, 2010, chpt 3).

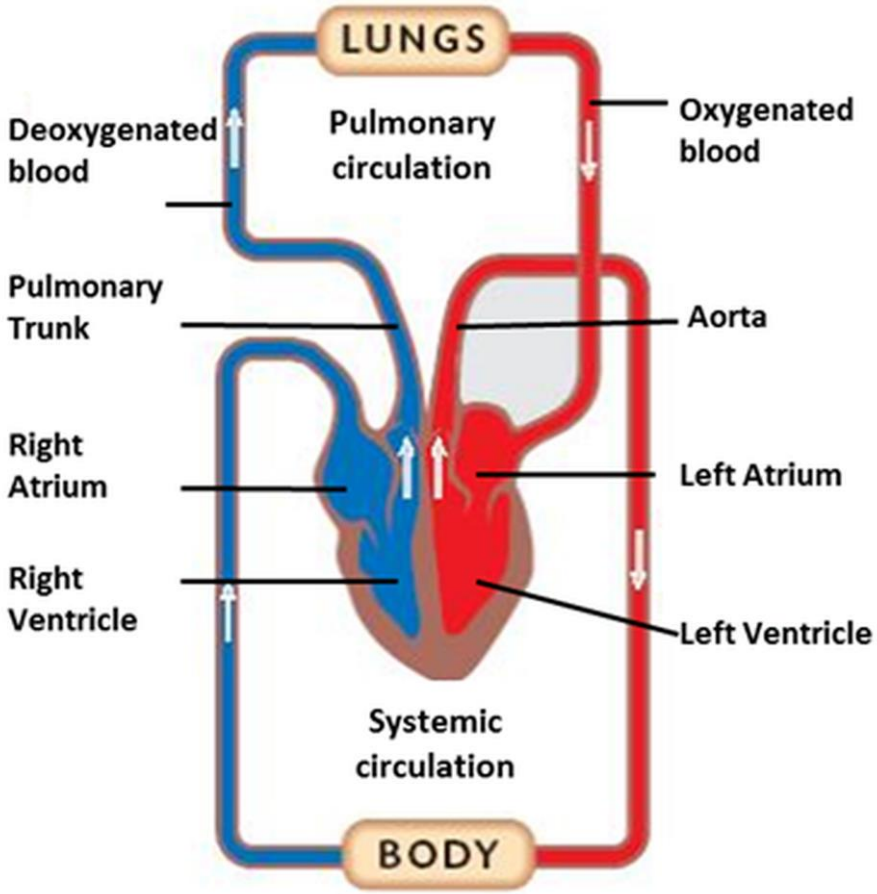

Figure 2.1.1 – The adult circulatory system: Schematic representation of the adult pulmonary and systemic circulation. Deoxygenated blood enters the pulmonary circulation via the right side of the heart. Oxygenated blood returns to the left side of the heart. From there blood enters the systemic circulation. After gas exchange between capillaries and tissue, deoxygenated blood then returns to the right side of the heart. http://leavingbio.net/circulatory%20system/circulatory%20system.htm

2.1.2 The Fetal Circulation System

Circulation in utero is markedly different from adult circulation (figure 2.1.2) as oxygenation of blood in the fetus occurs not in the lungs but in the placenta. The placenta receives deoxygenated blood from the fetal systemic organs and supplies oxygenated blood to the fetal systemic arterial system. For efficient blood flow the fetal cardiovascular system is designed so that most of the blood bypasses the lungs and the most highly oxygenated blood is delivered to the brain and myocardium. These circulatory adaptations are achieved in the fetus by both the preferential streaming of oxygenated blood and the presence of 3 intra-cardiac and extra-cardiac shunts. Thus, the fetal circulation can be defined as a 'shunt-dependent' circulation (Murphy, 2005).

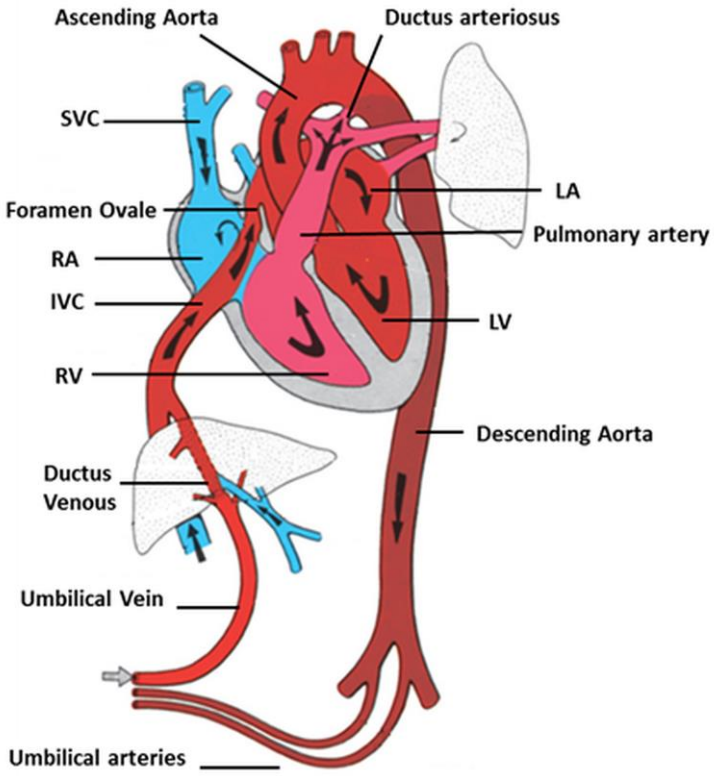

Figure 2.1.2 – The fetal circulatory system: A schematic representation of the fetal circulation. Blood oxygenation occurs at the placenta and not in the lungs giving rise to a shunt dependent circulatory system. http://www.yorksandhumberhearts.nhs.uk

Oxygenated blood at the placenta returns to the fetus via the umbilical vein, 50–60% of this placental venous flow bypasses the hepatic circulation via the ductus venosus (DV) to enter the IVC and join the extremely desaturated systemic venous flow. Preferential streaming of the high oxygenated blood starts at the junction of the IVC and the RA. The Eustachian valve tends to direct the more highly oxygenated blood, streaming along the dorsal aspect of the IVC, across the patent foramen ovale (PFO) and into the lower pressure LA (Murphy, 2005). Oxygen saturation in the LA is 65% (Dawes et al. 1954). Blood then flows through the ascending aorta via the LV where the majority of the blood is delivered to the brain and coronary circulation. Consequently ensuring that blood with the highest possible oxygen concentration is delivered to these vital structures.

Desaturated blood from the SVC is directed into the RV, and then ejected into the PA. Because of the high pulmonary vascular resistance (PVR) only about 12% of the RV output enters the pulmonary circulation, the remaining 88% crossing the ductus arteriosus (DA) into the descending aorta. The lower half of the body is thus supplied with relatively desaturated blood (Murphy, 2005). Deoxygenated blood then arrives back at the placenta via the umbilical artery.

The DA and PFO not only ensure the preferential streaming of high oxygenated blood to the essential organs but also ensure efficient blood flow bypassing the lungs. In fetal life the DA carries most of the right ventricular output (RVO) and develops to be the same size as the descending aorta approaching term (~10mm) (Agarwal et al. 2007).

Due to these circulatory shunts the right and left fetal ventricular pressures are very similar (Kiserud, 2005). The RV is thought to be the dominant ventricle; the RVO is generally higher than the left ventricular output (LVO) during the second half of pregnancy with the difference decreasing towards term (Kiserud, 2005). Similarly the RV wall and function is greater than the LV with this dominance decreasing towards term (Smolich, 1995).

2.2 Cardiovascular Physiology: Transition from Fetal to Extra-uterine Life

2.2.1 Normal Transition at Term

Several cardio-pulmonary adaptations must be made during the transition from fetal to extra-uterine life. The role of blood oxygenation must transfer from the placenta to the lungs, the DV and DA shunts must close and the LVO must increase (Murphy, 2005). With the placental circulation removed at birth there is a decrease in blood flow through the DV and a significant fall in the venous return through the IVC. This initiates the closure of the DV which closes passively around 4 days after birth (Kondo et al. 2001) separating the hepatoportal and systemic circulation.

PVR decreases gradually during late gestation up until birth, where after expansion of the lungs, there is a dramatic fall in PVR and an 8–10-fold increase in pulmonary blood flow. This drop in PVR may relate simply to expansion of the lungs, opening up pulmonary vessels, though stimulation of pulmonary stretch receptors resulting in reflex vasodilatation is thought to mediate, in part, this process (Murphy, 2005). Increased oxygen saturation of neonatal blood also reverses the pulmonary vasoconstriction caused by hypoxia, further reducing PVR.

The increase in pulmonary blood flow leads to a significant rise in pulmonary venous return to the LA. As stated above the decrease in IVC flow results in a fall in venous return to the RA. These two factors cause the LA pressure to exceed the RA pressure (Wilmshurst et al. 1994). The foramen ovale is pushed against the atrial septum and the atrial shunt is effectually closed separating the right and left chambers of the heart. This functional closure of the foramen ovale occurs within minutes to days of birth. Anatomical closure occurs later via tissue proliferation (Patten, 1931).

The exact mechanism of DA closure is complex and poorly understood, however the increased levels of oxygen in neonatal blood produces direct constriction of spiral of smooth muscle within the duct. It has been postulated that towards term the duct wall muscles become increasingly less sensitive to the dilating effects of prostaglandin and more responsive to the constrictive effects of oxygen

(Wyllie, 2003). The rapid fall after birth of prostaglandin E2 concentrations produced by the placenta adds to ductal constriction (Murphy, 2005).

Prior to birth the DA carries virtually all of the RVO in a right-to-left shunt. As the PVR drops the DA shunt becomes initially bidirectional (right-to-left during systole, left-to-right during diastole). Within hours the shunt then becomes purely left-to-right. However both the bidirectional and left-to-right phases carry a much lower proportion of the RVO than the antenatal right-to-left pattern, this decrease in shunt volume also contributes to functional closure. The actual closure of the ductus takes place in two stages. In healthy full term newborns, functional ductal closure occurs within 96 hours of birth (Reller et al. 1989) (Wyllie, 2003) separating the pulmonary and systemic circulation, blood flow resembles that of adults. This functional closure is followed later by anatomical closure via endothelial and fibrous tissue proliferation (Agarwal et al. 2007).

2.2.2 The Premature Cardiovascular System

Premature transition

All infants born <37 weeks gestation are considered preterm infants (Goldenberg et al. 1998). The preterm infant's cardiovascular system undergoes the transformation from fetal to extra-uterine life when it is not structurally equipped to do so. The transition and adaptation of the respiratory, endocrine, metabolic, and nervous systems from the intra-uterine to the extra-uterine environment are largely outside the scope of this thesis. The most abrupt adaptations are seen in the circulatory system as to maintain adequate blood flow to the developing organs in the two extreme environments require very different circulations as outlined above. The closure of the three shunts as part of the intra to extra-uterine transition has been shown to be delayed in preterm infants (Agarwal et al. 2007) (Danilowicz et al. 1966) (Ghiglia et al. 2008) (Kondo et al. 2001).

The delay in circulatory adaption is thought to contribute to abnormal hemodynamics and organ perfusion in preterm infants (Agarwal et al. 2007) (Schmitz et al. 2004) (Volpe, 1997). However the resultant effects of the immature circulatory system are numerous, complex and poorly understood as both the body tissues and the circulation supplying them are immature. The immature organs need an adequate blood supply for continuing development whilst being required to function as their mature counterparts. As well as the possible abnormal flow caused by the morphology, the capacity for autoregulation in preterm infants is thought to be limited (Greisen, 2005). It is thought that the immature preterm cardiovascular system and the resulting haemodynamics correlate to the presence and development of the pathologies seen in this population.

Closure of the Ductus Venous

A delayed closure of the DV has been found in preterm infants with no significant correlation to the closure of the ductus arteriosus or the condition of the infant. It is speculated that immaturity of the DV and possibly increased levels of dilating prostaglandins leads to a delayed obliteration of the vessel (Fugelseth et al. 1998). An open DV represents a portocaval shunt and may have metabolic and pharmacological consequences, but has been the subject of very little study as it is regarded as having little pathophysiological significance and is outside the scope of this thesis.

Closure of the Foramen Ovale

Delayed closure of the foramen ovale most commonly leads to left to right atrial shunting and consequently an increase in pulmonary blood flow (pure right to left shunting is uncommon in preterm infants), and may be an additional risk factor in the development of chronic lung disease (CLD) (Evans et al. 1994). Due to the multifactorial etiology of CLD in preterm infant, definite association between the two is challenging. Studies have also shown no clinical relevance to a PFO in

preterm and term infants (Ghiglia et al. 2008). In addition in 20% of healthy adults the FO has not closed completely leading to a small PFO (Wilmshurst et al. 1978). Consequently it is thought that in most neonates a PFO is benign (Ghiglia et al. 2008).

Closure of the Ductus Arteriosus

Persistent PDA is the prolonged opening of the DA and is clinically apparent in 60% of infants born before 28 weeks gestation and 20% of infants born after 32 weeks gestation (Wyllie, 2003). Closure of the duct in healthy preterm and term infants has been shown to occur within 4 days of birth (Reller et al. 1989). It is thought that insufficient smooth muscle migration and the increased sensitivity to prostaglandins of the ductal smooth muscle compared to term infants results in a prolonged opening of the duct after birth (Agarwal et al. 2007).

As PVR decreases and systemic vascular resistance (SVR) increases after birth, the pressure gradient across the DA from high systemic pressure to the low pulmonary pressure causes blood to flow through the duct predominantly from left to right. Hence the functionality of the DA is reversed from that of fetal circulation and blood now flows from the aorta into the pulmonary arteries (figure 2.2.1).

A prolonged left to right ductal shunt is thought to cause pulmonary hyper-perfusion and systemic hypo-perfusion (Agarwal et al. 1997). Consequently PDA has been associated with the common preterm pathologies, necrotising enterocolitis (Ryder et al. 1980), chronic lung disease (Jones et al. 1977), adverse neurodevelopmental outcome and congestive heart failure (Sasi et al. 2011), whether this association is causal or casual remains unclear as little is known about how persistent PDA effects blood flow patterns and distribution in the pulmonary arteries, aorta and surrounding vessels. It is important to note that the natural course of the duct is to close, although prolonged opening of the duct is thought to cause or exacerbate pathologies in this population.

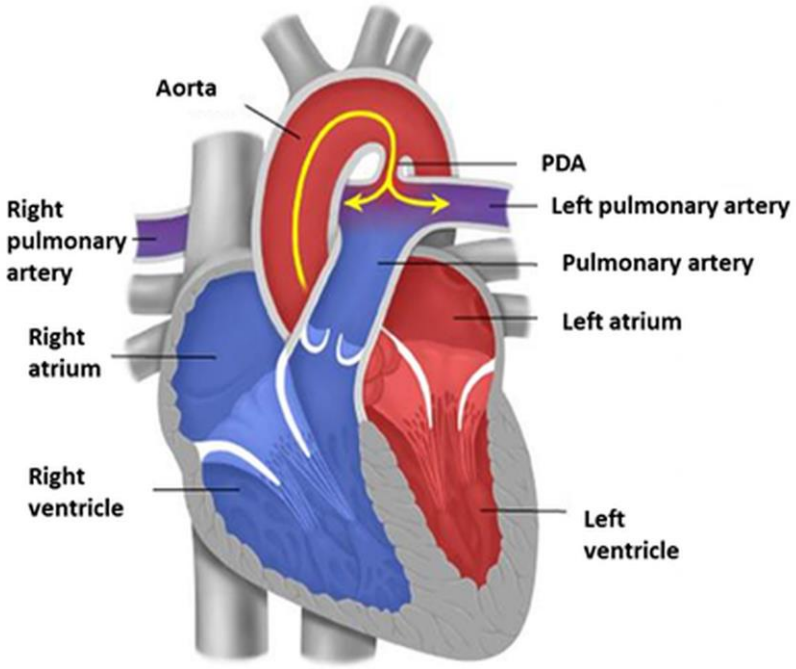

Figure 2.2.1 – Patent Ductus Arteriosus: Schematic representation of the Patent Ductus Arteriosus and the resultant flow after birth. The decrease in PVR and increase in systemic resistance creating the pressure gradient across the DA from high systemic pressure to the low pulmonary pressure causes blood to flow through the duct predominantly from left to right. http://www. drmiri.com

In the following chapters the diagnosis of PDA and current controversy over treatment approach are described fully. Work to quantify the ductal shunt volume and investigate the cardiac function, flow distribution and flow characteristics in the absence and presence of PDA is then presented. By providing additional quantitative flow and functional information the hemodynamic significance of the PDA and clinical association with pathology may be better understood. The following subsection in this chapter gives a brief overview of the previously mentioned pathologies associated with PDA.

2.3 Common Pathologies associated with PDA

Adverse neurodevelopmental outcome is common in the preterm infant population, a longitudinal study performed throughout England and Wales in 2009 demonstrated that 20-25% of infants born

<1kg have at least one major disability and a further 50% will have subtle disabilities presenting at school age (Mangham et al. 2009). Insufficient or alterations in cerebral blood flow (CBF) due to the immature preterm cardiovascular system are considered to play a major role in neurological development and subsequent neurological pathologies (Volpe, 1997). It is thought that systemic hypo-perfusion caused from large PDA shunt volumes has a negative effect on cerebral perfusion and may lead to injury in the immature brain (Lemmers et al. 2008) (Sasi et al. 2011).

Necrotizing enterocolitis (NEC) is one of the most common gastrointestinal conditions that is primarily present in preterm infants. The pathogenesis remains unclear but it is widely accepted that it is the death of intestinal tissue caused by mucosal injury. Incidence rates are inversely related to birth weight and gestational age, affecting 9% of infants with birth weight between 751-1000g with mortality rates ranging from 15-30% (Lin et al. 2006). NEC can occur anywhere in the gastrointestinal tract but is most commonly found in the small intestine and can be difficult to treat (Lin et al. 2006). There have been many studies to investigate the onset of the disease but the principal reasons are thought to be structural immaturity of the bowel wall and ischemia (Cheromcha et al. 1988). An ischaemic pathophysiology is also supported by the relatively high incidence of NEC in term infants with structural congenital heart disease.

It is suggested that in stressed preterm infants redistribution of cardiac output can occur to maintain sufficient blood flow to the vital organs such as the brain and kidneys causing diminished perfusion to intestinal mucosa. The reduced systemic perfusion associated with PDA is thought to exacerbate or lead to reduced abdominal flow (Coombes et al. 1990). Understanding of pathogenesis of adverse neurodevelopmental outcome and NEC in preterm infants is significantly hampered by the absence of useable biomarkers. In addition ultrasound flow measures are unreliable. A non-invasive, accurate measure of global cerebral and intestinal blood flow could significantly improve understanding of physiology and pathophysiology.

Chronic lung disease occurs in preterm infants who require mechanical ventilation and/or oxygen therapy for a primary lung disorder and results from oxidative stress and ventilator induced lung injury. Exposure to high oxygen concentrations and positive pressure ventilation can lead to damage of the immature lungs and result in abnormal reparative processes in the lungs (scaring of lung tissue) (Sankar et al. 2008). CLD has a multifactorial etiology, however the main factor in its pathogenesis is prematurity. Infants with CLD are more likely to have persistent respiratory symptoms later on in life. PDA contributes further to this process causing hyper-perfusion of the pulmonary circulation leading to pulmonary edema and vascular endothelial injury (Bancalari et al. 2005) (Marshall et al. 1999). Often infants with persistent PDA require long periods of respiratory support (Jones et al. 1977).

Cardiac function

It is common clinical belief that large ductal shunt volumes are associated with congestive heart failure (Agarwal et al. 2007) (Baylen et al. 1977) (Schmitz et al. 2003). This has arisen mainly from the idea that large shunt volumes lead to systemic hypo-perfusion and pulmonary hyper-perfusion due to cardiocirculatory dysfunction. Left to right ductal shunting increased blood flow returning to the LV leading to increased atrial and ventricular end diastolic pressure. This may lead to hypertrophy in infants with PDA (Baylen et al. 1977) (Schneider et al. 2006). Echocardiography studies have also shown a decrease in diastolic function in infants with a PDA (Schmitz et al. 2003), yet the association with shunt volume and cardiac function in preterm infants with PDA is poorly understood. The association with reduced systemic blood flow, respiratory distress syndrome, the observed ventricular enlargement and ventricular overload in PDA infants has meant that some ducts are treated in the effort to prevent cardiac failure (Sasi et al. 2011).

2.4 References

Agarwal R, Deorari AK, Paul VK. Patent ductus arteriosus in preterm neonates. AIIMS-NICU protocols. 2007.

Baylen BG, Meyer RA, Kaplan S, Ringenburg WE, Korfhagen J. The critically ill premature infant with patent ductus arteriosus and pulmonary disease – an echocardiographic assessment. J. Pediatr. 1975; 3: 423-432.

Bancalari E, Claure N, Gonzalez A. Patent ductus arteriosus and respiratory outcome in premature infants. Biol Neonate. 2005; 88: 192 – 201.

Cheromcha D, Hyman PE, Neonatal necrotizing enterocolitis. Inflammatory bowel disease of the newborn. Digestive Diseases and Sciences. 1988; 33(3): 78S-84S.

Coombs RC, Morgan MEI, Durbin GM, Booth IW, McNeish AS. Gut blood flow velocities in the newbom: effects of patent ductus arteriosus and parenteral indomethacin. Arch Dis Child. 1990; 65: 67-71.

Danilowicz D, Rudolph AM, Hoffman JIE. Delayed closure of the ductus arteriosus in premature infants. Pediatrics 1966; 37:74–8.

Dawes GS, Mott JC, Widdicombe JG. The foetal circulation of the lamb. J Physiol 1954; 126: 563–568

Evans N, Iyer P. Incompetence of the foramen ovale in preterm infants supported by mechanical ventilation. J. Pediatr. 1994; 125(5): 786-792.

Fugelseth D, Lindemann R, Liestol K, Kiserud T, Langslet A. Postnatal closure of ductus venosus in preterm infants ≤ 32 weeks. An ultrasound study. Early Hum Dev. 1998; 53:163-169.

Ghiglia S, Fesslova V. Patency of foramen ovale in fullterm and preterm neonates. A follow-up study. Pediatr Med Chir. 2008; 30(4): 192-196.

Goldenberg RL, Rouse DJ. Prevention of premature birth. N Engl J Med. 1998; 339: 313-320.

Greisen G. Autoregulation of cerebral blood flow in newborn babies. Early Hum Dev. 2005; 81: 423-428

Jones RWA, Pickering D. Persistent ductus arteriosus complicating respiratory distress syndrome. Arch Dis Child 1977; 52:274–81.

Kiserud T. Physiology of the fetal circulation. Semin in Fetal & Neonat Med. 2005; 10: 493-503

Kondo M, Itoh S, Kunikata T, Kusaka T, Ozaki T, Isobe K, S Onishi S. Time of closure of ductus venosus in term and preterm neonates. Arch Dis Child Fetal Neonatal Ed 2001; 85: F57–F59.

Lemmers PMA, Toet MC, van Bel F. Impact of patent ductus arteriosus and subsequent therapy with indomethacin on cerebral oxygenation in preterm infants. Pediatrics. 2008; 121: 142-147.

Levick JR. An introduction to cardiovascular physiology. Fifth edition. 2010

Lin PW, Stoll BJ. Necrotising enterocolitis. Lancet 2006; 368: 1271–83

Mangham LJ, Petrou S, Doyle LW, Draper ES, Marlow N. The Cost of Preterm Birth Throughout Childhood in England and Wales. Pediatrics 2009;123;e312-e327.

Marshall DD, Kotelchuck M, Young TE, Bose CL, Kruyer L, O'Shea TM. Risk factors for chronic lung disease in the surfactant era: a North Carolina population-based study of very low birth weight infants. North Carolina Neonatologists Association Pediatrics. 1999; 104(6): 1345–1350.

Murphy PJ. The fetal circulation. British Journal of Anaesthesia. 2005; 5(4).

Patten BM. The closure of the foramen ovale. American Journal of Anatomy. 1931;48:19- 44.

Reller MD, Zeigler ML, Rice MJ et al. Duration of ductal shunt in healthy preterm infants: an echocardiographic color flow Doppler study. J Pediatr 1989;112:441–6.

Ryder RW, Shelton JD, Quinan D. Necrotising enterocolitis: A prospective multicenter investigation. Am J Epidemiol;. 1980; 112: 113-123.

Sankar MJ, Agarwal R, Deorari AK, Paul VK. Chronic lung disease in newborns. AIIMS-NICU protocols. 2008

Sasi A, Deorari A. Patent ductus arteriosus in preterm infants. Indian Pediatr. 2011; 48: 301 – 308.

Schmitz L, Stiller B, Koch H, Koehne P, Lange P. Diastolic left ventricular function in preterm infants with a patent ductus arteriosus: a serial Doppler echocardiography study. Early Hum Dev. 2004; 76: 91-100.

Schneider DJ, Moore JW. Patent ductus arteriosus. Circ. 2006; 114: 1873 – 1882.

Smolich JJ. Ultrastructural and functional features of the developing mammalian heart: a brief overview. Reprod Fertil Dev. 1995; 7(3): 451-61.

Volpe JJ. Brain injury in the premature infant- from pathogenesis to prevention, brain Dev 1997; 19: 519-534

Wilmshurst PT, de Belder MA. Editorial. Patent foramen ovale in adult life. Br Heart J. 1994;71:209-212 rate of incidence of PFO in adults

Wyllie J. Treatment of patent ductus arteriosus. Semin Neonatol. 2003; 8:425-432.

Chapter 3

Neonatal Imaging: An Introduction to Magnetic Resonance Imaging

Due to the fragile state of preterm infants imaging modalities used in the population must be non-invasive, non-ionizing, relatively fast, suitable for non-cooperative patients and compatible with monitoring. This has led to ultrasound being the predominant modality used in neonatal and in particular neonatal cardiac assessments. In recent years however magnetic resonance imaging has become an invaluable research tool investigating preterm cerebral development (Boardman et al. 2006) (Counsell et al. 2005) (Miller et al. 2002) (Woodward et al. 2006). It is anticipated that the development of neonatal cardiac MRI has the potential to provide additional hemodynamic and functional information.

In the following subsections of this chapter ultrasound and MRI are discussed in more detail to provide a background into both techniques and context for subsequent studies. A brief description of Ultrasound is given, followed by an introduction to MRI, from the basic concepts of nuclear magnetic resonance (NMR) to image generation. A brief overview of cardiac MRI is then presented. This is followed by a more in depth description of phase contrast (PC) MRI. The technical aspects of performing MRI in preterm and term infants is then discussed.

3.1 Ultrasound

Medical ultrasound uses high frequency sound to aid in the diagnosis of patients. It produces high quality temporal and spatial information of structural anatomy and blood velocity traces and is easily available, non-invasive, non-ionizing and runs at a relatively low cost. Ultrasound techniques in the newborn can be performed in real time at the cotside, by a range of trained personnel, and if performed carefully need not significantly disturb infants' cardio-respiratory status (Groves et al.

2005a). The field of ultrasound is expansive, complex and for the most part outside the scope of this thesis. The basic principles and common usage are briefly described below for clarity in subsequent chapters.

3.1.1 Fundamental Principles

The generation of waves for the medical ultrasound is achieved by the piezoelectric effect, the mechanical oscillations of ultrasound piezoelectric crystals excited by electric pulses (Wild, 1950). As sound waves propagate through the body, reflections occur at the boundaries of tissues of varying acoustic densities, with the reflection proportionate to the difference in acoustic density. The time between emission of the propagated wave and arrival of the reflected wave depends on the speed of sound in tissue and the depth of the boundary and is directly used to create a depth axis in US images. Acoustic shadows occur behind boundaries with large acoustic differences where the sound is almost all reflected, such as bone and air interfaces. This can cause problems particular when imaging organs near the lungs such as the heart. The field of view (FOV) is also limited by the trade-off between high spatial resolution and imaging depth due to the attenuation of high frequencies within tissue (Hill, second Edition, 1986, chpt 4).

3.1.2 Echocardiography

Echocardiography is one of the most widely used diagnostic tests in cardiology and provides information on pumping capacity, internal chamber size quantification, wall thickness and the location and extent of any myocardial tissue damage (Levick, Fifth Edition, 2010, chpt 2) (Schiller et al. 1989) (Urheim et al. 2000). Many modes of ultrasound exist and are utilized in clinical and research examinations. Brief descriptions of two of the most common are given below.

M-mode (motion mode) echocardiography provides the position of anatomical features against time, giving display of the myocardium and valve leaflets (figure 3.1.1/2). This mode is also used to reveal and assess pathologies, abnormal wall motion, hypertrophy, as well as quantification of cardiac contractility. (Levick, fifth Edition, 2010, chpt 2)

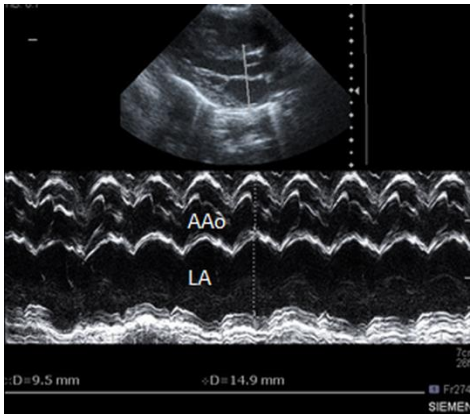

Figure 3.1.1 – M-mode image: depiction of the left ventricular outflow tract: The real time trace of the ascending aorta (AAo) and left atrium (LA) can be seen. Real time trace provides quantification of vessel and chamber diameter.

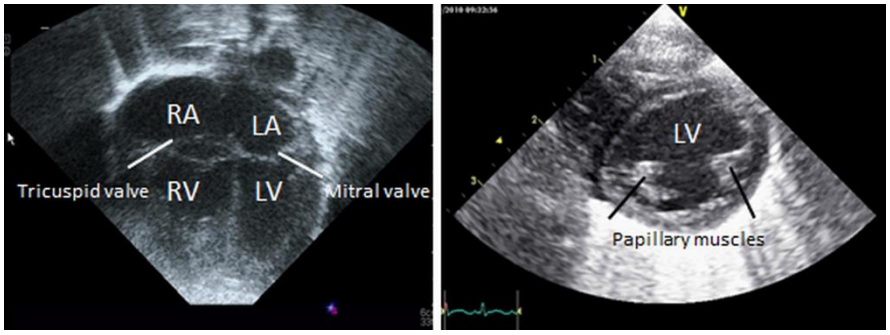

Figure 3.1.2 – Standard 4 chamber and short axis views in a neonate: Ultrasound provides real time images of valve movement and wall motion. Measurements can then be taken to quantify contractility. The four chamber of the heart (right and left atria and ventricles (RA, LA, RV, LV)) can be seen clearly.

Doppler echocardiography provides information of blood flow velocity from the frequency difference between emitted and received ultrasound waves. The difference in frequency is altered by and depends on the velocity of the flowing blood cells (Levick, fifth Edition, 2010, chpt2) (figure 3.1.3/4). Flow estimation using ultrasound is carried out by measuring the vessel diameter with the

transducer perpendicular to the vessel and blood velocity trace with the transducer parallel to the vessel. The diameter is then squared and multiplied by the velocity trace, which has been averaged over a few cardiac cycles.

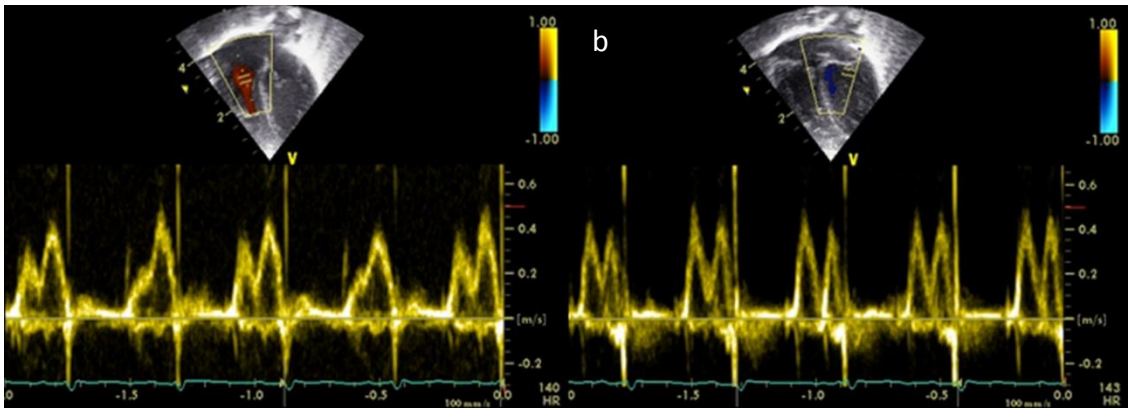

Figure 3.1.3 – Doppler ultrasound: Tricuspid (a) and mitral (b) valve inflow in a neonatal heart visualized with colour Doppler ultrasound.

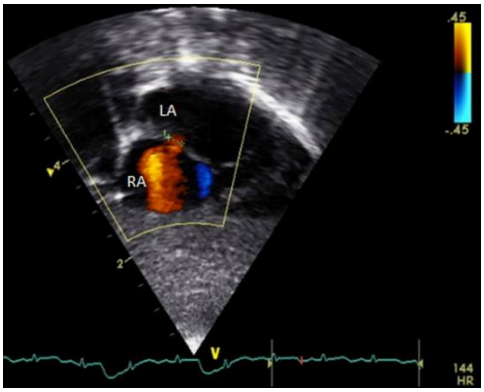

Figure 3.1.4 – Visualization of patent foramen ovale (PFO): the volume of shunt from the LA to the RA can be clearly visualized using colour Doppler ultrasound in a neonate.

3.1.3 Limitations

The relatively low cost, cot-side examinations, accessible user interface and high quality morphological information acquired has lead ultrasound to be the principal modality used in the neonatal clinic. However ultrasound has multiple limitations that reduce the accuracy and capability of functional assessments. Firstly the ability to image anatomy and vessels and therefore quantify

blood flow with ultrasound is limited by the imaging window; bone and air spaces within the body cause acoustic shadows. This and the topography of particular vessels can cause problems when angling the transducer correctly to estimating flow and diameter. This angle dependency to accurately measure the velocity trace and diameter when quantifying blood flow introduces variability and error within the measurement (Groves et al. 2005b). Secondly Doppler ultrasound assumes a constant velocity over the entire vessel area and the calculation of the area (diameter squared) assumes a circular vessel leading to inaccuracies in flow measurements. As a result ultrasound is a highly user dependent technique with often poor repeatability (Groves et al, 2005b) and consequently functional imaging is compromised. Often blood flow volume cannot be accurately quantified in some vessels and shunts, such as the common carotid arteries and PDA. Due to these limitations other imaging modalities are often needed to provide additional functional information.

3.2 Magnetic Resonance Imaging

Magnetic resonance imaging (MRI) is a multi-planar and multi-contrast modality used in a medical and research capacity, that utilizes the properties of protons in certain atomic nuclei. This imaging modality is principally based upon sensitivity to the presence of water to create an image. As the presence and properties of water can alter dramatically with pathology MRI is a very sensitive diagnostic technique. Its non-ionizing, non-invasive nature, flexibility and sensitivity to a broad range of tissue properties has led to MRI to be an attractive modality for patients and research. The multi-planar, multi-contrast nature of MRI allows blood flow quantification as well as structural information to be determined from relatively short scan times. Consequently MRI has become increasingly used in the clinical setting, with cardiac assessment as a growing application and is ideal for neonatal imaging.

3.2.1 Nuclear Magnetic Resonance

The fundamental principles of MRI originate from the work carried out in nuclear magnetic resonance. NMR is a physical phenomenon in which magnetic nuclei in a magnetic field absorb and re-emit electromagnetic radiation. The resonant frequency of this emitted radiation is directly proportional to the strength of the applied magnetic field and the magnetic properties of the isotope of the atoms. In 1952 Felix Bloch and Edward Purcell were granted a Nobel Prize for "their development of new methods for nuclear magnetic precision measurements". In 1973 Paul Lauterbur proposed using magnetic field gradients to distinguish between NMR signals originating from different locations creating "Zeugmatography" (Lauterbur et al. 1973). In addition, in 1973 Mansfield and Grannell described sensitizing tomographic image slices (Mansfield et al. 1973). These and numerous other studies combined with the development of superconducting magnets led to the development of MRI for the clinical and research environment.

3.2.2 MRI: Fundamental Principles

As MRI is derived from NMR its fundamental principles are established with the interaction between atomic nuclear spins and an applied magnetic field. The dominant nucleus in MRI is the hydrogen proton due to its abundance, water makes up 60-90% of most tissues (McRobbie, Second Edition, 2007, chpt 1.1). MRI relies on the ability to manipulate with a combination of magnetic fields, and then detect, the NMR properties of hydrogen protons or spins in water, fat and other organic molecules (Haacke, 1999, chpt 1.1). The NMR description of the individual hydrogen spins and changes in energy state requires a quantum mechanical approach. Yet given the large number of atoms contributing to the MR signal in imaging the human body a collection of spins can be considered as a spin packet and often a classical mechanical approach is sufficient for describing the behaviour of these spin systems.

Nuclear spin and magnetic moments

The particles within the atomic nucleus, nucleons (protons and neutrons), possess the quantum property spin, S, a quantum number that parameterizes the intrinsic angular momentum of a given particle (McRobbie, Second Edition, 2007, chpt 8.3). The spin of a nucleus is restricted to 0, integer and ½ integer values (as the nucleons individual spin combine or cancel) which can be defined with the magnetic quantum number m which ranges from –S to +S in integer steps. Hence the number of allowed angular momentum states are (2S+1). For the hydrogen nucleus there are two possible angular momentum states m = ±1/2. This rotating positively charge proton has an associated magnetic field known as the magnetic moment μ, which is related to S defined by equation 3.1.

$$\mu = \gamma \hbar S \tag{3.1}$$

Where γ is the gyromagnetic ratio and ħ = h/2π the reduced Planck's constant.

Magnetic moments within an external magnetic field

In the presence of an external magnetic field, B_0, the spins interact with the B_0 field and the corresponding energy E (described in equation 3.2) of their magnetic moments is directly proportional to the field strength (convention defines the z axis to be parallel with the direction of B_0). Each hydrogen proton can reside in one of the two, m=±1/2 quantized angular momentum or energy states depending on its internal energy (Haacke, 1999, chpt 1.3). The difference between the two energy states ΔE is described in equation 3.3.

$$E = \mu_Z B_0 \tag{3.2}$$

Where μ_z is the magnetic moment aligned with the B_0 along the z direction.

$$\Delta E = \gamma \hbar B_0 \tag{3.3}$$

The spins cannot align exactly along the B_0 field; due to their quantized angular momentum states, there orientation is also quantized. The spins of the hydrogen proton align almost parallel (spin up) and anti-parallel (spin down) with the B_0 field. The proton's spin therefore experience a torque and precess around the direction of the B_0 field with a precessional frequency proportional to the strength of the applied external B_0 field (see figure 3.2.1) described in equation 3.4.

$$\omega_0 = \gamma B_0 \tag{3.4}$$

where ω_0 is the precessional frequency corresponding to the B field experienced by the spin system, known as the Larmor frequency. In water the hydrogen proton has a $\gamma \approx 2.68 \times 10^8$ rad/s/T or $42.57 MH_z T^{-1}$.

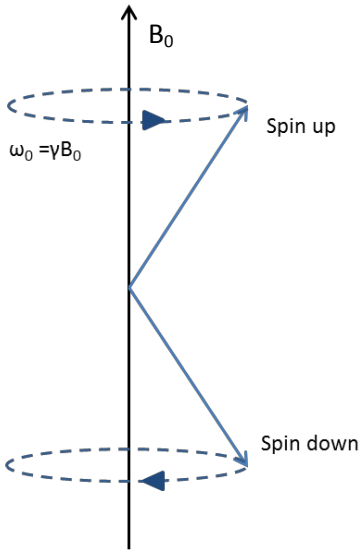

Figure 3.2.1 – Spin states of the hydrogen proton: a schematic representation of the two possible orientations of the hydrogen proton in an external B_0 field. These two energy levels are known as spin up (parallel) and spin down (anti-parallel). Both rotate in opposite directions at the Larmor frequency.

Population of Energy States and Signal Origin

The proton population of these two energy states, which is directly proportional to the ΔE (and therefore B_0 field strength) and inversely to temperature, is slightly preferential towards the lower energy state (parallel or spin up) (described by the Boltzmann distribution). This results in an excess

number of protons in the lower state ≈ 3 ppm per Tesla at room temperature (Haacke, 1999, chpt 1.3). This very small difference creates a net magnetization M_0 and is the origin of the signal needed to create an MRI image. Although this is small there are ≈ 10^{22} hydrogen protons per ml of water leading to M_0 of the order of μT for clinical field strengths (McRobbie, Second Edition, 2007, chpt 8.3).

Due to the sheer number of hydrogen protons in the human body and specifically within a voxel it is simpler to consider the averaged net magnetization of many protons (spin system) (Figure 3.2.2). A classical mechanical description can now be used for this macroscopic system. M_0 can now be used to describe the net macroscopic magnetization vector of the spin system that is aligned with the B_0 field. M_0 depends on the density of protons (spin density (ρ)) within a certain tissue type and more specifically the number of mobile spins available to align with the external B_0 field. The proton density determines the maximum signal S_0 from a certain tissue for a certain field strength. The magnitude of M_0 is considerably smaller than the main field and whilst aligned with the main field, cannot be detected. By applying an orthogonal magnetic field B_1 oscillating at the resonant Larmor frequency the net magnetization vector can be rotated such that a component of the magnetization lies in the orthogonal (transverse x-y) plane. Once the B_1 field is switched off the component of the magnetization that is in the transverse plane M_{XY} oscillates and is now a significant signal in the x-y plane that can be identified by coherent detection methods.

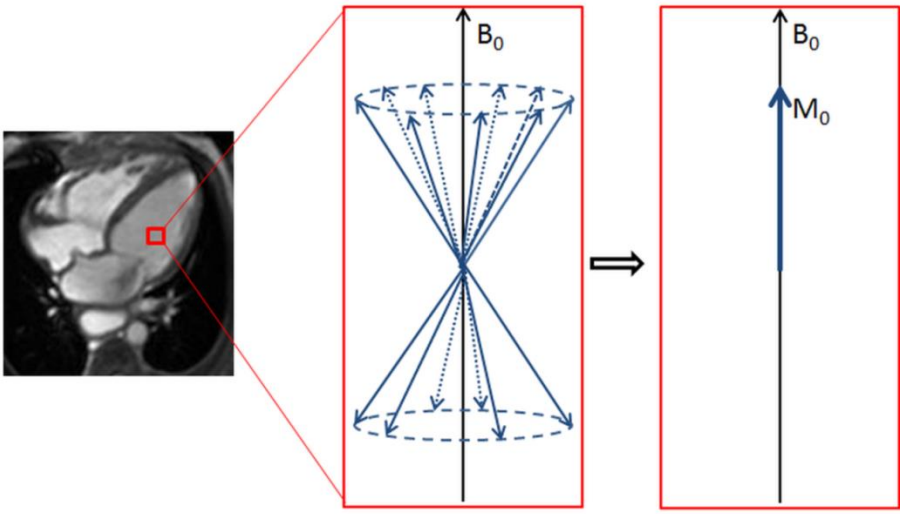

Figure 3.2.2 – Net magnetization: A spin system represented as the net magnetization vector M_0. Excess spins in the spin up energy state lead to a net magnetization aligned parallel along the B_0 field direction. This very small but measurable magnetization is the origin of MRI. This averaged macroscopic net magnetization representation of spin systems is used to define the generation of images.

3.2.3 Excitation: RF Pulses

Radio Frequency (RF) pulses within the transmit coil generate the oscillating B_1 field (convention is along the x axis). In the quantum description the B_1 field interacts with the net magnetization vector M_0 and excites the spins to the higher energy state. In the classical description, as the RF pulse is played out this excitation causes M_0 to spiral away from the z axis down towards the transverse plane (figure 3.2.3). At this point it easier to move away from the laboratory frame of reference with coordinates x, y, z and consider a rotating frame of reference with coordinate system x', y', z' that rotates about z' (in this example the rotating frame rotates at the Larmor frequency and therefore z = z'). In this frame B_1 is static and acts along the x' axis (see Figure 3.2.3). In this rotating frame M_0 is seen to flip down towards the transverse plane and align with the y' axis, the z (longitudinal) component of the net magnetization M_Z diminishes as the transverse component, M_{XY} increases. The degree at which M_0 is tilted away from the z' axis is known as the flip angle α, and can be manipulated by altering the duration (τ) or strength of the RF pulse, as described in equation 3.5.

$$\alpha = \int_0^t \omega_1(\tau)d\tau \quad (3.5)$$

where ω_1 is the Larmor frequency appropriate for B_1. The relationship between the flip angle and magnitude of M_{XY} and M_Z can be described in equations 3.6 and 3.7 (For a 90^o pulse all the magnetization is in the x-y plane).

$$M_{XY} = M_0 \cos \alpha \quad (3.6)$$

$$M_Z = M_0 \sin \alpha \quad (3.7)$$

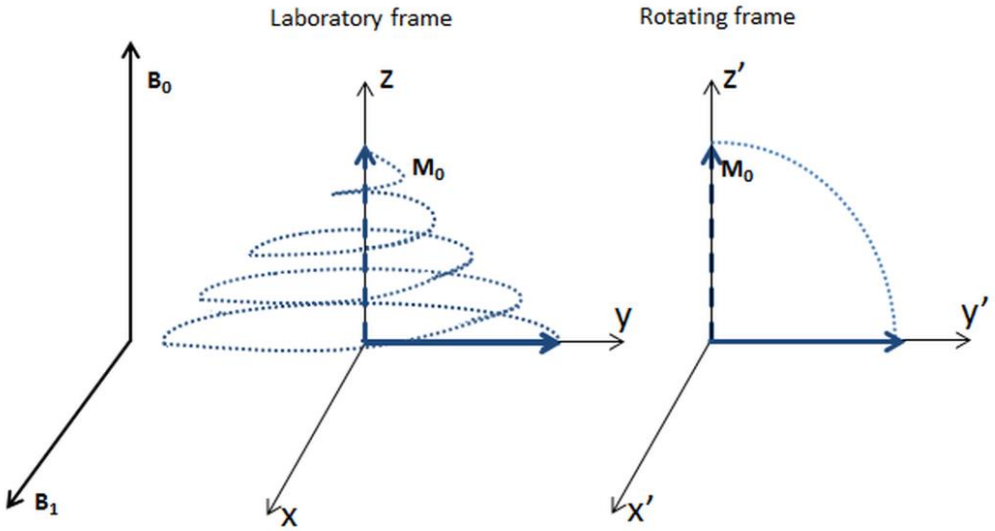

Figure 3.2.3 – Laboratory and rotating frames of reference: In the laboratory frame M_0 precesses around the z axis down to the transverse frame, when viewed in the rotating frame M_0 is simply flipped down to align with the y' axis. B_0 and B_1 are conventionally applied along the z and x axes respectively.

3.2.4 Relaxation: T_1, T_2 and T2* decay

After the RF pulse is switched off the excited protons begin to relax back to equilibrium. The process of relaxation in which energy exchange occurs can be separated into two interactions. Spin-spin interactions (T_2) diminish transverse magnetization via dephasing of the spins. Spin-lattice interactions (T_1) lead to an increase in longitudinal magnetization due to a net energy loss as spins relax back in to the lower energy state and realign along the z axis. The origin and effect of these decay times are fundamental to MRI as different tissues have inherently different decay times, manipulating these gives rise to different contrast images (T_1 or T_2 weighted images), a principal feature of an MRI examination.

Spin-spin relaxation - T_2 decay

The decay of the net transverse magnetization is known as T_2*, and is the combined dephasing of M_{XY} due to the spin-spin interaction and B_0 inhomogeneities and is on the order of ms to 10s of ms for most tissue (is usually longer for liquids than solids). T_2*can be differentiated into the loss of phase coherence between the spins due to intrinsic (T_2) and extrinsic (T_2') magnetic field inhomogeneities. T_2 decay occurs due to the interaction between magnetic moments of neighbouring protons (spin-spin relaxation); this causes variations in the local field seen by both protons. The precessional frequencies of the protons are altered and consequently dephase with respect to the Larmor frequency. Over time many spin-spin interactions occur at random, eventually all spins within a spin system will become out of phase with each other. The additional source of spin dephasing is the B_0 inhomogeneities caused by imperfections in the B_0 field inherent to the scanner and subject within it. These localized gradients accelerate the dephasing of the M_{XY}.

Spin-lattice relaxation – T_1 decay

T_1 decay is the relaxation of the spins back to equilibrium aligned with the B_0 field and is of the order of seconds for most tissue. T_1 characterises the spin-lattice decay or relaxation of the signal due to the interactions of the spins with their surrounds. The motion of the protons within a given lattice and their magnetic moment interactions will result in perturbations of the energy levels of the spin states (Haacke, 1999, chpt 1.3). Once the RF pulse is tuned off, this interaction result in the net loss of energy from the spins to the surrounding lattice (spin-lattice relaxation) and the magnetization vector returns to the z axis. Both T_1 and T_2 decay and the resultant longitudinal (M_Z) and transverse (M_X, M_Y) magnetization can be described by the Bloch equations 3.8 - 3.13 (Bloch, 1946) (McRobbie, Second Edition, 2007, chpt 8.6).

$$\frac{dM}{dt} = \gamma M \times B \tag{3.8}$$

B includes the static B_0 field and the rotating B_1 field. B_X, B_Y and B_Z can be expressed as

$$B_X = B_1 \cos \omega t,\ B_Y = B_1 \sin \omega t,\ \ B_Z = B_0 \tag{3.9-11}$$

By accounting for T_1 and T_2 equation 3.8 becomes

$$\begin{aligned} \frac{dM_X}{dt} &= \gamma(M_Y B_0 + M_Z B_1 \sin \omega t) - \frac{M_X}{T_2} \\ \frac{dM_Y}{dt} &= \gamma(M_Z B_1 \cos \omega t - M_X B_0) - \frac{M_Y}{T_2} \\ \frac{dM_Z}{dt} &= \gamma(M_X B_1 \sin \omega t + M_Y B_1 \cos \omega t) - \frac{M_Z - M_0}{T_1} \end{aligned} \tag{3.12}$$

By imposing the boundary conditions that immediately after the RF pulse $B_1 = 0$ and if the system was initially in equilibrium and a 90° RF pulse was applied along the x axis then at time t = 0, $M_X = 0$ $M_Z = 0$ and $M_Y = M_0$, then solving for M_X, M_Y and M_Z the above become.

$$M_X(t) = M_0 \sin \omega_0 t \cdot exp^{\frac{-t}{T_2}}$$
$$M_Y(t) = M_0 \cos \omega_0 t \cdot exp^{\frac{-t}{T_2}} \quad (3.13)$$
$$M_Z(t) = M_0 \left[1 - exp^{\frac{-t}{T_1}}\right]$$

Hence the transverse magnetization M_X and M_Y can be shown to oscillate at the Larmor frequency associated with B_0 and decay exponentially with the time constant T_2. The M_Z recovers back to M_0 with time constant T_1. As mentioned before different tissues have different T_1 and T_2 due to the environment in which the spins reside. By manipulating the transverse and longitudinal magnetization and the time at which the signal is sampled, the differentiation of different tissue types within a subject can be achieved. This is the fundamental principle that makes MRI a powerful diagnostic, anatomical and functional imaging modality. This is covered in more detail in the following sections.

3.2.5 Signal detection

Receiver coils are used to detect the MR signal. Within the laboratory frame the component of magnetization **M**, which is oscillating in the transverse plane, induces a small time varying voltage in the receiver coil that varies at the Larmor frequency that can be detected after the RF pulse is switched off. After the RF is switched off the spins dephase with respect to each other due to the previously mentioned B_0 inhomogeneities and spin-spin relaxation. The transverse component of **M**

relaxes back to align with the vertical z plane and the longitudinal magnetization increases. The oscillating signal decays to zero generally within a few ms (Figure 3.2.4), consequently in general multiple RF excitations are needed to allow adequate signal detection and sampling from an entire region of interest (ROI). This signal S is known as the Free Induction Decay (FID) and is described in equation 3.14.

$$S = exp^{\frac{-t}{T2*}} \cos \omega t \tag{3.14}$$

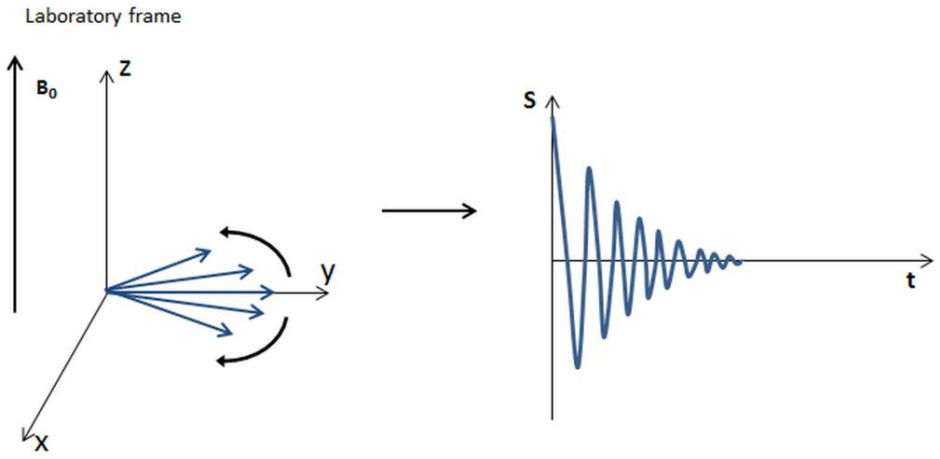

Figure 3.2.4 – FID: As soon as the RF pulse is switched off spins within a spin system start to dephase with respect to each other due to magnetic field inhomogeneities, spin-spin relaxation and tissue susceptibility reducing the transverse magnetization to zero. This translates to the oscillating signal induced in the receiver coil decaying exponentially over time (FID). The receiver coil is placed perpendicular to the main magnetic field and therefore only sensitive to the magnetization perpendicular B_0.

3.2.6 Spatial Encoding

The FID signal is not spatially localized and is generated from the ensemble of spin systems within the sensitive volume of the coil. Gradient fields produced by gradient coils are used to differentiate between signals generated from spins ensembles at different locations within the subject. Gradient coils induce a linear perturbation in the B_0 field several orders of magnitude smaller than B_0. This variation (intentional inhomogeneity) in the magnetic field causes spin ensembles at different

locations to precess at different frequencies and therefore induce signals that oscillate at varying ω determined by their location. Three gradient coils orthogonal to each other (G_x, G_y, G_z) are used to provide spatial encoding of a three dimensional coordinate system (in this example the gradients are applied along the cardinal axes, however they can be applied in any direction). Now the local field B(x,y,z) experienced by a spin system at location (x,y,z) is spatially dependent and is described in equation 3.15.

$$B(x,y,z) = [B_0 + xG_X + yG_Y + zG_Z] \tag{3.15}$$

The precessional frequency of spins will therefore depend on their spatial location within the gradient field G, and can be described with equation 3.16. Here the location is described by the position vector r = (x,y,z). The deviation from the Larmor frequency associated with the main polarising field ω_0 is therefore linear in r and G as described in equation 3.17. Consequently the phase will also be dependent on the spatial location. From equation 3.17 the resultant phase shift due to the additional applied gradients is described in equation 3.18.

$$\omega(r,t) = \omega_0 + \gamma(r \cdot G(t)) \tag{3.16}$$

$$\omega(r,t) = \gamma r \cdot G(t) \tag{3.17}$$

$$\varphi(r,t) = \gamma \int_0^t \big(r \cdot G(t)\big) dt' \tag{3.18}$$

Slice selective excitation

The gradient applied along the z axis, known as the slice select gradient G_{SS} is applied simultaneously with the RF pulse, which introduces a position dependent spread of precessional frequencies. The RF has a bandwidth BW_{RF} containing certain frequencies. Only the spins experiencing a magnetic field to cause precession at these resonant frequencies within BW_{RF} (spins at a particular location or slice) will interact with the RF and be flipped down to the transverse plane. A slice selective gradient applied along the z axis will cause excitation of spins in a transverse slice whose slice thickness Δz (figure 3.2.5) can be manipulated by altering the slope of the gradient (G_z) (figure 3.2.6) and RF bandwidth (BW_{RF}) as described in equation 3.19. Likewise the location of the slice is determined by the RF frequency. A rephasing gradient lobe is applied at the end of the G_{SS} to rephase the spins within the slice so that once the RF pulse is switched off all the spins within a slice are in phase again.

$$\Delta Z = \frac{BW_{RF}}{\gamma G_z} \tag{3.19}$$

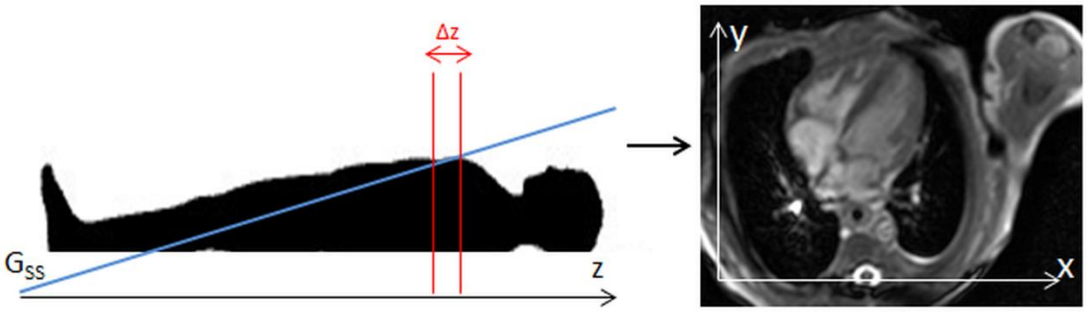

Figure 3.2.5 – Slice selection: A selective slice gradient G_{SS} (shown in blue) applied along the z axis simultaneously with the RF pulse will only cause excitation of spins whose precessional frequency is resonant with the RF pulse. Spins at the same z location will have the same precessional frequency leading to a

transverse slice (shown in red) being excited. Only spins within this slice contribute to the signal and therefore the image.

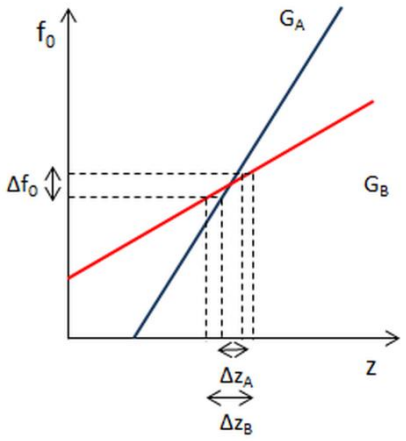

Figure 3.2.6 – slice manipulation: By altering the strength of the applied G_{SS} the slice thickness Δz can be increased or decreased. Likewise modifying the bandwidth of the RF pulse Δf_0 will have the same effect.

To spatially encode within the slice the x and y gradients are applied independently and are conventionally known as the phase encoding G_{PE} and frequency encoding G_{FE}. The following examples of G_{PE} and G_{FE} are described for Cartesian sampling for simplicity, however the same fundamental principles apply for any sampling trajectory.

Phase encoding

The phase encoding gradient G_{PE} is switched on after the RF pulse, but before signal acquisition. G_{PE} (for this example applied along the y axis) causes intentional dephasing (due to the different field strength experienced by the spins) as a function of spatial location along the y axis. This phase difference will remain after the G_{PE} is switched off until the signal decays due to T_2 relaxation. The spin's phase is determined by it position along the y axis hence phase encoding gradient (Figure 3.2.7).

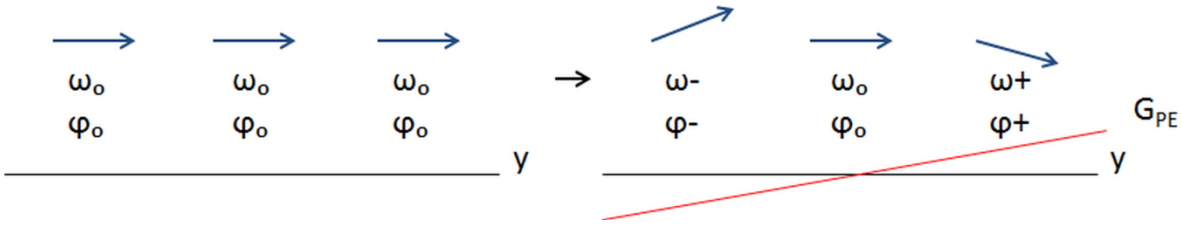

Figure 3.2.7 – Phase encoding: Applying the phase encoding gradient G_{PE} causes a linear field strength variation along the y axis. Spins with a different y location experience different field strengths and precess at different frequencies. The spins dephase with respect to each other, the phase difference remains after the gradient is switched off. The spins are therefore phase encoded along the y axis.

Frequency encoding

The frequency encoding gradient is switched on during signal acquisition (in this example and in figure 3.2.8 along the x axis) after the G_{PE}. This linear variation in the magnetic field will result in spatially dependent precessional spin frequencies along the x axis (see section 3.2.9).

MR imaging

To generate an MR image the MR sequence consists of multiple repetitions of the RF and G_{ss} combination followed by G_{FE} and different G_{PE} until all possible spatial frequencies are encoded. The repetition time (TR) denotes the time between RF pulses and will therefore determine the total scan time T_T as described in equation 3.20. The time between the RF pulse and the echo is termed echo delay time (TE). TR, TE and flip angle all contribute to the weighting (contrast) of the image.

$$T_T = TR \times N_Y \times N_{SA} \tag{3.20}$$

Where N_Y is the number of phase encoding steps and N_{SA} is the number of signal averages.

The MR sequence, including the RF pulse and spatial encoding gradients can be depicted with a pulse sequence diagram (Figure 3.2.8) which will be referred to later in this section.

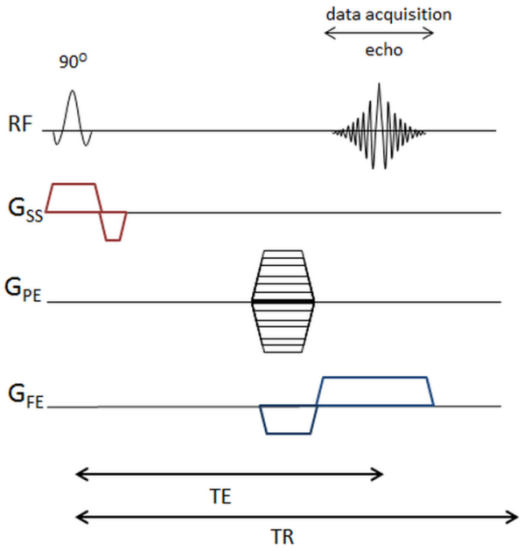

Figure 3.2.8 – The pulse sequence diagram: The three gradients G_{SS} (red), G_{PE} (black) and G_{FE} (blue) are presented. The G_{SS} is applied simultaneously with the RF pulse followed by a negative lobe or slice rephasing gradient so maintain signal. The G_{PE} is then applied followed by the G_{FE} or readout gradient. TE is denoted as the time between the RF pulse and signal or echo, TR is the time between RF pulses.

3.2.7 Data Sampling and k-space

The total signal detected (excluding relaxation effects) from the now spatially sensitized sample of spins is given in equation 3.21.

$$S(t) = \int \rho(r) exp^{i\varphi(r,t)}\, dr \tag{3.21}$$

Where ρ is the spin density or effective proton density of the sample. It is proportional to the number of nuclei per unit volume that contributes to the signal and is essentially the maximum

signal available under the conditions of an individual experiment. Hence the transverse magnetization is proportional to the effective proton density. By moving to the raw signal space (k-space) (Ljunggren, 1983) (Twieg, 1983), the reciprocal of coordinate space (the image domain) the received signals are represented as a matrix of spatial frequencies. In this way the result of the applied gradients can be better understood. The reciprocal vector k(t) and its relationship with the applied gradients is described in equation 3.22.

$$k(t) = \frac{\gamma}{2\pi}\int_0^t G(t)dt' \tag{3.22}$$

By substituting k(t) for $\varphi(r,t)$ in equation 3.21 the signal equation becomes

$$S(k) = \int \rho(r) exp^{i2\pi kr}\, dr \tag{3.23}$$

Hence the signal S(k) is the Fourier transform (FT) of the of the spin density ρ(r) over the integral of the gradient waveform. Therefore the spin density of the sample can be recovered by taking the inverse FT of the signal. The signal S(k) and the image are a Fourier transform pair, this is the fundamental principle that underlies MR data reconstruction. The data is collected in k-space and a FT is performed to generate the image. The k-space data and image pair are shown in figure 3.2.9.

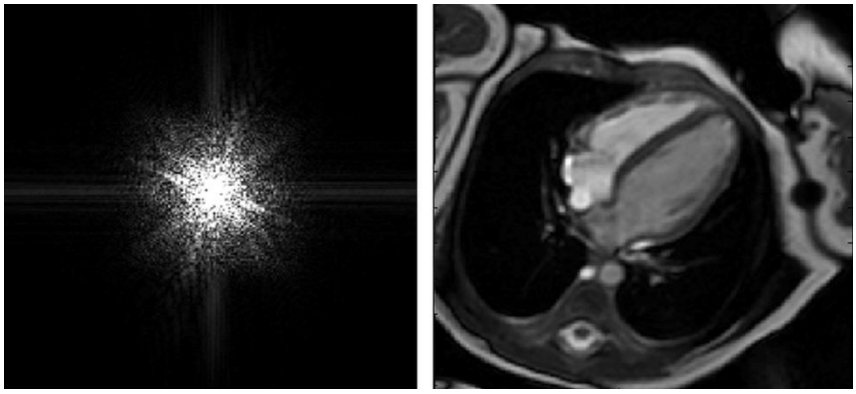

Figure 3.2.9 –The raw signal/k-space and the reciprocal MR image: The 2D FT recovers the image from the detected signal. The image and k-space are said to be a Fourier pair. A point in k-space with a particular frequency and phase will be generated from spins from everywhere in the image domain. In both cases only the magnitude data is presented.

Continuing the Cartesian example, in k-space the spatial encoding gradients G_{PE} and G_{FE} can be shown to populate the raw space matrix with k_x representing the frequency axis and k_y the phase axis. The application of G_{FE} and G_{PE} encodes the MR signal of the original object in spatial frequencies and can be thought of as defining a trajectory through k-space. In reality there is great flexibility in sampling strategies and k-space trajectories, a few examples of these are covered in some detail in the following sections.

The Nyquist criterion (Haacke, 1999, chpt 12.1), that the sampling rate must be at least twice the highest frequency or bandwidth must be met to avoid aliasing where wrapping of the image occurs due to incorrect assignment of location to spins. Being it's reciprocal the properties of k-space determine the parameters of the image space as shown in figure 3.2.10. The integral of the gradient determines maximum k-space line (k max) acquired and consequently the spatial resolution. The rate of passage across k-space is set by the amplitude of the gradient. Likewise the FOV is determined by the inverse of the minimum spatial frequency step, the phase encode steps. This constraint is also present in the frequency encode direction, oversampling by 2 and then cropping image ensures no aliasing. For sufficient sampling of k-space a suitable number of G_{PE} needs to be

applied to ensure adequate coverage of the object (spacing of k-space lines) being imaged at high enough spatial resolution (k max). This gives rise to long scan times.

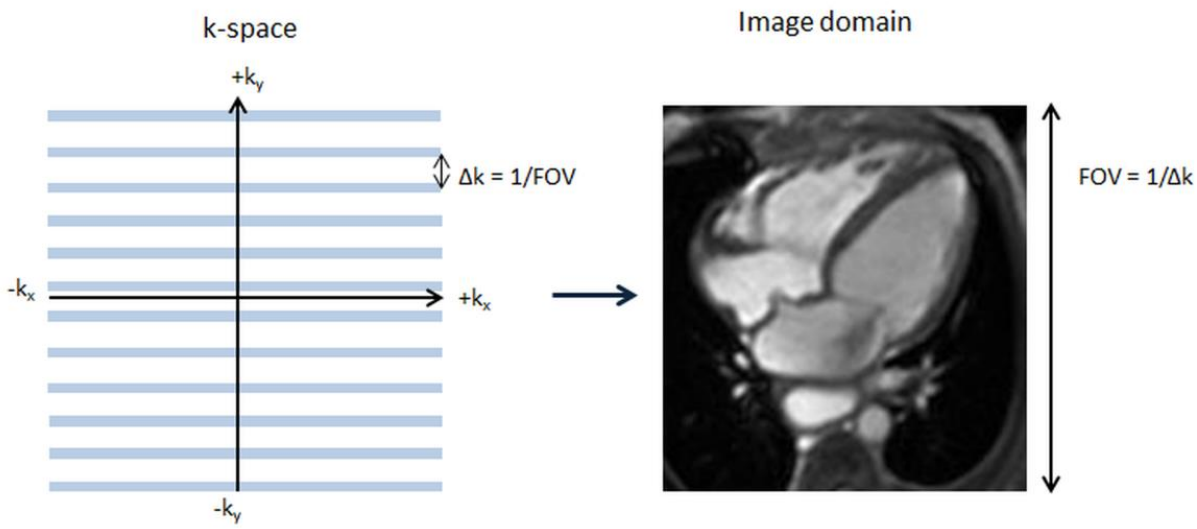

Figure 3.2.10 – k-space and its reciprocal image space: The spacing between lines in k-space Δk (phase encoding step) equates to 1/FOV in the image domain. Similarly the extent to which k-space is populated determines the pixel size in the image domain. For a high spatially resolved large FOV more many k-space lines close together need to be populated. This gives rise to long scan times.

3.2.8 Noise and Image Artefacts

All physical measurements include random noise which can affect the accuracy of the measurement. The signal to noise ratio (SNR) denotes the efficiency of any given imaging experiment, low SNR impairs the ability to differentiate between different tissues and background (Haacke, 1999, chpt 15.1). The origin of signal has been described in the previous subsections. In addition to the reduction of signal due to B_0 inhomogeneities or spin-spin relaxation, noise is also generated and arises predominantly from thermal fluctuations in the sample and in the receive coil electronics. This subsequently impacts on the image quality. Thermal noise is characterized by equal expected noise power components at all frequencies within the readout bandwidth (Haacke, 1999, chpt 15.1).

Sequences are frequently optimized to maximize the SNR by manipulating the imaging parameters such as voxel dimensions, TE and TR. The resultant SNR (excluding relaxation) and relation to the imaging parameters for an individual scan can be described in equation 3.24 (Hashemi, 2010, Third Edition chpt 12).

$$SNR \sim V\sqrt{(N_Y)(N_{SA})(T_S)} \quad (3.24)$$

Where V is the voxel volume, N_{SA} is the number of signal averages and T_s is the total time of signal acquisition and is determined by the number of frequency encoding steps divided by the receiver bandwidth (the bandwidth associated with the sampled signal, not the transmission bandwidth associated with the RF pulse BW_{RF}) N_x/BW.

As SNR is directly proportional to √scan time, longer scan time yields increased SNR; usually achieved by increasing the NSA. This highlights one of the core difficulties when scanning infants. The size and heat rate of preterm infants necessitate high spatial and temporal resolution sequences. However long scan times are unfavourable due to variable heart rates, patient instability and lack of co-operation in the neonatal cohort. Neonatal scanning will be covered later in this chapter. An increase in SNR can also be achieved by simply placing the receive coil closer to the subject and increasing the number of receive coil elements. Consequently there are numerous dedicated coils to image specific regions of the body.

As well as subject motion and poor SNR, image quality can be degraded by the apparent shift in the location of fat due to the chemical shift (Haacke, 1999, chpt 8) leading to blurred voxel edges, increased dephasing at tissue boundaries caused by differences in magnetic susceptibility and eddy currents.

Eddy currents

Eddy currents are induced in the conducting components of the magnet cryostat by the rapid switching of the gradients. Eddy currents build up during the time varying part of the gradient waveforms and decay during the constant periods. Hence the rate of eddy current build up is proportional to the slew rate of the gradient. The magnetic field produced by the eddy current opposes the change in the field inducing the eddy current (Lenz's law) (Bernstein, 2004, chpt 10.3). As a result the net gradient waveform experienced by a spin system is degraded, the resultant transient magnetic field generated combines with the gradient field and produces distortions in the gradient profile; resulting in image artefacts and reduced SNR. Eddy currents remain a problem for a number of sequences. In PC images (described in section 3.4) this manifests as a background phase error which can give rise to erroneous flow measurements.

There are 3 main strategies to reduce eddy current effects, gradient waveform pre-emphasis, active shielding and application specific post processing calibration and correction (Bernstein, 2004, chpt 10.3). Active shielding magnetically isolates the field gradients from the magnet cryostat by the use of 2 coils, the main inner coil and secondary outer coil. The outer coil produces a field that opposes the field from the main coil; the 2 coils are designed so that the net field outside the 2 coils (the fringe field) is zero. Eddy currents are mainly generated in conductive structures within this fringe field; by reducing this eddy currents are also reduced. Waveform pre-emphasis intentionally distorts the current waveform that is input into the gradient coil so that the pre-emphasis distortion cancels out the subsequently induced eddy current distortion. Both of these techniques are now implemented in most scanners to reduce eddy currents (Bernstein, 2004, chpt 10.3), however some flow quantification studies still account for background phase errors during data post processing (Rolf et al. 2011). Eddy currents compensation for PC MRI is discussed in more detail in section 3.4.

Shimming

Magnetic susceptibility variations between different tissues give rise to inhomogeneity in the applied field and lead to image artefacts. This is particularly relevant in SSFP sequences over the heart (see chapter 5). The extent of the variation in the applied field is determined by the subject and therefore has to be accounted for on an individual basis. The B_0 field inhomogeneity can be measured and then adjusted to maximize homogeneity over a ROI with the use of shim coils (McRobbie, Second Edition, 2007, chpt 15.3). Shimming can be automated or carried out manually.

3.2.9 MR Sequences

Due to the need for spatial encoding the FID is not measured directly; instead gradients are used to create echoes. There are two main echoes that form the foundation of all MR sequences, gradient echo (GE) and spin echo (SE).

Gradient echo sequence

Figure 3.2.8 represents a pulse sequence diagram for a gradient echo sequence. This technique is used to reduce scan time by reducing TR. Consequently the RF pulses used in GE sequences have a flip angle of less than 90^o. Rapid dephasing of the transverse magnetization is then induced by applying a negative gradient lope directly after the excitation pulse along the FE axis. A reverse gradient (positive lobe) is then applied to rephase the magnetization. This reverses the effect of the negative lobe but not dephasing due to B_0 inhomogeneities or spin-spin relaxation. The maximum signal S_{GE} depends on the FID decay and therefore T_2*(see equation 3.14).

In k-space the negative gradient lobe (pre-winder gradient) allows the entire k-space to be acquired from $-k_x$ to $+k_x$ and is half the duration or strength of the positive (readout) gradient lobe as shown

in figure 3.2.11. The centre of k-space represents zero phase and frequency encoding, when all the spins are coherent/rephased with respect to each other. The signal is therefore greatest at this point. The centre of k-space therefore contains contrast information. Correspondingly the outer edges of k-pace contain resolution information.

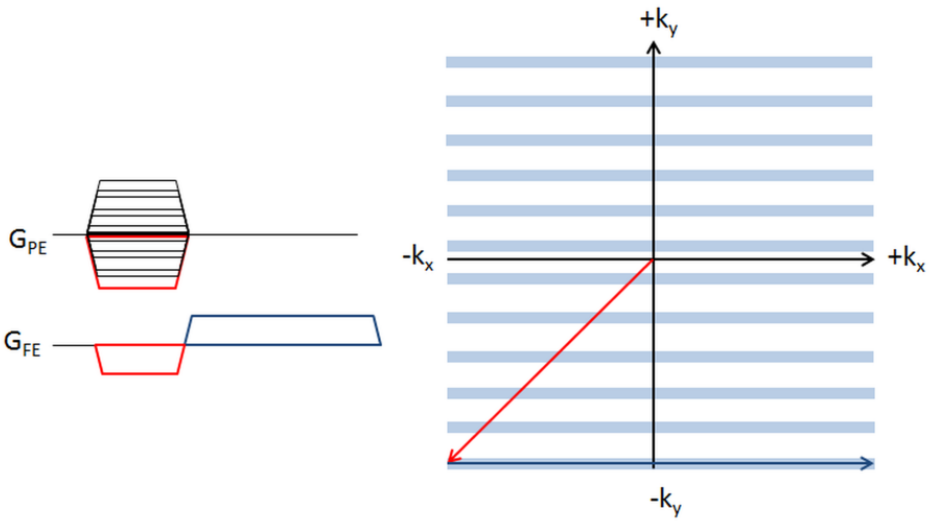

Figure 3.2.11 – Gradient echo pulse sequence diagram with the resultant trajectory though k-space: The first large negative G_{PE} lobe (red) applied with the pre-winder G_{FE} moves to $-k_x$, $-k_y$ (red arrow). The readout gradient (blue) is then applied during signal acquisition and moves across k-space along the frequency encode axis (k_x) filling in one line of k-space (blue arrow). This process is repeated with different strength G_{PE} to fill in the rest of k-space.

Spin echo sequence

The dominant cause of spin dephasing is inhomogeneities in the B_0 field; this can be reversed by applying an 180° RF pulse after the initial 90° pulse. After the 90° RF pulse the spins dephase naturally, at a time TE/2 the 180° pulse is applied. The 180° pulse flips the spins so that the initial phase dispersion is inverted, continuing evolution recovers the initial transverse magnetization, subsequently at time TE all spins are in phase again and will form a spin echo. This is known as a spin echo sequence, which with the resultant k-space trajectory is shown in figure 3.2.12. The resultant acquired signal is therefore determined by the spin-spin relaxation properties of the tissue as described in equation 3.25.

$$S_{SE} = S_0 exp^{\frac{-TE}{T2}} \quad (3.25)$$

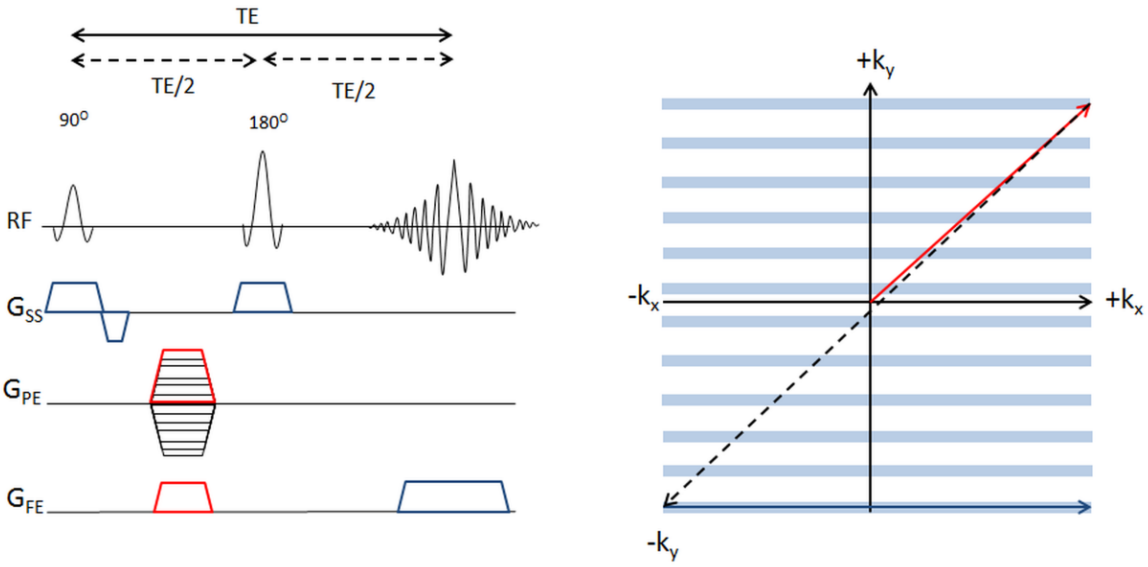

Figure 3.2.12 – Spin echo pulse sequence diagram and the resultant k-space trajectory: The positive GPE lobe and GFE applied together after the 90° pulse moves to $+k_x$, $+k_y$ (red arrow). The application of the 180° pulse causes the spins to precess in the opposite orientation and therefore their phase and frequency are reversed with respect to each other. This has the effect of moving to $-k_x$, $-k_y$ where the readout gradient is then applied and the first line of k-space is populated as in the GE pulse sequence.

There are numerous pulse sequences built around the principles of GE and SE. So far only linearly populating Cartesian k-space trajectories have been mentioned. In reality depending on the subject and desired measurement of the MR experiment, various trajectories and k-space filling patterns are utilized to maximize certain imaging parameters and trade off on others (Bernstein, 2004, chpt 11) (Haacke, 1999, chpt 10). For example accelerated acquisition techniques minimize acquisition time at the expense of SNR (Larkman et al. 2007) (Lustig et al. 2008).

3D sequences

All the previous pulse sequence examples and their resultant k-space trajectories have combined an excitation of a slice within the subject followed by spatial encoding in the x and y direction; they have therefore been 2 dimensional sequences. Multiple slices can be acquired along the object to create a 2D stack, yet often anisotropic voxels are acquired (the slice thickness is greater than the x,y, resolution) to meet SNR requirements (a larger slice contains more spins that contribute to the signal). In addition, the slice profile in reality is no perfect due to the time constraints on the RF pulse (Haacke, 1999, chpt 16). Occasionally isotropic high spatial resolution is require to adequately image an object. The addition of another phase encode gradient along the slice select axis allows spatial encoding within the excited slab along the z axis (3D sequences). Each z axis phase encoding step requires a full set of G_{PE} and G_{FE} steps (Figure 3.2.13) this leads to long scan times. For this reason 3D is most often applied to GE sequences. The scan duration for a 3D sequence is described in equation 3.26.

$$T_T = N_{SA} \times N_Z \times N_Y \times TR \qquad (3.26)$$

Where N_Y and N_Z are the number of phase encoding steps along k_Y and k_Z.

By utilizing 3D sequences thinner slices can be obtained with better profiles. The ability to change the number of phase encoding steps over the slab gives control over the minimum z partition thickness (spatial resolution along the slab direction or reconstructed slice thickness) without limitations on the RF amplitude or duration. Often the thicker slabs in 3D acquisitions are excited by lowering the slice/slab select gradient (see figure 3.2.6) however larger RF bandwidths can also be used. In this scenario this leads to shorter RF pulses, this means the TE can be reduced. This shorter TE and higher spatial resolution in the z direction reduce signal loss due to T_2* dephasing. Finally due to the √scan time dependence of SNR (equation 3.24), which is N_Z times longer in 3D imaging an

increase of √N_Z is achieved for 3D compared to a 2D sequences, with equivalent imagine parameters (Haacke, 1999, chpt 9). The SNR from a 3D sequence is described in equation 3.27.

$$\text{3D SNR} \sim v\sqrt{(N_Z)(N_Y)(N_{SA})(T_S)} \quad \rightarrow \quad \sqrt{N_Z} \times \text{2D SNR} \tag{3.27}$$

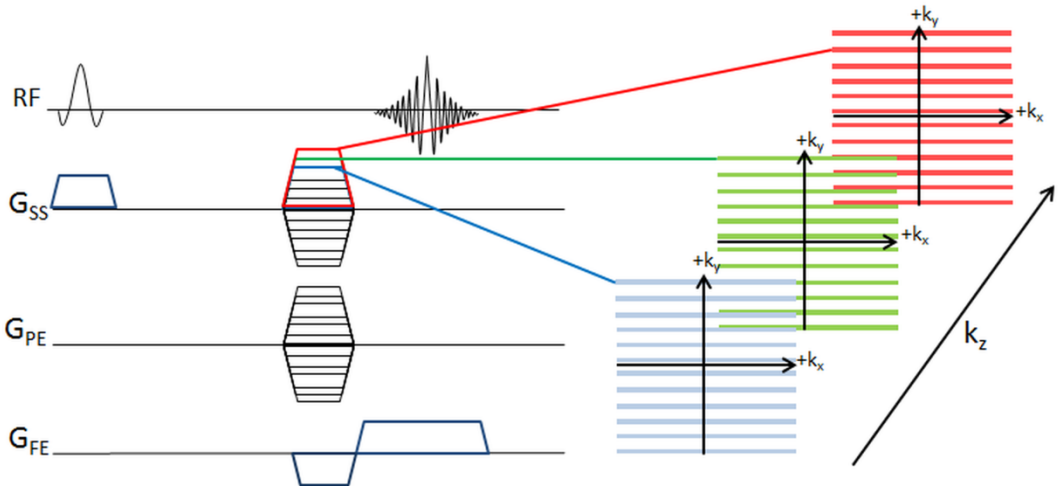

Figure 3.2.13 – 3D GE pulse sequence: The GSS applied during the RF pulse now excites a slab/volume, an additional phase encoding gradient applied along the z axis spatially encodes the volume along this direction. The largest positive lobe (red) and full set of GPE and GFE encodes the uppermost plane $+k_Z$ in the k-space 3D matrix. This process is continued (green and blue lobes) until all planes within the matrix are filled.

3.3 Cardiac MRI

Cardiac imaging first transpired in the late 1970s. Improvements in MR hardware (markedly high performance gradients) have led to robust and accurate imaging techniques capable of providing high quality morphological and functional imaging of the heart. Cardiac MRI provides unique methods of qualitative and quantitative evaluation of the heart for evaluating cardiac anatomy and function including cardiac viability, perfusion, blood flow, and vascular anatomy (Jerosch-Herold et al. 2004) (Markl et al. 2012) (Sandstede et al. 2000). Due to the numerous sequences that can be

utilized, a single CMR investigation can potentially provide more precise, informative data than other techniques combined (McRobbie, 2007).

3.3.1 ECG Trace

Due to the inherent sensitivity of MRI to motion the periodic beating of the heart can cause motion artefacts if not accounted for. The acquisition of data needs to be synchronized to an individual's heartbeat with successful electrocardiography (ECG) gating ensuring that each phase encoding step is performed at the same point in the cardiac cycle. ECG leads detect the changes in potentials at the surface of the skin as a result of the depolarization and repolarization of the cardiac muscle. Cardiac gated sequences are triggered from the detection of the QRS complex (figure 3.3.1).

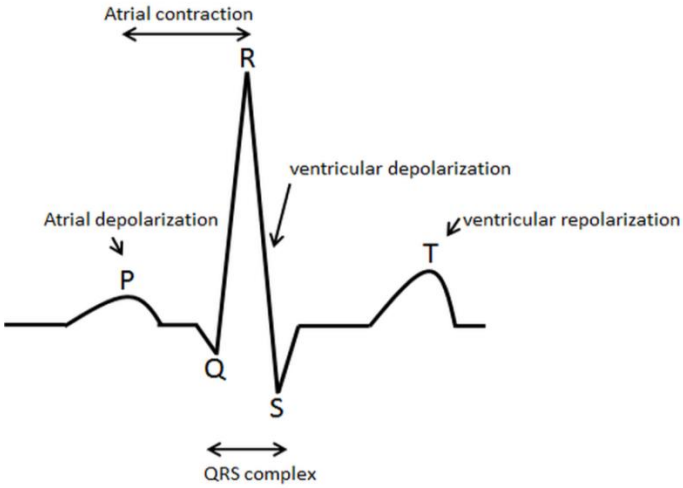

Figure 3.3.1 – ECG trace: ECG leads placed on the skin record the resultant changes in potential caused by the depolarization and repolarization of the heart (Einthoven, 1909). The P wave signifies atrial depolarization and the start of atrial contraction (P-R). The QRS complex represents ventricle depolarization where S coincides with the opening of the aortic valve. The T wave then denotes the repolarization of the ventricles. Atrial repolarization is not detected as it is asynchronous and slow.

The ECG trace can be distorted during an MRI scan due to the additional voltage induced by the gradients, RF pulse and pulsatile blood flow (the magneto-hydrodynamic effect) (Togawa et al. 1967). The magneto-hydrodynamic effect is caused by blood flowing at an angle to the high static main magnetic field. This will induce an electric field across the conductive flowing fluid (blood) leading to a voltage across the vessel known as the magneto-hydrodynamic effect (Abi-Abdallah et al. 2007). Peak aortic blood flow occurs at ventricular ejection inducing an additional voltage that is in general superimposed on the ECG trace during the S-T phase (Tenforde et al. 1983) (figure 3.3.2). This can cause false triggering (Nijm et al. 2006). Filtering of the ECG waveform reduces these effects but renders the trace nondiagnostic. The typical Einthoven's triangle placement of the leads is altered for an MRI scan (vector cardiac gating (VCG)) to reduce the differential voltage induced in the leads by the gradients, RF pulse and blood flow (McRobbie, Second Edition, 2007, chpt 14.4). The VCG trace however can still lead to erroneous triggering particularly in the preterm population where their small size limits the positioning of the leads.

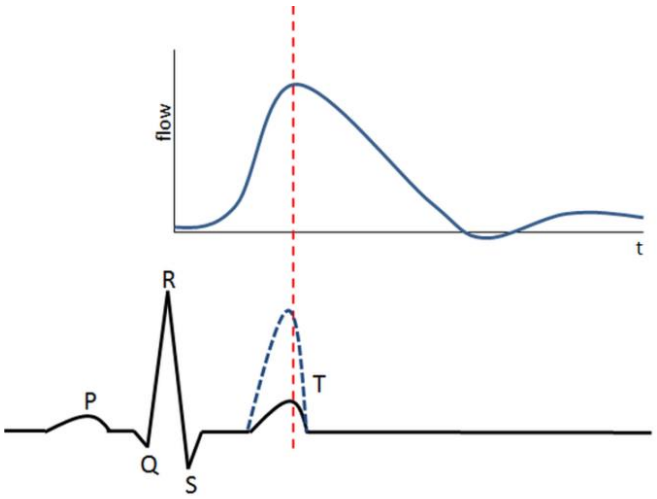

Figure 3.3.2 – ECG false triggering: Aortic blood flow causes an induced voltage (due to the magneto-hydrodynamic effect) within the ECG leads that is superimposed during the S-T phase. This can lead to false triggering. This effect can be seen when comparing flow arrival times in chapter 7.

3.3.2 Sequence Synchronization: Cardiac and Respiratory Gating in MRI

Cardiac gating

Once the R wave is detected the acquisition of k-space can be synchronized so that each line or section is acquired at the same point in the cardiac cycle. To temporally resolve the cardiac cycle the R-R interval is divided into cardiac phases. Lines of k-space are acquired at each cardiac phase contribute to different images (figure 3.3.3). Multiple heart beats are needed to acquire sufficient k-space lines for all the cardiac phase images. This leads to long scan durations yet eliminates motion artefacts from cardiac motion and allows quantification of cardiac function and flow.

Gating can be performed prospectively or retrospectively. In prospective gating the sequence acquisition is triggered from the R wave and a set number of cardiac phases are acquired. The last 10-15% of the cardiac cycle known as arrhythmia rejection (AR) period is not sampled. This is used to account and compensate for physiological heart rate variability. As a trade-off the flow in late diastole may not be measured correctly. In addition the number of k-space lines acquired for each cardiac phase is therefore limited by the heart rate and TR.

Retrospective gating assumes a stable heart beat where data is acquired continuously throughout the cardiac cycle. The cardiac wave form is used as a real time update of the G_{PE}. The data is then organized after the acquisition into N equally spaced cardiac phases throughout the entire R-R interval with no AR period. Due to physiological hear rate variability the data have to be interpolated to represent a mean cardiac cycle, this can lead to small inaccuracies (Lotz et al. 2002). In general a 10% increase or decrease from the assumed heart rate is tolerated, this threshold is known as the acceptance window. Large heart rate variability outside the R-R acceptance window leads to data being thrown away and reacquired, which can lead to very long scan times. An advantage of retrospective gating is that the entire cardiac cycle is sampled.

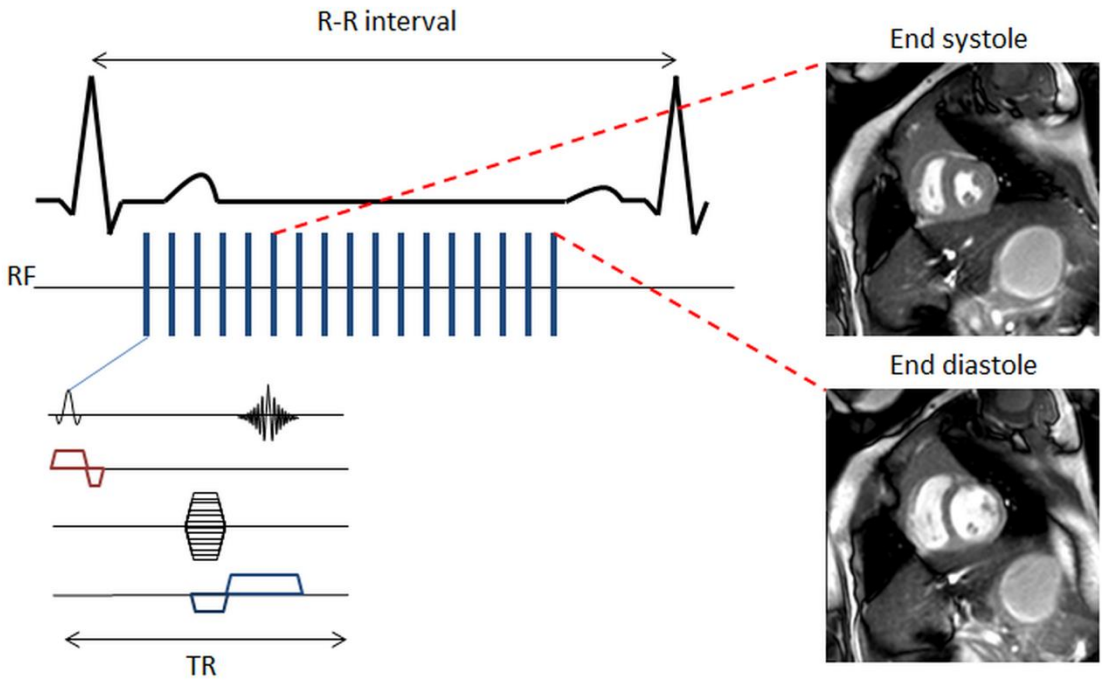

Figure 3.3.3 – ECG triggering and respective cardiac phases: The R-R interval is used to synchronise the acquisition of data. Blue lines indicate the start of each RF pulse, a number of k-space lines are then acquired which contribute to a single image of a single cardiac phase. In this diagram end systole and diastole are shown. Over many heart beats the entire k-space is sampled for each image of each cardiac phase.

Respiratory gating

As well as the periodic cardiac contractions, the heart and thorax undergo bulk motion caused by respiration. Inspiration and expiration causes diaphragmatic motion of the heart which is less periodic than the heart rate and does not produce a detectable potential. Consequently reducing respiratory artefacts can be challenging. The techniques proven most effective at reducing respiratory motion artefacts are navigator based respiratory gating, that use navigators placed over the diaphragm, or by essentially freezing out respiratory motion by perform fast sequences that acquire all the data during a single breath-hold. As breath-hold sequences are not feasible in infants and navigator sequences are lengthy all of the acquisitions in this thesis were performed during free breathing. This is feasible due to the rapid neonatal respiratory rate that produces mainly shallow abdominal bulk motion. This is covered more extensively in chapter 4.

Gated MRI sequences can be used for qualitative and quantitative assessment of myocardial function and blood flow distribution. There are numerous sequences utilized in a cardiac examination, many of which are outside the scope of this thesis. The fundamental principles of one technique that was extensively employed in this work are described in the following sections.

3.4 Phase Contrast MRI

The FT of the received MR raw data yields a complex image with both magnitude and phase information. In anatomical imaging the phase information is discarded. PC imaging exploits signal intensity to create an anatomical image and the phase information to create a velocity image. The basic principles of PC were initially described by Carr and Purcell in 1954 and the first in vivo studies were carried out in the 1980s (Moran et al. 1982) (Nayler et al. 1986). It is now a well validated imaging technique (Griel et al. 2002) (Hofman et al. 1995) (Lotz et al. 2002) (Powell et al. 2003) that is primarily used to image flow within blood vessels.

The inherent sensitivity of MRI to motion can be used to infer the velocity of spins using flow encoding gradients. While spatial information can be obtained from the phase and frequency of static spins, flow encoding gradients translates the motion of spins along a particular direction to a phase. By measuring all three directional components of the blood flow velocity field over an averaged cardiac cycle the complex three dimensional flow patterns present in intra and extra cardiac vasculature can be visualized and quantified (Bogren et al. 1997) (Buonocore, 1998) (Markl et al. 2003).

3.4.1 Velocity Encoding

Velocity encoding gradients

By using appropriate gradients the relationship between the phase of a spin and its movement along a gradient field can be determined. The direction of flow sensitivity is determined by the axis along which the gradients are applied. Typically velocity encoding gradients are applied along each one of the main gradient directions consecutively; however flow sensitivity along any arbitrary axis can be obtained by driving gradient coils simultaneously. To reduce minimum TR and TE the velocity encoding gradients are generally combined with other gradient lobes used in the imaging sequence, mainly the frequency encode and slice select axis. Flow encoding gradients are usually applied to GE sequences yet EPI, radial and spiral sequences have also been used (Körperich et al. 2004) (Pike et al. 1994) (Steeden et al. 2010).

Ordinarily bipolar gradients are used, of which the zeorth moment m_0 (the time integral of the gradient G_x) is zero to preserve spatial encoding. In other words static spins will acquire zero phase due to the applied velocity encoding bipolar gradient. The first moment m_1 however (the time integral of $G_x t$), produces a phase that is linearly proportional to velocity. Higher orders of motion can be quantified with other gradient forms whose zeroth and first moments are zero, but have non-zero higher moments.

Flow sensitivity: accruement of phase

From the previous discussion spins moving along the direction of an applied gradient acquire a phase proportional to the distance travelled and time integral of the gradient experienced by the spins. The phase of a given spin is the time integral of the precessional frequency as described in equation 3.28.

$$\varphi(t) = \int_0^t \omega \, dt' \tag{3.28}$$

In the example where the velocity encoding gradient is applied along the x axis, the phase shift is

$$\varphi(t) = \gamma \int_0^t (B_0 + G_X x) dt' \tag{3.29}$$

For spins moving in the x direction with constant velocity v so that x(t) = v.t, equation 3.29 becomes

$$\varphi(t) = \gamma \int_0^t (B_0 + G_X(x_0 + vt)) dt' \tag{3.30}$$

For a gradient of amplitude G and duration τ, the phase shift due to the distance travelled along x and therefore v will be

$$\varphi(t) = \gamma \int_0^t Gvt \, dt' \rightarrow \varphi(t) = \gamma m_1 v \tag{3.31}$$

Where m_1 is the first moment.

Background phase errors

MR sequences in particular GE sequences usually contain other contributions to the acquired phase. Background phase errors from B_0 inhomogeneities and eddy currents, chemical shift, magnetic susceptibility variations as well as the phase due to velocity all contribute to the measured phase. The resultant phase φ_{tot} , is then a linear addition of the gradient independent φ_B, gradient dependant φ_e sources of error and the acquired phase due to the velocity encoded gradients as shown in equation 3.32.

$$\varphi_{tot} = \varphi_B + \varphi_e(G) + \gamma \int Gvt\, dt \quad (3.32)$$

The first term φ_B, can effectively be eliminated by a subtraction of two measurements with different velocity encoding sensitivities (phase difference reconstruction). As a result a second complete data set is generally acquired with all imaging parameters fixed with the first moment either nulled or reversed. A complex subtraction of the two phase datasets is performed to eliminate this phase error. The second term φ_e, will still be present in the resulting PC image. These gradient-dependent errors are caused by gradient amplifier distortion, Maxwell terms and eddy currents (Rolf et al. 2011). The Maxwell terms are easy to predict (Bernstein et al. 1998) and the second order gradient terms are analytically corrected for in most scanners. In addition the assumption of gradient amplifier linear response has been shown to be reasonable (Rolf et al. 2011).

The outstanding phase errors are primarily due to the inaccuracies in the pre-emphasis calibration of amplitudes and time-constants to compensate for the eddy currents. These residual eddy currents that are not accounted for during the phase difference reconstruction and give rise to background phase error which can lead to inaccuracies in flow quantification (Rolf et al. 2011). In general pre-emphasis calibrations and active shielding that magnetically isolates the field gradients from the magnet cryostat are now implemented in most scanners to reduce this error and in most applications is not problematic (McRobbie, Second Edition, 2007, chpt 9.2). The errors in flow measurements due to eddy currents are most prominent at the edges of the bore where the maximum gradient switching occurs (Haacke, 1999, chpt 10). When scanning neonates these errors are minimized, due to the small size of this population the entire cardiovascular ROI is very close to the centre of the bore far from the fringe field. Consequently in the following studies involving PC measurements in preterm infants eddy current induces flow errors were considered negligible.

Velocity mapping: phase difference reconstruction

As mentioned above, to eliminate the φ_B error a complex subtraction of the 2 phase images is performed on a pixel by pixel basis in the image domain, known as a phase difference reconstruction (Moran et al. 1985) (figure 3.4.1.). The resultant phase difference of a voxel after reconstruction is therefore given by equation 3.33.

$$\Delta\varphi = \gamma \Delta m_1 v \tag{3.33}$$

Where Δm_1 is the difference between the first moments of the 2 velocity encoded gradients and is essentially the effective gradient that produces the overall phase shift $\Delta\varphi$.

This reduces unwanted phase variation and emphasizes flow. In addition, wild fluctuations of phase are seen in regions where signal magnitude is low as in air spaces; the velocity map image is often masked to reduce background noise from air spaces by multiplying the phase difference image by the magnitude image during reconstruction.

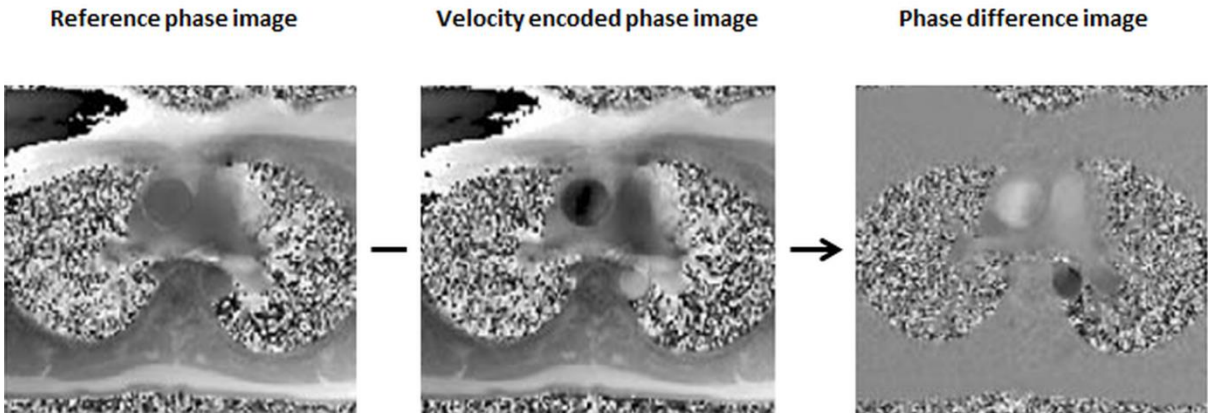

Gatehouse et al. 2005

Figure 3.4.1 – Phase difference reconstruction: The phase image of the 2 velocity encoded datasets, often one is denoted as the reference and the other as the velocity encoded dataset. These are then subtracted on a pixel by pixel basis to generate the phase difference image or velocity map.

The range of velocity encoding is determined by the difference in the first moments Δm_1 of the gradients. The gradients can be designed so that spins with a certain velocity accumulate a phase of π, known as VENC and has units of a length/unit time. Hence the relationship between VENC and Δm_1 is described by equation 3.35. The dynamic range of the phase difference reconstruction is $\pm\pi$, the flow direction and correct velocity can therefore only be determined when $|v| \leq$ VENC. Greater sensitivity to slow flow requires smaller VENC. Velocities outside this range will lead to aliasing or phase wrapping. Subsequently the VENC has to be defined for individual vessels of interest. Finally the velocity can be determined from the phase difference image as shown in equation 3.34 to generate a velocity map.

$$\text{VENC} = \frac{\pi}{\gamma \Delta m_1} \tag{3.34}$$

$$v = \left(\frac{\Delta\varphi}{\pi}\right)\text{VENC} \tag{3.35}$$

To encode velocity in all 3 spatial directions a single reference dataset can be acquired for the 3 velocity encoded datasets, reducing the number of acquisitions to 4 not 6. The time between the data acquisitions with different velocity encoding is kept to a minimum (usually interleaved within the same heart beat) to reduce misregistration artefacts during reconstruction caused by subject motion.

3.4.2 Blood Flow Quantification

Quantification of flow

Time resolved (ECG gated) PC MRI sequences can provide quantification of pulsatile flow, which is particularly beneficial when considering arterial blood flow. The volume of flow through a voxel can then be quantified by the product of the voxel area and the average velocity of spins within the voxel. The blood flow volume through a ROI i.e. a vessel is quantified by integrating the through plane flow of the individual voxels over the cross-sectional area of the vessel. In general this is performed with semi-automated software that tracks the position of the vessel over the cardiac cycle. Typically 2D PC sequences with velocity encoding along the slice direction are used to quantify blood flow volume through a specific vessel, with the slice positioned orthogonal to the vessel (Petersen et al. 2002) (Colletti et al. 2005).

Imaging parameters and sources of error

Common errors in PC imaging include phase offset errors, inadequate temporal and spatial resolution, misregistration of velocity encoding and accelerated flow. Phase offsets from background phase errors have been discussed in the previous subsection. Below the other sources in PC imaging of error are discussed.

Temporal resolution

Signal sampling and k-space acquisition is not continuous. Each frame represents the anatomy and velocity information at a different cardiac phase within the cardiac cycle. Undersampling of pulsatile blood flow and therefore inadequate temporal resolution can lead to an underestimation of the peak velocity and flow. In general between 20 and 30 cardiac phases or frames per cycle are

considered sufficient to capture/sample typical pulsatile flow in the heart and great vessels (Chai et al. 2005) (Lotz et al. 2002).

Spatial resolution

The resultant signal and phase of an individual voxel will be a summation of the spins within that voxel. Inadequate spatial resolution can cause significant partial volume effects at the vessel boundary, where voxels contain static and moving spins. In the magnitude image partial volume effects can lead to errors defining the vessel boundary. In the phase difference image partial volume effects can lead to an underestimation of flow and peak velocity (Lotz et al. 2002). Multiple studies in phantoms and in-vivo have investigated partial volume effects with accuracy of flow quantification and in general the number of voxels across the diameter of a vessel considered sufficient to accurately quantify flow ranges between 3 and 4 (Greil et al. 2002) (Hofman et al. 1995) (Lotz et al. 2002) (Tang et al. 1993).

Deviation of the imaging plane from the plane orthogonal to the vessel lumen can also lead to inaccuracies in the measured velocity. An angle of θ will lead to a velocity measurement of the true velocity*$\cos\theta$. However this error is small, 6% at 20° misalignment. For flow measurements this error is compensated by the $1/\cos\theta$ increase in apparent cross-sectional area. An angle of ±15-20° is considered tolerable as the increase in vessel area is compensated for by the increase in partial volume effects (Gatehouse et al. 2005) (Lotz et al. 2002) (Tang et al. 1993). Careful placement of the 2D PC acquisition orthogonal to the lumen and adequate spatial resolution minimizes this error.

Aliasing of velocity

The noise within the velocity image is determined by the VENC and the SNR of the magnitude image, and increases with larger VENC values. The SNR for the velocity map (Conturo and Smith, 1990) is shown in equation 3.32. Consequently to maximize $SNR_{\Delta\varphi}$, VENC should equal the maximum velocity within the blood vessel (Haacke, 1999, chpt 24). However setting the VENC below the maximum velocity within the vessel leads to aliasing (erroneous assignment of the velocity to acquired phase) and usually requires the scan to be repeated. In practice to avoid aliasing VENC is chosen to be slightly higher than the expected maximum velocity. In addition the selection of the VENC will impose requirements on the area under of the bipolar velocity-encoding gradients and will therefore part determines the minimum achievable TE and TR (Bernstein, 2004, chpt 15). Increasing the VENC to avoid aliasing requires smaller amplitude velocity encoding gradients and consequently decreases TE and TR. However, as mentioned above a VENC set considerably higher than the maximum velocity within the vessel of interest will result in a low $SNR_{\Delta\varphi}$.

$$SNR_{\Delta\varphi} \propto SNR_{mag} \left(\frac{|v|}{VENC}\right) \tag{3.36}$$

Accelerated flow

PC measurements are optimized for linear flow (second order moments are non-zero in simple bipolar gradients yet it is assumed that acceleration is minimal). Accelerated flow such as stenotic jets or turbulence cause errors in the flow measurement and may lead to artefacts (Petersson et al. 2010). In areas of acceleration or turbulence where velocities fluctuate rapidly, spatial misregistration errors (displacement) due to phase shifts from higher order motion, flow related signal loss due to intravoxel phase-dispersion, and ghosting, due to view-to-view variations can

occur (Peterson et al. 2010). Some studies have employed PC MR sequences with ultrashort echo times to reduce the signal loss artefacts (O'Brien et al, 2009). Others have used the effects of fluctuating velocity on the magnitude signal to map the intravoxel velocity standard deviation and infer information on turbulence (Dyverfeldt et al. 2006). However, carrying out flow assessments with PC MRI in these situations, in particular in patients with cardiovascular disease still remains challenging (chapter 6).

3.4.3 4D PC MRI

To fully represent the complex flow patterns in the heart and surround vessels, 3D structural information and 3 directional velocity information is needed. The application of 4D PC MRI to investigate blood flow hemodynamics in various anatomical locations was realized over 20 years ago (Moran, 1982) (Kilner et al. 1993) (Firman et al. 1993). Since then numerous studies of blood flow hemodynamics in healthy and diseased adult subjects have been carried out (Bogren et al. 1997) (Kilner et al. 2000) (Markl et al. 2003, 2011). The conventional term 4D, refers to the time resolved 3 dimensional data with velocity encoding in all 3 directions. Achieving isotropic spatial resolution with comprehensive time resolved flow information over the entire volume provides a rich dataset. Consequently enabling retrospective quantification of flow (within vessels of sufficient calibre) at any anatomical location within the volume, visualization of streamlines, time resolved particle traces (figure 3.4.2) (Valverde et al. 2010) (Markl et al. 2004), quantification of turbulence (Dyverfeldt et al. 2008, 2009), pulse wave velocity (chapter 7) (Markl et al. 2010) (Metafratzi et al. 2002) (Gang et al, 2004) and secondary vascular parameters such as wall shear stress (Oyer et al. 1998) (Hope et al. 2010).

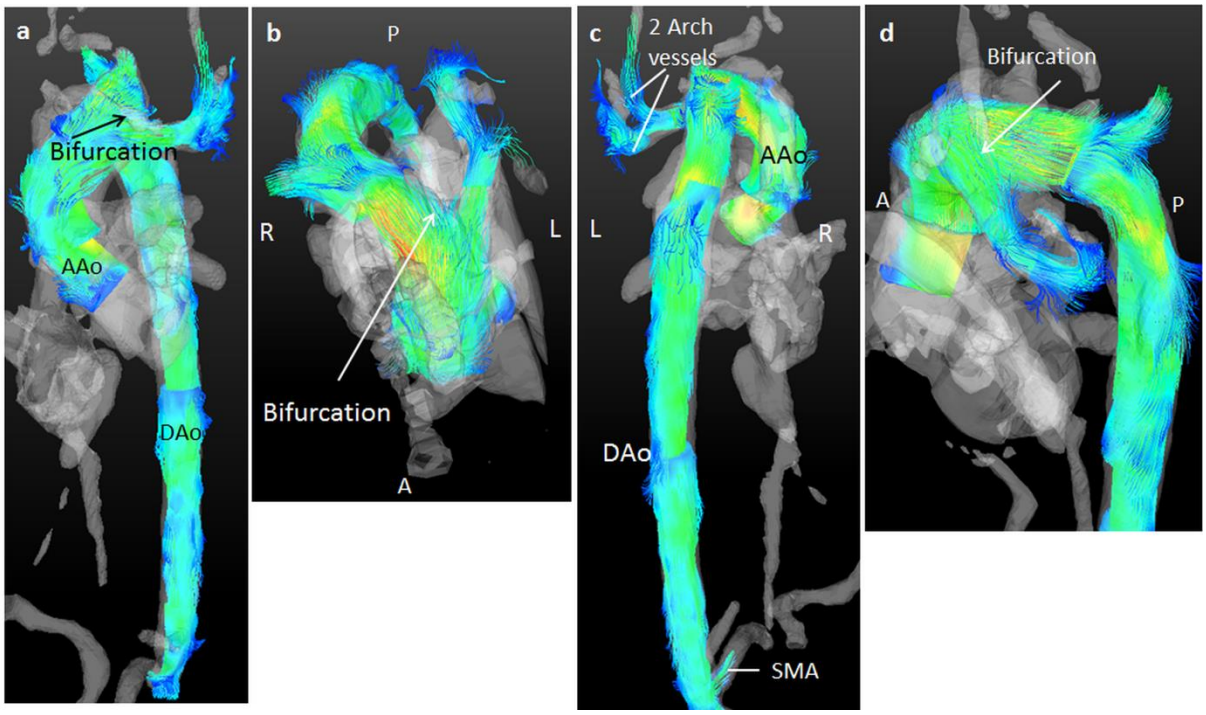

Figure 3.4.2 – Time resolved particle traces of an aortic bifurcation: The resultant visualization depicts the hemodynamic blood flow within a 1.7kg infant born at 35^{+6} weeks gestation with an aortic bifurcation. An iso-surface rendering of the velocity data generates a pseudo angiogram where the vasculature can be seen. Anterior (A), posterior (P), left (L) and right (R) are indicated on the figures. The aorta is rotated to provide 4 different view to aid visualization. a: by generating particle traces during systole from the time resolved velocity data the blood flow within the ascending and descending aorta (AAo, DAo) and point of bifurcation along the arch can be seen. b: the aortic bifurcation can be seen from above. c and d: blood flow within the right common carotid and subclavian artery (2 arch vessels) can be seen following from the bifurcation. Blood flow through the superior mesenteric artery (SMA), which supplies the small intestine can be visualized. Blood flow cannot be visualized re-joining the DAo, indicating that vessel constriction has occurred. The uses and practicalities of 4D PC MRI in preterm infants will covered in chapter 6 and 7. The infant shown here is purely to illustrate the visualization of the velocity flow field and its potential within the preterm cohort and will not appear in the subsequent studies.

The translation to the clinical environment has been slow due to lengthy acquisitions and the substantially manual processing needed for analysis. The need to collect time resolved high spatial resolution volumetric data combined with 3 directional velocity encoding leads to long scan times. Multiple acceleration techniques have been used to reduce scan time to a clinically feasible duration including parallel imaging (Thunberg et al. 2005) (Baltes et al. 2005), different sampling strategies (Barger et al. 2000) and different k-space trajectories (Johnson et al. 2008).

3.5 Cardiac MRI in the Preterm and Neonatal Population: Considerations

Quantification of cardiac function and blood flow volumes with echocardiography are unreliable (Groves et al. 2008); consequently many pathologies in the preterm population remain poorly understood leading to uncertainly over treatment approach. The development of neonatal cardiac MRI has the potential to provide additional hemodynamic and functional information. However the small size (figure 3.5.1), high heart rate, instability and lack of patient cooperation necessitate an optimized approach when scanning preterm and term infants.

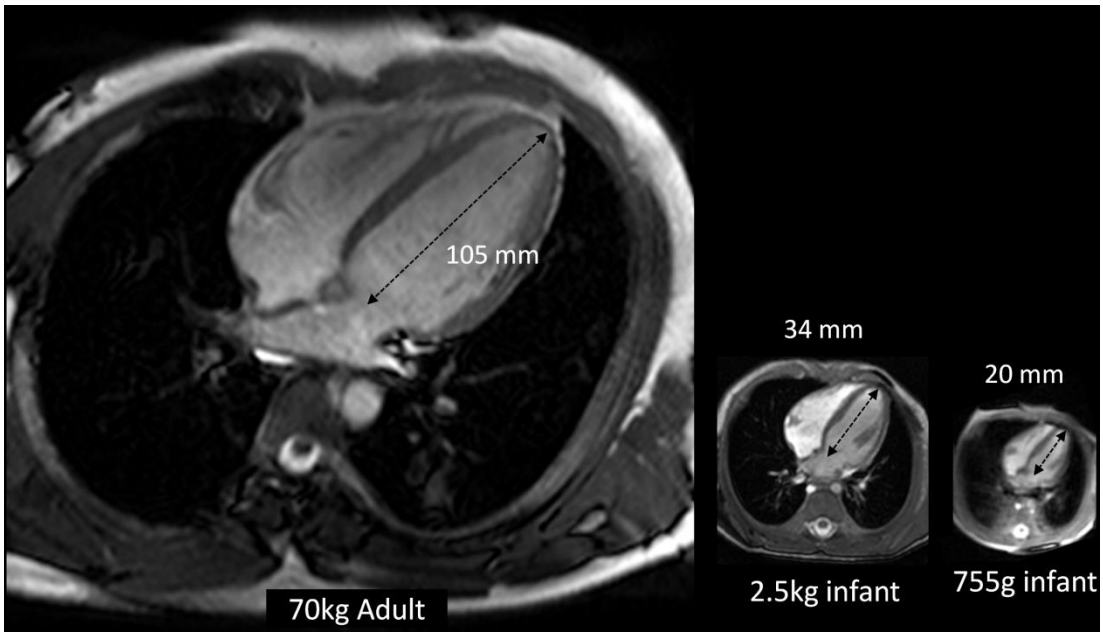

Figure 3.5.1 – Relative size of an adult, preterm and extremely preterm infant: A transverse slice depicting the relative size of a 70kg adult, preterm 2.5kg and extremely preterm 755g infant to scale.

Pre-scan preparation

The environment and level of routine monitoring present on the neonatal unit must be maintained during the MRI scan. This requires MR compatible respiratory support systems, blood saturation (SaO2 levels) and auxiliary temperature monitoring, respiratory and heart rate as well as

temperature control. When sedation is not given lack of patient cooperation can be problematic. All the studies presented in the thesis were carried out without sedation or anaesthesia. Instead the feed and wrap technique (Merchant et al. 2009) was adopted with a good success rate. Acoustic noise protection was achieved by applying mouldable dental putty to the outer ears and followed by neonatal ear muffs.

Considerations

Preterm and term infants heart rates can range from 100-180bpm often with periods of apnea and bradycardia (Polin, 2008). This leads to long scan times due to rejection of data and limited k-space sampling per heartbeat. This small R-R interval also limits the k-space trajectories that can be utilized.

High spatial resolution is required to image the very small neonatal cardiovascular structures; however the use of contrast enhanced imaging is not widely used or preferable in this cohort. From a methodological point of view the preterm vasculature is also often more tortuous than adults, consideration over slice placement and study design is needed (chapter 4). The weight and size of the infants involved in the studies presented in this thesis ranged from 600g to 3.5kg, consequently to maximize SNR in even the smallest infants two different receive coils were utilized for subjects above and below 2kg. However SNR is still limited and this restricts the extent of acceleration techniques that can be applied.

Shimming can also be problematic in neonates. Automated shim methods are generally adequate to provide high quality adult cardiac images. However these methods are less successful in neonates as the small regions of interest and therefore small shim volumes required lead to insufficient SNR for the system to calculate the appropriate shim values. In addition, without contrast enhancement

multiple NSA are used to increase image SNR. The resultant long scan times can be problematic in SSFP sequences due to drifts in the resonant frequency (chapter 5).

In the following work chapters these considerations are highlighted and approaches to tackle several of these issues are described.

3.6 References

Abi-Abdallah D, Robin V, Drochon A, Fokapu O. Alterations in human ECG due to the MagnetoHydroDynamiceffect: A method for accurate R peak detection in the presence of high MHD artifacts. DOI 10.1109/IEMBS.2007.4352673

Baltes C, Kozerke S, Hansen MS, Pruessmann KP, Tsao J, Boesiger P. Accelerating cine phase-contrast flow measurements using k-t BLAST and k-t SENSE.Magn Reson Med 2005;54:1430–1438.

Barger AV, Peters DC, Block WF, et al. Phase-contrast with interleaved undersampled projections. Magn Reson Med 2000; 43:503–509.

Bernstein MA, King KF, Zhou XJ. Hand book of MRI pulse sequences. 2004

Bernstein MA, Zhou XHJ, Polzin JA, King KF, Ganin A, Pelc NJ, Glover GH: Concomitant gradient terms in phase contrast MR: Analysis and correction. Magn Reson Med 1998; 39: 300-308.

Bloch F. Nuclear Induction. Physical Review. 1946; 70: 460 – 474.

Boardman JP, Counsell SJ, Rueckert D, Kapellou O, Bhatia KK, Aljabar P, Hajnal J, Allsop JM, Rutherford MA, Edwards AD. Abnormal deep grey matter development following preterm birth detected using deformation-based morphometry. NeuroImage. 2006; 32: 70-78.

Bogren HG, Mohiaddin RH, Kilner PJ, Jimenez-Borreguero LJ, Yang GZ, Firmin DN. Blood flow patterns in the thoracic aorta studied with three-directional MR velocity mapping: the effects of age and coronary artery disease. J Magn Reson Imaging 1997; 7: 784–793.

Buonocore MH. Visualizing blood flow patterns using streamlines, arrows, and particle paths. Magn Reson Med 1998;40: 210–226.

Carr HY, Purcell EM. Effects of diffusion on free precession in nuclear magnetic resonance experiments. Phys Rev 1954;94:30–38.

Chai P, Mohiaddin R. How we perform cardiovascular magnetic resonance flow assessment using phase-contrast velocity mapping. J. Cadiovasc Mag Res. 2005; 7: 705 – 716.

Colletti PM: Evaluation of intracardiac shunts with cardiac magneticresonance. Curr Cardiol Rep 2005, 7(1):52-8.

Conturo TE, Smith GD. Signal to noise in phase angle reconstruction: Dynamic range extension using phase reference offsets. Magn Reson Med. 1990; 15: 420-437.

Counsell SJ, Boardman JP. Differential brain growth in the infant born preterm: Current knowledge and future developments from brain imaging. Semin Fetal Neonat Med. 2005; 10: 403 – 410.

Dyverfeldt P, Sigfridsson A, Kvitting J, Ebbers T. Quantification of intravoxel velocity standard deviation and turbulence intensity by generalizing phase-contrast MRI. Magn Reson Med. 2006; 56: 850–858.

Dyverfeldt P, Kvitting JP, Sigfridsson A, Engvall J, Bolger AF, Ebbers T. Assessment of fluctuating velocities in disturbed cardiovascular blood flow: in vivo feasibility of generalized phasecontrast MRI. J Magn Reson Imaging 2008;28:655–663.

Dyverfeldt P, Gardhagen R, Sigfridsson A, Karlsson M, Ebbers T. On MRI turbulence quantification. Magn Reson Imaging 2009;27:913–922.

Firmin DN, Gatehouse PD, Konrad JP, Yang GZ, Kilner PJ, Longmore DB. Rapid 7-dimensional imaging of pulsatile flow. Comput Cardiol IEEE Comput Soc Lond 1993;14:353–356

Gang G, Mark P, Cockshott P, et al. Measurement of pulse wave velocity using magnetic resonance imaging. Conf Proc IEEE Eng Med Biol Soc 2004;5:3684–3687.

Gatehouse PD, Keegan J, Crowe LA, Masood S, Mohiaddin RH, Kreitner K, Firmin DN. Applications of phase-contrast flow and velocity imaging in cardiovascular MRI. Eur J Radiol. 2005; 15: 2172-2184.

Greil G, Geva T, Maier SE, Powell AJ. Effect of acquisition parameters on the accuracy of velocity encoded cine magnetic resonance imaging blood flow measurements. J Magn Reson Imaging. 2002; 15:47–54

Groves AM, Kuschel CA, Knight DB, Skinner JR. Cardiorespiratory stability during echocardiography in preterm infants. Arch Dis Child 2005a; 90(1):86-87.

Groves AM, Kuschel CA, Skinner JR. The Neonatologist as an echocardiographer. NeoReviews. 2005b; 7: 391 – 399.

Groves AM, Kuschel CA, Knight DB, Skinner JR. Echocardiographic assessment of blood flow volume in the superior vena cava and descending aorta in the newborn infant. Arch Dis Child Fetal Neonatal Ed. 2008; 93: F24-F28.

Haacke EM, Brown RW, Thompson MR, Venkatesan R. Magnetic resonance imaging. Principles and Sequence design. 1999

Hashemi RH, Bradley WG, Listanti CJ. MRI The basics. Third Edition. 2010.

Hill CR, Bamber JC, Harr GR. Physical principles of medical ultrasonics. Second Edition. 1986.

Hofman MBM, Visser FC, van Rossum AC, Vink GQM, Sprenger M, Westerhof N. In Vivo validation of magnetic resonance blood volume flow measurements with limited spatial resolution in small vessels. MRM. 1995; 33: 778-784.

Hope MD, Hope TA, Urbania TH, Higgins CB. Four-dimensional flow magnetic resonance imaging with wall shear stress analysis before and after repair of aortopulmonary fistula. Circ Cardiovasc Imaging 2010;3:766–768.

Jerosch-Herold M, Seethamraju RT, Swingen CM, Wilke NM, Stillman AE. Analysis of myocardial perfusion MRI. J. Magn reson Imag. 2004; 19: 758 – 770.

Johnson KM, Lum DP, Turski PA, Block WF, Mistretta CA, Wieben O. Improved 3D phase contrast MRI with off-resonance corrected dual echo VIPR. Magn Reson Med 2008;60:1329–1336.

Kilner PJ, Yang GZ, Mohiaddin RH, Firmin DN, Longmore DB. Helical and retrograde secondary flow patterns in the aortic arch studied by three-directional magnetic resonance velocity mapping. Circulation 1993;88(5 Pt 1):2235–2247.

Körperich H, Gieseke J, Barth P, Hoogeveen R, Esdorn H, Peterschröder A, Meyer H, Beerbaum P. Flow volume and shunt quantification in pediatric congenital heart disease by real-time magnetic resonance velocity mapping. Circ. 2004; 109: 1987 – 1993.

Larkman DJ, Nunes R. Parallel magnetic resonance imaging. Phys Med Biol. 2007; R15-R55.

Lauterbur PC. Image formation by induced local lnteractions: examples employing nuclear magnetic resonance. Nature. 1973; 242: 190.

Levick JR. An introduction to cardiovascular physiology. Fifth edition. 2010

Ljunggren S. A simple graphical representation of fourier-based imaging methods. J Mag Res. 1983; 54: 338–343.

Lotz J, Meier C, Leppert A, Galanski M. Cardiovascular flow measurement with phase-contrast MR imaging: basic facts and implementation. Radiographics. 2002; 22:651–671

Lustig M. Donoho DL, Pauly JM. Sparse MRI: The application of compressed sensing for rapid MR imaging. MRM. 2007; 58: 1182 - 1195.

Mansfield P, Grannel PK. NMR 'diffraction' in solids? J. Phvs. C Solid State Phys. 1973; 6: L422.

Markl M, Chan FP, Alley MT, et al. Time-resolved three-dimensional phase-contrastMRI. JMagn Reson Imaging 2003;17:499–506.

Markl M, Draney MT, Hope MD, et al. Time-resolved 3-dimensional velocity mapping in the thoracic aorta: visualization of 3- directional blood flow patterns in healthy volunteers and patients. J Comput Assist Tomogr 2004;28:459–468.

Markl M, Wallis W, Brendecke S, Simon J, Frydrychowicz A, Harloff A. Estimation of global aortic pulse wave velocity by flow-sensitive 4D MRI. Magn Reson Med 2010;63:1575–1582.

Markl M, Kilner PJ, Ebbers T. Comprehensive 4D velocity mapping of the heart and great vessels by cardiovascular magnetic resonance. 2011: 13:7-29

Markl M, Frydrychowicz A, Kozerke S, Hope M, Wieben O. 4D flow MRI. J. MRM. 2012a; 36: 1015-1036.

McRobbie DW, Moore EA, Graves MJ, Prince MR. MRI from picture to proton. Second Edition. 2007.

Metafratzi ZM, Efremidis SC, Skopelitou AS, De Roos A. The clinical significance of aortic compliance and its assessment with magnetic resonance imaging. J Cardiovasc Magn Reson 2002;4: 481–491.

Merchant N, Groves A, Larkman DJ, Counsell SJ, Thomson MA, Doria V, Groppo M, Arichi T, Foreman S, Herlihy DJ, Hajnal JV, Srinivasan L, Foran A, Rutherford M, Edwards AD, Boardman JP. A patient care system for early 3.0Tesla magnetic resonance imaging of very low birth weight infants. Early Hum Dev. 2009; 85: 779-83.

Miller SP, Vigneron DB, Henry RG, Bohland MA, Ceppi-Cozzio C, Hoffman C, Newton N, Partridge JC, Ferriero DM, Barkovich AJ. Serial quantitative diffusion tensor MRI of the premature brain: development in newborns with and without injury. J Mag Reson Imag. 2002; 16: 621 – 632.

Moran PR. A flow velocity zeugmatographic interlace for NMR imaging in humans. Magn Reson Imaging 1982;1:197–203.

Nayler GL, Firmin DN, Longmore DB. Blood flow imaging by cine magnetic resonance. J Comput Assist Tomogr. 1986; 10: 715–722.

Nijm GM, Swiryn S, Larson AC, Sahakian AV. Characterization of the magnetohydrodynamic effect as a signal from the surface electrocardiogram during cardiac magnetic resonance imaging. Computers in Cardiology 2006;33:269−272.

O'Brien K, Myerson S, Cowan B, Young A, Robson M, Freemasons N, Trust W, Fellowship S. Phase contrast ultrashort TE: a more reliable technique for measurement of high-velocity turbulent stenotic jets. Magn Reson Med. 2009; 62: 626–636.

Oyre S, Paaske WP, Ringgaard S, et al. Automatic accurate noninvasive quantitation of blood flow, cross-sectional vessel area, and wall shear stress by modelling of magnetic resonance velocity data. Eur J Vasc Endovasc Surg 1998;16:517–524.

Petersen SE, Voigtlander T, Kreitner KF, Kalden P, Wittlinger T, Scharhag J, Horstick G, Becker D, Hommel G, Thelen M, Meyer J: Quantification of shunt volumes in congenital heart diseases using a breath-hold MR phase contrast technique–comparison with oximetry. Int J Cardiovasc Imaging 2002, 18(1):53-60.

Petersson S, Dyverfeldt P, Gardhagen R, Karlsson M, Ebbers T. Simulation of phase contrast MRI of turbulent Flow. Magn Res Med. 2010; 64: 1039 -1046.

Pike GB, Meyer CH, Brosnan TJ, Pelc NJ. Magnetic resonance velocity imaging using a fast spiral phase contrast sequence. MRM. 1994; 32: 476-483.

Powell AJ, Tsai-Goodman B, Prakash A, Greil GF, Geva T. Comparison between phase-velocity cine magnetic resonance imaging and invasive oximetry for quantification of atrial shunts. Am J Cardiol. 2003; 15: 523–1525

Rolf MP, Hofman MBM, Gatehouse PD, Bloch KM, Heymans MW, Ebbers T, Graves MJ, Totman JJ, Werner B, Van Rossum AC, Kilner PJ, Heethaar RM. Sequence optimization to reduce velocity offsets in cardiovascular magneticresonance volume flow quantification - A multi-vendor study. J. Cardio Magn Res. 2011: 13-18

Sandstede J, Lipke C, Beer M, Hofmann S, Pabst T, Kenn W, Neubauer S, Hahn D. Age- and gender-specific differences in left and right ventricular cardiac function and mass determined by cine magnetic resonance imaging. Europ Radiol. 2000; 10: 438 – 442.

Schiller NB, Shah PM, Crawford M, DeMaria A, Devereux R, Feigenbaum H, Gutgesell H, Reichek N, Sahn D, Schnittger I. Recommendations for quantitation of the left ventricle by two-dimensional echocardiography. American Society of Echocardiography Committee on Standards, Subcommittee on Quantitation of Two-Dimensional Echocardiograms. J American Soc Echocardio: 1989; 2(5): 358-367

Steeden JA, Atkinson D, Taylor AM, Muthurangu V. Assessing vascular response to exercise using a combination of real-time spiral phase contrast MR and noninvasive blood pressure measurements J. Magn. Reson. Imaging. 2010; 31: 997–1003.

Tang C, Blatter DD, Parker DL. Accuracy of phase-contrast flow measurements in the presence of partial-volume effects. J. Magn. Reson Imaging. 1993: 3: 377-385.

Tenforde TS, Gaffey CT, Moyer BR, Budinger TF. Cardiovascular alterations in Macaca monkeys exposed to stationary magnetic fields: experimental observations and theoretical analysis. Bioelectromag 1983;4(1):1-9.

Thunberg P, Karlsson M, Wigstrom L. Accuracy and reproducibility in phase contrast imaging using SENSE. Magn Reson Med 2003;50:1061–1068.

Togawa T, Okai O, Oshima M. Observation of blood flow e.m.f. in externally applied strong magnetic field by surface electrodes. Med Biol Eng 1967;5(2):169-70.

Twieg DB. The k-trajectory formulation of the NMR imaging process with applications in analysis and synthesis of imaging methods. Med Phys. 1983; 10: 610–621.

Urheim S, Edvardsen T, Torp H, Angelsen B, Smiseth OA. Myocardial strain by doppler echocardiography.Validation of a new method to quantify regional myocardial function. Circulation. 2000; 102: 1158-1164.

Valverde I, Simpson J, Schaeffter T, Beerbaum P. 4D phase-contrast flow cardiovascular magnetic resonance: comprehensive quantification and visualization of flow dynamics in atrial septal defect and partial anomalous pulmonary venous return. Pediatr Cardiol 2010;31:1244–1248.

Wild J. The Use of Ultrasonic Pulses for Measurement of Biologic Tissues and the Detection of Tiasue Density Change, Surg. 1950; 127(2): 183-188.

Woodward LJ, Anderson PJ, Austin NC, Howard K, Inder TE. Neonatal MRI to predict neurodevelopmental outcomes in preterm infants. N Engl J Med. 2006; 355: 685 – 694.

Chapter 4

Blood Flow Distribution in the Preterm Circulation: Quantification of PDA Shunt Volume and its Impact

The work in this chapter describes a technique to quantify cardiac output and global distribution of systemic blood flow in preterm and term infants using PC MRI. The accuracy and repeatability of this technique is then analysed. Blood flow distribution to the upper and lower body in healthy preterm and term infants is then presented as a function of corrected gestational age (cGA) to establish the normative range. This same technique is then used to quantify ductal shunt volume and its effect on global blood flow distribution in infants with prolonged patency of the ductus arteriosus. The significance of the presence of PDA on upper and lower body blood flow is then determined. Ductal shunt volumes were also related to echocardiography measures to determine the most robust echo measure of ductal flow.

In addition, investigations into regional blood flow distributions in preterm and term infants are then carried out. PC MRI was used to quantify cerebral blood flow in a preliminary cohort of 5 healthy infants and quantify flow to the abdominal organs in a larger group of healthy and PDA infants. These preliminary studies are presented in the final subsections of this chapter.

4.1 Quantification of PDA Shunt Volume and the Resultant Flow Distribution

4.1.1 Introduction

Persistently PDA is a common congenital condition in neonates and is clinically apparent in 60% of infants born before 28 weeks gestation (Wyllie, 2003). PDA has been correlated with multiple

adverse outcomes, including adverse neurodevelopmental outcome, chronic lung disease, pulmonary haemorrhage, necrotizing enterocolitis (NEC), intra-ventricular haemorrhage, whether this association is causal or casual remains unclear (Coombes et al. 1990) (Evans et al. 1996) (Gonzalez et al. 1996) (Kluckow et al. 2000). More than 40 randomized controlled trials have been carried out to assess optimal treatment for PDA, but none have shown improvements in mortality or significant long-term morbidity (Bose et al. 2007) (Wyllie, 2003). Hence, despite over 30 years of research studies involving thousands of infants, the evidence for pharmacological closure of the duct is inconclusive (Sasi et al. 2011).

Controversy also exists over appropriate indications for treatment varying from prophylaxis on the basis of gestation to treatment only when a PDA is demonstrably significant (Wyllie, 2003). Added complication arises by differing diagnostic criteria for ductal patency or significance: the definition of a hemodynamically significant duct varies among neonatologists and is a source of contention. In addition echocardiography, the current modality used for PDA assessment cannot determine the clinical significance of the duct. Measurements of cardiovascular morphology and visualization of ductal flow patterns are used to indicate the volume of ductal shunting, with high shunt PDA thought to be more clinically significant. These factors have led to little consensus over appropriate treatment which varies between sites (Laughon et al. 2007) (Fig 4.1.1) and is thought to result in up to 64% of infants being treated unnecessarily (Wyllie, 2003).

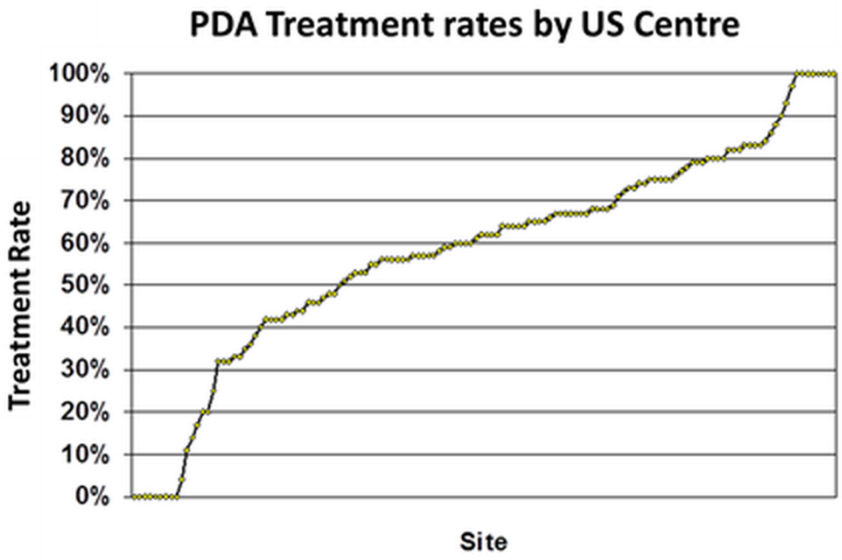

Figure 4.1.1 – PDA treatment rates: Data from 134 Pediatric Group NICUs in the USA between 1997 and 2004 (Laughon et al. 2007). The graph illustrates that treatment rate as a proportion of infants diagnosed with PDA and varies between 0-100% across sites and exemplifies that there is no consensus over treatment.

Treatment of PDA

The argument for enforced ductal closure is that high volume systemic to pulmonary shunting causes both pulmonary hyper-perfusion and global or regional systemic hypo-perfusion (Agarwal et al. 2007) (Groves et al. 2008a) (Laughon et al. 2007): it is thought that PDA may cause preferential steal of systemic blood flow (diminished perfusion to the lower body due to blood flow through duct). Treatment ranges from surgical ligation to medication, but optimum timing of intervention remains unclear (Wyllie, 2003).

Surgical ligation is performed via a left posterolateral thoracotomy and the duct is either tied or clipped. Most surgical complications often are related to the thoracotomy yet inadvertent ligation of the left pulmonary artery and descending aorta have been reported (Wyllie, 2003). Medication either in the form of Indomethacin or Ibruprofen uses non selective cyclo-oxygenase inhibitors that inhibit prostaglandin synthesis causing vasoconstriction (Sasi et al. 2011). This results in functional closure of the duct within 48 hours in 79% of infants (Wyllie, 2003), though relapse has been shown in up to 33% of infants. Vasoconstriction however, is not targeted and occurs in the cerebral and

gastrointestinal arterial supplies (Coombes et al. 1990) (Edwards et al. 1990). Renal impairment and pulmonary and gastrointestinal haemorrhage have also all been associated with this medical treatment (Wyllie, 2003). The risks of a surgical procedure on such a fragile population and that the medication is toxic have added to the increasing speculation that intervention to close a PDA may be unwarranted (Benitz, 2010) (Chorne et al. 2007) (Knight, 2001) (Overmeire, 2007).

Current assessment

Echocardiography is currently used for PDA assessment, but degree of assessment varies across sites (Sehgal et al. 2009). Typically the standard full evaluation includes measurement of ductal diameter, peak systolic and end-diastolic ductal blood flow velocity ratio, ratio of left atrial diameter to aortic root and reversal of diastolic flow in the descending aorta (Wyllie, 2003). However these markers only establish the presence of a duct and indicate shunt volume and not the hemodynamic significance or volume of flow through the duct (Evans et al. 2004). Ductal shunt volume cannot be quantified reliably by echocardiography due to air spaces within the lungs.

Many echocardiography studies investigating abdominal and cerebral blood flow volumes in the presence of a PDA (Coombes et al. 1990) (Lemmers et al. 2008) have shown a reduction in regional flow. Conversely a study carried out by Shimada *et al*. 1994 suggested that despite large left-to-right ductal shunting, the preterm heart is capable of mounting a compensatory increase of cardiac output sufficient to maintain unchanged cerebral blood flow velocity, but is unable to maintain postductal organ blood flows because of decreased perfusion pressure (ductal steal) and localized increase in vascular resistance. This study however, only quantified cerebral blood flow velocity and not flow volume due to the imaging window and did not quantify the shunt volume or the association with blood blow distribution.

Although echocardiography offers high sensitivity for detection of a PDA and patterns of blood flow, it has limited ability to quantify volumes of flow (Chew et al. 2003) (Groves et al. 2008b) either

within the duct or in the surrounding vessels. As a result the previously mentioned clinical studies have all been weakened by a limited ability to quantify PDA shunt volume and its impact on total systemic and pulmonary blood flow with accuracy. Hence there is a need for the development of techniques to accurately assess the hemodynamic impact of the duct to aid future clinical trials in determining treatment approach.

PC MRI provides a non-invasive technique to quantify blood flow that is not limited by the imaging window or image angle-dependent (Fogel et al. 2000) (Gatehouse et al. 2005) (Tan et al. 2001) (Varaprasathan et al. 2002). An initial study carried out by Sieverding *et al*. 1992 quantified intra cardiac shunt volumes in 6 children with congenital heart diseases via PC flow measurements in the great vessels. It has previously been shown that PC MRI has improved reproducibility when quantifying flow compared to echocardiography in the neonatal population (Groves et al. 2011). The neonatal unit at Queen Charlotte's and Chelsea Hospital's neonatal unit has adopted an approach of non-intervention for the PDA, leaving the duct to close naturally in >90% of preterm infants (unpublished data). This has provided the opportunity to study the duct at a point along its natural history.

Objective

The aim of the work presented in this section was firstly to investigate the global flow distribution in control (infants with closure of PDA confirmed by echo) preterm and term infants using PC MRI. Secondly to develop a technique to quantify ductal shunt volume and the impact of PDA on systemic blood flow volume in neonates, with scope to aid future clinical trials. Finally by relating ductal shunt volumes also to echocardiography measures the most robust echo measure of patency could be determine. This study has since been accepted for publication in NMR in Biomedicine (Broadhouse et al. 2013).

4.1.2 Patients and Methods

The study was approved by the North West London Research Ethics Committee (06/Q0406/137) and written informed parental consent was obtained in all cases.

Study cohort

Cardiac MR images were obtained from 77 infants who were inpatients at Guys and St Thomas' Hospital and Queen Charlotte's and Chelsea Hospital, median (range) gestational age $31^{+4}(24^{+3}\text{-}38)$ weeks, cGA $33^{+6}(26^{+4}\text{-}38^{+6})$ weeks, birth weight 1495(525-3760) grams, weight at scan 1575(660-3760). All infants were scanned using acoustic ear protection, pulse oximetry, vector ECG monitoring and without sedation or anesthesia (Merchant et al. 2009). No respiratory compensation techniques were used as the rapid and shallow neonatal respiratory motion patterns and multiple averages meant that no significant motion artefacts were observed in any of the subjects (figure 4.1.2b, c and d).

Seventeen infants had PDA demonstrated on echocardiography, with 1 of those infants also having a small (2mm) muscular ventricular septal defect (VSD). This infant was not excluded from the study since this intracardiac shunt would not bias our assumptions about left ventricular output (LVO), SVC flow and blood flow in the descending aorta (DAo). Sixty infants had normal cardiac anatomy (persistent patency of the foramen ovale was considered a developmental variant and was seen in 13 of the infants in the study).

Sixteen infants required low flow supplemental oxygen or nasal continuous positive airway pressure via an MR compatible system (Merchant et al. 2009) but all infants were stable and tolerating full enteral feeds during the scan. None of the infants were mechanically ventilated during the scan. All infants had an echo performed within 24 hours of MRI scan by an operator with >10 years of

experience in neonatal echocardiography. There was no change in respiratory status in any infant between MRI and echo scans.

Echocardiography measures

All echocardiographic images were acquired using a Vivid 7 ultrasound machine (GE Healthcare, Milwaukee, WI) with a 10MHz sector probe. Ductal diameter was assessed at the point of maximal ductal constriction on colour Doppler. Care was taken to minimise the colour gain settings to avoid exaggeration of ductal diameter (Skinner et al. 2001). Peak systolic and end diastolic ductal blood flow velocity ratio (ED/Max flow) was assessed using continuous wave Doppler. The ductal flow pattern is dependent on diameter and systemic and pulmonary vascular resistance and therefore indicative of shunt volume (Su et al. 1999). Ratio of left atrial diameter to aortic root (LA:Ao) was assessed using leading edge-leading edge technique from M mode Doppler in the long axis view (Skinner et al. 2001). The left atrium is thought to dilate due to increased preload from the addition shunt volume (Sehgal et al. 2009). Reversal of diastolic flow in the descending aorta (regurgitant fraction) was assessed using pulsed wave Doppler from a high parasternal view with angle correction (Skinner et al. 2001). Regurgitant fraction indicates systemic blood flow steal during diastole as LV pressure decreases maximizing the pressure gradient across the duct. Ductal diameter of ≥ 1.5mm, ED/Max flow < 50%, LA:Ao > 1.4 and reversal of diastolic flow in the descending aorta are all thought to indicate high volume ductal shunting (Skinner et al. 2001).

This full protocol was carried out in all but 6 PDA infants who became unsettled, causing the echo protocol to be cut short. These measures were then correlated to PC MRI ductal shunt volume values to determine the association.

PC MRI Acquisition

Data was acquired on a Philips 3-Tesla MR Achieva scanner (Best, Netherlands) using a specialised 8 channel pediatric body receive coil for infants above 2kg and a small extremity receive coil for infants below 2kg. Standard single slice retrospectively gated PC MRI sequences (optimized from the previous study (Groves et al. 2011) with spatial resolution of 0.6x0.6mm, slice thickness = 4mm, TR/TE = 5.9/3.1ms and number of signal averages (NSA) = 3 were employed to achieve sufficient voxel coverage of the vessels of interest for a robust and reliable measurement in even extremely preterm infants while keeping scan duration to a minimum. The velocity encoding was calibrated for a VENC of ±120/150cms^{-1} for LVO and DAo sequences and 60/80cms^{-1} for SVC sequences. Acquisition time for each 2D PC scan ranged between 1 and 4 minutes due to heart rate variability and arrhythmia rejection. Table 4.1.1 shows the sequence parameters for the 3 PC scans used in this study.

Scan	spatial resolution (mm)	cardiac phases	FOV (mm)	Slice thickness (mm)	TR/TE (ms)	flip angle (degrees)	PE direction	NSA	VENC cm/s	scan duration (mins)
LVO	0.6x0.6	20	90-120	4	5.9/3.1	10	AP	3	120-150	1-4
SVC	0.6x0.6	20	90-120	4	5.9/3.1	10	AP	3	60-80	1-4
DAo	0.6x0.6	20	80-120	4	5.9/3.1	10	AP	3	120-150	1-4

Table 4.1.1 2D PC MRI scan parameters: Table shows the scan parameters for the 3 PC sequences used in this study.

PC sequence optimization

Evaluation of coils and SNR

Optimization of the previously mentioned PC acquisition (Groves et al. 2011) relied heavily on the addition of the paediatric body and small extremities coil (previous neonatal scans were acquired

with a flex M coil). Evaluation of the small extremities and paediatric coils was carried to assess the available SNR gain if any over the Flex M coil. The Flex M consisted of 2 separate coil elements that were placed above and below the subject, the small extremities coil consisted of 8 elements in a semi flexible design and the paediatric body coil consisted of 8 elements in a rigid cylindrical design. SNR was calculated in 1ltr phantom containing doped water. In addition, in vivo SNR measurements from the small extremities and paediatric body coil were calculated in 2 neonates.

RF spoiled GE sequences (spatial resolution = 1.88x2.5mm, slice thickness = 10mm, TR/TE = 20/5ms) were used to quantify SNR in the phantom bottle. Single central plane sagittal and coronal and multiple transverse slices were acquired with each coil. SNR was determined by calculating the mean and standard deviation (SD) of the signal over 40 dynamic scans on a voxelwise basis. Noise was then estimated by averaging the SD within a ROI inside the phantom. It was not feasible to calculate SNR in neonates with the same method as above due to cardiac motion, consequently PC sequences were used, firstly to calculated SNR from the gated magnitude images and secondly to assess performance of the coils using a PC sequence. Three transverse PC sequences (identical parameters as above) were acquired at the level of the pulmonary arteries in 2 infants with both the small extremities and paediatric coil. The 2 infants had cGA 27+3 and 33+1 weeks and weight at scan 660g and 1880g. SNR was calculated by averaging the magnitude signal and SD over the 20 cardiac phases on a voxelwise basis. Noise was then estimated by averaging the SD within an ROI in static tissue.

Although the Flex M provided more SNR in the phantom than the Paediatric body coil, the SNR was un-uniform and over the region of the heart (centre of the phantom) was slightly less than the Paediatric coil (figure 4.1.2). The diameter of the 1ltr phantom was approximately the same as the torso and arms of a 1.5kg infant. When scanning infants, the top element of the Flex M is placed on top of the infant, the arms and blankets often add to the distance between the heart and the coil elements which would reduce SNR in this region. In addition the closed design of the paediatric body

and small extremities coils led to the infants being more settled during the scan; consequently longer scans could be tolerated.

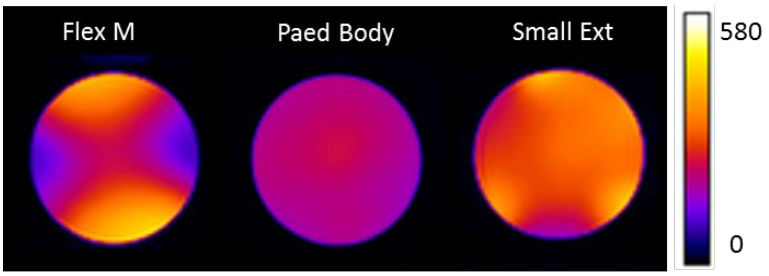

Figure 4.1.2 SNR phantom test: the SNR in a transverse plane in the 1ltr phantom from the Flex M, small extremities and paediatric coils.

The SNR was noticeably larger in neonates using the small extremities coil, for the infant ~2kg there was minimal difference in SNR seen between the 2 coils (figure 4.1.3). It was therefore decided that infants <2kg would be scanned in the small extremities coil and infant >2kg be scanned with the paediatric body coil.

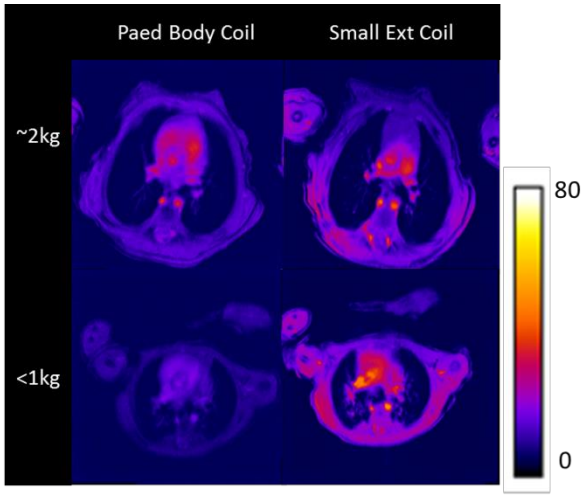

Figure 4.1.3 SNR calculated from PC sequences: (at the level of the pulmonary arteries) using the small extremities and paediatric body coils in a 660g and 1880g preterm infant.

Parameter optimization

The magnitude of the gradients was increased from minimum to maximum as the risk of peripheral nerve stimulation was minimal due to the proximity of the infants to the iso-centre of the bore. This subsequent decrease in scan duration, the increase in SNR from the new paediatric and small extremities coil and infants settling for longer in the scanner, and therefore tolerating longer scans allowed the spatial resolution to be increased from 1.2-0.6mm for the 2D PC acquisitions. In Chapter 6 and 7 4D PC MRI in preterm infants is introduced. The increase in SNR and decrease in scan duration from the previously mentioned alterations permitted 4D PC sequences to be acquired at 1mm isotropic spatial resolution (previously spatial resolution = 2.5mm isotropic, Groves et al. 2012) in infants in a tolerable time frame.

Background phase errors

Background phase errors in the PC acquisitions were determined from a phantom scan. Directly after an infants had been scanned a gelatine phantom was placed at the same position within the bore of the magnet, in the receive coil, as the infant. The 3 LVO, SVC and DAo 2D PC scans were then acquired again with identical geometry. A 1ltr gelatine phantom was used instead of a water phantom to minimize movement of the sample from table motion which would add to apparent background phase errors in the PC image. Firstly no visible change in velocity was visible in any of the 3 scans (figure 4.1.4). ROIs were then determined within the phantom at the same position as the vessels of interest. Flow was calculated using viewforum in the same manner as from the LVO DAo and SVC sequences in infants. Average cross-sectional velocity for all 3 ROIs was below $0.2cms^{-1}$. This would give rise to and error in stroke volume of ~ 1.8%. This error was determined to be acceptable in the clinical setting.

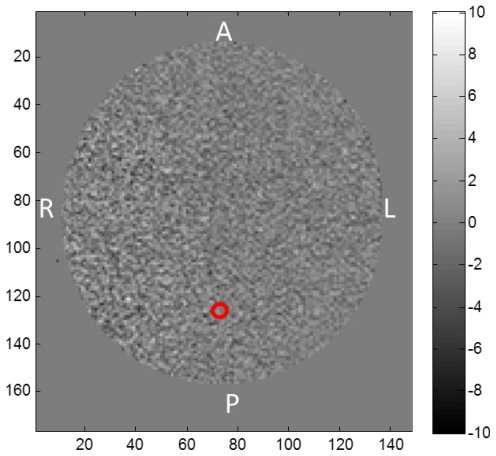

Figure 4.1.4 Background phase errors: background phase image in a 1Ltr gelatine phantom. The red ROI of interest denotes the position of the DAo ROI. Average cross-sectional velocity was found to be below 0.2cms^{-1} for all ROIs and therefore background phase errors were considered negligible.

Acquisition alignment

Assessment of volume of flow directly within the PDA is not currently possible since the individual morphology and position of the duct varies greatly between subjects and the duct can be very tortuous or too short to accommodate an imaging slice (Agarwal et al. 2007) (see chapter 6). Therefore we assumed that in the absence of ductal shunting LVO should equal total systemic blood flow (upper + lower body flow), and in the presence of ductal shunting the difference between LVO and total systemic flow would equal the ductal shunt volume.

Pilot scans were acquired to view the vessels of interest to ascertain the straightest section of the vessel adequate for the slice thickness of the PC sequences and to position the sequences perpendicular to the centreline of the vessel so as to minimize partial volume effects. A slice thickness of 4mm was chosen as this was shown to be adequate to reduce partial volume errors whilst preserving SNR.

LVO was quantified at the level of the aortic valve (figure 4.1.5a and b). Arterial upper body flow cannot reliably be assessed by PC-MRI since the topology of the brachiocephalic, left common

carotid and left subclavian arteries does not allow for positioning of a single PC-MRI imaging plane (figure 4.1.6). Volume of flow in the SVC is increasingly recognised as a marker of upper body flow in neonatal haemodynamic assessments (Kluckow et al. 2000) therefore upper body flow was quantified in the SVC at the level of the pulmonary trunk (figure 4.1.5c). Lower body flow was quantified in the DAo at the level of the diaphragm (figure 4.1.5d). Quantifying lower body flow in the inferior vena cava (IVC) was not possible since the IVC and hepatic veins merge immediately adjacent to the right atrium.

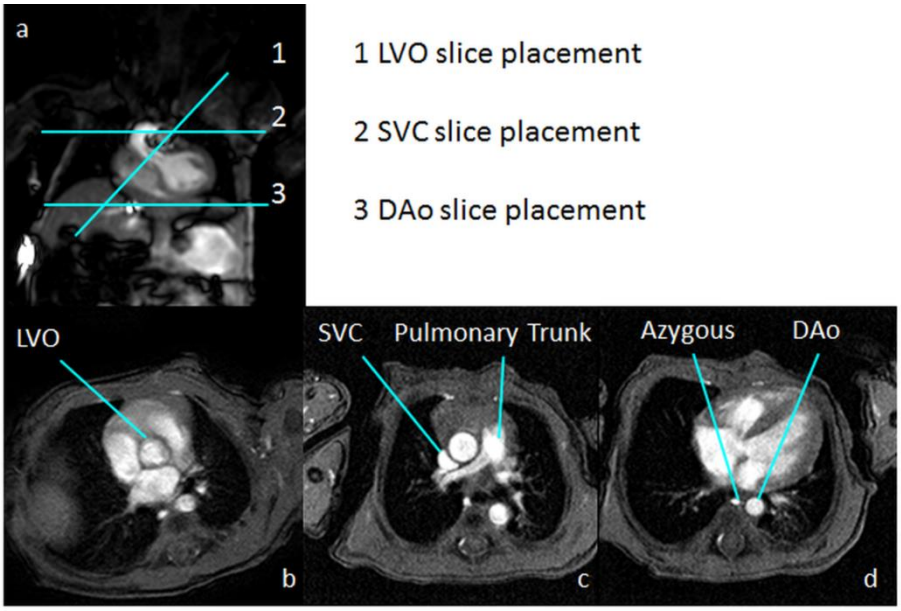

Figure 4.1.5 Study design: a: Anatomical position of the 3 PC MRI sequences. PC MRI sequence to quantify b: LVO, c: SVC flow volume and d: DAo flow volume. PC MRI sequences were acquired during free breathing. Images show no significant respiratory motion artefacts.

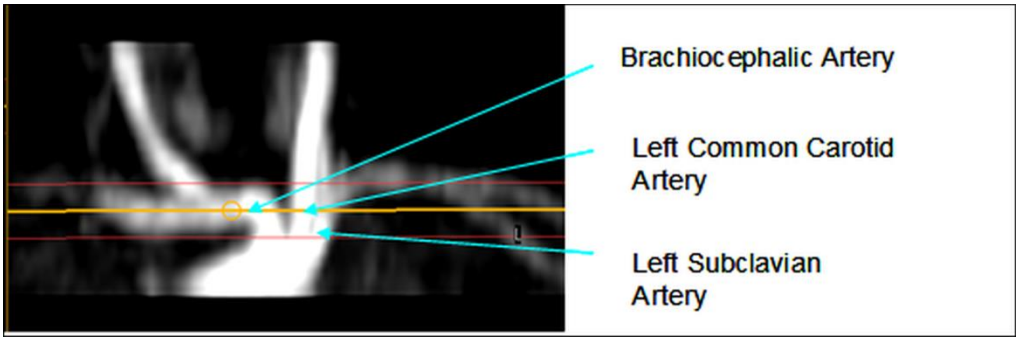

Figure 4.1.6 Brachiocephalic, left common carotid and left subclavian arteries: Angiogram of the brachiocephalic, left common carotid and left subclavian arteries in a preterm infant. Yellow (centre) and red (edge) lines show the placement of a 4mm thick PC MRI sequence. Topology of these vessels meant that flow could not be quantified accurately in all 3 vessels using just 1 sequence.

Data processing

Sequence analysis and flow volume quantification for PC datasets was performed using a commercial workstation (Philips ViewForum). Automated vessel edge detection was used for all vessels of interest, with manual correction where necessary. Once defined in the first cardiac phase the software tracks the vessel of interest over the cardiac cycle using edge detection algorithms. Flow is then calculated at each time point of the cardiac cycle, generating a flow curve and volume of flow value for each vessel of interest.

Statistical analysis

A Bland-Altman intra-observer repeatability analysis (Bland et al. 1986) of the LVO, DAo and SVC sequences was performed in 10 infants to verify the accuracy of the optimized PC sequence in the small neonatal vessels. Mean difference of measures, limits of agreement (loa) and repeatability index (normalized loa = loa/mean of measures, RI) were calculated. PC and required pilot sequences were repeated within the same scan session 5 or more minutes apart. Analysis was carried out blinded by a single observer. Due to time constraints, repeating all 3 PC sequences in the same scan

was not possible therefore LVO, DAo and SVC scan re-scan was not necessarily carried out in the same 10 infants.

Bland-Altman analysis was used to compare LVO and total systemic blood flow PC values to verify the decision in systemic blood flow slice placement. Mean difference of measures, loa and normalized loa (loa/mean of measures) were also calculated. This also illustrated the magnitude of the ductal shunt volume in infants with PDA, which was then calculated in ml/kg/min and as a percentage of LVO.

Normative ranges of SVC, DAo and LVO were plotted (against cGA) to establish normal ranges of flow volumes in the control infants. The impact of ductal shunt volume was assessed to determine whether infants with PDA had altered global flow volumes. To examine whether preferential steal (diminished perfusion of blood to upper or lower body due to blood flow through duct) was predominantly from the lower body in PDA infants, the ratio of upper and lower body flow was also plotted. Flow volumes were normalized by weight at scan instead of body surface area (as is sometimes reported) as this is the convention in neonatal hemodynamic studies. There is little consensus on how to reliably calculate body surface area and length measurements can often be erroneous in the neonatal population.

An unpaired Student's t-test was used to compare LVO, lower body flow and upper body flow volumes in infants with and without PDA. Multiple linear regressions were carried out on upper body and lower body flow volumes and upper/lower body flow ratio correcting for gestational age to investigate if an association with PDA shunt volume and decreased systemic blood flow existed. Linear regression was carried out on ductal shunt volume and echocardiographic measures to establish the strength of association of each measure of duct flow. A spearman's rank correlation was carried out on ductal shunt volume and regurgitant fraction due to the spread of data. Ductal shunt volume was represented as a percentage of LVO. Statistical significance was determined by a p value < 0.05.

4.1.3 Results

Intra-observer analysis

In 10 infants Bland-Altman intra-observer repeatability analysis of LVO, DAo and SVC sequences was carried out and gave a scan-rescan RI (equivalent to 95% confidence interval) of 11.5%, 11.9% and 12.8% respectively. Table 4.1.2 shows the median (range) weight at scan, RI, loa and mean difference from the Bland-Altman analysis.

Sequence	Weight at scan (median(range)grams)	RI%	loa ml/kg/min	Mean difference ml/kg/min
LVO	1540(1100-2840)	11.5	-22.3 - 31.9	4.8
DAo	1775(1100-3450)	11.9	-18.4 - 12.7	-2.9
SVC	1440(1100-3450)	12.8	-10.6 - 15.6	2.5

Table 4.1.2 - Bland-Altman Analysis: Median (range) weight at scan, RI, limit of agreement and mean difference values from the Bland-Altman analysis of LVO, DAo and SVC repeatability.

Infants without ductal shunting

In 60 infants (median (range) gestational age 33(24^{+3}-38) weeks, cGA 34^{+5}(26+4-38^{+6}) weeks, birth weight 1775(560-3760)grams, and weight at scan 1910(745-3760) grams) closure of the ductus arteriosus was confirmed by echocardiography. In these infants our initial assessment suggested that total systemic flow was slightly greater than LVO (mean difference -12.2 ml/kg/min). However population anatomic variation in the azygos venous system means that there is often a significant contribution to the SVC flow volume from the lumbar and pelvic veins. This flow would effectively be double-counted using our technique since the flow would be imaged both arterially in the descending aorta and venously in the superior vena cava which includes azygos drainage. By calculating the volume of azygos flow at the level of the diaphragm (figure 4.1.5d) the contribution

from lumbar and pelvic veins was calculated, and subtracted from the SVC flow in order to evaluate the correct upper body flow.

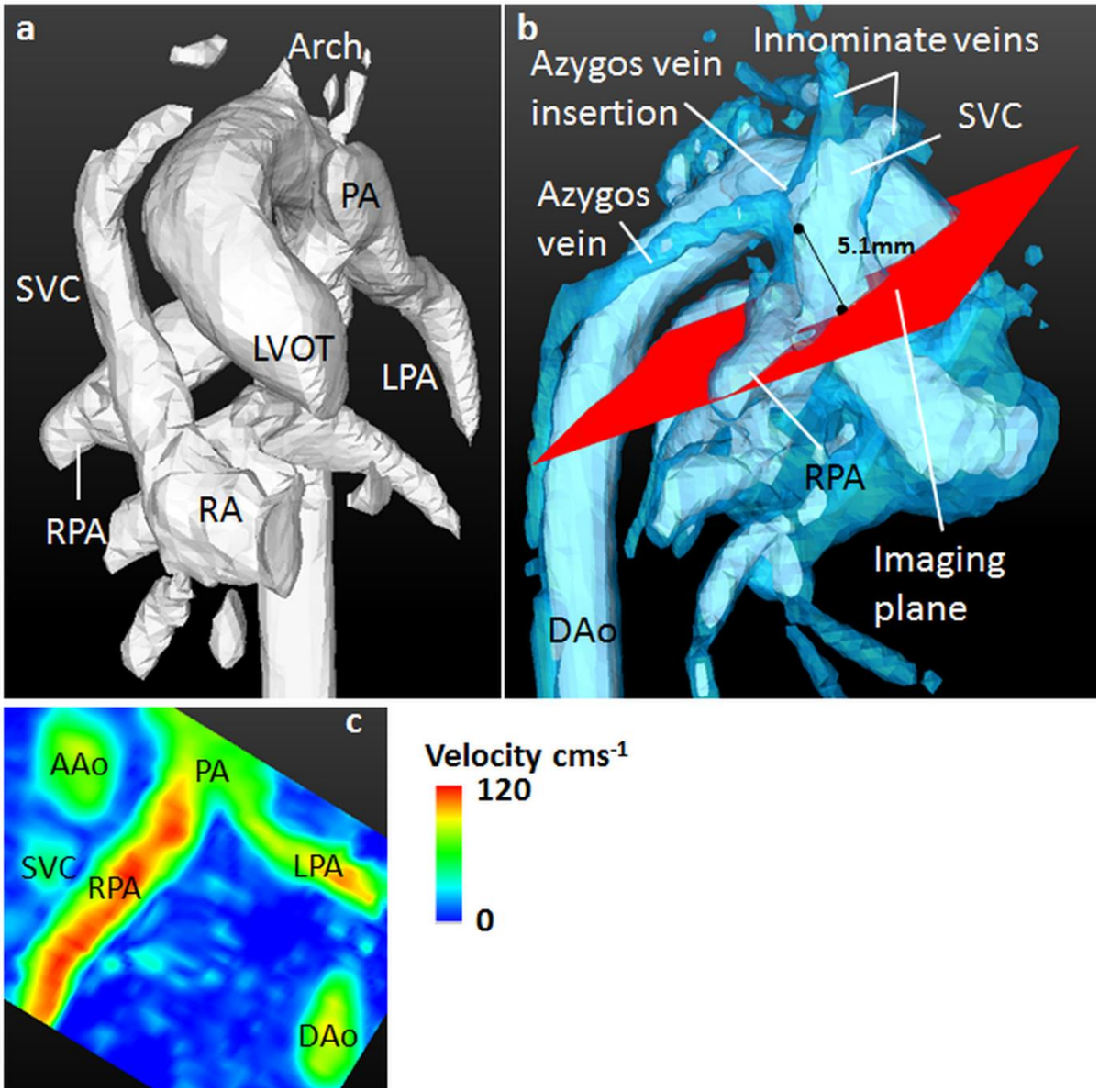

Figure 4.1.7 - The azygos system: The Azygos vein that drains the chest cavity and some of the lower body is shown to join the SVC just below the right and left innominate veins. An iso-volume rendering of the aorta generated from the sum of squares of 4D PC velocity dataset. a: the aorta, left ventricular outflow tract (LVOT) SVC, pulmonary artery (PA), right PA (RPA), left PA (LPA) and right atrium (RA) are clearly shown in a 875g infant. The position of the SVC imaging plane is shown in red. b: lowering the threshold of the isosurface rendering reveals low velocity blood flow (in blue). The innominate veins, azygos vein and insertion point into the SVC can clearly be seen, again the position of the imaging plane is shown in red. The distance between the insertion point and SVC plane was found to be 5.1mm. With a slice thickness of 4mm all of the azygos flow would be included in the quantification of SVC flow at the PC acquisition level. The resultant velocity field within the plane can be shown in c.

Bland-Altman scan rescan analysis

The Bland-Altman plot (figure 4.1.8) shows that total systemic flow (Upper body (SVC - azygos) + lower body (DAo flow)) closely matched LVO, with mean difference 2.06 ml/kg/min, loa -27.8 to +32.0 ml/kg/min and normalized loa (RI) = 13.2%. Therefore with this protocol ductal shunt volume can be determined within 13.2% of LVO. Azygos flow was found on average to be 5.7% of LVO.

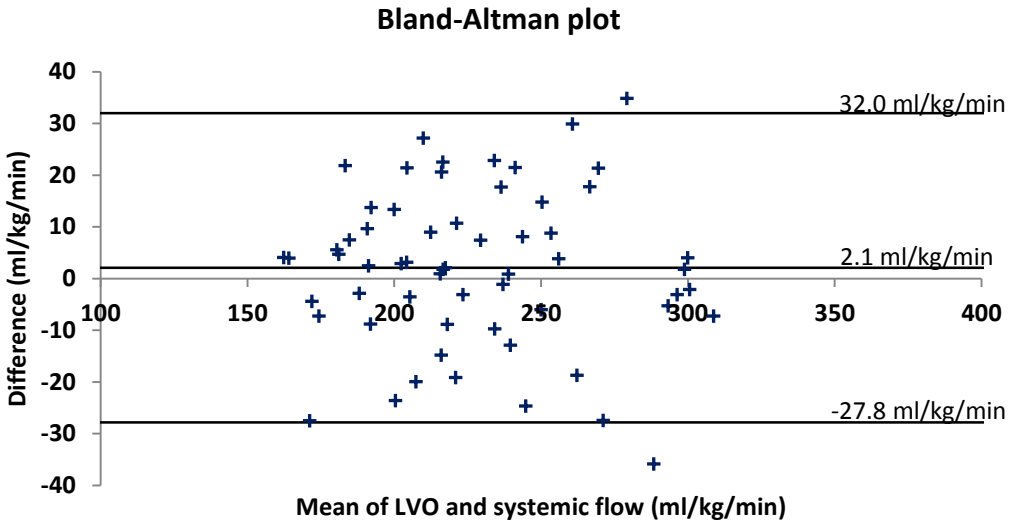

Figure 4.1.8 – Bland-Altman analysis: LVO and systemic blood flow as measured by PC MRI in 60 control infants. LVO and systemic flow values showed good agreement.

Infants with ductal shunting

Seventeen infants had a PDA confirmed by echocardiography (median (range) gestational age 27(24^{+3}-31^{+1}) weeks, cGA 29^{+4}(27^{+3}-36^{+1}) weeks, birth weight 975(525-1400) grams and weight at scan 1140(660-2400) grams). PDA was treated in 2 of the 17 infants. One with Ibuprofen prior to the scan and indomethacin after, the duct closed shortly after the second course of treatment. The second was treated once prior to the scan with Ibuprofen. Both were still patent at the time of the MRI scan. None of the PDA infants underwent surgery to close the duct. All of the 17 PDA infants

survived and there were no incidences of NEC in this cohort. No infant included in this study went on to require treatment for prolonged ductal patency.

Volume of ductal shunt

Ductal shunt volume was calculated for all 17 PDA infants as the difference between LVO and total systemic flow and ranged between 6.4 and 74.2% of LVO. PDA infants were also plotted on the Bland-Altman to demonstrate the extent of the ductal shunt volume (figure 4.1.9). Three of the infants with PDA lay within the Bland-Altman loa and would not therefore be differentiated from the control infants without the echo results.

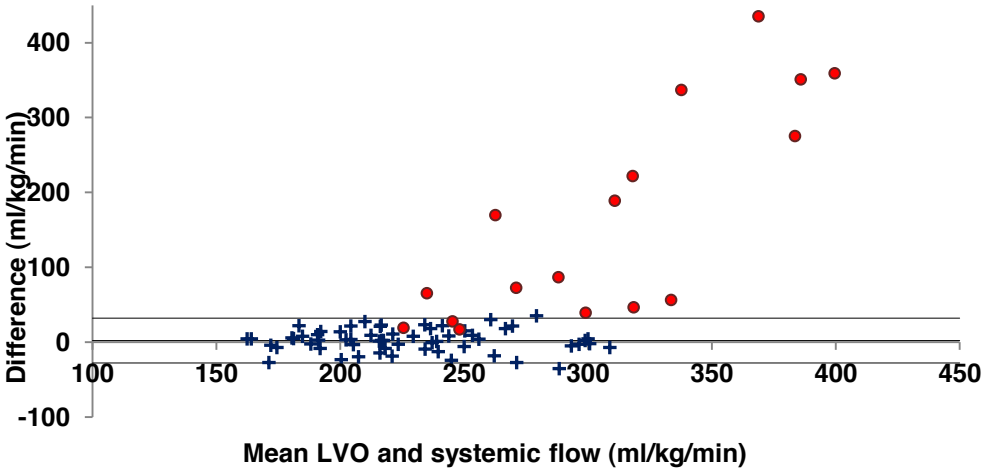

Figure 4.1.9 – Ductal shunt volume: Bland-Altman plot of LVO and total systemic blood flow ((SVC – azygos) + DAo flow volume). Control infants (+) and PDA infants (●). Ductal shunt ranged between 6.4 and 74.2% of LVO.

Impact of PDA on LVO and systemic blood flow

The normative ranges show that all but 4 infants with PDA had LVO above the control group 95% confidence limits (figure 4.1.10a). All 17 infants with PDA had upper body blood flow volumes within or above the control group 95% confidence limits (figure 4.1.10b). All but 4 of the PDA infants had lower body flow volumes within or above the control group 95% confidence limits. These 4 infants were 1.98, 1.99, 2.82 and 3.60 SD below the mean and had ductal shunt volumes of 61.9%, 48.8%, 66.5% and 74.2% of LVO respectively (figure 4.1.10c). All but 3 PDA infants remained with the normative range for upper/lower body flow ratio (figure 4.1.10d). This may indicate that preferential steal occurs predominantly from the lower body flow.

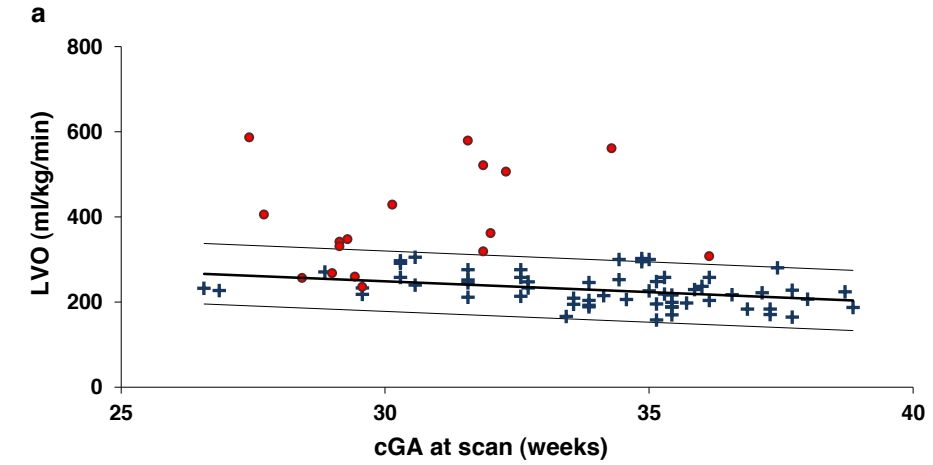

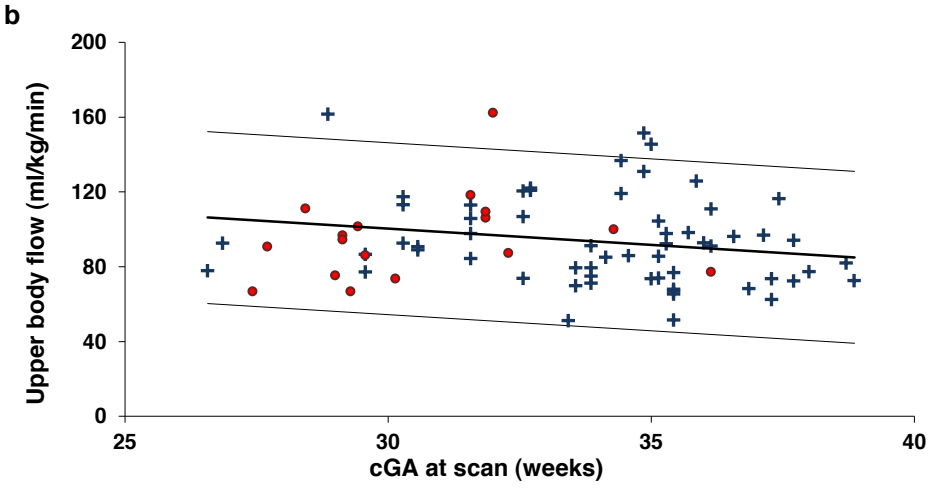

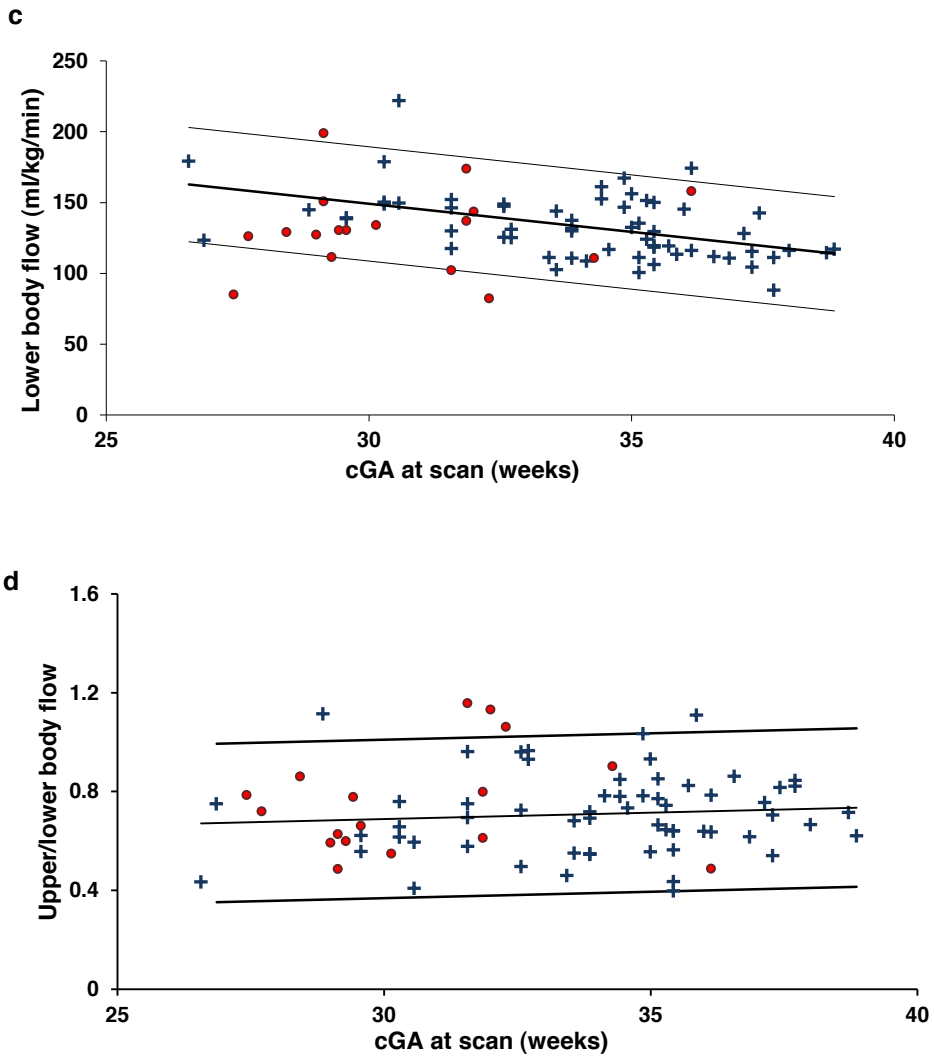

Figure 4.1.10 – Normative ranges: Normative ranges (with respect to gestational age) of blood flow in 77 infants with (●) and without (+) PDA, black lines show the mean and population range at 95% confidence limits. a: LVO. b: Upper body flow (SVC – Azygos flow). c: Lower body flow (DAo flow). d: ratio of upper and lower body flow.

Comparison of controls and PDA infants: t-tests and multiple linear regression analysis

An unpaired Student's t-test showed a significant increase in LVO in PDA infants ($p < 0.001$). Upper and lower body flow volumes and ratio of upper and lower body flow were not significantly different between infants with and without a PDA ($p = 0.75$, $p = 0.81$ and $p = 0.43$ respectively) (table 4.1.3). However multiple linear regression analysis correcting for gestational age showed that there was a significant association between ductal shunt volume as a % of LVO and a decrease in both upper and

lower body flow (p=0.03 and p<0.001 respectively). There was no significant relationship between upper/lower flow ratio and ductal shunt volume (d) when correcting for GA (p = 0.55). Table 4.1.4 shows the resultant equation, coefficients and p values for each multiple linear regression. Graphs are shown in appendix 4.1.

	Controls	PDA infants	p value
LVO	228(39)	389(120)	<0.001
Upper Body	93(25)	96(23)	0.75
Lower Body	133(24)	131(30)	0.81
Upper/lower	0.71(0.16)	0.73(0.21)	0.43

Table 4.1.3 – Unpaired student t-test: Mean(SD) values of LVO, upper and lower body flow (ml/kg/min) and upper/lower body flow ratio for control and PDA infants. P values for unpaired student's t-test between control and all PDA infants.

Independent variable	equation	p value
upper body flow	= -2.4GA – 0.3d +172.2	0.03
lower body flow	= -3.8GA – 0.7d +257.8	<0.001
upper/lower body flow	= 0.001GA +0.002d +0.7	0.55

Table 4.1.4 – Multiple linear regression: results from multiple linear regression analysis.

Echo measures

Ductal shunt volume (ml/min/kg and as a % of LVO) quantified by PC MRI and echo measures of duct diameter, LA:Ao ratio, DAo regurgitant fraction and ED/Max ductal flow are shown for each PDA infant in table 4.1.5. Duct diameter was assessed in all but 1 PDA infant, in this infant a constricted duct was observed but diameter was not quantified. Due to patient unrest some echo exams were stopped prematurely. As a consequence DAo regurgitant fraction was assessed in all but 3 infants, in 1 of these infants reversal of flow was observed but not quantified. LA:Ao ratio was assessed in all

but 2 infants, in 1 of these infants a dilated left atrium was observed but not quantified. ED/Max ductal flow was assessed in all but 4 infants, again in 2 of these infants the flow pattern was observed but not quantified.

GA	cGA	BW g	Wt at scan g	shunt vol %LVO	Shunt vol ml/min/kg	PDA diameter mm	DAo regurgitant fraction	LA:Ao ratio	ED/max ductal flow
24+3	27+3	525	660	74.2	435	1.8	0.36	1.95	0.34
31+1	32+2	1180	1180	66.5	397	2.4	Reversal, nq	Dilated LA, nq	Unrestrictive, nq
26+3	34+2	790	1390	62.4	350	2.4	0.31	1.71	0.35
28+4	31+4	1400	1430	62.0	359	2.4	Not assessed	2.07	0.37
25+4	31+6	680	1125	52.7	309	1.7	Not assessed	2.00	0.50
26+1	30+1	990	1075	51.6	221	1.2	0.34	1.55	0.43
25+3	27+5	1140	1140	48.7	169	2.3	0.32	1.81	0.52
25+4	27+5	960	960	46.5	189	1.8	0.36	1.77	0.48
25+3	27+4	1175	1175	26.0	86	0.9	0	1.51	0.64
24+5	29	615	770	24.3	65	0.9	0	1.63	0.70
26+2	36+1	905	2400	23.5	72	1.6	0	1.16	Not assessed
26+3	32	1000	1430	15.5	56	0.6	0	1.71	0.69
25+3	27+4	890	890	13.5	46	1.0	0	1.65	0.52
27+2	31+6	895	1215	12.1	39	1.0	0	1.27	Not assessed
27+3	29+3	1033	1035	10.4	27	1.0	0	1.13	0.67
27+5	29+4	975	975	7.9	18	1.1	0	1.14	0.45
27+5	28+4	1230	1230	6.4	20	Constricted, nq	0	Not assessed	Constricted, nq

Table 4.1.5 –Echo measures: GA, cGA, birth weight (BW), weight at scan, ductal shunt volume values in ml/kg/min and as a percentage of LVO and the corresponding echo measures of duct diameter, regurgitant fraction, LA:Ao and ED/Max flow measurements for individual PDA infants. An LA:Ao of greater than 1.4 is considered as a dilated left atrium. ED/Max ductal flow of less than 50% is considered to show a non-restrictive duct. nq denotes where measures were observed but not quantified.

Table 4.1.6 shows the R^2 and p value for the linear regression of ductal shunt volume (as a percentage of LVO) and diameter, LA:Ao and ED/max flow. Due to the nature of the data a

spearman's rank correlation was used to assess the relationship between regurgitant fraction and ductal shunt volume. Regurgitant fraction was shown to be the highest predictive echo measure of ductal flow with an $R_S = 0.82$.

	R^2	P value
Regurgitant fraction	0.82	NA
Diameter	0.63	<0.001
LA:Ao	0.57	0.002
ED/max flow	0.56	0.004

Table 4.1.6 –Echo measures and association with ductal shunt volume: R^2 and p values for the linear regression between ductal shunt volume as a percentage of LVO and the four echo measures, regurgitant fraction, duct diameter, LA:Ao and ED/Max flow.

4.1.4 Discussion

In this study a PC MRI protocol to quantify ductal shunt volume and its impact on distribution of global systemic blood flow has been presented. To the author's knowledge this is the first study of any kind that has accurately quantified ductal shunt volume and the resultant systemic flow in preterm infants. In the following subsection study considerations, limitations, possible significance of results and implications are discussed.

PC MRI is a highly validated technique for quantification of blood flow volume (Gatehouse et al. 2005) (Tan et al. 2001) (Varaprasathan et al. 2002). While not yet widely available in the neonatal unit setting the data in this study demonstrates that cardiac MRI assessment of PDA is achievable. Out of the 450 pilot and PC sequences only 30 had to be repeated due to subject motion or unstable heart rate. In addition median (range) scan duration for pilot and all 3 PC sequences was 11:19 (7:31 – 25:15) minutes and analysis of each data set performed off line took between 10-15 minutes.

While not prohibitive in a research setting, (to establish the feasibility of quantifying ductal shunt volume this was acceptable) this could be considered too long for clinical exams when compared to echocardiography.

However, previous clinical trials to determine appropriate PDA treatment approach have all been weakened by a limited ability to quantify PDA shunt volume and its impact on total systemic and pulmonary blood flow with accuracy. The inconclusiveness of the previous clinical trials (Bose et al. 2007) (Laughon et al. 2007) (Wyllie, 2003) has not only lead to the controversy over treatment approach but shows that there is no systematic data from which to draw conclusions. There is a need to develop techniques to accurately assess the hemodynamic impact of the duct. The additional information and accuracy provided by PC MRI when quantifying flow volumes, particularly in the thorax where the echo imaging widow is limited, could be valuable when understanding the cardiovascular impact of prematurity and PDA. Future analysis of PDA with both modalities could provide a more accurate evaluation of the hemodynamic significance of the shunt and aid future clinical trials.

Protocol considerations and limitations

To perform cardiac MRI successfully in the neonatal population requires an optimized approach. The necessity for high spatial resolution to accurately quantify flow in the small and tortuous neonatal thoracic vessels and multiple averages to preserve SNR leads to long scan times. The sequence parameters reported here were optimized to keep scan duration to an acceptable length for this uncooperative population whilst providing adequate resolution and SNR.

It was found that a slice thickness below 4mm led to poor quality data due to inadequate SNR. The curvature of the aorta and this threshold slice thickness required LVO to be quantified at the level of the aortic valve and not at the level of the pulmonary trunk at the same time as upper body flow.

Likewise upper body flow was quantified in the distal SVC and not the brachiocephalic, left common carotid and left subclavian arteries or proximal SVC.

Although good agreement was found in initial Bland-Altman analysis of LVO and systemic flow (the sum of SVC and DAo), a mean difference of -10.6 ml/kg/min was observed. Taking azygos flow into account improved agreement between LVO and systemic flow dramatically reducing this difference (+2.06 ml/kg/min). This is biologically plausible since the differences between the arterial and venous vascular distributions would mean that flow in the azygos at this level would otherwise be counted twice (the flow is produced from the arterial system within the distribution of the DAo, but drains into the distribution of the SVC). This is demonstrated in figure 4.1.7 which shows the morphology of the great vessel derived from a 4D PC MR sequence (4D PC MRI in preterms is discussed in chapter 6). The azygos insertion is clearly depicted directly proximal to the left and right innominate veins. The distance between this insertion and the middle of the SVC plane (level with the pulmonary bifurcation) was found to be 5.1mm in an 875g infant. A slice thickness of 4mm at this level would therefore include the azygos flow.

A competing explanation to the azygos flow and source of error could be the difference in LVO and systemic flow could also be explained by misalignment of the LVO PC acquisition. The SVC and DAo are relatively straight; therefore planning the placement of the SVC and DAo PC acquisitions to lie orthogonal to the vessel lumen in each case was relatively easy. In comparison, the LVO tract curves into the ascending aorta and arch. This could lead to partial volume effects and underestimation of the true velocity and hence underestimate LVO. An angle of θ between the mean vessel direction within the slice and the normal to the slice will lead to a velocity measurement of the true velocity*cosθ. However this error is small, 6% at 20° misalignment. For flow measurements this error is compensated by the 1/cosθ increase in apparent cross-sectional area. An angle of ±15-20° is considered tolerable as the increase in vessel area is compensated for by the increase in partial

volume effects (Gatehouse et al. 2005) (Lotz et al. 2002) (Tang et al. 1993). As the PC slice thickness (4mm) was much, much less than the radius of the arch this error was considered negligible.

It is generally considered that 3 – 4 complete voxels across the diameter of the vessel of interest are needed for accurate flow measurement (Greil et al. 2002) (Hofman et al. 1995) (Lotz et al. 2002). This was also verified in house on a healthy adult volunteer, where number of voxel across the diameter N_D, of the DAo was varied from 3 to 8 (data not included in thesis). The $N_D = 8$ was taken as the "gold standard" and compared to the other 3 flow measurements, all of which remained below the 10% clinically acceptable error limit. Taking the lower acceptable resolution limit, with the current resolution, flow within a vessel of diameter ≥1.8mm can be accurately quantified. In smaller infants voxel coverage of the azygos vein was insufficient (mean (range) of azygos vein diameter 2.3 (1.3 – 3.4) mm), potentially leading to inaccuracy when quantifying flow in these smaller vessels. As the azygos flow contributed on average to only 5.7% of LVO this error was considered negligible.

Results and possible significance

Previously blood flow volumes through patent ducts have been unknown. In this study the observed ductal shunt volume ranged between 6.4 – 74.2% of LVO in the 17 PDA infants examined. Eight of these infants had high ductal shunting (defined as greater than 45% of LVO) from the systemic to the pulmonary circulation. With this volume of steal from the systemic blood flow, upper and lower body flow volumes were expected to be significantly diminished in these infants. Treatment is often carried out due to this assumption that systemic perfusion is reduced (Agarwal et al. 2007). However, quantification of global flow distribution showed that in all subjects the upper body flow, and in the majority of PDA infants the lower body flow were within or above the normal range even in the presence of high volume ductal shunt (up to 74.2% of LVO) (figure 4.1.10b).

The preservation of upper body flow in all PDA infants could support the suggestion that forced closure of the duct with the aim of maintaining cerebral perfusion may be unfounded (Shimada et al. 1994). The majority of PDA infants remained within the lower body flow normal range, 2 of the 17 PDA infants had lower body flow below the population normal range (2 lay just on the lower 95% confidence limit). This could be seen as potentially supporting the hypothesis that ductal steal occurs predominantly from the lower rather than the upper body circulation (Groves et al. 2008a). Since PDA is associated with the risk of NEC, decreased DAo flow below the normal range may be clinically significant, and could support a strategy of clinical intervention to close a PDA and preserve lower body flow. However, none of the infants with PDA in this study developed NEC and from multiple linear regression analysis (appendix 4.1) there was no significant difference between upper/lower flow ratio in infants with and without PDA. This highlights that the association between NEC and PDA is complex and multifactorial.

While the majority of PDA infants lie within the population range for systemic blood flow, multiple linear regressions correcting for gestational age did show significant associations between both decreased upper and lower body flow volume and ductal patency (graphs shown in appendix 4.1). However it is still unclear how this tendency of patent ducts to decrease global blood flow effects regional blood flow distribution. Abdominal regional blood flow in the presence of a PDA is investigated in the following subsection. The final subsection then presents cerebral flow data in 5 infants and discusses feasibility of this protocol in this cohort. It is important to note that the reduction in upper and lower body flow is only apparent from the multiple linear regression trend and not when observing the majority of PDA infants in isolation. From flow values alone the majority of PDA infants could not be distinguished from controls. Various studies have indicated that around 64% of PDA infants may be treated unnecessarily (Wyllie, 2003). Considering the risks of surgical ligation and toxic medication employed for the treatment of PDA, this data suggests that forced closure of the duct to prevent systemic hypo-perfusion in the infants within this study (all of which had good short term outcomes) would have been unnecessary.

It is clear that maintaining systemic flow in the presence of duct requires significantly increased LVO; this was also shown in Shimada *et al*. 1994. In the majority of PDA infants the heart is able to mount an increase in SV to compensate for the ductal shunt volume and consequent systemic steal. Whether this is an active response predominantly due to an increase in heart rate, or whether this is simply a result of the increased preload from the extra shunt volume that causes the heart to contract more forcefully due to the Frank-Starling mechanism is not clear from the data presented in this chapter. This increase in LVO will likely be associated with increased workload on the heart and the potential for pathological ventricular remodeling (Baylen et al. 1975) (Baylen et al. 1977) (Lewandowski et al. 2012). From visual analysis hearts seemed enlarged in PDA infants; the impact of ductal shunting on left ventricular mass and cardiac function is investigated in chapter 5.

The presence of a PDA has also been associated with poor respiratory outcome, pulmonary hemorrhaging and pulmonary hyper-perfusion (Agarwal et al. 2007) (Laughon et al. 2007). The volume of steal from the systemic circulation will cumulatively increase the pulmonary flow, potentially worsening respiratory function and increase the risk of pulmonary pathologies. Yet the exact amount of blood entering the lungs with the additional shunt volume and relation to respiratory outcome is unknown. Efforts were made to measure blood flow in the pulmonary trunk, right and left pulmonary arteries in the presence and absence of a PDA from PC MRI. Yet the small size and curvature of these vessels lead to partial volume errors and poor image quality (data not included in this thesis), consequently quantification of pulmonary flow was not validated in this cohort. A preliminary study to assess total pulmonary blood flow from SSFP stack analysis (chapter 5) of the right ventricular output (RVO) was carried out and presented in chapter 5. Pulmonary flow in the presence of a PDA was inferred from the summation of RVO and ductal shunt volume and was shown to be significantly increased in PDA infants. However, Bland-Altman analysis of LVO and RVO from stack analysis in control infants showed relatively poor agreement and it was concluded that improved spatial resolution and/or stack orientation is needed to accurately quantify right ventricular volume and therefore RVO and pulmonary flow (see chapter 5 for full details). Although

pulmonary flow is increased in PDA infants more work is needed to understand the association with respiratory outcome. This is an interesting area for future work and is discussed in more detail in chapter 8.

Currently MRI assessment of PDA is not possible in most neonatal units; therefore the correlation between ductal shunt volume (as measured by PC MRI) and 4 echocardiography measures commonly used to assess clinical significance of the PDA was evaluated. All 4 measures show good correlation with ductal shunt volume. DAo regurgitant fraction was found to have the highest correlation with ductal flow. Due to the large observer dependency in echo measurements in the absence of MRI data a complete assessment of the duct involving all 4 echo measures and not just ductal diameter could be used to assess ductal shunt volume. However, as shown in the above results a large shunt volume may not be a determinate of aberrant systemic blood flow or pathology. Future systematic outcome related trials combining echocardiographic and MRI assessment would be needed in order to explore possible associations between ductal shunt volume, treatment and outcome.

Limitations of the cohort

This study has two significant limitations. Firstly a relatively small number of infants with PDA were studied. Although data has been presented suggesting that a high volume ductal shunt may not always cause systemic hypo-perfusion, multiple linear regression analysis showed that ductal shunt volume was correlated with a significant decrease in upper body flow when correcting for gestational age. Therefore abnormal volumes of systemic and upper body flow in other infants cannot be rule out.

Secondly all the PDA infants within this study were imaged at a time of clinical stability outside the transitional period. It may be that at other time points, particularly in the first few days of life during

the circulatory transition where dramatic changes occur in preload conditions, myocardial contractility and systemic and pulmonary vascular resistance, the volume of systemic blood flow is further compromised by ductal shunt. This data therefore cannot be used to infer the potential impact of intervention to reduce ductal shunt volume in the first postnatal days.

4.1.5 Conclusion

In summary PC MRI can be used to accurately quantify the volume of ductal shunt and its impact on global systemic blood flow distribution in neonates with high repeatability. This protocol indirectly quantifies ductal shunt volume and systemic blood flow in preterm and term infants from measurements of left ventricular output and descending aortic and superior vena caval flow. Initial data suggest that even in the presence of high ductal shunt volume, upper body blood flow may be relatively maintained in infants outside the transitional period. Due to the improved repeatability in flow measurements, minimal observer dependency and good agreement between systemic and LVO flow this PC MRI technique could be used in the future to facilitate trials of targeted intervention to close a PDA. The effectiveness of forced closure via medication is still debatable (Wyllie, 2003). Performing a power analysis with 95% confidence interval and false negative rate of 5%, the minimum number of infants needed to detect a 30% decrease in shunt volume post intervention in infants with high ductal shunting (above 33% of LVO) would be 18 in both the intervention and placebo groups. This is a clinically feasible number of infants and would provide valuable information on the effectiveness of forced closure by medication.

4.2 Quantification of Abdominal Blood Flow Distribution in Infants with and without PDA

4.2.1 Introduction

NEC is one of the most common gastrointestinal conditions that is primarily present in preterm infants. Incidence rates are inversely related to birth weight and gestational age, affecting 9% of infants with birth weight between 751-1000g with mortality rates ranging from 15-30% of case (Lin et al. 2006). NEC can occur anywhere in the gastrointestinal tract but is most commonly found in the small intestine and can be difficult to treat (Lin et al. 2006).

The pathogenesis of NEC remains unclear but it is widely accepted that it is the death of intestinal tissue caused by mucosal injury. It is suggested that in stressed preterm infants redistribution of cardiac output can occur to maintain sufficient blood flow to the vital organs such as the brain and kidneys causing diminished perfusion to intestinal mucosa. Blood flow to the intestine between the 2nd part of the duodenum and the transverse colon is supplied primarily by the Superior Mesenteric Artery (SMA) (figure 4.2.1).

There have been many studies to investigate the onset of the disease but the principal reasons are thought to be structural immaturity of the bowel wall and ischemia (Cheromcha et al. 1988). Many studies have also looked into the correlation between incidence of NEC and PDA (Cheromcha et al. 1988) in preterm and term infants. These studies have shown that the presence of PDA is a risk factor for developing NEC. It is thought that preferential steal during diastole causes blood to flow from the mesenteric arteries back into the aorta and through the PDA, creating an intestinal hypo-perfusion state, thus compromising the gut diastolic blood flow (Dollberg et al. 2005).

Several ultrasound studies have evaluated the peak blood flow velocity in the SMA in infants with NEC and infants who were suspected of developing NEC and have shown that SMA velocity is increased after the development of symptoms of necrotising enterocolitis, suggesting that total gut ischaemia is not present at the time that the disease is clinically apparent, although it may precede

the onset of symptoms and play a part in the pathogenesis of the disorder (Kempley et al. 1992). These somewhat contradicting results illustrate the multifactorial nature of NEC and add to the debate whether PDA is causal or casual in this pathology.

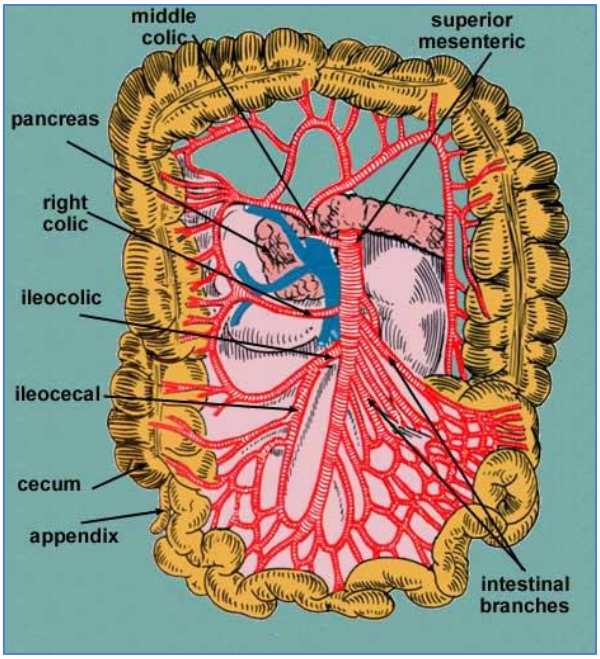

Figure 4.2.1 –The principal veins and arteries that supply the intestine: The SMA supplies the intestine from the lower part of the duodenum through 2/3 of the transverse colon as well as the pancreas. http://home.comcast.net/~wnor/sup&infmesentericart.htm

Objective

Echocardiographic techniques can estimate volume of SMA flow (Van Bel et al. 1990), however these measures have not yet been validated and are limited by the acquisition due to air spaces in the gut (Taylor, 1990). The aim of this study was to assess the feasibility of performing PC MRI assessments of abdominal visceral blood flow in newborn preterm infants. To then establish a normative range in healthy preterm infants and to potentially provide more insight into the hemodynamic effects of PDA on abdominal flow.

4.2.2 Patients and Methods

The study was approved by the North West London Research Ethics Committee (06/Q0406/137) and written informed parental consent was obtained in all cases.

Study cohort

In this initial study 28 infants with median (range) gestation 32^{+2}(24 – 37+6) weeks, corrected gestation at scan 34^{+2}(27^{+4} – 40) weeks, birth weight 1750(560 – 2800) grams and weight at scan 1850(745-2800) grams were scanned. Infants were scanned with the same routine monitoring and ear protection as outlined in the previous section. No respiratory compensation techniques were used. Twelve infants required low flow supplemental oxygen or nasal continuous positive airway pressure via an MR compatible system but all infants were stable and tolerating full enteral feeds during the scan. None of the infants were mechanically ventilated during the scan. There was no incidence of NEC and none of the infants were treated for prolonged PDA.

PC MRI Acquisition

Data was acquired on a Philips 3-Tesla MR Achieva scanner (Best, Netherlands) using a specialised 8 channel pediatric body receive coil for infants above 2kg and a small extremity receive coil for infants below 2kg. Three 2D PC MR retrospectively gated sequences with spatial resolution = 0.6x0.6mm, slice thickness = 4mm, TR/TE = 5.9/3.1ms and NSA =3 were used to quantify volume of flow in the DAo proximal to the celiac plexus at the level of the diaphragm (total lower body flow), in the abdominal DAo distal to the renal arteries (distal DAo) and in the proximal SMA (figure 4.2.2). Table 4.2.1 shows the scan parameters for the SMA and Distal DAo PC sequences. A pilot angiogram was used to plan the location of the PC sequences. VENC was calibrated as ±120-150cms^{-1}, ±120-

150cms^{-1} and ±80-100cms^{-1} for the DAo, DAo distal and SMA sequences respectively. Lower body flow was taken to be the flow in the DAo at the level of the diaphragm. Intestinal flow was taken as SMA flow, visceral non SMA (VnonSMA) flow (celiac plexus plus inferior mesenteric and renal artery flow) was taken as proximal DAo - SMA - distal DAo flow. Acquisition time ranged between 1-4 minutes depending on HR variability.

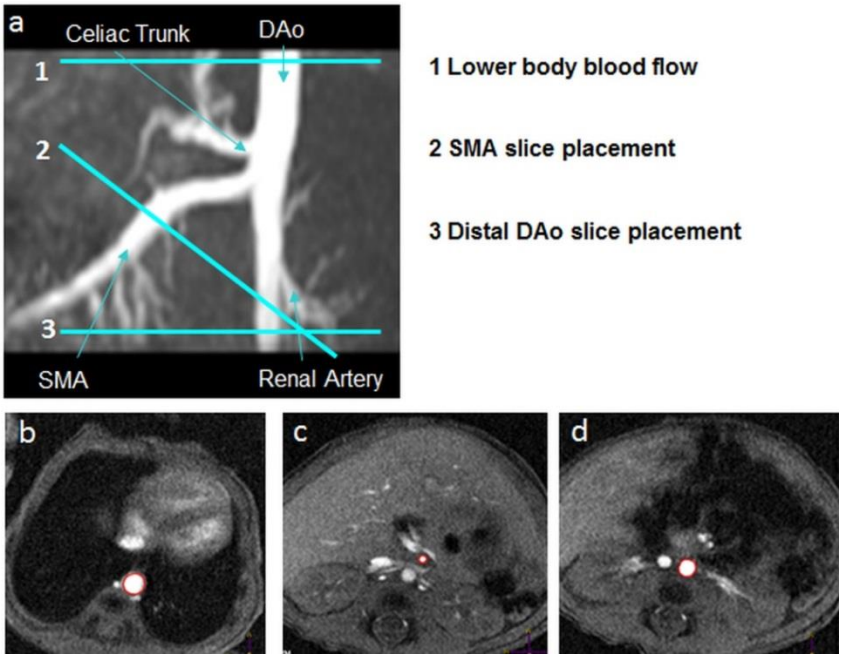

Figure 4.2.2 – Study design: PC MRI sequence to quantify Lower blood flow, Intestinal blood flow and distal DAo flow volume. Angiography of the abdominal arteries in a 1.5kg infant: shows slice location of all three sequences.

Scan	spatial resolution (mm)	cardiac phases	FOV (mm)	Slice thickness (mm)	TR/TE (ms)	flip angle (degrees)	PE direction	NSA	VENC cm/s	scan duration (mins)
SMA	0.6x0.6	20	80-100	4	5.9/3.1	10	AP	3	80-100	1-4
Distal DAo	0.6x0.6	20	80-100	4	5.9/3.1	10	AP	3	120-150	1-4

Table 4.2.1 Abdominal 2D PC MRI scan parameters.

Data processing

As in the previous study, sequence analysis and flow volume quantification for the PC datasets was performed using a commercial workstation (Philips ViewForum). Automated vessel edge detection was used for all vessels of interest, with manual correction where necessary. Once defined in the first cardiac phase the software tracks the vessel of interest over the cardiac cycle using edge detection algorithms. Flow is then calculated at each time point of the cardiac cycle, generating a flow curve and volume of flow value for each vessel of interest.

Statistical analysis

Bland-Altman analysis was carried out on scan re-scan of the SMA with spatial resolution 0.6mm in 10 infants to assess the repeatability of the quantification of the intestinal blood flow volume in the small SMA vessel. Pilot angiograms and PC sequences were repeated within the same scan session 5 or more minutes apart. Analysis was carried out by a single observer. Mean difference of measures, loa and RI were calculated.

Corrected gestational age was plotted against DAo, SMA and VnonSMA to establish normative ranges in control infants and to assess impact of PDA on regional flow volume distribution in the preliminary data.

4.2.3 Results

Bland-Altman analysis of SMA scan re-scan measurements in 10 infants with a spatial resolution of 0.6mm (median (range) gestational age 33(25^{+3} – 35^{+4}) weeks, cGA 35^{+6}(27^{+4} – 40) weeks, birth weight 1770(695 – 2420) grams and weight at scan 1860(900 – 2416) grams) gave loa = -8.1 to +6.4 ml/kg/min, mean difference of -0.9 ml/kg/min and RI 24.7% (Figure 4.2.3).

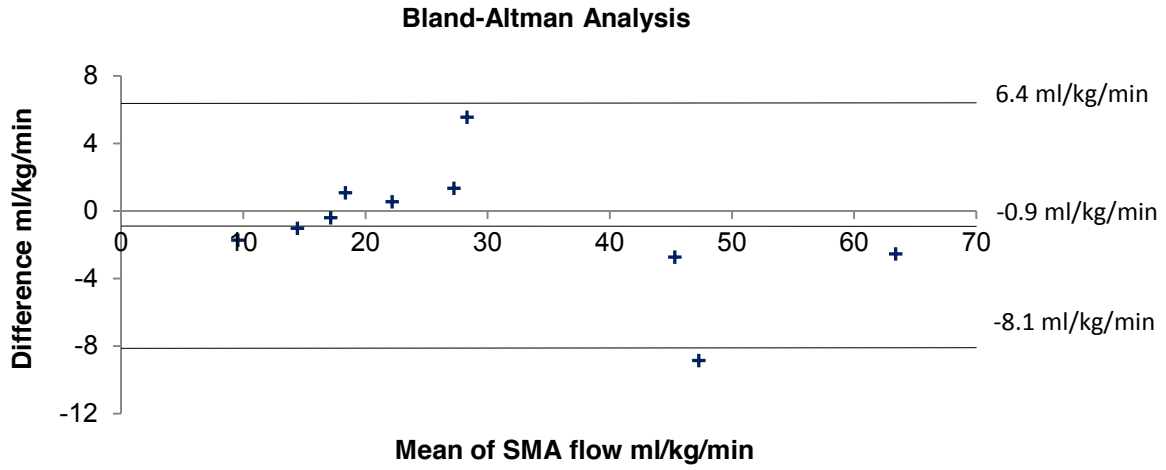

Figure 4.2.3 – Bland-Altman repeatability analysis: Scan re-scan of PC MRI SMA sequence in 10 infants. Tramlines show loa and mean difference.

Infants without ductal shunting

Twenty four infants (median (range) gestational age 33(24-37^{+6}) weeks, cGA 34^{+4}(27^{+4}-40) weeks, birth weight 1795(560 – 2800) grams and weight at scan 194(745 – 2800) grams) had closure of the arterial duct confirmed by echocardiography.

Infants with ductal shunting

Four of the infants scanned (median (range) GA 25^{+4} (25^{+3} – 28^{+4}) weeks, cGA 27^{+5}(27^{+4} – 31^{+4}) weeks, birth weight 1070(805 – 1400) grams and weight at scan 1070(805 – 1430) grams) had PDA as determined by echo with a shunt volume ranging from 16-62% of LVO as measured by PC MRI from the previous study.

Two PDA infants had lower body flow below the population range (figure 4.2.4a) (both 1.99 SD below the mean). Despite this all infants with PDA had SMA flow values within the normal range (figure4.2.4b). One of the PDA infants had visceral non SMA flow well below the normative range

(3.25 SD below the mean). All the sequences were acquired in all but 1 of the 4 PDA infants, this infant woke up and consequently the Distal Dao sequence was not acquired. This meant that visceral non SMA could not be calculated for this infant.

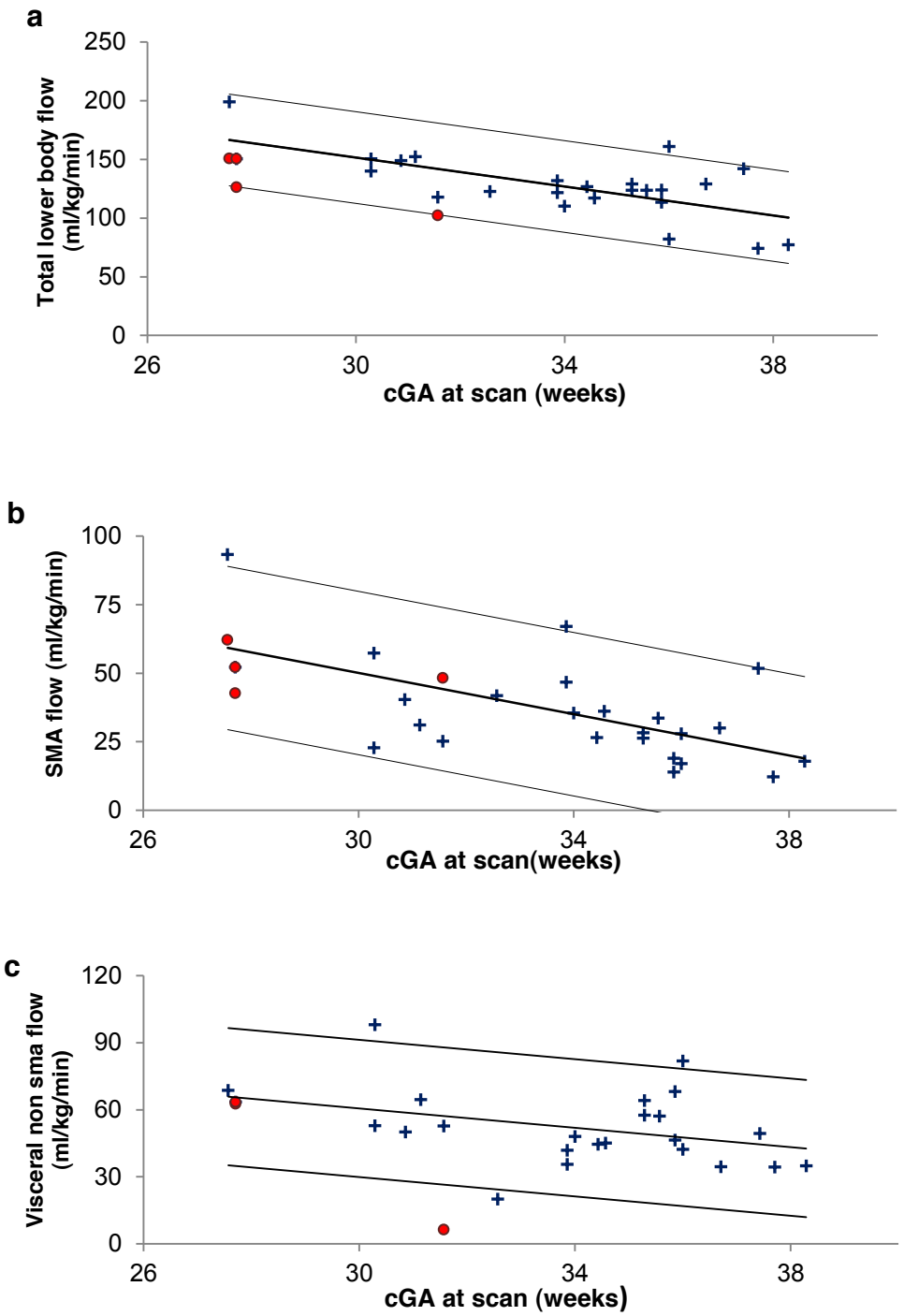

Figure 4.2.4 – Normative ranges: a: total lower body, b: SMA and c: visceral non SMA blood flow correcting for cGA in 28 infants with (●) and without (+) PDA. The 3rd Distal DAo sequence was not acquired in the final PDA infant as the child woke up during the acquisition.

4.2.4 Discussion

Abdominal blood flow ranges in preterm infants and impact of PDA on flow have not been defined with accuracy. PDA has been associated with NEC principally due to the suggestion that high ductal shunting leads to reduced systemic perfusion. Yet the pathogenesis of NEC is multifactorial, whether this correlation is causal or casual is unknown. In this initial study a PC MRI protocol to quantify abdominal flow in the absence and presence of ductal shunting was presented. The effect of PDA on this regional blood flow distribution in preterm and term infants was assessed in a small number of stable infants outside the transitional period. The discussion presented here aims to consider the initial results and assess feasibility of SMA quantification with PC MRI.

Repeatability analysis and protocol limitations

Bland-Altman repeatability analysis of scan re-scan SMA measurements showed a moderate agreement with loa -8.1 to +6.4 ml/kg/min, mean difference of -0.9 ml/kg/min and RI of 24.7%. However this is clearly less robust than flow quantification in the larger SVC, DAo and aorta in a similar cohort of infants. With the current spatial resolution of 0.6mm the average (range) number of voxels across the diameter of the SMA was 3.9(3 – 5.1), potentially leading to inaccuracy when quantifying SMA flow in the smaller infant's vessels. However, no inverse linear trend was observed when plotting number of voxels across diameter of vessel against absolute difference in the 2 measures (data not included in thesis).

A proportion of the variability seen in the scan re-scan flow quantification may be related to genuine physiological variation as opposed to measurement error due to the relation between intestinal blood flow and food intake. Intestinal blood flow in adults has been shown to increase significantly after feeding, DAo and SMA flow were seen to increase by 30% and 200% 20 minutes after food intake (Wieben et al. 2013). The response to feeding has also been shown to be associated with type

of food; increase in intestinal blood flow can vary from 30-130% from baseline depending on type of food (Taylor, 1990). Whether the same response is seen in preterm infants is unknown. All infants were fed before the scan as part of the scan preparation (Merchant et al. 2009). Repeated PC MRI Scans were performed 5 or more minutes apart, this may account for some of the variation seen in the Bland-Altman analysis.

Results, possible significance

In this initial study a relatively small number of PDA infants was studied all of whom were stable and outside the transitional period. Although two of the PDA infants had total lower body flow on the lower 95% confidence limit, SMA flow was maintained in all PDA infants even in the presence of high ductal shunt volume (up to 62% of LVO). From this and the previous study, results indicate that global and regional flow can be maintained even in the presence of a high shunt volume in preterm and term infants with PDA. This highlights the complex association between PDA and NEC. The high incidence of NEC in PDA infants could in part be due to the fact that incidence and prolonged patency of the ductus arteriosus are inversely related to gestational age (Wyllie, 2003). The immature intestinal wall in the preterm infant that is required to function as its term counterpart for food uptake is also thought to be a factor in the pathogenesis of NEC (Cheromcha et al. 1988). Both NEC and PDA could be a result of, and exacerbated by prematurity.

Cohort limitations

The potential dependency on time after feed mentioned above may also impact on the normal ranges. All infants were fed before the scan, the type and amount of feed was variable. Although the PC MRI acquisitions were acquired around the same time from the start of the MRI examination the time to settle the infant before the scan varied. The data presented here was not a longitudinal

study and represents blood flow at one time in point per individual. Potential variation or widening of the normal ranges may arise due to the response of intestinal blood flow to food intake.

As there are few ultrasound SMA flow studies (Coombs et al. 1990) (Kempley et al. 1992) (Taylor, 1990) and none have been validated it is unknown whether the PC scan repeatability is a marked improvement on echo values. However measurements of SMA flow using ultrasound are problematic. Due to air spaces within the gut Van Bel *et al*. 1990 measured SMA blood flow with velocity and area measurements taken at different locations along the SMA; this would have led to inaccuracies in flow calculation. PC MRI has the potential to quantify abdominal flow distribution in preterm infants and provide valuable additional information on intestinal blood flow. Potentially, with accurate visceral flow measurements, the role of ischemia in the pathogenesis of NEC could be established.

4.2.5 Conclusion

In summary a 2D PC MRI protocol to quantify and assess distribution of abdominal blood flow in preterm and term infants was presented. The impact of PDA on intestinal blood flow was then investigated. The initial results from 4 PDA infants show that intestinal blood flow was maintained, even in the presence of a large ductal shunt volume. The inconclusiveness of the previous clinical trials (Bose et al. 2007) (Laughon et al. 2007) (Wyllie, 2003) shows that there is no systematic data from which to draw conclusions. With the additional information provided by PC MRI techniques the association between ductal shunt volume, global and regional blood flow hemodynamics and resultant pathologies seen in this cohort may be investigated. Further acquisition of data accounting for different feeding regimes is needed to accurately establish if a trend exists between shunt volume and decreased intestinal flow. This study demonstrates that quantification of abdominal blood flow and distribution of this flow is feasible in the preterm population. A normative range for

this cohort has been established and initial data suggesting intestinal flow can be maintained in the presence of high shunt volume has been presented.

4.3 Quantification of Cerebral Blood Flow in Neonates

4.3.1 Introduction

Adverse neurodevelopmental outcome is common in the preterm infant population (Mangham et al. 2009). The left and right internal carotid and basilar arteries supply cerebral blood flow. Insufficient or alterations in cerebral blood flow (CBF) due to the immature preterm cardiovascular system, are considered to play a major role in neurological development and subsequent neurological pathologies (Volpe, 1997). It is thought that systemic hypo-perfusion caused from large PDA shunt volumes has a negative effect on cerebral perfusion and may lead to injury in the immature brain (Lemmers et al. 2008) (Sasi et al. 2011).

Although upper body flow was quantified and shown to remain within the normal range for all PDA infants studied multiple linear regressions correcting for gestational age did show significant associations between decreased upper body flow volume and ductal patency. It is still unclear how this tendency of patent ducts to decrease global blood flow effects regional blood flow distribution. CBF measurements in preterm infants are rare in the clinical practice and most studies present ultrasound based methods to quantify CBF volume in neonates (Ehehalt et al. 2005) (Varela et al. 2012). However, these can be prone to error and in general have poor repeatability due to the difficult imaging window brought about by the location of the left and right internal carotid and basilar arteries within the skull (Gill et al. 1985). Accurate CBF assessment requires robust blood flow volume and brain volume measurements. Blood flow measurements are the most problematic of the 2 due to the small calibre of the vessels supplying the brain. PC MRI combined with anatomical

MRI brain volume measurements has previously been used to quantify CBF in neonates, this same protocol was shown to be accurate and reproducible in adults (Varela et al. 2012). However, this protocol was not validated in infants. Accurate observations of cerebral blood flow in infants with PDA could provide insight into the association with adverse neurodevelopmental outcome.

Objectives

The aim of this study was to assess the feasibility of quantifying blood flow within the internal carotid and basilar arteries to aid in the quantification of CBF measurements in preterm infants. Initial data was collected in 5 infants and initial results are presented below.

4.3.2 Patients and Methods

Study cohort

Five preterm and term infants with median(range) GA $33^{+6}(30^{+4} – 37^{+4})$ weeks, cGA 38(31 – 43) weeks, birth weight 1450(810 – 3490) grams and weight at scan 2680(875 – 4550) grams were scanned. Infants were scanned with the same routine monitoring and ear protection as outlined in the above. No respiratory compensation techniques were used.

PC MRI Acquisition

Data was acquired on a Philips 3-Tesla MR Achieva scanner (Best, Netherlands) using a specialised 8 channel pediatric body receive coil for infants above 2kg and a small extremity receive coil for infants below 2kg. A single PC MR sequence with spatial resolution 0.4x0.4mm, slice thickness 4mm,

TR/TE and NSA = 3 was used to quantify blood flow within the left and right internal carotid and basilar arteries. It was assumed that blood to the brain is supplied via these 3 arteries (Varela et al. 2012). A pilot angiogram was used to plan the location of the PC sequences (figure 4.3.1). VENC was calibrated as ±80cms^{-1} this value was chosen from previous PC blood flow measurements in neonates (Varela et al. 2012). The previous study by Varela et al (2012) employed the same PC MRI protocol but with inplane spatial resolution 0.6x0.6. From the abdominal flow study presented previously it was felt that a spatial resolution of 0.4x0.4 was appropriate in the smaller infants in this study. Table 4.3.1 shows the scan parameters for the 2D PC MRI to quantify cerebral blood flow.

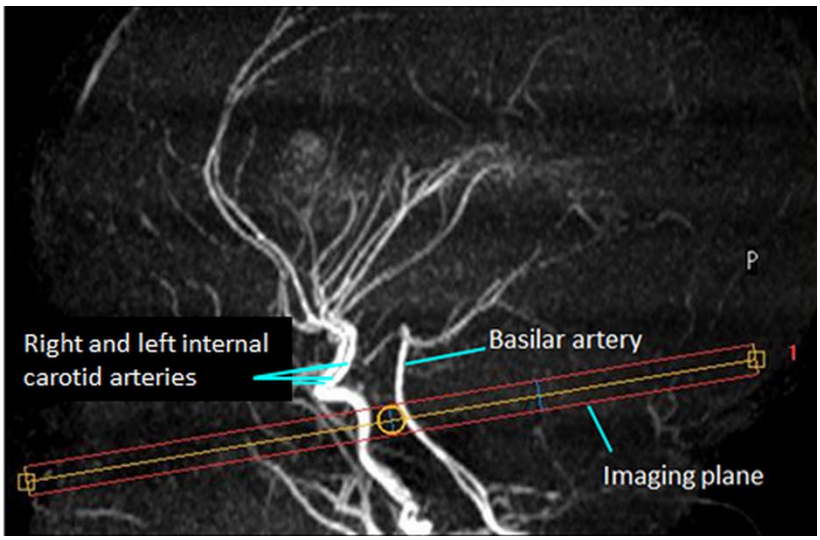

Figure 4.3.1 – Quantification of cerebral flow: Angiogram of the left and right internal carotid and basilar arteries in a preterm infant. Yellow (centre) and red (edge) lines show the placement of a 4mm thick PC MRI sequence.

Scan	spatial resolution (mm)	cardiac phases	FOV (mm)	Slice thickness (mm)	TR/TE (ms)	flip angle (degrees)	PE direction	NSA	VENC cm/s	scan duration (mins)
cerebral	0.4x0.4	20	80-90	4	6.1/3.1	10	AP	3	80	2-5

Table 4.3.1 Cerebral 2D PC MRI scan parameters.

Data processing

As in the previous studies presented above, sequence analysis and flow volume quantification for the PC datasets was performed using a commercial workstation (Philips ViewForum). Automated vessel edge detection was used for all vessels of interest, with manual correction where necessary. Once defined in the first cardiac phase the software tracks the vessel of interest over the cardiac cycle using edge detection algorithms. Flow is then calculated at each time point of the cardiac cycle, generating a flow curve and volume of flow value for each vessel of interest.

Statistical analysis

Bland-Altman analysis was carried out on scan re-scan to assess the repeatability of the quantification of the cerebral blood flow volume. Pilot angiograms and PC sequences were repeated within the same scan session 5 or more minutes apart. Analysis was carried out by a single observer. Mean difference of measures, loa and RI were calculated.

4.3.3 Results

Mean flow volume, loa, mean difference and RI for the scan re scan Bland-Altman analysis of the right and left internal carotid and basilar artery and global flow are shown in table 4.3.2.

vessel	Mean flow volume ml/min	loa (ml/min)	mean difference (ml/min)	RI%
right internal carotid	28.2	-9.0 to +8.2	-0.4	30.5
left internal carotid	25.2	-4.4 to +4.4	0	17.4
basilar artery	14.1	-0.5 to +1.7	0.6	7.6
Global cerebral flow	67.5	-8.3 to +8.7	0.2	12.6

Table 4.3.2 – Bland-Altman analysis of cerebral flow measures: Scan rescan of right and left internal carotid and basilar artery and global cerebral flow as measured by PC MRI. Mean flow volume, loa, mean difference and RI are shown.

4.3.4 Discussion

This preliminary study presents cerebral blood flow volume data from PC MRI analysis in 5 infants. Repeatability analysis of global cerebral flow is encouraging and suggests that robust flow measures are feasible with this protocol in the neonatal cohort. However, further data is needed to validate this protocol with the current imaging parameters. Additional quantification of cerebral flow in preterm and term infants and association with ductal shunt volume will provide valuable information into the hemodynamic impact of the duct on flow distribution and association with adverse neurodevelopmental outcome.

4.4 Reference

Agarwal R, Deorari AK, Paul VK. Patent Ductus Arteriosus in Preterm Neonates. AIIMS-NICU protocols. 2007.

Allen HD, Goldberg SJ, Valdes-Cruz LM, Sahn DJ**.** Use of echocardiography in newborn infants with patent ductus arteriosus: a review. *Pediatric Cardiology*. 1982. 3: 65-70.

Baylen BG, Meyer RA, Kaplan S, Ringenburg WE, Korfhagen J. The critically ill premature infant with patent ductus arteriosus and pulmonary disease – an echocardiographic assessment. J. Pediatr. 1975; 3: 423-432.

Baylen B, Meyer RA, Korfhagen J, Benzing G, Bubb ME, Kaplan S. Left ventricular performance in the critically ill premature infant with patent ductus arteriosus and pulmonary disease. Circulation. 1977; 55: 182-188.

Benitz WE. Treatment of persistent patent ductus arteriosus in preterm infants: time to accept the null hypothesis. J Perinatol. 2010; 30: 241-252.

Bland JM, Altman DG. Statistical methods for assessing agreement between two methods of clinical measurement. Lancet. 1986; 327: 307 – 310.

Bose CL, Laughon MM. Patent ductus arteriosus: lack of evidence for common treatments. Arch Dis Child Fetal Neonatal Ed. 2007; 92: F498-F502.

Broadhouse KM, Price AN, Durighel G, Cox DJ, Finnemore AE, Edwards AD, Hajnal JV, Groves AM. Assessment of PDA Shunt and Systemic Blood Flow in Newborns Using Cardiac MRI. NMR BioMed DOI: 10.1002/nbm.2927.

Cheromcha DP, Hyman PE, Neonatal necrotising enterocolitis. Inflammatory bowel disease of the newborn. Digestive Diseases and Sciences. 1988; 33:78S-84S.

Chew M, Poelaert CJ. Accuracy and repeatability of pediatric cardiac output measurement using Doppler. Intensive Care Med. 2003; 29: 1889-1894.

Chorne N, Leonard C, Piecuch R, Clyman RI. Patent ductus arteriosus and its treatment as risk factors for neonatal and neurodevelopmental morbidity. J. Pediatr. 2007; 119: 1165-1174.

Coombes RC, Morgan ME, Durbin GM, Booth IW, McNeish AS. Gut blood flow velocities in the newborn: effects of patent ductus arteriosus and parenteral indomethacin. Arch Dis Child. 1990; 65: 1067-71.

Edwards AD, Wyatt JS, Richardson C et al. Effects of indomethacin on cerebral haemodynamics in very preterm infants. Lancet 1990; 335: 1491–1495

Ehehalt S, Kehrer M, Goelz R, Poets C, Schoning M. Cerebral blood flow volume measurements with ultrasound: interobserver reproducibility in preterm and term infants. Ultrasound in Med. & Biol. 2005; 31: 191 – 196.

Evans N, Kluckow M. Early ductal shunting and intraventricular haemorrhage in ventilated preterm infants. Arch Dis Child. 1996; 75: F183-F186.

Evans N, Malcolm G, Osborn D, Kluckow M. Diagnosis of patent ductus arteriosus in preterm infants. NeoReviews. 2004; 5: 86-97.

Fogel MA. Assessment of cardiac function by magnetic resonance imaging. Pediatr Cardiol. 2000; 21: 59-69.

Gatehouse PD, Keegan J, Crowe LA, Masood S, Mohiaddin RH, Kreitner K, Firmin DN. Applications of phase-contrast flow and velocity imaging in cardiovascular MRI. Eur J Radiol. 2005; 15: 2172-2184.

Gill RW. Measurement of blood flow by ultrasound: Accuracy and sources of error. Ultrasound Med Biol 1985; 11: 625– 641.

Gonzalez A, Sosenko IRS, Chander J, Hummler H, Claure N, Bancalari E. Influence of infection on patent ductus arteriosus and chronic lung disease in premature infants weighing 1000 grams or less. J.Pediatr. 1996; 128: 470-478.

Greil G, Geva T, Maier SE, Powell AJ. Effect of acquisition parameters on the accuracy of velocity encoded cine magnetic resonance imaging blood flow measurements. J Magn Reson Imaging. 2002; 15:47–54

Groves AM, Kuschel CA, Knight DB, Skinner JR. Does retrograde diastolic flow in the descending aorta signify impaired systemic perfusion in preterm infants? Pediatr. Res. 2008a; 63: 89-94.

Groves AM, Kuschel CA, Knight DB, Skinner JR. Echocardiographic assessment of blood flow volume in the superior vena cava and descending aorta in the newborn infant. Arch Dis Child Fetal Neonatal Ed. 2008b; 93: F24-F28.

Groves AM, Chiesa G, Durighel G, Goldring ST, Fitzpatrick JA, Uribe S, Razavi R, Hajnal J, Edwards AD. Functional cardiac MRI in preterm and term newborns. Arch Dis Child Fetal Neonatal Ed. 2011; 96: F86-F91.

Hofman MBM, Visser FC, van Rossum AC, Vink GQM, Sprenger M, Westerhof N. In Vivo validation of magnetic resonance blood volume flow measurements with limited spatial resolution in small vessels. MRM. 1995; 33: 778-784.

Kempley ST, Gamsu HR. Superior mesenteric artery blood flow velocity in necrotising enterocolitis. Arch Dis Child. 1992; 67:793-796.

Kluckow M, Evans N. Ductal shunting, high pulmonary blood flow, and pulmonary hemorrhage. J. Pediatr. 2000; 137: 68-72.

Kluckow M, Evans N. Superior vena cava flow in newborn infants: a novel marker of systemic blood flow. Arch Dis Child Neonatal Ed. 2000; 82: F182-F187.

Knight DB. The treatment of patent ductus arteriosus in preterm infants. A review and overview of randomized trials. Semin Neonatol. 2001; 6: 63-73.

Laughon M, Bose C, Clark R. Treatment strategies to prevent or close a patent ductus arteriosus in preterm infants and outcomes. J. Perinatol. 2007; 27: 164-170.

Lemmers PMA, Toet MC, van Bel F. Impact of patent ductus arteriosus and subsequent therapy with indomethacin on cerebral oxygenation in preterm infants. Pediatrics. 2008; 121: 142-147.

Lewandowski AJ, Augustine D, Lamata P, Davis EF, Lazdam M, Francis J, McCormick K, Wilkinson AR, Singhal A, Lucas A, Smith NP, Neubauer S, Leeson P. Preterm heart in adult life cardiovascular magnetic resonance reveals distinct differences in left ventricular mass, geometry, and function. Circ 2013; 127: 197-206.

Lin PW, Stoll BJ. Nectrotising enterocolitis. Lancet. 2006; 368:1271-1283.

Lotz J, Meier C, Leppert A, Galanski M. Cardiovascular flow measurement with phase-contrast MR imaging: basic facts and implementation. Radiographics. 2002; 22:651–671

Mangham LJ, Petrou S, Doyle LW, Draper ES, Marlow N. The Cost of Preterm Birth Throughout Childhood in England and Wales. Pediatrics 2009;123;e312-e327.

Merchant N, Groves A, Larkman DJ, Counsell SJ, Thomson MA, Doria V, Groppo M, Arichi T, Foreman S, Herlihy DJ, Hajnal JV, Srinivasan L, Foran A, Rutherford M, Edwards AD, Boardman JP. A patient care system for early 3.0Tesla magnetic resonance imaging of very low birth weight infants. Early Hum Dev. 2009; 85: 779-83.

Overmeire B. Patent Ductus Arteriosus: How Aggressive Should We Be? Neonatology. 2007; 91:318

Sasi A, Deorari A. Patent ductus arteriosus in preterm infants. Indian Pediatr. 2011; 48: 301 – 308.

Sehgal A, McNamara PJ. Does echocardiography facilitate determination of hemodynamic significance attributable to the ductus arteriosus. Eur J Pediatr. 2009;168:907-14.

Shimada S, Kasai T, Konishi M, Fujiwara T. Effects of patent ductus arteriosus on left ventricular output and organ blood flows in preterm infants with respiratory distress syndrome treated with surfactant. J. Pediatr. 1994; 125(2): 270-277.

Sieverding L, Jung WI, Klose U, Apitz J. Noninvasive blood flow measurement and quantification of shunt volume by cine magnetic resonance in congenital heart disease. Preliminary results. Pediatr Radiol 1992; 22: 48–54

Skinner J. Diagnosis of Patent Ductus Arteriosus. Semin Neonatol. 2001; 6: 49-61.

Tan RS, Mohiaddin RH. Cardiovascular applications of magnetic resonance flow measurement. Rays. 2001; 26: 71-91.

Tang C, Blatter DD, Parker DL. Accuracy of phase-contrast flow measurements in the presence of partial-volume effects. J. Magn. Reson Imaging. 1993: 3: 377-385.

Taylor GA. Blood Flow in the Superior mesenteric artery: Estimation with Doppler US. Radiology. 1990; 174: 15-16.

Van Bel F, Van Zwieten PH, Guit GL, Schipper J. Superior mesenteric artery blood flow velocity and estimated volume flow: duplex Doppler US study of preterm and term neonates. Radiology. 1990;174:165-169

Varaprasathan GA, Araoz PA, Higgins CB, Reddy GP. Quantification of Flow Dynamics in Congential Heart Disease: Applications of Velocity-encoded Cine MR Imaging. RadioGraphics. 2002; 22: 895-905.

Varela M, Groves AM, Arichi T, Hajnal JV. Mean cerebral blood flow measurements using phase contrast MRI in the first year of life. NMR BioMed. 2012; 25: 1063 – 1072.

Wieben A, Roldan-Alzate A, Reeder SB, Schiebler ML, Nagle SK, Archer CW, Landgraf BR, Grist TM, Francois CJ. 4D flow MRI for non-invasive assessment of mesenteric ischemia. Proc ISMRM 2013; 0063.

Wyllie J. Treatment of patent ductus arteriosus. Semin Neonatol. 2003; 8: 425-32.

Chapter 5

Neonatal Left Ventricular Function and Impact of PDA

Data from the previous study indicates that LVO is significantly increased in infants with PDA. However the resultant impact on cardiac function is unknown. In the following chapter the left ventricular (LV) function in neonates with and without PDA is assessed using MRI. Firstly a brief overview of the mechanisms and measures of cardiac function and failure are given. This is followed by a brief introduction into a prominent acquisition used in cardiac functional MRI assessment, steady state free precession (SSFP) stack sequences. Morphological and functional cardiac data in healthy preterm and term infants is then presented. Normative ranges for LV parameters such as wall thickness and fractional thickening in healthy preterm and term are determined. The impact of ductal shunt volume on LV dimension and function is determined. Next a preliminary study to first, evaluate the pulmonary flow in the presence of a PDA from right ventricular volumetric analysis and secondly to assess the feasibility of RV functional analysis from SSFP stacks is presented. In the concluding section data from treated PDA infants are presented and discussed, highlighting possible future studies to better understand the impact of PDA and treatment approach.

5.1 The Heart

5.1.1 Cardiac Function

Unlike skeletal muscle, cardiac myocytes are coupled together electrically; consequently cardiac contraction involves every single myocyte. Contractile force therefore cannot be increased from the inclusion of additional myocytes, but is regulated by the stretch of the fibres during diastole and modifying intracellular Ca^{2+} levels (Levick, Fifth Edition, 2010, chpt 3). The intracellular mechanisms

that initiate the depolarization of myocytes are outside the scope of this thesis. Instead the work presented here builds upon the mechanical properties of cardiac muscle, the inherent mechanisms for altering stroke volume (SV), cardiac output and function. The relationship that governs cardiac function, SV and contractility can be described by the Frank Starling mechanism and Laplace's Law.

5.1.2 Measures of Cardiac Function

The **Frank Starling mechanism** states that "the energy of contraction of the intact heart increases as a function of diastolic distension" (Levick, Fifth Edition, 2010, chpt 6). An increase in blood volume will stretch the ventricular wall, increasing the load (known as preload) experienced by each muscle fibre, causing cardiac muscle to contract more forcefully. Preload is the end volumetric pressure that extends the right or left ventricle of the heart to its greatest geometric dimensions under variable physiologic demand. As this cannot be easily measured *in vivo,* parameters such as end diastolic volume (EDV) and pressure are used. Hence the force that any single cardiac muscle fibre generates is proportional to the preload, and the stretch on the individual fibres is related to the end diastolic volume of the left and right ventricles. This mechanism enables the heart to maintain an efficient blood supply during exercise. Maximum contractile force and therefore SV is produced from an optimum preload. Loading larger or smaller than this optimal value will decrease the force and therefore the output the muscle can achieve (figure 5.1.1).

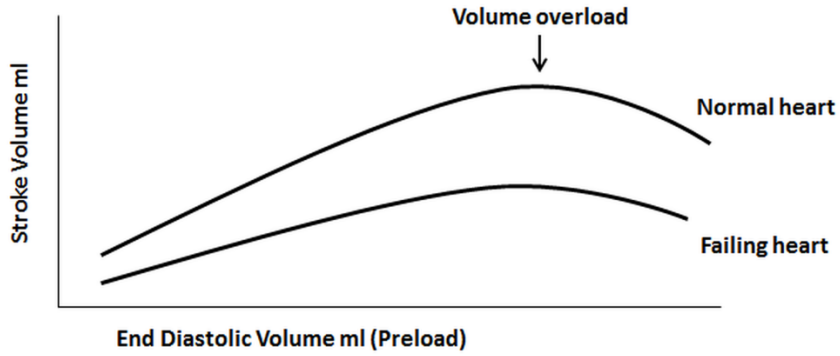

Figure 5.1.1 – Frank Starling mechanism: The schematic relationship between end diastolic volume and SV is shown for a normal and failing heart. Maximum SV is produced from an optimum preload. Loading larger or smaller than this optimal value decreases the contractile force and therefore the output the muscle can achieve. The contractile force is decreased in a failing heart.

Laplace's Law is an important physical constraint on cardiac performance. It describes the relationship between the transmural pressure "P" difference, the radius of the ventricular cavity "R", and myocardial wall tension "T" shown in equation 5.1 (Valentinuzzi et al. 2011).

$$P.R = 2.T \tag{5.1}$$

As a consequence of this linear relationship, a dilated heart requires more contractile force to pump the same amount of blood compared to the heart of normal size. This often leads to hypertrophy as the wall thickness increases to normalize the wall tension (afterload). Afterload**,** the tension or stress developed in the wall of the ventricle during ejection, is the pressure that the chambers of the heart must generate in order to eject blood out of the heart. Thus it is a consequence of the systemic pressure (for the left ventricle) and pulmonic pressure or pulmonary artery pressure (for the right ventricle). The pressure in the ventricles must be greater than the systemic and pulmonary pressure to open the aortic and pulmonic valves, respectively. As afterload increases, cardiac output

decreases. In normal cardiac function the Frank-Starling mechanism adequately compensates for the mechanical disadvantage imposed by Laplace's law.

5.1.3 Cardiac failure: Association with PDA

Heart failure is the global term for the physiological state in which cardiac output is insufficient to meet the demands of the body. This comprehensive term covers any condition that reduces the efficiency of the myocardium via damage or overload. Consequently this increase in workload will lead to alterations in the heart itself. The general outcome is that cardiac output is reduced. In adults cardiac failure can be caused by multiple conditions including hypertension and myocardial infarction, in each case specific physiological markers are used to diagnose cardiac failure.

It is common clinical belief that large ductal shunt volumes are associated with congestive heart failure (Agarwal et al. 2007) (Baylen et al. 1977) (Schmitz et al. 2003). This has arisen mainly from the idea that large shunt volumes lead to systemic hypo-perfusion and pulmonary hyper-perfusion due to cardiocirculatory dysfunction. The association with reduced systemic blood flow, respiratory distress syndrome, the observed ventricular enlargement and ventricular overload in PDA infants has meant that some ducts are treated in the effort to prevent cardiac failure. However the pathogenesis and markers used in adults to determine cardiac failure may not directly apply to the preterm population. For example the pathophysiology that leads to pulmonary edema in adult cardiac failure patients is not equivalent in preterm infants with PDA. Undoubtedly there is a significant effect on myocardial function in the preterm PDA infant (Sasi et al. 2011); systemic blood flow can be maintained even in the presence of a large ductal shunt volume, the preterm infant maintains systemic flow by increasing cardiac output. However, whether these infants have cardiac failure is questionable.

Relatively few studies have investigated the resultant impact of PDA on cardiac function. Several echocardiography studies have shown an increase in left ventricular cavity dimension and SV in PDA infants (Baylen et al. 1977) (Shimada et al. 1994). It is thought that this is primarily due to an increase in preload for the additional shunt volume (Sasi et al. 2011). A number of studies have also examined the resultant diastolic function in the presence of a PDA, a reduction in the isovolumetric relaxation time (IVRT) and long axis shortening in infants with large PDA was found (Schmitz et al. 2003) (Schneider et al. 2006). Schmitz *et al.* 2003, concluded that nonphysiological additional preload due to the presence of a PDA, leads to the reduction in IVRT and therefore alteration in diastolic function. However, the clinical significance of this, when treating a PDA has yet to be established. All of the above studies have been limited by the accuracy of echocardiography to quantify intra cardiac cavity dimensions and flow volumes. In addition none of these studies have been able to associate cardiac function with ductal shunt volume and the resultant systemic flow. Consequently the resultant cardiac function in the presence of a PDA and clinical significance is still poorly understood.

5.2 Cardiac MRI Function Analysis: bSSFP Imaging

Global and regional cardiac contractile function can be quantified using ECG gated rapid Gradient Echo (GE) cine sequences. There are numerous rapid GE sequences all of which are SSFP sequences. However balanced SSFP (bSSFP) has become a prominent diagnostic and functional tool in cardiovascular MRI owing in part to the inherent excellent blood myocardium contrast from the T2/T1 weighted contrast and very high SNR efficiency (Scheffler et al. 2003).

The bSSFP sequence was first described by Carr et al. 1954 yet only became widely employed in the last 15 years. During sequence acquisition the magnetization vector is modified from each TR due to multiple excitation pulses and T1 and T2 relaxation. Under certain conditions (constant flip angle,

dephasing and TR) the magnetization will establish a steady state after several TRs (steady state free precession) (Scheffler et al. 2003). The gradient induced dephasing within each TR is exactly zero in a bSSFP sequence and therefore the contrast is a product of T1 and T2 contributions, leading to high signal intensity from liquids and fats and subsequently providing good blood myocardium contrast (Carr et al. 2001) (Schar et al. 2004).

Although not optimal for diagnostic imaging, the contrast ratio, fast acquisition time and high SNR make bSSFP sequences well suited for morphological imaging and segmentation algorithms. Subsequently numerous studies have employed bSSFP techniques to quantify cardiac functional measures such as ejection fraction (EF) and cardiac volumetric measures such as myocardial mass. In addition adult left and right ventricular output measures have been validated (Lorenz et al. 1999) (Alfakih et al. 2003) and systolic and diastolic functional in cardiac failure patients has been analysed using this technique (Grothues et al. 2002).

However bSSFP images can suffer from band artefacts which degrade the quality of the image and hinder segmentation software. Inhomogeneities in the B_0 field cause local resonant frequencies within the excited volume to exceed the primary pass bandwidth which is inversely proportional to TR. For successful bSSFP imaging accurate shimming over the region of the heart to ensure that the B_0 variation remains below 1/TR and stability in the resonant frequency during the acquisition is needed (Schar et al. 2004).

Translating and utilizing this technique successfully in the neonatal population requires a distinct approach (Price et al. 2012). The increased spatial resolution required to adequately image the very small neonatal cardiac structures significantly reduces SNR. The rapid heart rate in this population (average 160bpm) increases the temporal resolution required to obtain useful functional assessment, reducing the potential for acceleration methods. This leads to long multiple averaged scans. The increased gradient demand also lengthens TR, narrowing the frequency range between bands. Subsequently, prolonged multiple-averaged scans are required to gain sufficient SNR in

neonatal CMR, and ultimately both the requirements for successful bSSFP tend to fail using standard cardiac protocols. Consequently the neonatal cardiac assessment studies presented in the following sections employ an optimized bSSFP imaging technique that implement active frequency stabilization combined with image based shimming, full details are given in Price et al. 2012.

5.3 Neonatal Left Ventricular Function and Impact of PDA

5.3.1 Introduction

The previous study to quantify ductal shunt volume (chapter 4) demonstrated a significant relationship between increased LVO ml/kg/min and ductal shunt volume as a % of LVO ($p < 0.001$). In addition, from observation infants with PDA appeared to have enlarged myocardium and larger ventricular cavity volumes than the "healthy" control preterm infants (figure 5.3.1). Shimada *et al.* 1994 found an increase in cardiac output associated with the presence of a large PDA. They suggested that the heart of the preterm infant is capable of mounting a compensatory increase of cardiac output sufficient to maintain unchanged cerebral blood flow, but is unable to maintain postductal organ blood flows because of decreased perfusion pressure (ductal steal) and localized increase in vascular resistance.

Clinical cardiovascular features associated with the presence of PDA, as well as the systolic murmur related with blood flowing through the duct, include prominent precordial pulsations (Agarwal et al. 2007) which reflect the increased workload. The effect of this increased workload on the preterm heart due to the increase in cardiac output is unknown. However it is thought that the shunting of blood from the systemic circulation to the pulmonary circulation in PDA infants may result in congestive cardiac failure (Agarwal et al. 2007) (Sasi et al. 2011).

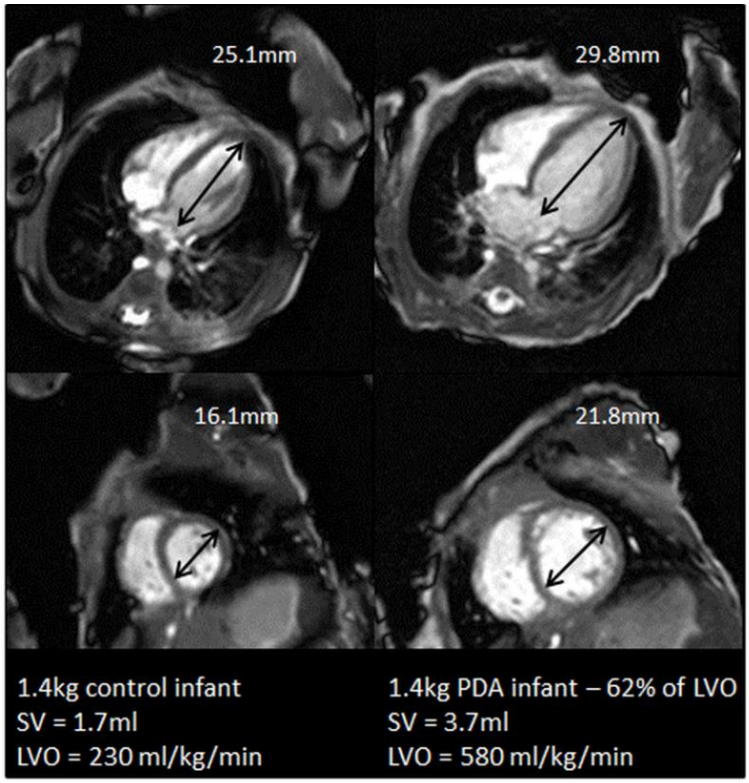

Figure 5.3.1 – Enlarged heart of a PDA infant: 4 chamber and short axis views in a 1.4kg control infant (left) and PDA (right) infant with a shunt volume of 62% of LVO. Figure shows the apparent increase in left ventricular dimensions.

Objective

The aim of this study was to quantify ventricular dimension and function with optimized bSSFP stack sequences (Price et al. 2012) in infants with and without PDA to determine the extent of enlargement and the subsequent effect on cardiac function.

The work in this subsection has been submitted to Circulation cardiovascular imaging and is currently under review.

5.3.2 Patients and Methods

The study was approved by the North West London Research Ethics Committee (06/Q0406/137) and written informed parental consent was obtained in all cases.

Study cohort

Cardiac MRI was performed in 43 infants with median (range) gestational age (GA) $30^{+3}(24^{+3} – 39^{+1})$ weeks, corrected GA (cGA) $34^{+2}(37^{+3} – 39^{+3})$ weeks, birth weight 1400(525 – 3050) grams and weight at scan 1690(660 – 3050) grams, who were inpatients at St Thomas' and Queen Charlotte's and Chelsea Hospital. All infants had an echo performed within 24 hours of MRI scan by an operator with >10 years of experience (AMG) in neonatal echocardiography. Fourteen infants had PDA as determined by echo. Persistent patency of the foramen ovale was considered a developmental variant and was seen in 4 of the infants in the study.

All infants were scanned using acoustic ear protection, pulse oximetry, vector ECG monitoring and without sedation or anaesthesia (Merchant et al. 2009). Seventeen infants required low flow supplemental oxygen or nasal continuous positive airway pressure via an MR compatible system but all infants were stable and tolerating full enteral feeds during the scan. None of the infants were mechanically ventilated during the scan. There was no change in respiratory status in any infant between MRI and echo scans.

Pre-scan history

PDA was treated in 2 infants, both with Ibuprofen 2 days and 59 days prior to the scan. Both were still patent at the time of the MRI scan. None of the PDA infants subsequently underwent surgery to close the duct. All of the 14 PDA infants survived and there were no incidences of NEC in this cohort. No infant included in this study went on to receive further treatment for prolonged ductal patency.

Acquisition

Data were acquired on a Philips 3-Tesla MR Achieva scanner (Best, Netherlands) using a specialised 8 channel pediatric body receive coil for infants above 2kg and a small extremity receive coil for infants below 2kg. A retrospectively gated 2D bSSFP short axis 10 slice stack, (in-plane resolution = 1x1mm, slice thickness = 4mm, TR/TE = 3.8/1.9 ms, cardiac phases = 20) was placed over the heart,

aligned with the mitral value using previously acquired pilot scans. Negative slice gap was adjusted for individual infants so that the 10 slices covered apex to base of left ventricle. NSA ranges between 2 and 8 depending on size and stability of infant. Acquisition time ranges between 2 and 8 minutes. No respiratory compensation techniques were used. Table 5.1.1 shows the scan parameters for the bSSFP stack sequence.

Scan	spatial resolution (mm)	cp	FOV (mm)	Slice thickness (mm)	Slice gap (mm)	TR/TE (ms)	flip angle (degrees)	PE direction	NSA	scan duration (mins)
SA Stack	1x1	20	FH/RL = 100-120 AP = 30-50	4	-2.5 - 0	3.8/1.9	35	RL	2-8	2-8

Table 5.3.1 Shorts axis bSSFP stack scan parameters.

Data processing

Quantification of LVO and ductal shunt volume from PC sequences was performed using a commercial workstation (Philips ViewForum). Automated vessel edge detection was used for all vessels of interest, with manual correction where necessary. Quantification of LVO via PC was carried out in full in all but 4 (2 PDA and 2 control) infants due to subject unrest.

Stacks were segmented and LV function was quantified using freely available software Segment v1.8 R1172 (http://segment.heiberg.se) (Heiberg et al. 2010). Myocardial borders were defined by performing a detailed manual tracing of the epi and endocardium at end systole and end diastole (ES and ED) time frames. A “first glance” ED and ES time frame was chosen from a mid-ventricle slice, the endocardial border was defined in each slice at this and the time frame either side until the maximum and minimum volume was found. ED and ES time frames were then set to the maximum and minimum volumes respectively. The epicardial border was then defined for these two time points for every slice. Long axis motion was corrected for by measuring the mitral value

displacement on a 4 chamber pilot scan between the ED and ES time points taking an average of 3 measures.

Myocardial and ventricular cavity volumes were determined by summing the area of each slice over the length for ED and ES time points the two volumes were then averaged. Myocardial mass calculations were carried out by multiplying the left ventricular myocardial volume by 1.05g/ml (Katz et al. 1988). This value is widely accepted as the density of healthy adult myocardium and was obtained from ex-vivo adult experimental data.

Myocardial wall thickness and fractional thickening assessment was carried out using the 6 mid cavity sections as defined by the 17 sector American Heart Association model (Cerqueira et al. 2002) (figure 5.3.2). Eighty thickness values for each sector were obtained from radial spokes that originate at the centre of the endocardial area. Myocardial thickness was defined where the endo/epicardial borders dissect the radial spokes. These 80 values were then averaged to generate a thickness value for each sector (Heiberg et al. 2010).

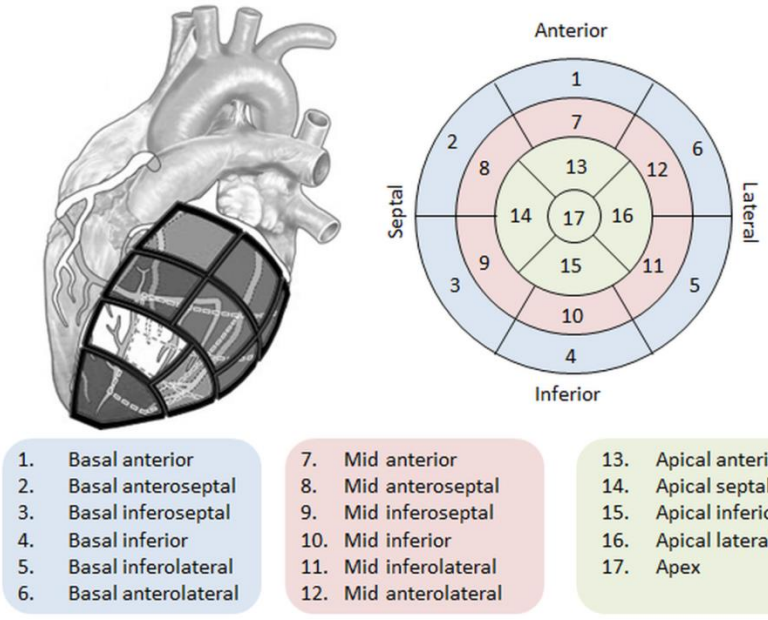

Figure 5.3.2 – 17 segmentation AHA model: The four regions and 17 sectors are shown on the segmentation of the left ventricle. Wall analysis was carried out on the 6 mid cavity sections shown in red in the figure. http://imaging.onlinejacc.org/mobile/article.aspx?articleid=1215021.

Papillary muscles and trabeculae were excluded from the blood pool area for evaluation of the blood volume parameters EDV, SV, LVO and EF (defined as EDV-ESV/EDV). Papillary muscles and trabeculae were included in the blood pool volume for calculation of the myocardial wall parameters wall thickness, fractional thickening (defined as (ES wall thickness – ED wall thickness)/ED wall thickness) and LV mass (figure 5.3.3). This is convention (Heiberg et al. 2010).

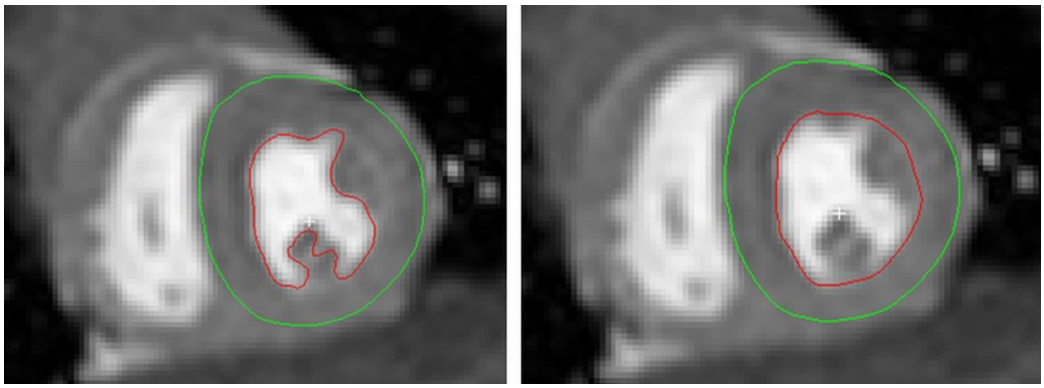

Figure 5.3.3 – Endo and epicardium segmentation: Segmentation for blood volume (left) and myocardial wall (right) parameter evaluation. Papillary muscles and trabeculae were excluded from the blood pool area for evaluation of the blood volume parameters and were included in the blood pool volume for calculation of the myocardial wall parameters.

Laplace's law states a linear relationship between ventricular diameter and wall stress. Therefore to maintain cardiac function, any scenario producing increased left ventricular diameter would be expected to also produce a proportional increase in myocardial thickness. To examine whether any increase in LV mass in infants with PDA is proportionate or disproportionate to extent of LV blood volume change the ratio between LV myocardial volume and LV blood pool volume (MyoV/EDV) was examined. This relationship was investigated further by differentiating between PDA infants with high (>33% LVO) and low <33% LVO) shunt volume. This arbitrary threshold was chosen as quantification of shunt volume via PC MRI indicated that 6 infants had a shunt volume above 48% LVO and 6 infants had shunt volume below 26% LVO. As stated previously the PC protocol and therefore ductal shunt volume quantification was carried out in full in all but 2 PDA infants due to subject unrest, hence these infants were not included in the above analysis.

Statistical analysis

Bland-Altman analysis was carried out to assess agreement between LVO, and SV values from PC and stack acquisitions. Mean difference of measures, 95% loa and RI (normalized loa) were calculated. Heart rate (HR) variability between the LVO PC and stack acquisitions was also analysed. LVO PC sequences were not acquired in 4 infants due to patient unrest; subsequently these infants were not included in the Bland-Altman analysis.

The LV output measures LVO, SV, EF, and ventricular dimensions EDV and LV mass normalized by weight at scan (as is convention in the neonatal population) were plotted against corrected gestational age to visually assess the impact of PDA on LV measures. EDV was plotted against SV to investigate the relationship between filling and SV in control and PDA infants to look for evidence of alteration in the Frank Starling curve (Levick, Fifth Edition, 2010, chpt 6). For visual assessment of impact of hypertrophy on LV function LV mass was plotted against EF.

An unpaired Student's t-test compared EDV, SV, LVO, EF, LV mass, ED wall thickness, fractional thickening and MyoV/EDV ratio in infants with and without PDA. Analysis was carried out in Microsoft Excel (2010). Linear regressions were carried out in control infants to determine association between EF and the ventricular measures LV mass and EDV. Multiple linear regressions were carried out in PDA infants to determine association between LV mass, EDV and MyoV/EDV ratio with ductal shunt volume correcting for cGA and postnatal age. Association between EF and LV mass, EDV and ductal shunt volume was also investigated in the PDA infants. To assess whether differences in LV mass could be related primarily to illness severity rather than PDA shunting, the association between number of days on respiratory support from birth to discharge and LV mass correcting for cGA, postnatal age and ductal patency was investigated. Significance was determined by a p value < 0.05. Analysis was carried out in Microsoft Excel (2010). Ductal shunt volume was calculated in all but 2 infants as these infants became unsettled. These infants were therefore not included in the multiple linear regression analysis.

5.3.3 Results

Control infants: Twenty nine neonates (controls) median (range) GA at birth $33^{+2}(25^{+5} – 39^{+1})$ weeks, cGA $34^{+6}(31^{+1}\text{-}39^{+3})$ weeks, birth weight 1820(695 – 3045) grams and weight at scan 1880(790 – 3045) grams had closure of the arterial duct confirmed by echo and were otherwise considered "healthy" neonates.

PDA infants: Fourteen infants had PDA as determined by echo median (range) GA $26^{+2}(24^{+3} – 31^{+1})$ weeks, cGA $29^{+5}(27^{+3} – 36^{+1})$ weeks, birth weight 930(525 – 1400) grams and weight at scan 1100(660 – 2400) grams. In the 12 infants who underwent the full PC protocol shunt volume ranged between 12 – 74% of LVO (table 5.3.2) (full details given in chapter 4).

GA	cGA	BW kg	Wt at scan kg	ductal shunt volume % LVO
24^{+3}	27^{+3}	0.53	0.66	74.2
31^{+1}	32^{+2}	1.18	1.18	66.5
28^{+4}	31^{+4}	1.40	1.43	62.0
25^{+4}	31^{+6}	0.68	1.13	52.7
26^{+1}	30^{+1}	0.99	1.08	51.6
27	29^{+2}	1.14	1.14	48.7
27	29^{+1}	1.18	1.18	26.0
26^{+2}	36^{+1}	0.91	2.40	23.5
25^{+5}	27^{+5}	0.81	0.81	15.5
25^{+3}	30^{+4}	0.85	0.88	15.0
27	29^{+1}	0.89	0.89	13.5
27^{+2}	31^{+6}	0.90	1.22	12.1

Table 5.3.2 – Ductal shunt volumes: GA, cGA, birth weight (BW), weight (Wt) at scan and corresponding ductal shunt values as determined by PC MRI for 12 infants with PDA.

Bland-Altman analysis

Bland-Altman analysis (Bland et al. 1986) of LVO and SV and HR was carried out in 39 infants (27 control and 12 PDA infants) to assess agreement of PC and stack output values. LVO PC sequences were not acquired in 4 infants due to patient unrest. Table 5.3.3 shows the loa, normalized loa, mean difference and mean difference as a percentage of the mean from the Bland-Altman analysis. Good agreement was found between PC and stack LVO and SV values.

Bland-Altman analysis	**RI%**	**LOA**	**mean diff**	**mean diff %**
LVO ml/kg/min	15.8	-76.3 - +20.1	28.1	9.2
SV ml/kg	13.4	-0.49 - +0.06	0.21	10.4
HR bpm	9.5	-11.8 - +16.2	-2.21	-1.5

Table 5.3.3 – Bland-Altman analysis: of PC and bSSFP stack LVO, SV and averaged HR measures. The table presents loa, RI%, and mean difference as an absolute value and a percentage for all 3 measures.

Analysis of Cardiac Dimensions and Output

Unpaired Student's t-tests showed that EDV, SV, LVO, ED wall thickness and LV mass are significantly increased in PDA infants. There was no significant difference between EF in both groups (table 5.3.4).

	Mean(SD) controls	Mean(SD) PDA	P value
LVO ml/kg/min	260(56)	455(119)	<0.001
SV ml/kg	1.82(0.29)	2.95(0.78)	<0.001
EDV ml/kg	2.47(0.38)	4.00(1.35)	<0.001
LV mass g/kg	1.39(0.23)	2.58(0.52)	<0.001
EF	74.4(4.5)	75.6(8.6)	0.45
MyoV/EDV	0.54(0.08)	0.67(0.17)	0.02

Table 5.3.4 – Unpaired Student's t-test: Analysis of LVO, function and hypertrophic measures showing mean(SD) and p-values for control and PDA groups.

For visual analysis EDV, SV, LVO, LV mass (normalized by weight at scan), HR and EF were plotted against cGA (figure 5.3.4 a, b, c, d, e and f). Heart rate in all PDA infants remained within the 95% confidence limits. LV mass is dramatically increased in PDA infants with all but 3 above the 95% confidence limits. Mean (range) EF was found to be 74.4(60.3 – 89.4)% in control infants. All but 2 infants had an EF within or above the 95% confidence limits and all were above the adult threshold of >50% for normal EF (Levick, Fifth Edition, 2010, chpt 2) (Zile et al. 2001).

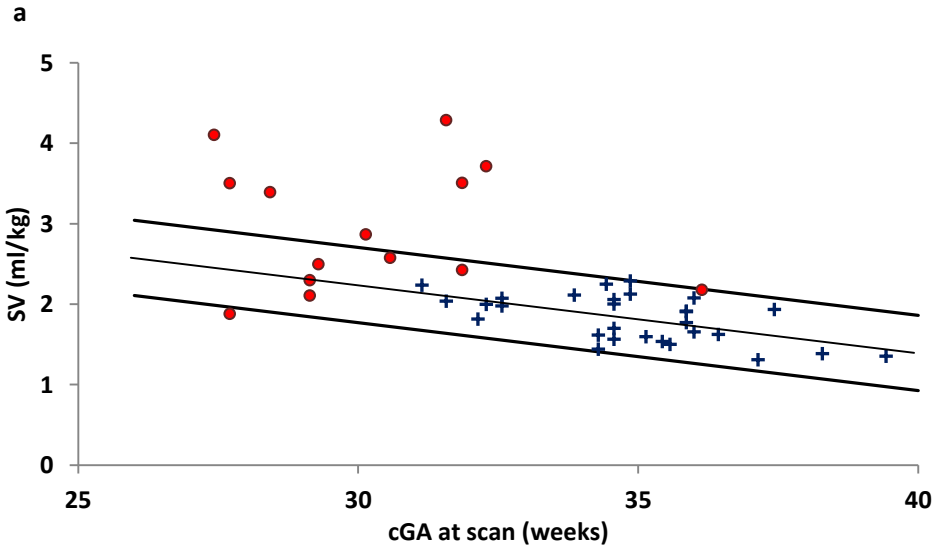

b

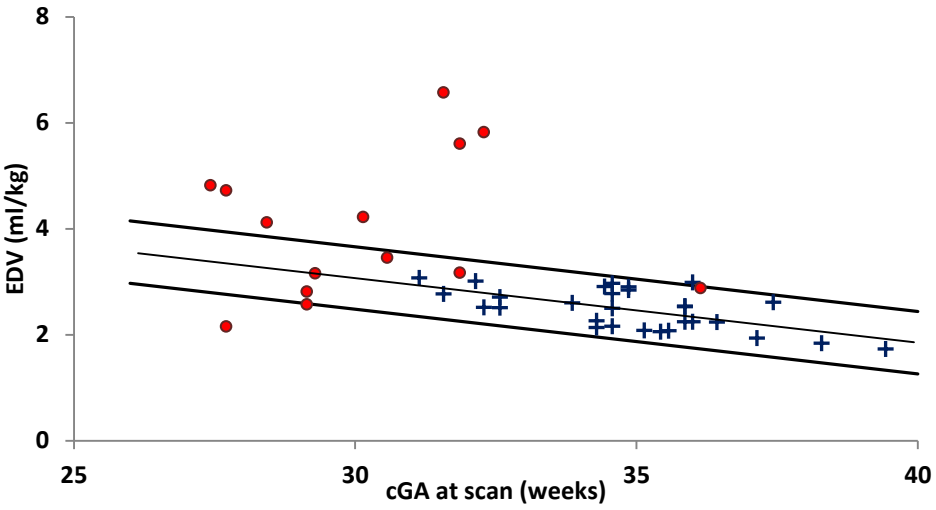
8
6
4
2
0
EDV (ml/kg)
25
30
35
40
cGA at scan (weeks)

c

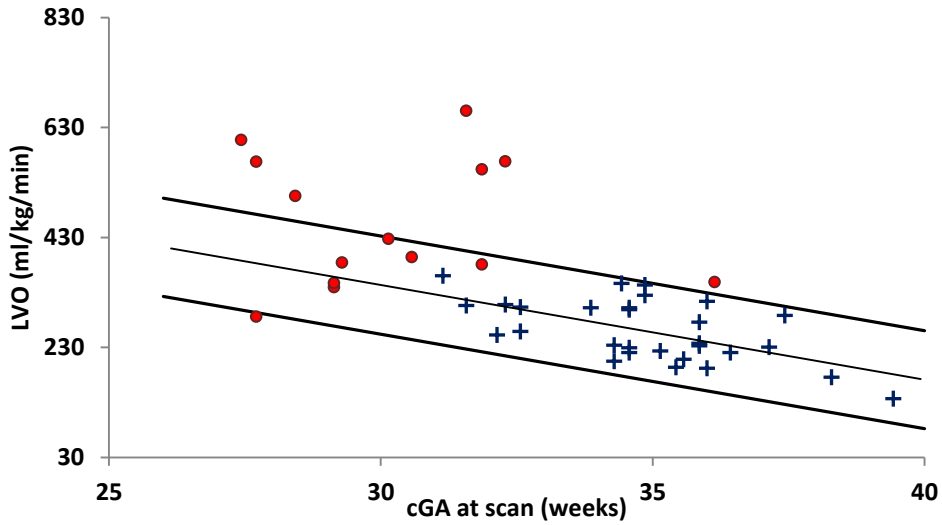
830
630
430
230
30
LVO (ml/kg/min)
25
30
35
40
cGA at scan (weeks)

d

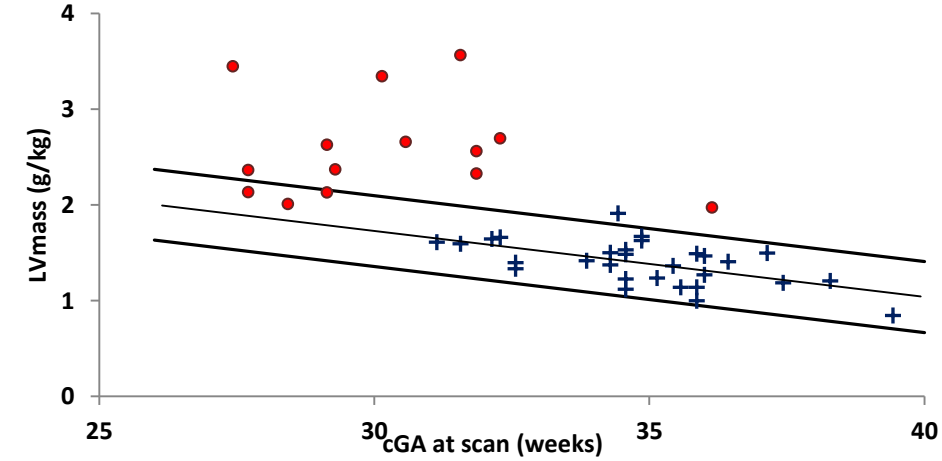
4
3
2
1
0
LVmass (g/kg)
25
30
35
40
cGA at scan (weeks)

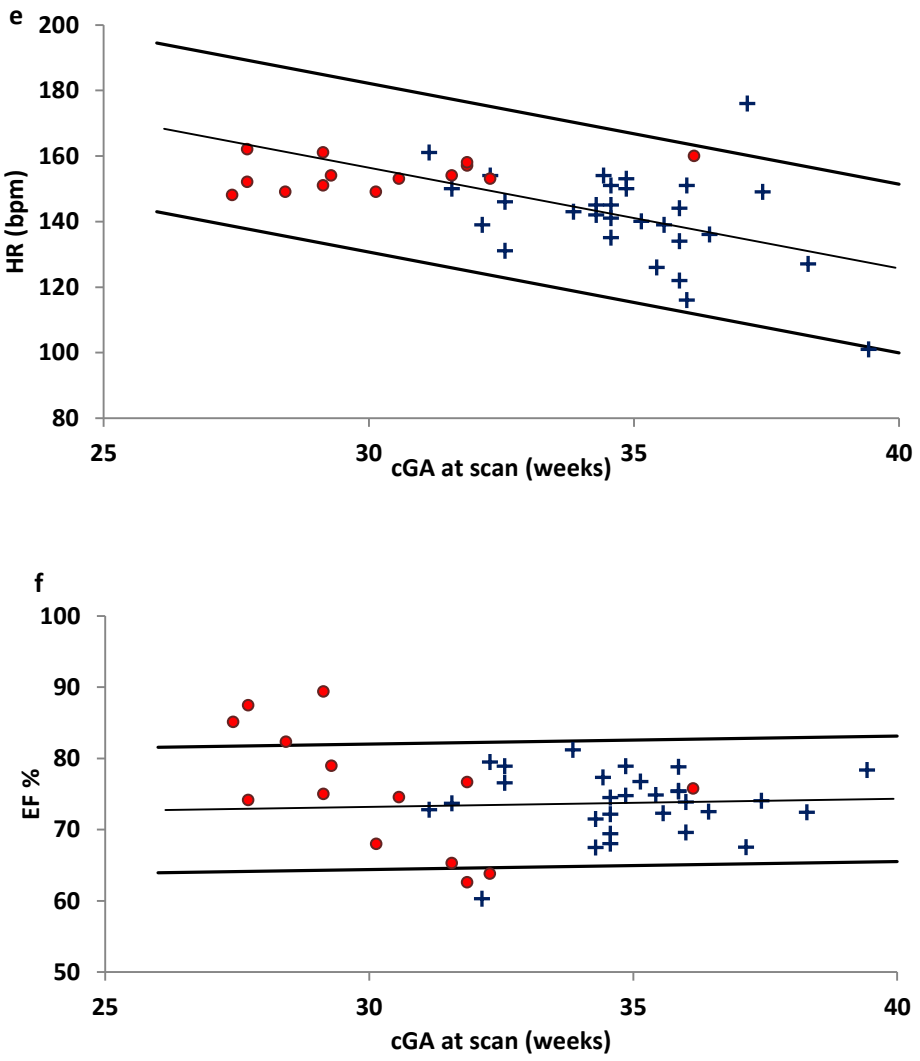

Figure 5.3.4 – Normative ranges: Scatter plots with trend line and 95% confidence limits of a: EDV, b: SV, c: LVO, d: LV mass, e: HR and f: EF in 43 infants with (●) and without (+) PDA.

Myocardial mass and Function analysis

Scatterplots show ED thickness normalized by weight at scan and fractional thickening for the 6 mid cavity sections in control and PDA infants (figure 5.3.5a and b). Myocardial fractional thickening was lowest in section 2 and 3 as these include the septal wall and highest in the anterior sections of the myocardium as expected. Unpaired Student's t-tests showed that ED wall thickness normalized by weight at scan was significantly increased in infants with PDA for all 6 mid cavity sections. There was

no significant difference in fractional thickening found between control and PDA infants (table 5.3.5).

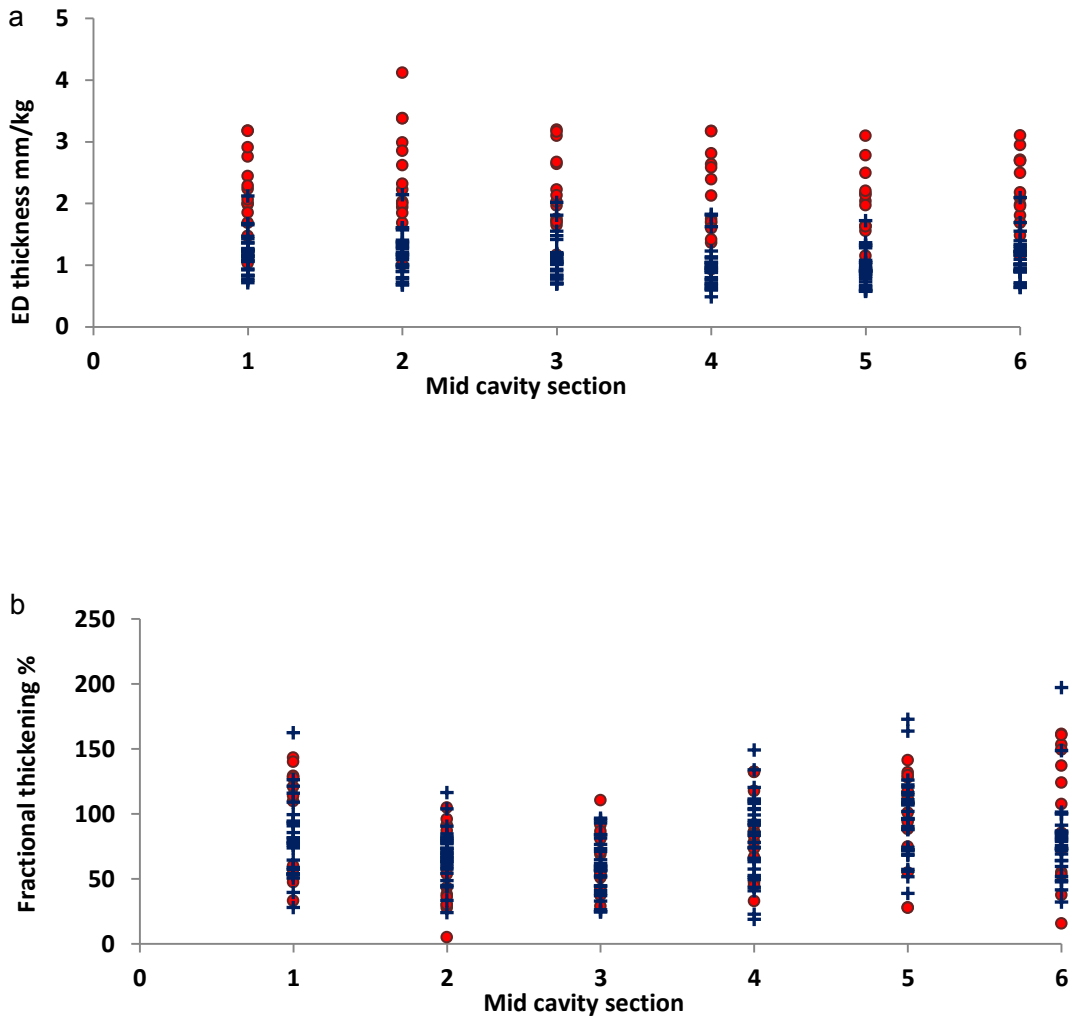

Figure 5.3.5 – ED thickness and fractional thickening: Scatterplots give a visual representation of a: ED thickness and b: fractional thickening in infants with (●) and without (+) PDA.

	ED thickness mm/kg			fractional thickening %		
section	**Mean controls**	**Mean PDA**	**P value**	**Mean controls**	**Mean PDA**	**P value**
1-mid anterior	1.17	2.22	<0.001	79	94	0.24
2-mid anteroseptal	1.16	2.45	<0.001	68	55	0.13
3-mid inferoseptal	1.09	2.21	<0.001	59	62	0.62
4-mid inferior	0.95	2.09	<0.001	81	83	0.85
5-mid inferolateral	0.92	1.96	<0.001	95	96	0.95
6-mid anterolateral	1.10	2.21	<0.001	80	100	0.20
Global	1.07	2.19	<0.001	77	82	0.57

Table 5.3.5 – Myocardial functional analysis: t-test analysis of the 6 mid cavity AHA myocardial sections. Individual mid cavity sections and global Wall thickness and fractional thickening values, mean and p-values are shown for both control and PDA groups.

Cardiac function analysis

The group estimated Frank Starling curve showed no evidence of reaching any maximum, i.e. even PDA babies with very large EDV remained on the same linear trend line (figure 5.3.6).

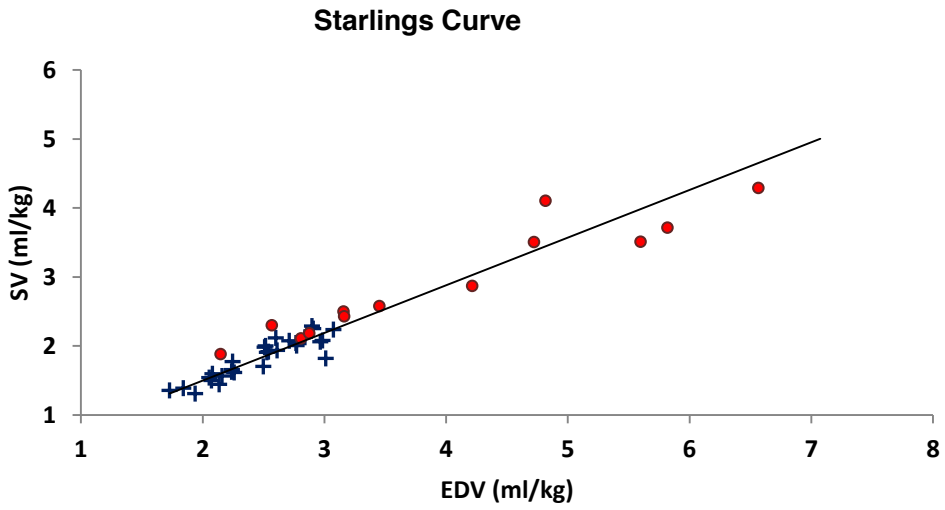

Figure 5.3.6 – Population Frank Starlings curve: for infants with (●) and without (+) PDA.

For visual analysis of the impact of hypertrophy on LV function, LV mass was plotted against EF (figure 5.3.7). All PDA infants remain within or above the population range.

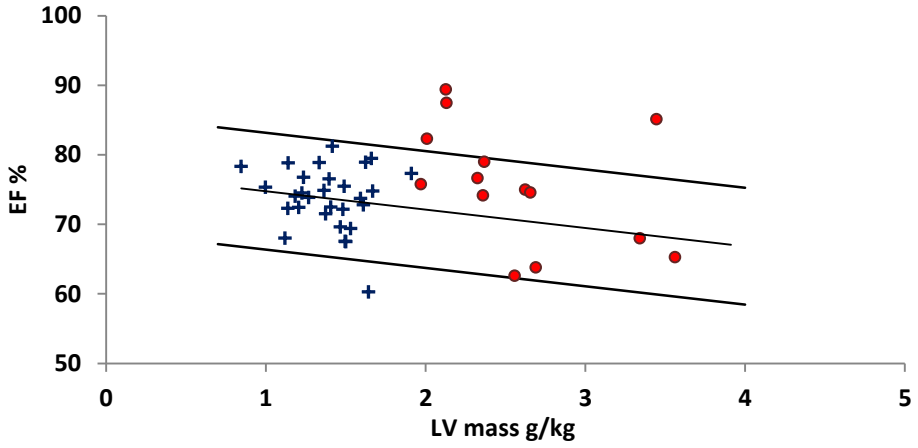

Figure 5.3.7 – Visual analysis of impact of hypertrophy: LV mass plotted against EF for infants with (●) and without (+) PD to visually assess the impact of hypertrophy on LV function.

Measure of Hypertrophy

A linear relationship was found between LV myocardial volume and EDV in control infants ($R^2 = 0.66$) and PDA infants (figure 5.3.8). To investigate the relationship between LV mass and EDV and examine the extent of enlargement in PDA infants the ratio of MyoV/EDV was plotted.

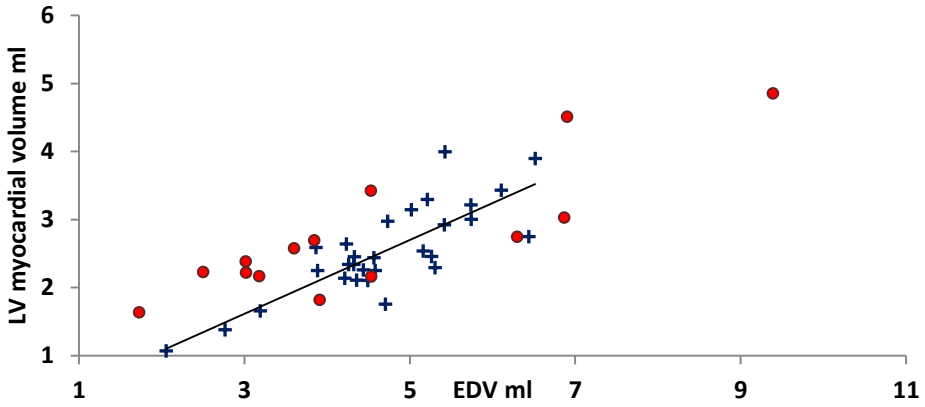

Figure 5.3.8 – LV myocardial volume vs EDV: A liner relationship was found between increase EDV and LV volume in infants with (●) and without (+) PDA.

The ratio of MyoV/EDV is approximately constant with increasing EDV in control infants. An inverse relationship is observed in the PDA infants where MyoV/EDV decreases with increased EDV and shunt volume with 7 of the PDA infants above the 95% confidence limits (figure 5.3.9a). By differentiating between low (<33% of LVO) and high (>33% LVO) shunt volume the inverse relationship between shunt volume and MyoV/EDV ratio is highlighted (figure 5.3.9b).

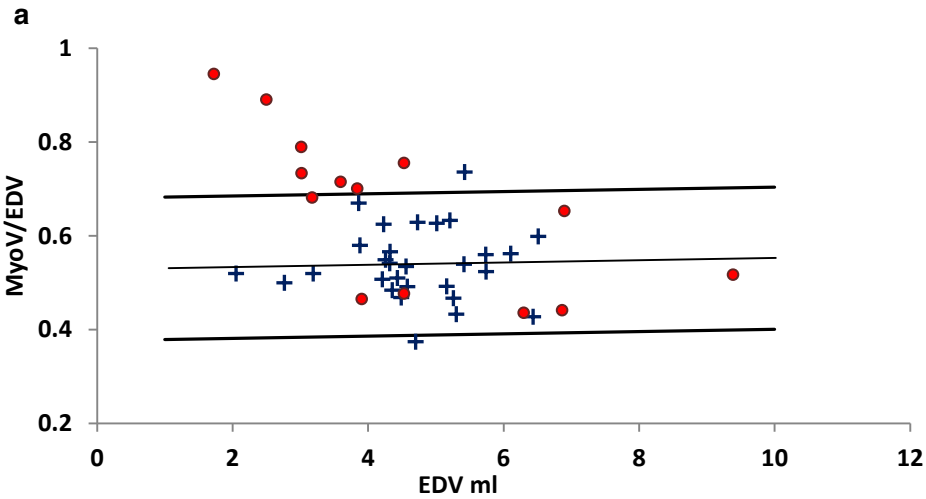

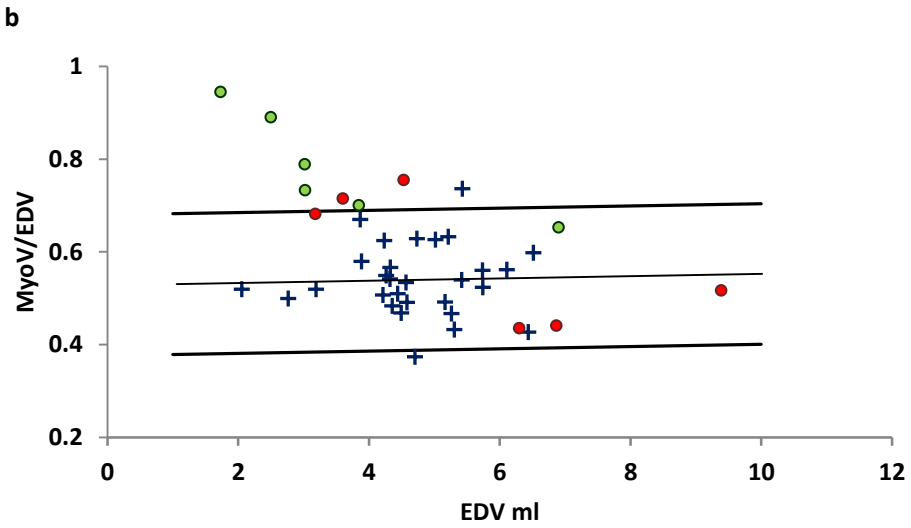

Figure 5.3.9 – Measure of hypertrophy: a: Normative range of MyoV/EDV ratio against EDV in infants with (●) and without (+) PDA. b: The relationship between increased MyoV/EDV ratio and decreased shunt volume is illustrated by differentiating between PDA infants with low (●) and high (●) shunt volume.

Regression analysis: association of PDA

Linear regression analysis showed no significant relationship between EF and EDV or LV mass in control infants. There was no significant association between EF and ductal shunt volume or LV mass, however a significant inverse relationship was found between EF and EDV ($p = 0.006$) in PDA infants. The significant positive associations between LV mass and ductal shunt volume, and between EDV and ductal shunt volume both persisted when correcting for cGA and postnatal age (post) in multiple linear regression ($p = 0.03$ and 0.003 respectively). A significant inverse relationship between MyoV/EDV and ductal shunt volume persisted when correcting for both cGA and postnatal age ($p = 0.004$). No significant association between number of days on respiratory support (resp) and LV mass correcting for cGA, postnatal age and ductal patency was found. Table 5.3.6 shows the equation and p value from the resultant multiple linear regression analysis. Graphs of the linear and multiple linear regression analysis are shown in appendix 5.1.

dependant variable	equation	p value
MyoV/EDV	-0.05cGA+0.001post-0.005d+2.3	0.03
EDV	0.24cGA-0.02post+0.05d-4.9	0.003
LVmass	-0.07cGA+0.01post+0.02d+3.9	0.004
LVmass	-0.12cGA+0.01post+0.02d-0.003resp+5.7	0.47

Table 5.3.6 – Multiple linear regression: association between LV volumetrics and ductal shunt volume.

5.3.4 Discussion

The previous chapter presented data indicating that in the presence of high PDA shunt volume upper and lower body flow volume are somewhat reduced, but levels remain within or close to the normal range for neonates. Suggesting that global systemic perfusion may be relatively maintained even in the presence of high volume ductal shunt in infants outside the transitional period. This was shown to be achieved by significantly increased cardiac output. It is common clinical belief that large ductal shunt volumes are associated with congestive heart failure (Agarwal et al. 2007) (Baylen et al. 1977) (Schmitz et al. 2003). However the impact of the increase in cardiac work on function in these infants was unclear. In this study data assessing left ventricular dimension and function in neonates with and without PDA was presented. To the author's knowledge this is the first study to assess and relate cardiac function to ductal shunt volume in preterm and term infants. In the following subsection study considerations, limitations, possible significance of results and implications are discussed.

Quantification of left ventricular volumes, SV and EF in adults via bSSFP stack imaging has been well validated and has often been used as the "gold standard" when compared to other MRI and echo techniques (Ichikawa et al. 2003) (Pattynama et al. 1994) (Thiele et al. 2002). The accuracy of cardiac MRI LV mass measurements has been validated using post-mortem hearts (Myerson et al. 2002). Cardiac MRI in neonates is a promising tool that potentially can provide detailed functional

information in the cohort. Although assessment of cardiac function with cardiac MRI is well documented in adults and paediatrics (Alfakih et al. 2003) (Fogel, 2000) (Keller et al. 1986) (Lorenz et al. 1999), validation data did not extend back to neonatal population. The above bland-Altman analysis has since been published in Price *et al.* 2012 as part of a validation study that gives a detailed explanation of the tailored bSSFP stack sequence with additional scanner optimizations used in this study to assess cardiac function in preterm infants.

Protocol considerations and limitations

LVO measurement by 2D PC MRI have been shown to have significantly improved repeatability than echocardiography measures (Groves et al. 2011) and is the only other feasible method to quantify ventricular outputs in this fragile population. LVO measurements from 2D PC MRI were used to assess the accuracy of functional assessment by segmentation of the bSSFP stacks. Bland-Altman analysis was therefore carried out to assess agreement between LVO, and SV values from PC and stack acquisitions in this small challenging cohort. Good agreement was found between PC and bSSFP stack LVO values (normalized loa 15.8%, mean bias 28.6 ml/kg/min and loa -77.7 - +20.5 ml/kg/min). This variability was only slightly higher than that seen in measurements of heart rate, suggesting that a significant proportion of the variability seen in flow quantification may be related to genuine physiological variation as opposed to measurement error. However the mean bias of 9.2% suggests that either stack analysis is systematically overestimating and/or PC quantification is systematically underestimating LVO values.

One potential cause of this bias is the PC sequences have slice thickness 4mm and were positioned at the level of the aortic valve; in infants this slice thickness is too large to place before the coronary arteries and therefore this would not have been included in the PC LVO measurements. The coronary flow accounts for around 5% of the LVO (Ramanathan et al. 2005), potentially accounting

for some of the disparity between PC and bSSFP measures. bSSFP slices are also vulnerable to partial volume errors. Relative slice thickness ranged between 2 – 4mm and since the curvature of the myocardial wall will be greatest during systole in the apical slices; this could lead to partial volume errors where the blood pool volume is underestimated at this location and time point leading to overestimation of SV and therefore LVO. Both these factors may lead the stack and PC analysis to slightly overestimate and underestimate LVO measurements and therefore could explain the mean difference between the two methods.

Results and possible significance

When assessing LV function in the presence of PDA normative ranges for EDV, SV, LVO, LV mass, HR and EF in 43 infants with and without PDA were described. Visual assessment and unpaired t-tests showed that EDV was significantly increased in PDA infants, suggesting volume loading on the heart. In addition SV, LVO and LV mass were increased, demonstrating increased workload. Despite widely held clinical beliefs that PDA presents clinically with increased HR, infants with PDA in this study had HR consistently within the normal range. This indicated that LVO was increased in PDA infants primarily by an increase in SV due to a larger ventricular cavity size (EDV) than increase in HR. Despite the increase in left ventricular volume loading and workload there was no significant difference in EF between control and PDA infants. As a point of interest the distribution of HR in PDA infants was smaller than in controls: all PDA infants had a HR between 149 and 162bpm. Whether or not this indicates less HR variability, demonstrating cardiac and autonomic stress within this cohort is unclear but worthy of further study.

In control infants mean (range) EF was found to be 74.4(60.3 – 89.4)%. Furthermore no significant relationship was found between EF and EDV or LV mass in control infants, suggesting that these infant's hearts are well within their comfortable functioning range. The data presented here

suggests that overall maintenance of contractile function in PDA infants. All PDA infants in this study had EF well above the threshold of >50% that determines normal EF in healthy adults (Levick, Fifth Edition, 2010, chpt 2) (Wahr et al. 1983) (mean (range) was found to be 75.6(62.6 – 89.4). While a significant inverse relationship was found between EF and EDV ($p = 0.006$) in PDA infants all but 2 infants had EF within or above the normal range. The Frank Starling curve shows that all of the PDA infants appear to remain on the same linear trend as control infants; there is no evidence of a drop in SV with very large EDV. The increase in SV and LVO observed above is primarily due to an increase in preload caused by the additional shunt volume. It appears that in general the Frank-starling mechanism adequately compensates for the mechanical disadvantage imposed by Laplace's law in these enlarged hearts, suggesting an overall maintenance of contractile function. Cardiac output is known to significantly decrease shortly after surgical ligation (Kimball et al. 1996) (Noori et al. 2007) primarily due to the decrease in LV preload. The resultant cardiac function after treatment via medication is not so well documented. Initial investigations of consequent left ventricular function after medication is presented in the following subsection.

While contractile function is generally maintained there in clearly a significant increase in LV mass in the PDA infants. This increase is not explained by differences in cGA and postnatal age. Assessment of the correlation between ductal shunt volume and this enlargement was investigated by considering the relationship between EDV and the ratio of MyoV/EDV. This ratio was almost constant in control infants. The MyoV/EDV was higher overall in PDA infants potentially suggesting disproportionate hypertrophy. Yet multiple linear regression showed a significant association between increased MyoV/EDV and decreased ductal shunt volume in PDA infants. Indicating that infants with lower shunt volumes may have hypertrophic growth which is more disproportionate than infants with high shunt volumes.

This relationship appears counter intuitive and warrants examination in a larger cohort of infants. However lower ductal shunt volumes could be indicative of high pulmonary vascular resistance,

which could lead to increased right ventricular afterload and subsequently lead to overall increased myocardial mass in these lower shunt volume infants. However there was no significant association between number of days on respiratory support from birth to discharge and LV mass correcting for cGA, postnatal age and ductal patency. However this could be due to the small number of infants and the number of confounding factors.

Studies have shown that in response to increase work requirements either via pressure or volume overload a rapid increase in myocardial mass occurs. Yet it is unclear whether this is due to hypertrophy (growth or preexisting myocytes) or hyperplasia (an increase number of myocytes due to mitotic division) or a mixture of both processes (Dowell et al. 1978). It is thought that spontaneous mitotic activity rapidly declines during the first few weeks of neonatal life. After this period cardiac enlargement due to increased work load is due to hypertrophy. Animal studies in neonatal and adult rats where pressure and volume induced cardiac enlargement was generated have shown normal heart function was maintained in neonatal rats. This difference in function between adult and neonate rats may correlate to the absence or presence of cardiac muscle proliferation during adaptive cardiac growth (Dowell et al. 1978). The same mechanisms could occur in the PDA infants involved in this study and may part explain the maintenance of cardiac function seen in this cohort, where hyperplasia is the main cause of enlargement.

Infants born premature are known to have decreased diastolic function, more markedly relaxation than compliance (Kozak-Barany et al. 2001), investigation of regional myocardial strain, stress and torsion would provide a comprehensive assessment of cardiac function. The preterm and neonatal heart undergoes significant structural and functional changes shortly after birth to provide the circulation sufficient for extra-uterine life. Assessment of the structure and orientation of myofibers in preterm, neonatal and adult bovine and human hearts have demonstrated the plasticity of the neonatal heart (Chen et al. 2013) (Mekkaoui et al. 2013). A progressive increase in density and myocyte arrangement has been shown towards term (Mekkaoui et al. 2013). Although the

arrangement of myofiber structure into the helical pattern seen in adults occurs early in the second trimester, the dense sheet arrangement only begins after this; the myocardium is still developing after term (Mekkaoui et al. 2013). How this impacts on cardiac function in the preterm heart is unclear. These areas of work and possible future work are discussed in more detail in chapter 8.

Limitations of the cohort

This study has three significant limitations. Firstly a relatively small number of PDA infants were studied at a time of clinical stability outside the transitional period. Although the data presented here suggests that cardiac function is maintained even in infants with a high ductal shunt volume, it may be that at other points, particularly in the first few days of life during the circulatory transition where dramatic changes occur in preload conditions, myocardial contractility and systemic and pulmonary vascular resistance that PDA infants may not be within this regime.

Secondly data has only been presented at one time point in the duct's history; there is no temporal data of the ductal shunt volume and resultant cardiac status. The duration of the heart's transition to adapt to the increased volume load or whether this enlargement persists long after the closure of the duct is unknown. Although there was no significant association between EF and shunt volume the ventricular dimensions were significantly increased, whether this increase in LV mass is due to hypertrophy or hyperplasia is difficult to determine and if this is evidence of pathological ventricular remodelling is unclear.

Thirdly due to the nature of PDA there was a significant difference in cGA between control and PDA infants: there are relatively few infants <30 week cGA without a PDA in this study. Graphic comparison between control and PDA infants was performed by linear extrapolation of the 95% confidence limits, it is feasible that infants <30 weeks cGA without a PDA do not follow this linear trend.

5.3.5 Conclusion

In summary this study presents data on left ventricular dimension and function in preterm and term infants with and without PDA. From PC MRI data the impact of ductal shunt volume on ventricular dimension and function could then be assessed. LVO, EDV and LV mass were found to be significantly increased in PDA infants. Moreover a significant association was found between increased LV mass and ductal shunt volume. A significant increase in MyoV/EDV was found in PDA infants suggesting that these hearts may be disproportionately hypertrophic. However EF and fractional thickening remained within the normal range and no association was found between EF and ductal shunt volume. Furthermore when plotting the Frank Starling curve all control and PDA subjects were consistent with a single linear trend with no evidence of a decline that may indicate heart failure.

It is common clinical belief that large ductal shunt volumes are associated with congestive heart failure and this plays a role in the decision for forced closure. Yet the data presented here suggests that left ventricular function is generally maintained in these enlarged hearts. The ability to accurately quantify shunt volume and associated ventricular dimension and function provides valuable insight into the impact of the increased cardiac work load and volume loading due to the PDA. Further study is needed to determine the long term impact of this apparent remodelling and impact of treatment.

The data presented in this study indicates that global function is maintained in the enlarged hearts of the PDA infants. However, only global wall function and wall function parameters were evaluated. The additional blood volume entering the pulmonary circulation in PDA infants can lead to pulmonary hyper-perfusion and respiratory problems. However, the impact of this increased LVO on the pulmonary circulation, consequent right ventricular afterload and right ventricular dimension and function was not assessed in this study. In the following subsection a preliminary study to first

evaluate the pulmonary flow in the presence of a PDA from right ventricular volumetric analysis and secondly to assess the feasibility of RV functional analysis from bSSFP stacks is presented.

5.4 Right Ventricular Output, Function and Pulmonary Flow

5.4.1 Introduction

In addition to the systemic hypo-perfusion, large shunt volumes can cause pulmonary hyper-perfusion (Agarwal et al. 2007) (Laughon et al. 2007). The extra blood volume overloads the immature lungs and leads to pulmonary hypertension; the RV is therefore required to generate more pressure to eject the same volume of blood into the pulmonary artery, increasing the workload on the side of the heart that, in normal term infants, is within the low pressure system. The volume of steal from the systemic circulation will cumulatively increase the pulmonary flow (pulmonary flow is further increased by left to right shunt through a PFO, yet no infant within this study had a PFO as determined by echo), the extra blood flow overloading the immature lungs is also thought to lead to or exacerbate respiratory pathology seen in this cohort.

As with many of the pathologies associated with PDA, the relationship between ductal shunt volume respiratory pathology, status and outcome is complex. Another consideration is that large shunt volumes are indicative of low pulmonary resistance and low shunt volumes are due to not only a constricting duct but high pulmonary pressure (reducing the pressure gradient across the duct). There is clearly a multifaceted association between pulmonary flow, ductal shunt volume and the association with RV function and respiratory status.

The data presented in the previous study indicates that the left ventricular function is generally maintained in the presence of a PDA, yet this ventricle is under different conditions than the RV. In the situation of a left to right shunt (as in all the PDA infants in this study) the LV experiences increased preload due to the shunt volume, the same shunt volume leads to an increase in RV

afterload. Whether RV function is maintained in preterm PDA infants without the additional preload to generate a more forceful contraction is worth investigating and may provide insight into the association with pulmonary pathology.

Objectives

The aim of this initial study was to quantify the RVO (and therefore total pulmonary flow) to infer pulmonary flow in the presence and absence of a PDA and to assess the feasibility of RV functional analysis from the existing bSSFP stack protocol.

5.4.2 Patient and Methods

Study cohort

Quantification of total pulmonary blood flow was carried out in 17 preterm and term infants. Eight control infants with median (range) GA 33^{+6} (27^{+6} – 39^{+1}) weeks, cGA 35^{+6} (31^{+1} – 40^{+1}) weeks, birth weight 2120(765 – 3050) grams and weight at scan 2110(790 – 3055) grams were scanned. Nine infants with PDA with median (range) GA 27 (24^{+3} – 28^{+4}) weeks, cGA 27^{+5} (27^{+4} – 31^{+6}) weeks, birth weight 960(530 – 1400) grams and weight at scan 1075(660 – 1430) grams were scanned. PDA was confirmed by echo and quantified by PC MRI (chapter 4). Shunt volume ranged between 12.1 – 74.2% of LVO.

Data processing

As mentioned previously the analysis in this study was performed on the previously presented bSSFP stacks. From the existing bSSFP short axis stack data the right ventricular endocardium was

segmented in a free available software Segment v1.8 R1172 (http://segment.heiberg.se) (Heiberg et al. 2010). Endocardial borders were defined by performing a detailed manual tracing at ES and ED time frames. A “first glance” ED and ES time frame was chosen from a mid-ventricle slice, the endocardial border was defined in each slice at this and the time frame either side until the maximum and minimum volume was found. ED and ES time frames were then set to the maximum and minimum volumes respectively. Long axis motion was corrected for by measuring the tricuspid value displacement on a 4 chamber pilot scan between the ED and ES time points taking an average of 3 measures.

In control infants total pulmonary blood flow was taken as the RVO. In PDA infants, total pulmonary flow was calculated as RVO plus ductal shunt volume (as all PDA infants had left to right ductal shunts, from the systemic circulation to the pulmonary circulation) determined by PC MRI (chapter 4).

Statistical analysis

Bland-Altman analysis was carried out to assess the correlation between LVO and RVO values from stack analysis in the 8 control infants (closure of the foramen ovale was determined by echo). Analysis was carried out by a single observer. Mean difference of measures, loa and RI were calculated. A normative range of pulmonary flow was established from this preliminary data and the impact of PDA was investigated. Although epicardial boarders were not determined and hence myocardial wall thickness and function could not be evaluated, the EF in the PDA infants was assessed.

5.4.3 Results

Loa, mean difference and RI for the Bland-Altman analysis of the LVO and RVO from stack analysis are shown in table 5.4.1. A relatively poor agreement was found (RI = 39.4%).

	loa ml/min/kg	mean difference ml/min/kg	RI %
LVO vs RVO	-90.5 to 96.8	3.13	39.4

Table 5.4.1 – Bland-Altman analysis of LVO vs RVO: Loa, mean difference and RI are shown for the comparison of LVO and RVO from stack analysis.

The normative range as shown in figure 5.4.1 shows that pulmonary blood flow is significantly increased in PDA infants, with all but 3 above the upper 95% confidence limit. Mean (range) EF was found to be 85(77 – 85)% in PDA infants.

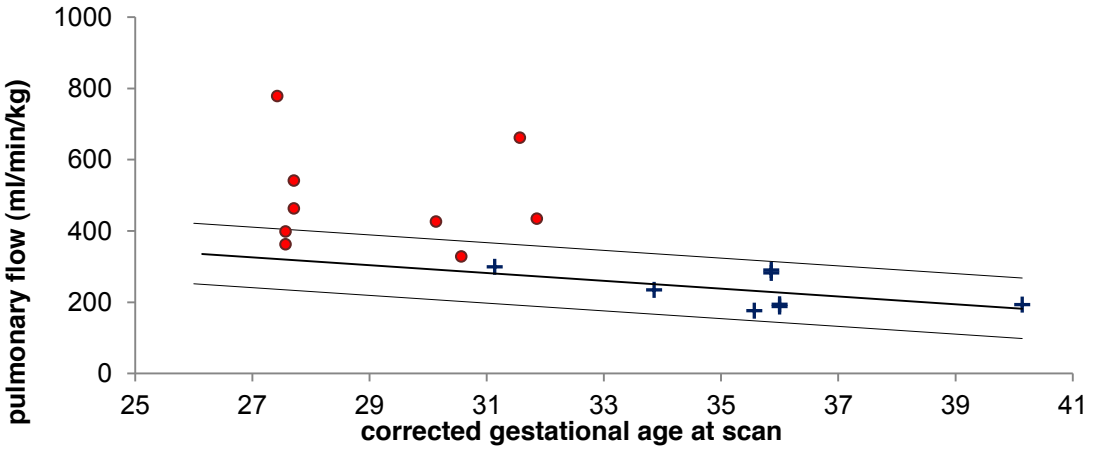

Figure 5.4.1 - Pulmonary blood flow: Normative range with trend line and 95% confidence limits of pulmonary blood flow calculated from RVO stack analysis in 17 infants with (●) and without (+) PDA.

5.4.4 Discussion

Segmentation of the right ventricle was carried out in 17 infants with and without PDA to firstly assess the feasibility of RV functional analysis from existing bSSFP stacks and secondly to calculate the total pulmonary flow in the presence of a shunt. Although the study presented in the previous subsection to assess LV dimension and function contained 29 control infants only 8 are presented here. From visual analysis of the RV only these 8 datasets were considered to provide full coverage of the RV and have reasonable image quality to delineate the RV endocardium from the trabeculae. Due to the non-uniform profile and thinner myocardial wall thickness of the RV, it is often difficult to determine RV blood pool from trabeculae (and possibly moderator band) with the current spatial resolution (1x1mm) and slice thickness (4mm). The tricuspid valve often does not reside in line with the plane of the mitral valve, but at an oblique angle to it (Levick, Fifth Edition, 2010, chpt 2) and consequently, some datasets did not provide full coverage of the RV throughout the cardiac cycle.

There is still some disagreement over the most appropriate 2D slice orientation for segmentation of the RV in adults (Schulz-Menger et al. 2013). Some studies opt for a trans-axial slice orientation for better delineation of the tricuspid valve, while others use the short axis stack used in this study for improved depiction of the RV myocardial wall and trabeculae. An additional advantage of the short axis contiguous slice method is that with adequate spatial resolution and coverage, both LV and RV dimension and function can be assessed from one scan. The relatively poor agreement found from Bland-Altman analysis of the comparison between LVO and RVO from stack analysis (RI = 39.4%) suggests that the current bSSFP short axis stack is not optimal for RV volumetric and functional analysis.

The RV myocardium-tissue boarder contrast was not adequate to allow semi-automated or manual segmentation of the epicardial boarder with confidence, therefore functional analysis of the RV myocardium was not performed. However from volumetric analysis, EF was found to be 82.5(76.7 – 85.4)% in PDA infants. Although this range is similar to the LV EF (75.6(62.6 – 89.4)%) and well above

the adult threshold for normal EF in adults, considering the above concerns over accuracy, whether this indicates that RV function is maintained in the PDA infants in this study is unclear.

From the RVO values, pulmonary flow was then quantified in an additional 9 PDA infants from the summation of RVO and shunt volume (determined by PC MRI, chapter 4). The normative range indicates, as expected, that pulmonary flow is significantly increased (over 10 SD above the mean) in the presence of a PDA (this data is referred to in chapter 4). Although some care is needed when interpreting this data as the Bland-Altman analysis showed relatively poor agreement, it is clear that PDA causes pulmonary hyper-perfusion.

In summary, to gain a comprehensive understanding of the impact of the duct, both RV and LV function needs to be investigated. However, the data presented here demonstrates that the current bSSFP short axis stack protocol is not optimal for RV volumetric or functional analysis. With improved spatial resolution and the additional information of the pulmonary flow and impact of PDA on RV function could be assessed accurately and provide further insight into the association between PDA, RV function and respiratory pathology. This is an area of future work and is discussed in more detail in chapter 8.More work is needed to this is discussed in more detail in the future work section in chapter 8.

5.5 Treatment of PDA and Corresponding Cardiac Function

5.5.1 Introduction

In the first section data were presented suggesting that left ventricular function may be maintained even in the presence of high ductal shunt volume (74% of LVO). In addition left to right shunting provides an increased left ventricular filling volume and therefore preload. Subsequently, in the infants involved in the previous study it appears that the Frank-starling mechanism adequately compensates for the mechanical disadvantage imposed by Laplace's law in these enlarged hearts.

Multiple echocardiography studies have been carried out to investigate ventricular performance after surgical ligation of the PDA (Kimball et al. 1996) (Noori et al. 2007). Studies suggest that LVO was significantly decreased 24 hours after ligation primarily due to the decrease in LV preload, however contractility and diastolic function did not change. The resultant cardiac function after treatment via medication is not so well documented. The duration of the heart's transition to adapt to the decreased volume load after ligation or medication or whether the left ventricular enlargement persists long after the closure of the duct is unknown.

Objective

The aim of the initial study was to investigate the resultant left ventricular function after treatment of the PDA.

5.5.2 Patients and methods

The study was approved by the North West London Research Ethics Committee (06/Q0406/137) and written informed parental consent was obtained in all cases.

Study cohort

Five Infants with median (range) GA $25^{+3}(24^{+3} – 26^{+3})$ weeks, cGA $32(30^{+2} – 35^{+2})$ weeks, birth weight 690(640 – 910) grams and weight at scan 1270(745 – 2180) grams were scanned. Infants were treated for PDA with ibuprofen prior to the MRI scan and had had ductal closure confirmed by PC MRI and echocardiography.

Acquisition

As in the previous study data was acquired on a Philips 3-Tesla MR Achieva scanner (Best, Netherlands) using a specialised 8 channel pediatric body receive coil for infants above 2kg and a small extremity receive coil for infants below 2kg. The same retrospectively gated free breathing 2D bSSFP short axis 10 slice stack acquisition placed over the heart, aligned with the mitral value using previously acquired pilot scans was acquired.

Data processing

Once more stacks were segmented and LV function was quantified using freely available software Segment v1.8 R1172 (http://segment.heiberg.se) (Heiberg et al. 2010). Myocardial borders were defined as previously, by performing a detailed manual tracing of the epi and endocardium at ES and ED time frames. Long axis motion was corrected for by measuring the mitral value displacement on a 4 chamber pilot scan between the ED and ES time points taking an average of three measures. From this analysis myocardial and ventricular cavity volumes were obtained in the same way as the previous study. The 6 mid cavity sections from the 17 sector American Heart Association model (Cerqueira et al. 2002) was employed for myocardial assessment of ED thickness and fractional thickening.

Statistical analysis

Treated infants were superimposed onto the normative ranges of LV output measures LVO, SV, EF, and ventricular dimensions EDV and LV mass to visually assess the impact of treatment of PDA. These measures were also plotted against postnatal age to identify if treated PDA infants were exposed to large shunt volumes for the same amount of time. In addition treated infants were added to the scatterplots of control and PDA ED myocardium thickness (normalized by weight at

scan) and fractional thickening for the averaged 6 mid cavity myocardial sections to investigate the resultant wall thickness and function. The resultant EDV and SV were plotted on the Frank Starling curve to investigate the relationship between filling and SV in treated PDA infants. Finally the relationship between MyoV/EDV and EDV was investigated in these infants and visually compare to control and PDA infants.

5.5.3 Results

In this initial observational study 5 infants treated for PDA with ibuprofen prior to the MRI scan and had had ductal closure determined by PC MRI and echocardiography were scanned. Age, weight and treatment information is given in table 5.5.1. All infants were determined to have a clinically significant duct via echocardiography before treatment (a ductal diameter >1.5mm). From the previous echo analysis in chapter 4 ductal diameter had a significant association with increased ductal shunt volume ($p < 0.001$). This suggests that all 5 infants had large shunt volumes prior to treatment.

GA	cGA	postnatal age at scan	postnatal age at treatment	days between treatment and scan	treatment
25^{+3}	30^{+4}	36	16	20	6d of ibuprofen
25^{+5}	30^{+2}	32	18	14	3d of ibuprofen
24^{+3}	35^{+2}	76	23	53	1d of ibuprofen
26^{+3}	32	39	8	31	1d of ibuprofen
24^{+5}	34^{+6}	71	13	58	2d diuretics 3d of ibuprofen

Table 5.5.1 – Treatment information: GA, cGA, postnatal age in days at scan and at treatment, days between treatment and scan and treatment type are given for all 5 infants treated for PDA.

EDV, SV, LVO, LV mass (normalized by weight at scan), HR and EF in treated PDA infants were plotted against cGA and superimposed on the previous normative range graphs (figure 5.5.1 a, b, c, d, e and f). A larger distribution of EDV was observed in treated PDA infants than controls. 1 infant had SV below (2.2 SD below the mean) the normal range. All treated PDA infants had LVO, HR and EF within the 95% confidence limits. Two infants had LV mass above and 1 below the normal range.

a

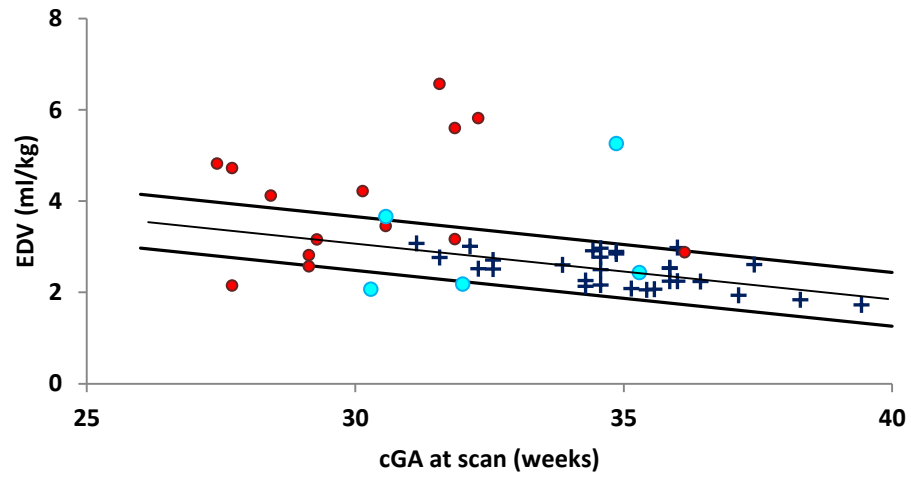

b

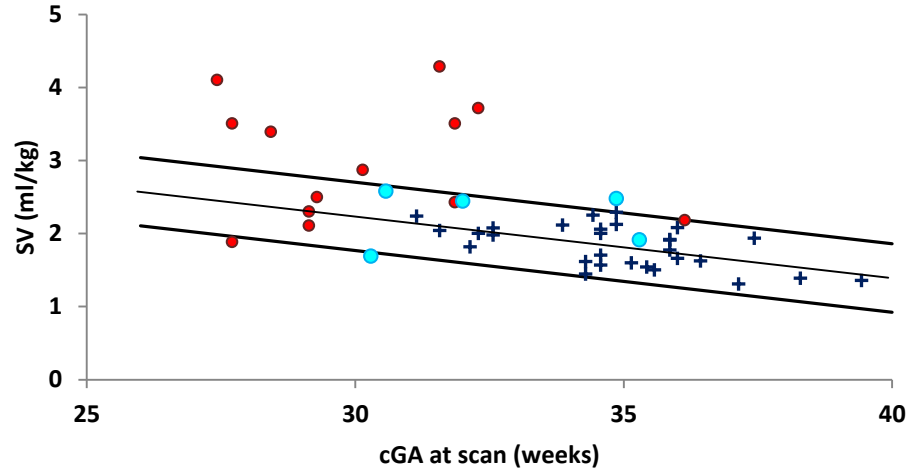

c

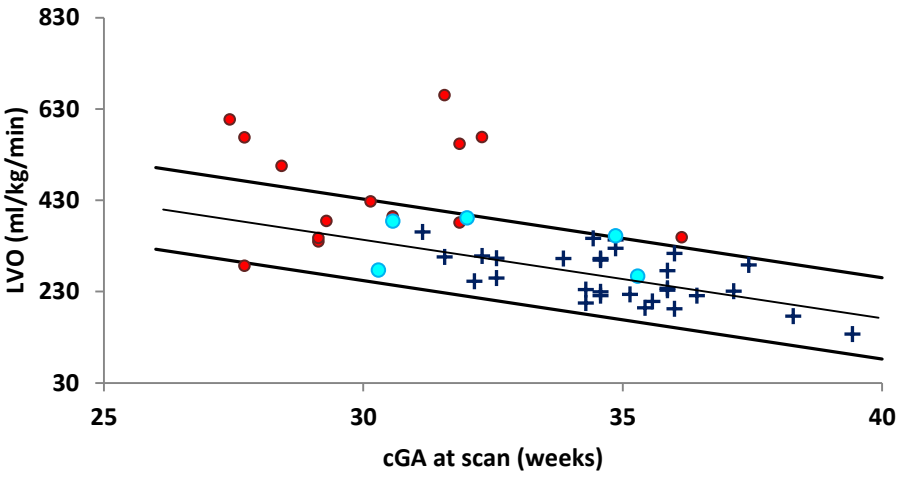
830
630
430
230
30
LVO (ml/kg/min)
25
30
35
40
cGA at scan (weeks)

d

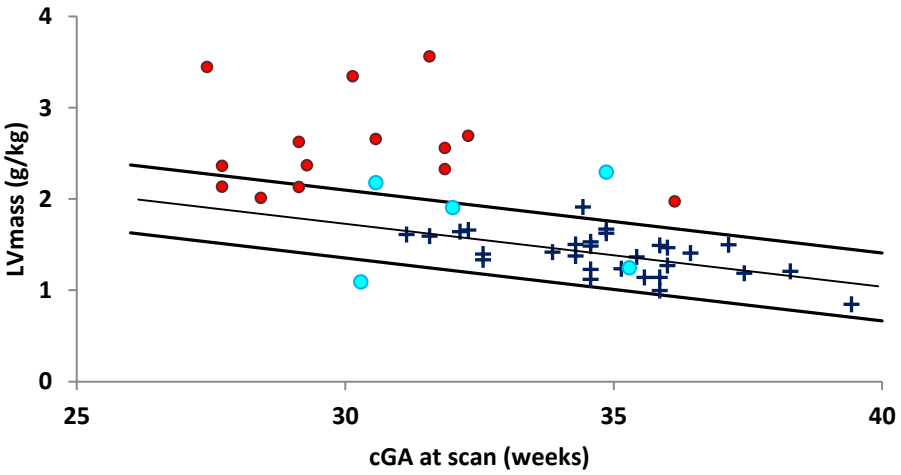
4
3
2
1
0
LVmass (g/kg)
25
30
35
40
cGA at scan (weeks)

e

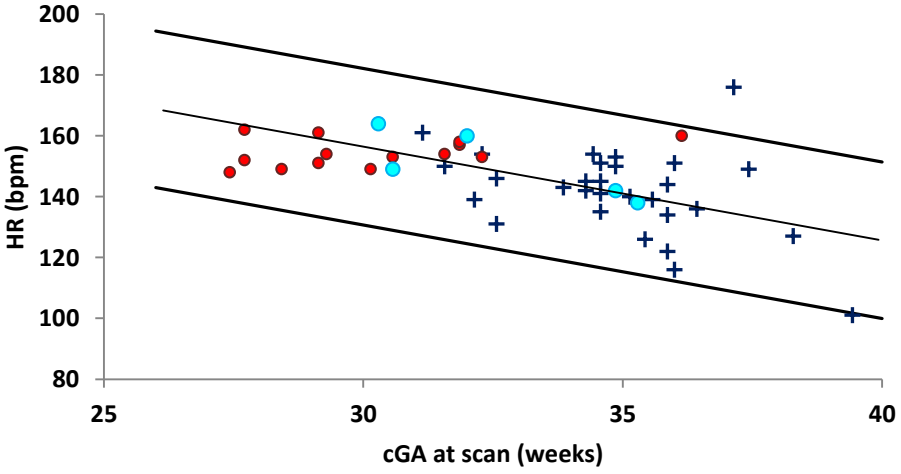
200
180
160
140
120
100
80
HR (bpm)
25
30
35
40
cGA at scan (weeks)

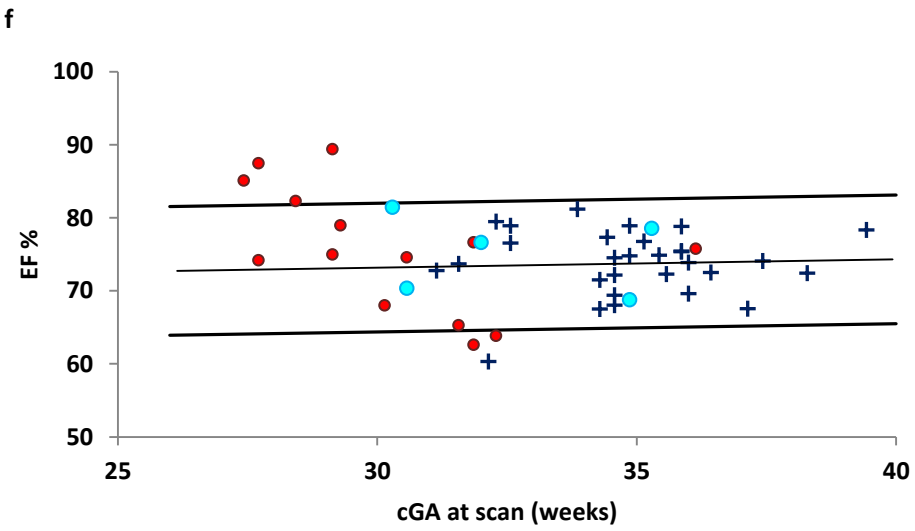

Figure 5.5.1 – Normative ranges: Scatter plots with trend line and 95% confidence limits of a: EDV, b: SV, c: LVO, d: LV mass, e: HR and f: EF in 48 infants with (●) and without (+) PDA and treated for a PDA (●).

EDV, SV, LVO, LV mass (normalized by weight at scan) and EF were then plotted against postnatal age (figure 5.5.2a, b, c, d and e). Postnatal ages at treatment are also displayed on the graphs as dotted lines. This indicates that these 5 infants were treated outside the transitional period at around the same postnatal age that the previous PDA infants were scanned. Again the distribution of EDV is larger in the treated PDA infants than controls. SV and LVO are maintained in all but 1 infant. Two infants have LV mass above the normal range. However EF is maintained.

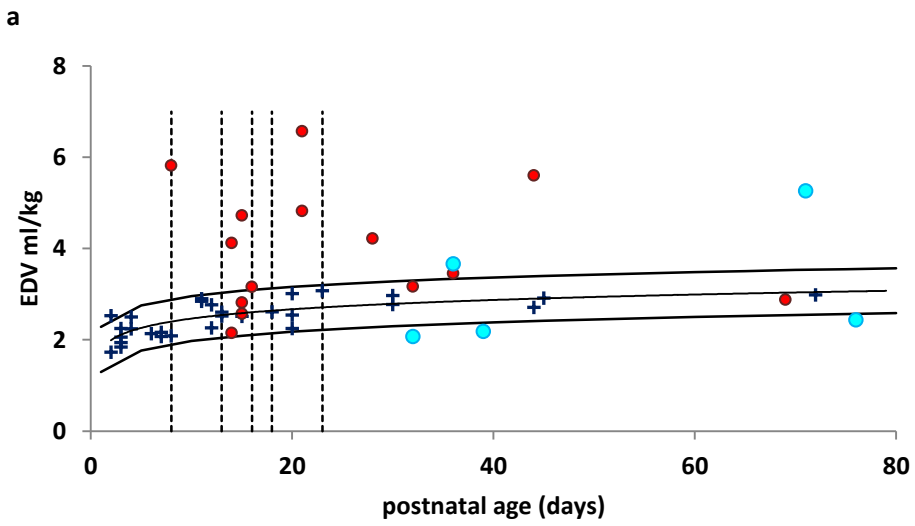

b

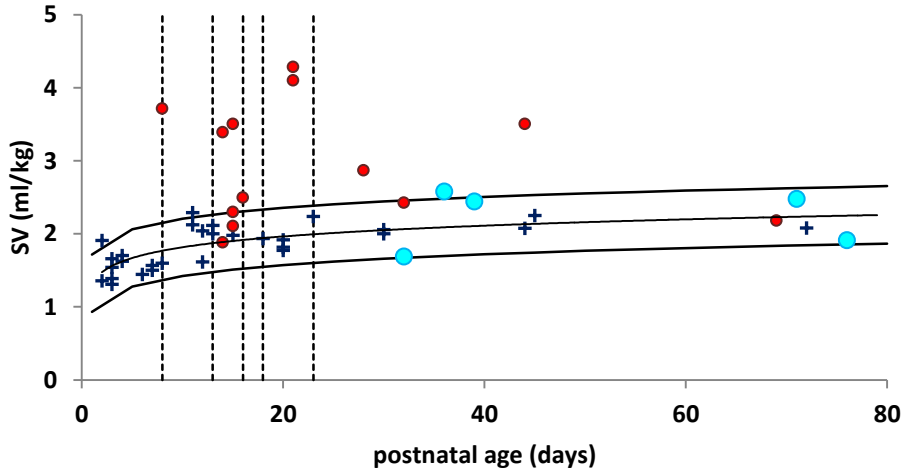
SV (ml/kg)
0
1
2
3
4
5
0
20
40
60
80
postnatal age (days)

c

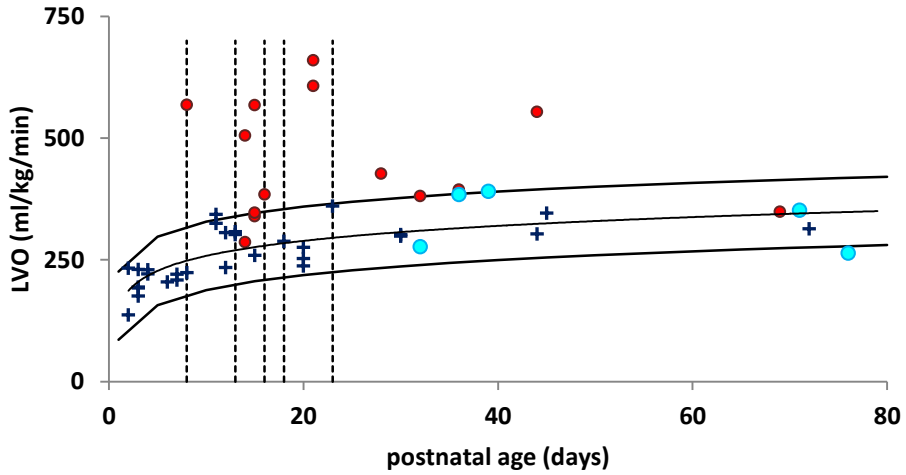
LVO (ml/kg/min)
0
250
500
750
0
20
40
60
80
postnatal age (days)

d

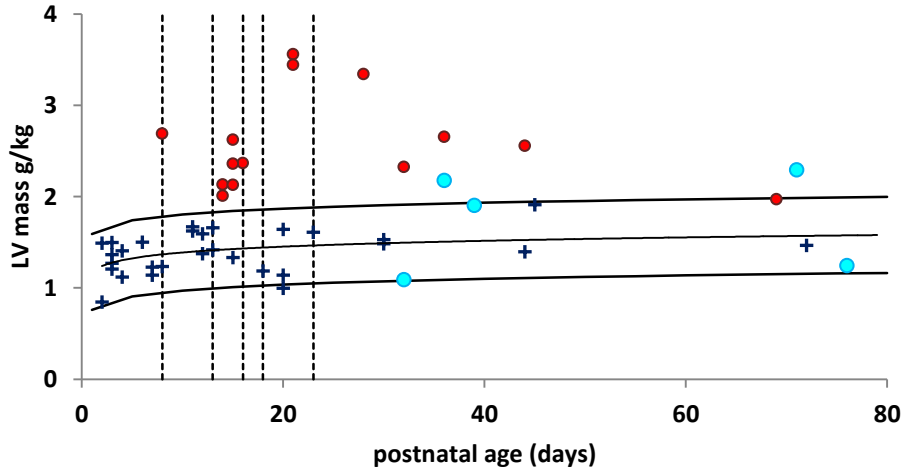
LV mass g/kg
0
1
2
3
4
0
20
40
60
80
postnatal age (days)

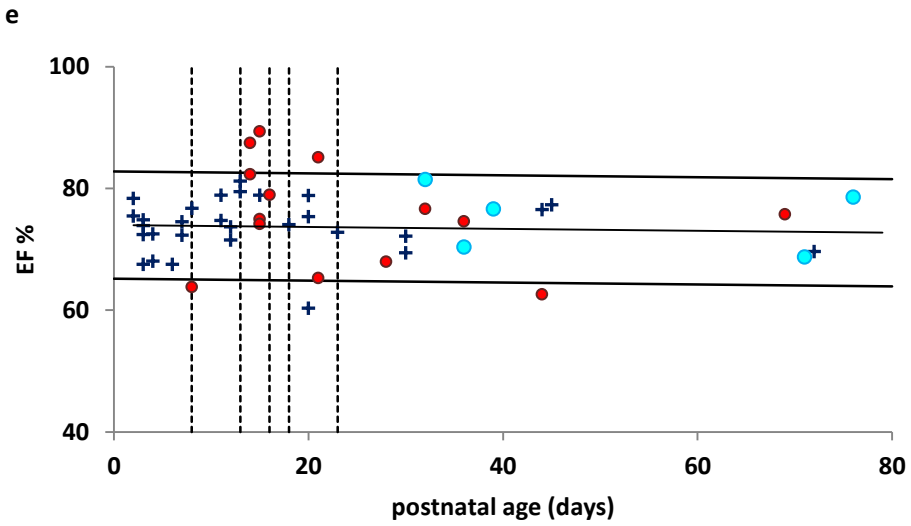

Figure 5.5.2 – Postnatal normative ranges: Scatter plots with trend line and 95% confidence limits of a: EDV, b: SV, c: LVO, d: LV mass, e: EF plotted against postnatal age in 48 infants with (●), without (+) and treated for a PDA (●).

Fractional thickening Scatterplots show ED thickness normalized by weight at scan and fractional thickening for the 6 mid cavity sections in control, PDA and treated PDA infants (figure 5.5.3a and b). ED thickness and fractional thickening appear to be within the control distribution.

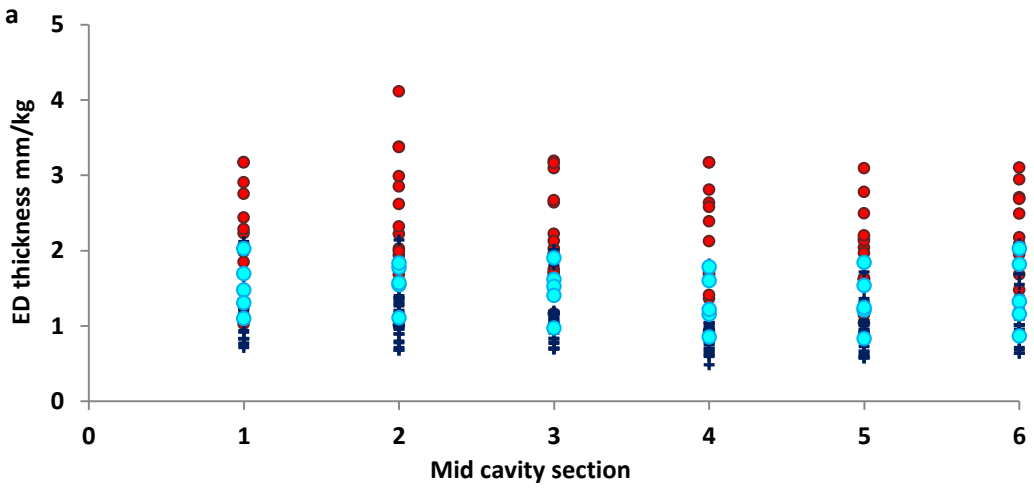

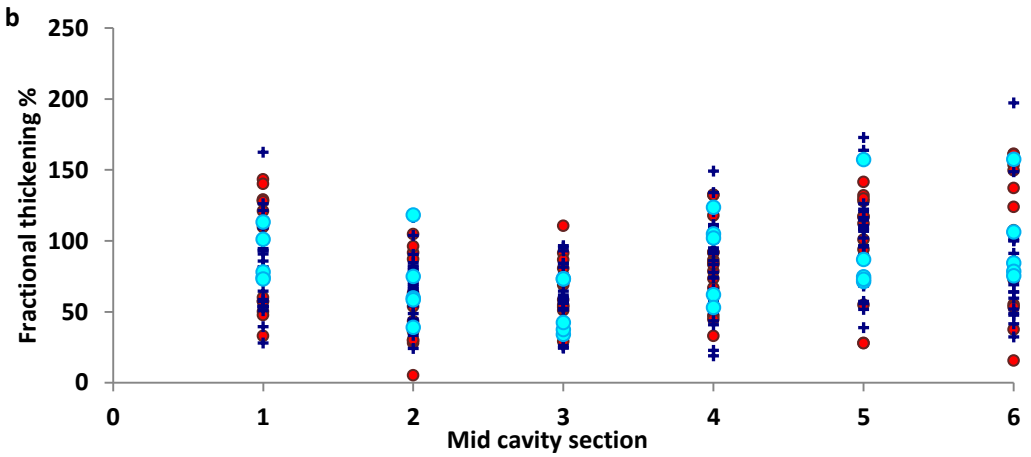

Figure 5.5.3 – Myocardial wall analysis: a: ED wall thickness and b: fractional thickening in infants with (●), without (+) and treated for PDA (●).

The group estimated Frank Starling curve showed that the infant with the largest EDV deviated away from the linear trend (figure 5.5.4).

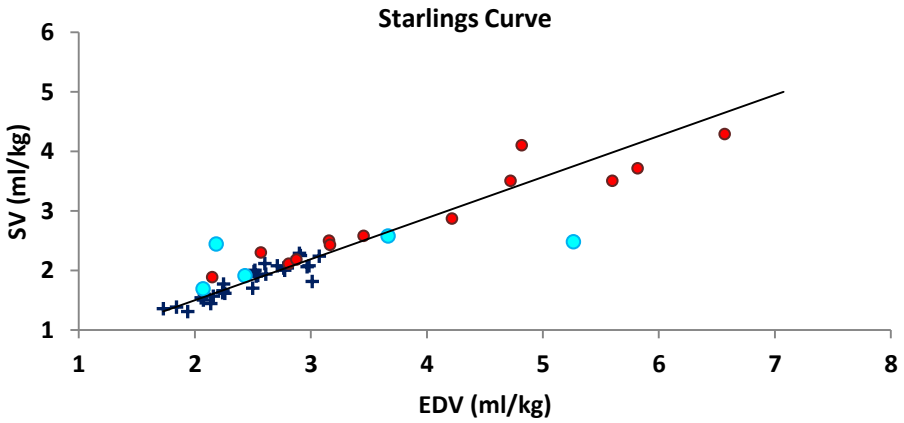

Figure 5.5.4 – Frank Starling curve: Population starling curve for infants with (●), without (+) and treated for PDA (●).

The ratio of MyoV/EDV was plotted against EDV and 2 infants were outside the normal range, 1 above and 1 below (figure 5.5.5).

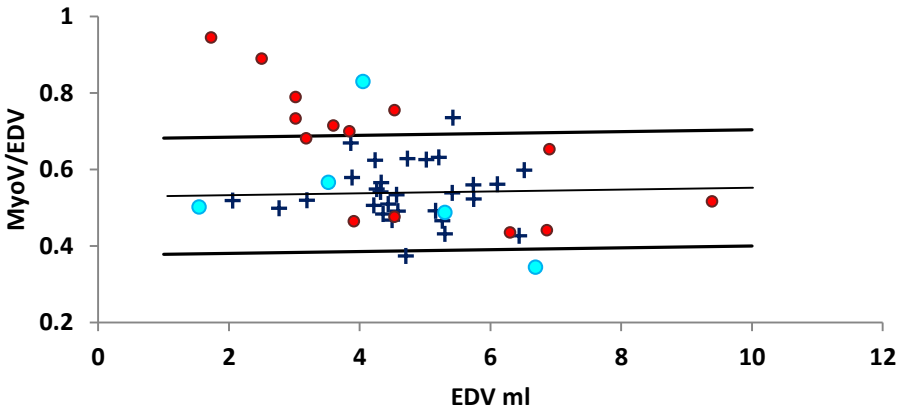

Figure 5.5.5 – Measure of hypertrophy: Normative range of MyoV/EDV ratio against EDV in infants with (●), without (+) and treated (●) PDA.

5.5.4 Discussion

Cardiac output is known to decrease after surgical ligation (Kimball et al. 1996) (Noori et al. 2007), however the resultant cardiac function after treatment via medication is not so well documented. The duration of the heart's transition to adapt to the decreased volume load after ligation or medication or whether the left ventricular enlargement persists long after the closure of the duct is unclear. This initial study presents additional left ventricular volumetric and functional analysis data in 5 infants who were treated for PDA. All five infants were treated with ibuprofen for what was considered a significant duct (>1.5mm diameter as assessed by echocardiography), outside the transitional period and had ductal closure determined by echo and PC MRI. Data from the previous section were used to compare and assess the resultant output and functional measures in these treated infants.

Protocol considerations and limitations

Ductal shunt volume was not quantified by PC MRI before treatment was given; hence the volume of left ventricular overload due to the PDA was not known. However as mentioned above all 5 infants had a duct diameter >1.5 mm prior to treatment. Furthermore a strong association was found between ductal diameter and shunt volume from the echocardiography measure analysis in the previous study. In addition the treatment of these 5 infants was during the same post natal age time window as the observation point used to study the infants that still had a PDA in the previous study. Median (range) postnatal age for treated and PDA infants was 16(8-23) days and 18(8-69) days respectively. This would suggest that these infants had high shunt volume and therefore increased SV and enlarged LV prior to treatment and that these 5 infants endured large shunt volumes for around the same duration as the PDA infants before they were treated. From these assumptions the comparison between control, treated and PDA infants was made. However, this study was not a longitudinal study, population information about ductal shunt volume and resultant function are presented from one time point only. Consequently the discussion presented here aims to consider the observations seen from these preliminary data, with the significant limitations stressed and deliberate future areas of study. However this study does indicates the impact of treatment on left ventricular dimension and function and emphasizes the need for further investigation to aid targeted treatment.

Results and possible significance

As expected all of the 5 infants had LVO below the upper confidence limit post treatment. In general the LVO measures of LVO and SV appeared reduced in the treated PDA cohort compared to the PDA group. The distribution of EDV, LV mass and MyoV/EDV was larger in treated PDA infants than controls with 2 above the normative range, however EF was maintained. Without longitudinal data

the clinical significance of this cannot be determined. ED thickness and fractional thickening appeared to reside within the control range. If the previous assumption is made that prior to treatment left ventricular blood volume was significantly increased then treatment of the duct may have reduced the resultant enlargement seen in the PDA infants.

One infant treated for PDA appeared below the linear trend on the Frank Starling population curve. This may suggest that in some infants with larger left ventricles with absence of a large preload the Frank Starling mechanism is not adequate to compensates for the mechanical disadvantage imposed by Laplace's law at the time of the scan. However, it should be remembered that PDA, its association with pathologies and outcome are multifactorial.

Multiple echocardiography studies have been carried out to investigate ventricular performance after surgical ligation (Kimball et al. 1996) (Noori et al. 2007) and suggest that although LVO is significantly decreased in the first 24 hours, contractility and diastolic function are unchanged. The resultant cardiac function after treatment via medication is not so well documented. The duration of the heart's transition to adapt to the decreased volume load after treatment or whether the left ventricular enlargement persists long after the closure of the duct is unknown. In addition recent broader studies in both humans and animals (Bensley et al. 2010) (Lewandowski et al. 2012) suggest that prematurity leads to remodelling of the myocardium which alters its final structure in adulthood. This study indicates that further investigation is needed to fully understand not only the impact of prematurity but the temporal nature and extent of remodelling in the presence of a PDA and how the heart then adapts after treatment.

In summary the work in this chapter demonstrates the feasibility of assessing left ventricular dimensions and function in preterm and term infants. The techniques and work presented in this chapter could be employed to perform a longitudinal study to quantify ductal shunt volume and resultant left ventricular function prior to and after treatment.

5.6 References

Agarwal R, Deorari AK, Paul VK. Patent Ductus Arteriosus in Preterm Neonates. AIIMS-NICU protocols 2007.

Alfakih K, Plein S, Thiele H, Jones T, Ridgway JP, Sivananthan MU. Normal Human left and right ventricular dimensions for MRI as assessed by turbo gradient echo and steady-state free precession imaging sequences. Journal of Magnetic Resonance Imaging. 2003; 17:323-329.

Baylen BG, Meyer RA, Kaplan S, Ringenburg WE, Korfhagen J. The critically ill premature infant with patent ductus arteriosus and pulmonary disease – an echocardiographic assessment. J. Pediatr. 1975; 3: 423-432.

Bensley JG, Stacy VK, De Matteo R, Harding R, Black MJ. Cardiac remodelling as a result of pre-term birth: implications for future cardiovascular disease. Europ Heart Journal. 2010; 31: 2058 – 2066.

Bland JM, Altman DG. Statistical methods for assessing agreement between two methods of clinical measurement. Lancet. 1986; 327: 307 – 310.

Broadhouse KM, Price AN, Durighel G, Cox DJ, Finnemore AE, Edwards AD, Hajnal JV, Groves AM. Assessment of PDA Shunt and Systemic Blood Flow in Newborns Using Cardiac MRI. NMR in Biomedicine. DOI: 10.1002/nbm.2927.

Carr HY, Purcell EM. Effects of diffusion on free precession in nuclear magnetic resonance experiments. Phys Rev. 1954; 94: 30–38.

Carr JC, Simonetti O, Bundy J, Li D, Pereles S, Finn JP. Cine MR angiography of the heart with segmented true fast imaging with steadystate precession. Radiology 2001;219:828–834.

Cerqueira MD, Weissman NJ, Dilsizian V, Jacobs AK, Kaul S, Laskey WK, Pennell DJ, Rumberger JA, Ryan T, Verani MS. Standardized myocardial segmentation and nomenclature for tomographic imaging of the heart: A statement for healthcare professionals from the cardiac imaging committee of the council on clinical cardiology of the American Heart Association. American Heart Association. 2002; 105:539-542

Chen J, Zhang L, Allen JS, Hu L, Caruthers SD, Lanza GM, Wickline SA. Diffusion tensor MRI revealed developmental changes of cardiomyocyte architecture in pig hearts. Proc ISMRM 2013; 0483.

Dong SJ, MacGregor JH, Crawley AP, McVeigh E, Belenkie I, Smith ER, Tyberg JV, Beyar R. Left ventricular wall thickness and regional systolic function in patients with hypertrophic cardiomyopathy. A three-dimensional tagged magnetic resonance imaging study. Circulation. 1994; 90: 1200-1209.

Fogel MA. Assessment of cardiac function by magnetic resonance imaging. Pediatr Cardiol. 2000; 21:59-69.

Groves A, Finnemore AE, Cox DJ, Broadhouse KM, Price AN, Durighel G, Ekitzidou G, Hajnal JV, Edwards AD. Validation study on the accuracy of echocardiographic measurements of systemic blood flow volume in newborn infants. Submitted for publication

Groves AM, Chiesa G, Durighel G, Goldring ST, Fitzpatrick JA, Uribe S, Razavi R, Hajnal JV, Edwards AD. Functional cardiac MRI in preterm and term newborns. Arch Dis Child Fetal Neonatal Ed 2011; 96: F86–F91.

Grothues F, Smith GC, Moon JCC, Bellenger NG, Collins P, Klein HU, Pennell DJ. Comparison of interstudy reproducibility of cardiovascular magnetic resonance with two-dimensional echocardiography in normal subjects and in patients with heart failure or left ventricular hypertrophy. Am J Cardiol. 2002; 90:29–34

Guyton AC, Hall JE. Textbook of medical physiology. Philadelphia: W.B. Saunders; 1995.

Heiberg E, Sjögren J, Ugander M, Carlsson M, Engblom H, Arheden H, Design and Validation of Segment – a Freely Available Software for Cardiovascular Image Analysis, BMC Medical Imaging, 10:1, 2010.

Igarashi H, Shiraishi H, Endoh H, Yanagisawa M. Left ventricular contractile state in preterm infants: Relation between wall stress and velocity of circumferential fiber shortening. American Herat Journal. 1994; 127: 1336-1340.

Katz J, Milliken MC, Stray-Gundersen J, Buja LM, Parkey RW, Mitchell JH, Peshock RM. Estimation of human myocardial mass with MR imaging. Radiology 1988;169:495–498.

Keller AM, Peshock RM, Malloy CR, Buia LM, Nunnally R, Parkely RW, Willerson JT. In Vivo Measurement of Myocardial Mass Using Nuclear Magnetic Resonance Imaging. JACC. 1986; 8:113-117.

Kozak-Barany A, Jokinen E, Saraste M, Tuominen J, Valimaki I. Development of left ventricular systolic and diastolic function in preterm infants during the first month of life: A prospective follow-up study. J. Pediatr. 2001; 139: 539 – 545.

Laughon M, Bose C, Clark R. Treatment strategies to prevent or close a patent ductus arteriosus in preterm infants and outcomes. J. Perinatol. 2007; 27: 164-170.

Levick JR, An introduction to cardiovascular physiology. Fifth edition. 2010.

Lewandowski AJ, Augustine D, Lamata P, Davis EF, Lazdam M, Francis J, McCormick K, Wilkinson AR, Singhal A, Lucas A, Smith NP, Neubauer S, Leeson P. Preterm heart in adult life cardiovascular magnetic resonance reveals distinct differences in left ventricular mass, geometry, and function. Circ 2013; 127: 197-206.

Lorenz CH, Walker ES, Morgan VL, Klein SS, Graham Jr TP. Normal human right and left ventricular mass, systolic function, and gender differences by cine magnetic resonance imaging. J Cardiovasc Magn Reson 1999; 1: 7–21.

Myerson SG, Bellenger NG, Pennell DJ. Assessment of left ventricular mass by cardiovascular magnetic resonance. Hypertension. 2002; 39: 750 – 755.

Mekkaoui C, Porayette P, Jackowski MP, Kostis W, Dai G, Sanders S, Sosnovik DE. Diffusion MRI tractography of the developing human fetal heart. Proc ISMRM 2013; 0481.

Ramanathan T, Skinner H. Coronary blood flow. Continuing Education in Anaesthesia, Critical Care & Pain. 2005; DOI 10.1093/bjaceaccp/mki012

Price AN, Malik S, Broadhouse KM , Finnemore AE, Durighel G, Cox DJ, Edwards AD, Groves AM, Hajnal JV. Neonatal cardiac MRI using prolonged balanced SSFP imaging at 3T with active frequency stabilization. Magn Reson Med. 2012

Sasi A, Deorari A. Patent ductus arteriosus in preterm infants. Indian Pediatr. 2011; 48: 301 – 308.

Shimada S, Kasai T, Konishi M, Fujiwara T. Effects of patent ductus arteriosus on LVO and organ blood flows in preterm infants with respiratory distress syndrome treated with surfactant. J. Pediatr. 1994; 125(2): 270-277.

Schar M, Kozerke S, Fischer SE, Boesiger P. Cardiac SSFP imaging at 3 tesla. Magn Reson Med 2004;51:799–806.

Scheffler K, Lehnhardt S. Principles and applications of balanced SSFP techniques. Eur Radiol. 2003; 13:2409–2418.

Schmitz L, Stiller B, Koch H, Koehne P, Lange P. Diastolic left ventricular function in preterm infants with a patent ductus arteriosus: a serial Doppler echocardiography study. Early Hum Dev. 2004; 76: 91-100.

Schneider DJ, Moore JW. Patent ductus arteriosus. Circ. 2006; 114: 1873 – 1882.

Schulz-Menger J, Bluemke DA, Bremerich J, Flamm SD, Fogel MA, Friedich MG, Kim RJ, Von Knobelsdorff-Brenkenhoff F, Kramer CM, Pennell DJ, Plein S, Nagel E. Standardized image interpretation and post processing in cardiovascular magnetic resonance: Society for Cardiovascular Magnetic Resonance (SCMR) Board of Trustees Task Force on Standardized Post Processing. J. Cardiovas Magn Reson. 2013; doi:10.1186/1532-429X-15-35-15-35.

Smolich JJ, Ultrastructural and functional features of the developing mammalian heart: a brief overview. Reprod Fertil Dev. 1995; 7(3): 451-61.

Valentinuzzi ME, Kohen AJ. Laplace's Law: What it is about, where it comes from, and how it is often applied in physiology. IEEE PULSE. 2011; 74-81.

Zile MR, Gaasch WH, Carroll JD, Feldman MD, Aurigemma GP, Schaer GL, Ghali JK, Liebson PR. Heart failure with a normal ejection fraction is measurement of diastolic function necessary to make the diagnosis of diastolic heart failure. Circulation 2001; 104:779-782.

Chapter 6

Neonatal Cardiovascular Hemodynamics: 4D PC MRI

In the following chapter 4D PC MRI is utilized to visualize aortic flow patterns in the presence and absence of a PDA. The flow field was observed by generating particle traces and velocity vectors at specific locations along the aorta in preterm infants with and without PDA. Observed neonatal flow characteristics are then compared to previously reported adult data. The limitations and possible future work are then discussed.

6.1 4D PC MRI

6.1.1 Introduction

Two dimensional PC imaging is a fundamental tool in cardiac MRI assessment protocols, used to quantify blood flow and cardiac and valve function (Gatehouse et al. 2005) (Markl et al. 2012a). 4D PC MRI (3 dimensional data with time resolved velocity encoding in all 3 spatial directions) allows retrospective analysis of the hemodynamics of any anatomical location within the entire volume of interest (Markl et al. 2012a). This kind of comprehensive dataset has been utilized to not only quantify blood flow but to visualize the complex 3 dimensional flow patterns present in the extra cardiac vasculature. In addition hemodynamic biomarkers such as pulse wave velocity, wall shear force, pressure gradients and the presence of turbulence have all been analysed (Dyverfeldt et al. 2009) (Frydrychowicz et al. 2009) (Markl et al. 2010). Yet it is only recently that 4D PC MRI has been utilized in the clinical setting. Initiated by early work of Kilner *et al.* 1993, Firmin *et al.* 1993, Buonocore *et al.* 1998 and many others, and the introduction of acceleration techniques, faster post

processing and data analysis tools have aided the translation of 4D PC MRI into the clinical environment.

A 4D PC data set represents the full time resolved blood flow velocity vector field within the acquired cardio-vasculature of interest. The blood flow is characterized by the 3 dimensional velocity vector field via the visualization of particle traces. Particle traces are the 3D time resolved trajectories of a fluid element (massless particle) in the blood flow field over a certain period of time, i.e. the cardiac cycle. Therefore the temporal evolution of the flow field over the averaged multiple cardiac cycles that make up the time resolved 4D PC dataset can be observed (Kilner at al, 2000).

The complex flow patterns within the healthy adult aorta that include the rotational flow in the ascending aorta and arch in late systole have been visualized and well documented (Kilner et al. 1993) (Markl et al. 2004). Studies of the aorta in patients with cardiovascular pathology have found a correlation between abnormal flow patterns and secondary vascular parameters such as wall shear stress. It is thought that these aberrant flow patterns may lead to, or exacerbate cardiovascular disease (Weigang et al. 2008).

Successful translation of 4D PC MRI to the neonatal population would allow a comprehensive study of the cardiovascular flow patterns present in preterm infants and hemodynamic impact of prematurity and the PDA. The flow pattern within the duct can vary over the cardiac cycle due to the varying pressure gradient across the duct from systole to diastole (Skinner, 2001). In addition turbulent blood flow is present at bifurcations and sharp bends within the vasculature (Dyverfeldt et al. 2008). Whether the additional shunt volume, shunt flow pattern and bifurcation of the duct at the inferior wall of the aortic arch creates turbulent flow regimes that disrupt the efficient transport of blood within the aorta is unknown.

Translating standard 4D PC MRI sequences to this population is problematic due to the size of the infant's vessels. This necessity for high spatial resolution to accurately visualize and quantify flow

characteristics leads to long scan times which are unfavourable in this non cooperative population. In addition the use of acceleration techniques is limited owing to the low SNR due to patient size and inability to use contrast enhancement in these fragile infants. Hence the strategy employed in this thesis has been to minimise the likelihood of movement and maximise the available signal via dedicated pre-scan preparation (Merchant et al. 2009) and small receiver coils.

Objectives

The aim of this study was to assess the feasibility of 4D PC MRI to aid the investigation of cardiovascular hemodynamics in preterm infants in the absence and presence of PDA.

6.1.2 Patients and Methods

The study was approved by the North West London Research Ethics Committee (06/Q0406/137) and written informed parental consent was obtained in all cases.

Study cohort

4D PC Cardiac MRI was performed in 9 infants with median (range) gestational age (GA) 26(25^{+3} – 32) weeks, corrected GA (cGA) 32^{+2}(30^{+4} – 36^{+5}) weeks, birth weight 875(560 – 1740) grams and weight at scan 1275(875 – 2065) grams, who were inpatients at Queen Charlotte's and Chelsea and St Thomas' Hospitals. All infants were scanned with acoustic ear protection, pulse oximetry, vector ECG monitoring and without sedation or anaesthesia (Merchant et al. 2009). Seven infants required low flow supplemental oxygen or nasal continuous positive airway pressure via an MR compatible

system but all infants were stable and tolerating full enteral feeds during the scan. None of the infants were mechanically ventilated during the scan.

Acquisition

Scans were performed on a Philips 3T MR Achieva scanner (Best, Netherlands) using a specialised 8 channel pediatric body receive coil for infants above 2kg and a small extremity receive coil for infants below 2kg. 4D PC sequences (retrospective gating, spatial resolution = 1mm isotropic, TR/TE = 5.6/3.1ms and cardiac phases = 20) were aligned sagittal oblique providing full coverage of the aortic arch. Pilot scans of the aorta aligned sagittal oblique and of the ascending and descending aorta aligned in the transverse plane at the level of the pulmonary bifurcation were used to plan the position of the 4D PC MR sequence (figure 6.1.1). The 3 directional velocity encoding was calibrated for the range of ±150cms^{-1} and acquisition time ranged between 7 and 15 minutes depending on size of field of view and heart rate of the infant. To assess agreement between 4D and 2D PC acquisitions, LVO and DAo blood flow were also quantified just above the aortic valve and at the level of the diaphragm with 2 2D PC sequences (spatial resolution = 0.6mm in plane, slice thickness = 4mm, TR/TE = 5.9/3.1ms, VENC = ±120/150ms^{-1} and cardiac phases = 20) (for full details see chapter 4). No undersampling or respiratory compensation techniques were used. The 2D and 4D PC sequences were acquired ~20 minutes apart. Scan parameters are shown in table 6.1.1.

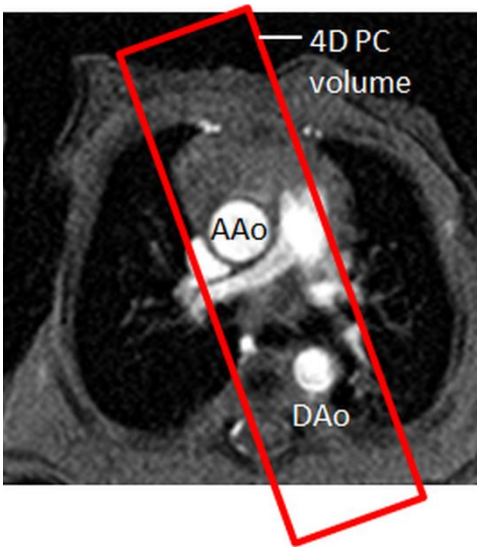

Figure 6.1.1 – Placement of the 4D PC MRI sequence: One of the pilot sequences used to plan the position of the 4D PC MRI sequence aligned in the transverse plane at the level of the pulmonary bifurcation is shown. A schematic of the 4D PC volume is shown in red.

Scan	spatial resolution (mm)	cp	FOV (mm)	TR/TE (ms)	flip angle (degrees)	PE direction	NSA	VENC cm/s	scan duration (mins)
4D PC	1x1x1	20	FH = 80 AP = 80-100 RL = 11-17	5.9/3.1	5	AP/RL	1	150 uniform for all directions	7-15

Table 6.1.1 4D PC MRI scan parameters

Data processing

Firstly the freely available pre-processing software velomap_tool (Bock et al. 2007) was used to generate a pseudo angiogram. The absolute velocity data were weighted with the magnitude image to generate a time resolved 4D PC angiogram. A time independent 3D PC angiogram was then generated from the squared sum of the individual 4D PC angiography datasets to enhance velocity and supress noise within the data (Bock et al. 2007). This was then exported with the 4D PC dataset.

An isosurface volume rendering (a surface of constant value in the 3 dimensional sum of squares velocity field) of the aorta was generated from the 3D PC angiogram using commercially available software (EnSight; CEI, Apex, NC, USA) (figure 6.1.2). This gave a visualization of the vascular morphology within the 3D volume and was used to determine the location of clip planes orthogonal to the aortic lumen for flow quantification and seed regions for pathlines. Using this software it was also possible to unwrap any pixels that had aliased due to the true velocity exceeding the imaging parameter VENC. A small fraction of the lumen was aliased in 2 dataset in the DAo at peak systole, aliased velocity was corrected by manually selecting the aliased pixels and unwrapping them (equation 6.1) (Bock et al. 2007).

$$V_{max} = V_{aliased} - (Sign_{Valiased} * 2 * VENC) \quad (6.1)$$

Where V_{max} is the recovered velocity value and $V_{aliased}$ is the aliased velocity. This is accurate provided V_{max} does not exceed 2*VENC.

The clip planes were exported and flow was then quantified at these locations using a matlab based software tool flow_tool (Stalder et al. 2008), (MathWorks Matlab). The vessel of interest was tracked over all cardiac phases and flow was then calculated at each time point of the cardiac cycle by manual segmentation of the vessel lumen.

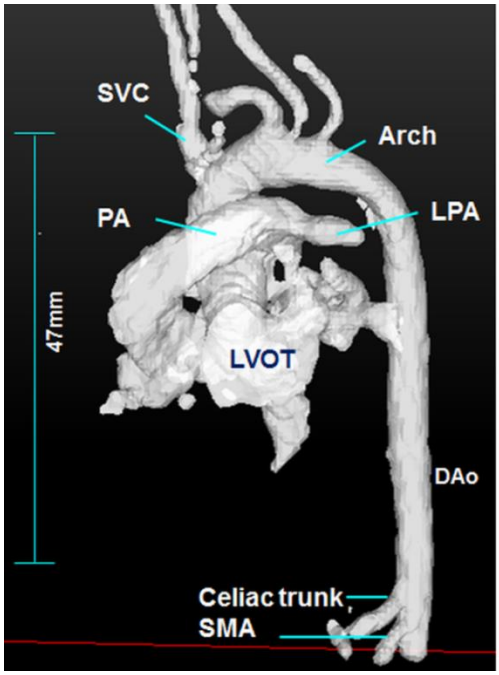

Figure 6.1.2 – Visualization of the cardio vasculature: An iso-volume rendering of the aorta generated from the pseudo sum of squares angiogram in a 1.3 kg infant. The major vessels such as the SVC, PA, LPA, aorta, celiac trunk, SMA and left ventricular outflow tract (LVOT) are clearly visible.

The angiogram depicting vessel morphology and particle traces within the aorta were visualized in all cases. The PDA could be resolved and visualized in the 2 of the 5 PDA infants (P1 and P2). Both these infants had high ductal shunt volumes over 33% of LVO as determined by 2D PC MRI (chapter 4). The duct and ductal flow could not be visualized in the infants with low shunt volume. The work in this chapter focuses on a comparison between a control and 1 of the large ductal shunt volume PDA infants (P1) to compare flow fields in the presence and absence of a PDA. Particle traces of the blood flow field within the control and PDA preterm aorta were visualized within Ensight (EnSight; CEI, Apex, NC, USA). These 2 infants were chosen for the comparison of particle traces due to the closely matched GA and cGA. Vessel morphology and velocity data from the second large shunt volume PDA infant (P2) is presented in the discussion to highlight features of aortic flow in the presence of a PDA.

Seven clip planes were positioned along the aorta, 2 within the ascending aorta (AAo), 3 within the arch and 2 in the DAo (figure 6.1.3 shows the 3 regions where the clip planes where positioned). The

position of each clip plane was determined visually. The vessel lumen was then segmented from the velocity information within the clip plane with a circular region of interest. Five hundred particle traces were then seeded from the 7 circular clip planes during systole and diastole. Velocity vectors at each clip plane were then created to observe flow characteristics at peak systole (the 3rd cardiac phase in these 2 infants). Clip planes were interpolated to provide a reconstructed resolution of 0.25x0.25mm providing 16 velocity vectors per original pixel.

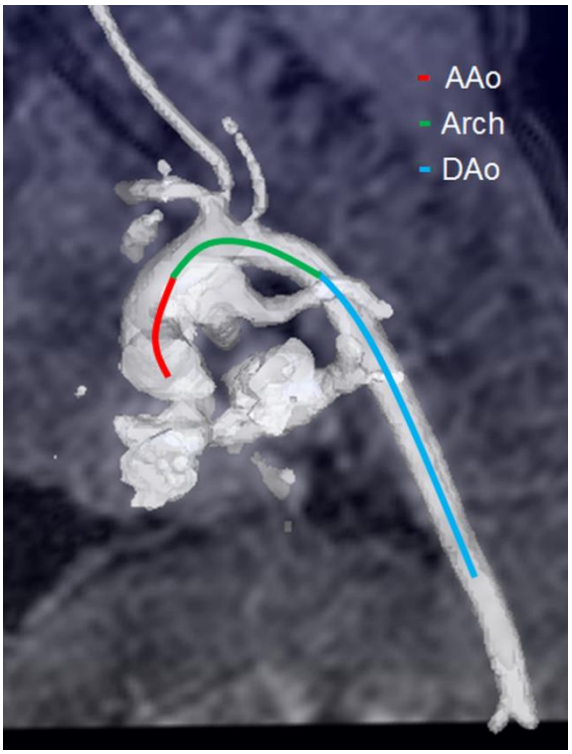

Figure 6.1.3 – Analysis regions along the aorta: AAo (red), arch (green) and DAo (blue) regions of the aorta are visually defined from the isosurface-volume rendering of the sum of squares of the velocity data in a 1.6kg infant. The aorta is shown against the anatomical magnitude data where the diaphragm and spine can clearly be depicted.

Statistical analysis

Blood flow was quantified in the ascending aorta just above the aortic valve in the left ventricular outflow tract and in the DAo at the level of the diaphragm (figure 6.1.4) from 2D and 4D PC

sequences. Bland-Altman analysis was carried out to assess agreement between LVO and DAo blood flow quantified from 2D and 4D PC sequences. Mean difference, loa and normalized loa (loa/mean of measures) were calculated.

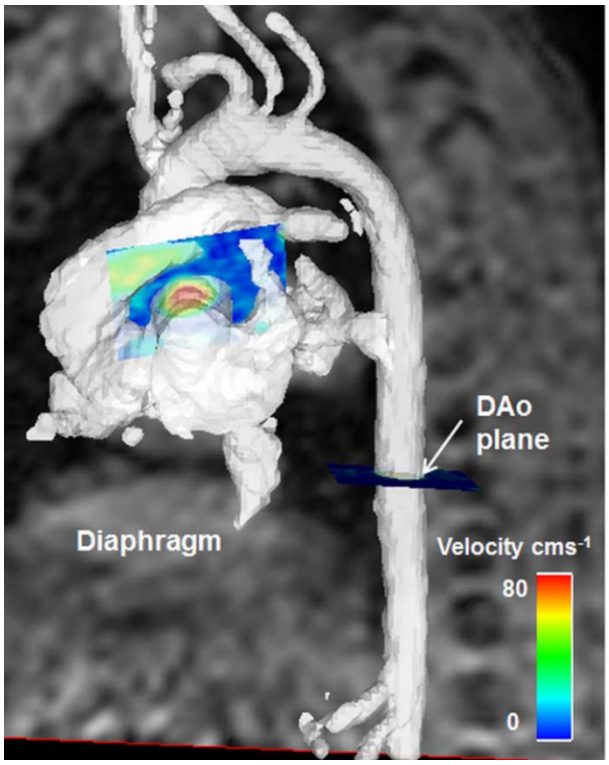

Figure 6.1.4 – 4D Flow quantification: The location of the clip planes to quantify blood flow in the ascending aorta just above the LVOT and in the DAo at the level of the diaphragm are shown in relation to the angiogram in Ensight (EnSight; CEI, Apex, NC, USA).

6.1.3 Results

4D datasets were acquired in 9 preterm and term infants with median (range) GA 26^{+3}(25^{+3} – 32) weeks, cGA 32(30^{+4} – 36^{+5}) weeks, birth weight 895(680 – 1740) grams and weight at scan 1330(875 – 2065) grams. 5 infants had PDA confirmed by echo and shunt volumes ranged from 12.1 – 52.7% of LVO (quantified by PC MRI, see chapter 4) as shown in table 6.1.2.

GA	cGA	BW grams	Wt at scan grams	PDA % of LVO
27^{+2}	31^{+6}	895	1215	12.1
25^{+3}	30^{+4}	850	875	15.4
26^{+3}	32	1000	1430	15.9
24^{+6}	31^{+1}	720	1130	43.5
25^{+4}	31^{+6}	680	1125	52.7

Table 6.1.2 – PDA infants: GA, cGA, birth weight (BW), weight (Wt) at scan and ductal shunt volume as a % of LVO in 4 infants with PDA.

Comparison of 2D vs 4D PC flow measurements

Due to subject unrest the DAo 2D PC sequences was not acquired in 1 infant as the MR exam was ended early. Therefore Bland-Altman variability analysis between 2D and 4D PC sequences was carried out in 9 LVO and 8 DAo measurements. Both showed good agreement (figure 6.1.5). Table 6.1.3 shows the mean flow, loa normalized loa and mean difference in ml/min and as a % of LVO and DAo measures. Bland-Altman analysis of heart rate (HR) measurements between the 4D and 2 2D LVO and DAo sequences are also shown to demonstrate the physiological variation between scans.

	mean	loa	Norm loa	mean difference	mean difference %
LVO ml/min	420	-36.7 – 79.7	13.9	21.5	5.1
DAo ml/min	212	-42.1 – 40.6	19.5	-0.8	-0.4
HR LVO bpm	158	2 – 13	3	8	5
HR DAo bpm	159	-9 - 21	9	6	4

Table 6.1.3 – Bland-Altman analysis: Mean, loa, normalized loa and mean difference values from Bland-Altman analysis of 2D and 4D PC LVO and DAo flow measurements. Bland-Altman analysis was also carried out on the HR measurements from the 4D and 2 2D scans. HR LVO represents the comparison between the single 4D and LVO 2D scans; HR DAo represents the comparison between the single 4D and DAo 2D scans.

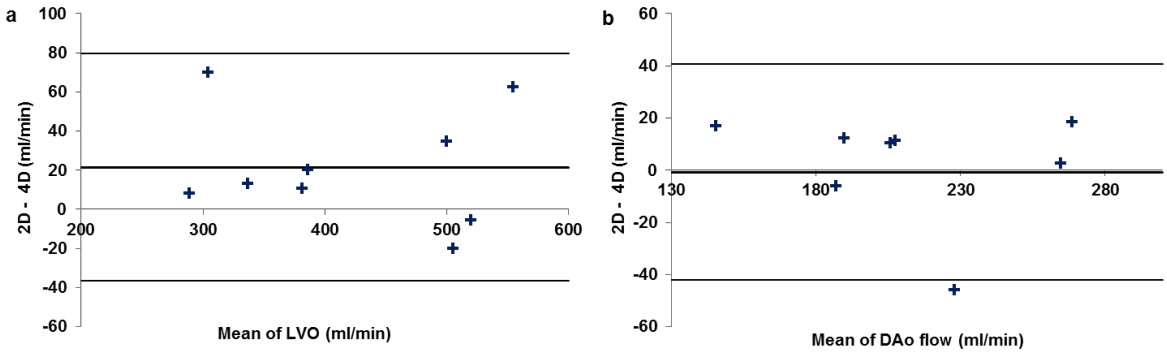

Figure 6.1.5 – Agreement between 4D and 2D PC flow measurements: Bland-Altman analysis between a: LVO and b: DAo flow measures from 2D and 4D PC acquisitions. Black lines denote the mean difference and loa.

Aortic hemodynamics: visualization of flow patterns

Aortic flow characteristics were visualized in an infant with a large ductal shunt volume (43.5% of LVO as determined by 2D PC MRI, chapter 4) and a control infant to compare blood flow characteristics in the presence and absence of PDA. GA 25^{+3}, 24^{+6} weeks, cGA 30^{+4}, 31^{+1} weeks, birth weight 805, 720 grams and weight at scan 960, 1130 grams respectively. The PDA infant was due for surgical ligation that was carried out 1 day after the MRI scan. However, at the time of scan upper and lower body flow remained within the normal range established in chapter 4. The control infant was chosen for the comparison due to the closely matched GA and cGA.

Particle traces were determined to depict the aortic blood flow field in the control (Figure 6.1.6a) and PDA infant (P1) (figure 6.1.6b) at peak systole (40 – 80ms after the R wave). In both cases the aorta has been rotated around the head-foot axis to view the flow field from 4 angles and aid visualization. Peak velocity within the aorta is seen to be slightly higher in the PDA infant. In figure 6.1.6b low left to right shunting through the PDA during peak systole can be visualized.

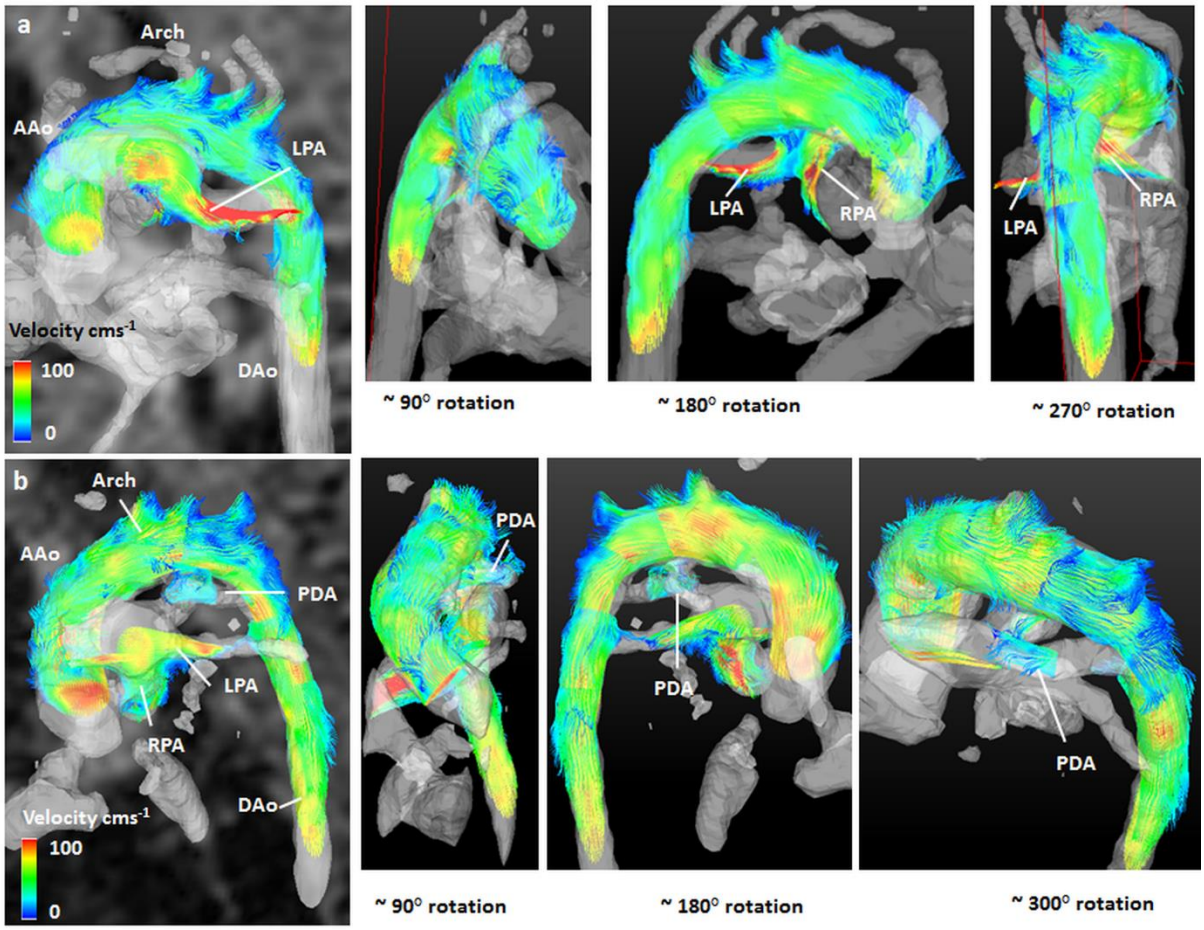

Figure 6.1.6 – Aortic blood flow field: The aorta and pulmonary vessels are shown with the aid of the angiogram. Particle traces seeded from 7 locations along the arch and within the pulmonary trunk allow visualisation of the cradiovacular blood flow field during peak systole (40-80ms of cardiac cycle) in a: a control infants and b: in P1 PDA infant. the colour of the particle traces signifies the velocity. In both cases the arch has been rotated around the head- foot axis to allow visualization of the 3 dimensional flow field within the aorta and RPA and LPA. The PDA is very tortuous and leaves the aorta in the proximal DAo. There is low left to right shunting through the PDA durring peak systole.

Particle traces were then seeded from the same locations as before during diastole (200 – 240ms after the R wave) in the PDA infant. Three views are shown to depict the tortuous morphology of the duct (figure 6.1.6b). Particle traces were seen to flow from the aortic arch into the duct (figure 6.1.7) indicating that preferential steal through the duct is from the arch and not the descending aorta in this particular PDA infant. Flow within the ascending aorta is shown to be slow and non-laminar in mid diastole. A helical rotational flow pattern within the right pulmonary artery can be seen during diastole.

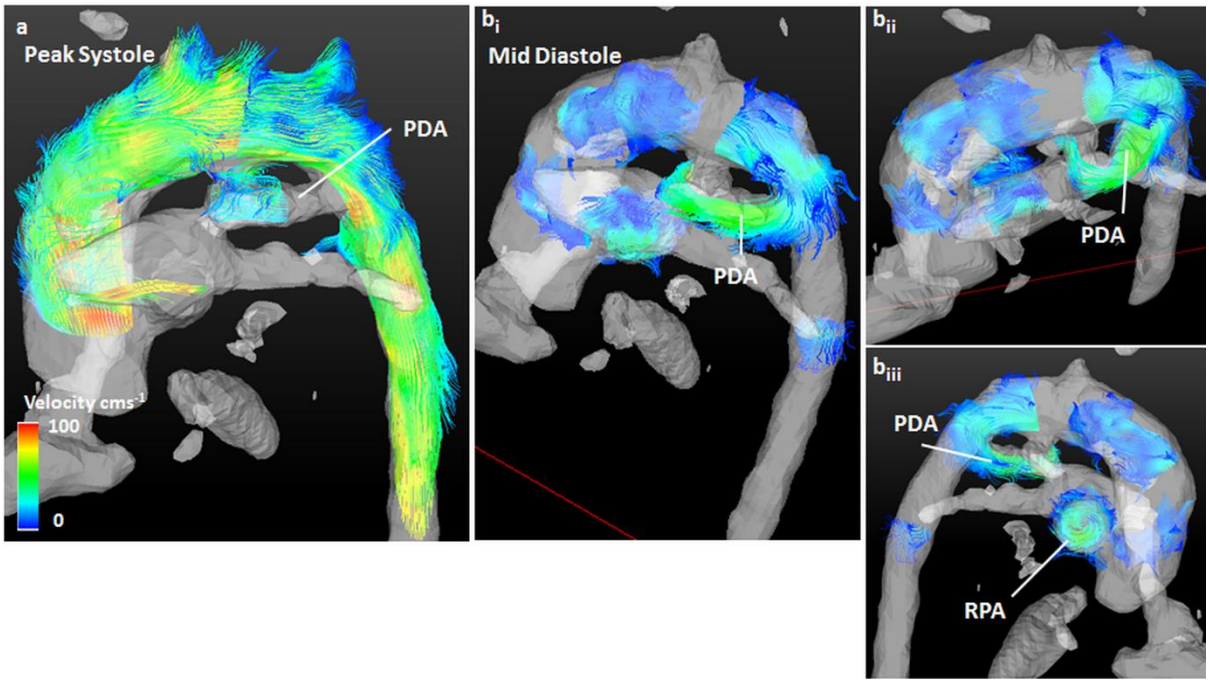

Figure 6.1.7 – Visualization of a ductal shunt: the angiogram displays the aorta and pulmonary vessels. Aortic and pulmonary blood flow during a: systole and b: diastole is visualized with Particle traces, the colour signifies the velocity of each particle trace. Low left to right shunting through the duct is apparent during systole. During diastole chaotic, slow flow is visible throughout the AAo and arch, however particle traces can clearly be seen flowing from the aortic arch and into the duct at the proximal DAo. This is expected as the decrease in right ventricular pressure during diastole maximizes the pressure gradient across the duct, facilitating ductal blood flow. Again the aorta has been rotated about the z axis to allow visualization of the 3 dimensional flow patterns. bii: The tortuous morphology of the duct can be seen. biii: Rotational flow is observed in the RPA.

Nature of flow patterns: comparison between and control and PDA infant

3D blood flow characteristic within the aorta are thought to be strong indicators for the cardiovascular health of adult individuals (Lorenz et al. 2012) (Morbiducci et al. 2011). Through particle traces the time resolved trajectories of a massless particle in the blood flow field can be visualized. As this is the temporal evolution of the entire flow field over time the spatially varying characteristics of flow across the lumen can be difficult to assess. From visualization of velocity vectors produced at the 7 clip plane locations at peak systole (3rd cardiac cycle in these 2 infants) peak flow characteristics within the AAo, arch and DAo could be observed.

Figures 6.1.8a/b show the location of the clip planes and corresponding velocity vectors for the peak systolic cardiac phase in the 2 previous control and PDA infants. Two clip planes lie within the AAo, 3 within the arch and 2 within the DAo in both infants. Velocity vector images (figure 6.1.8 aii-aviii and bii-bviii) are orientated with the subject head-foot direction along the vertical axis from top to bottom and the subject left-right running along the horizontal axis left to right. Direction of flow is then directed out of the page so that the observer is looking back along the aorta towards the LVO. The colour and length of the velocity vectors depict the magnitude of the speed of flow at this 1 particular time point within the cardiac cycle. Velocity vectors were visualized in all 9 infants in this manner, data from the further 7 infants are shown in the supplementary material in the appendix 6.1.

The velocity field within the proximal AAo (figure 6.1.8 a/b ii) appears somewhat laminar with faster flow within the centre of the lumen in both infants. The velocity field in the distal AAo (a/b iii) is marginally chaotic as the beginning of rotational flow forms. The velocity field within the arch (a/b iv – vi) shows a clockwise (with respect to the direction of flow) helical flow pattern (a corkscrew-like motion along the principal direction of flow) in both the PDA and control infant. In the control infant the fastest leading edge of the helical flow pattern is at the superior wall of the arch. This leading fast outside flow then rotates around to the inferior wall of the aorta by the proximal DAo (avii), becoming more laminar at the distal DAo (a viii). This helical flow appears to rotate faster in the PDA infant, with the leading edge rotating from the superior wall to inferior wall of the aorta within the length of the arch (b iv – vi) becoming more laminar in the proximal DAo (b vii).

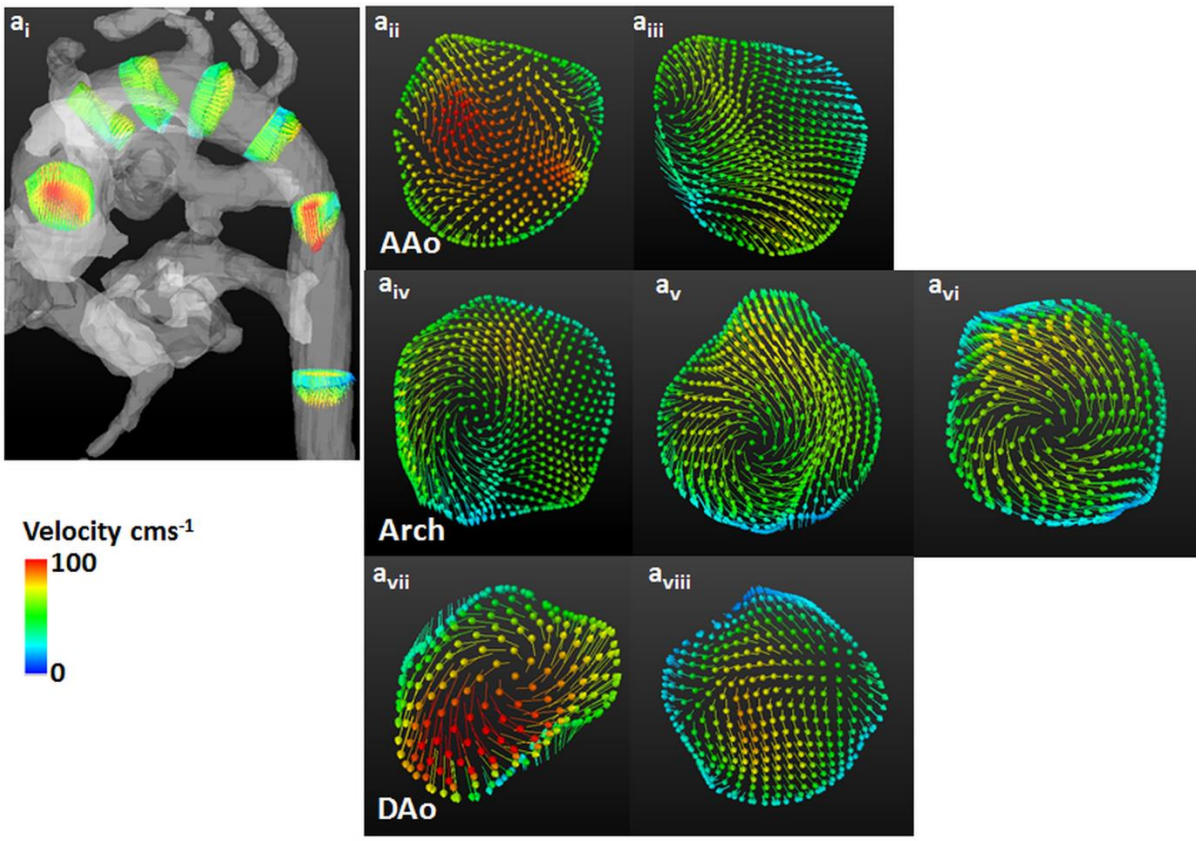

Figure 6.1.8a – Flow patterns within a healthy preterm infant: ai: the location of the 7 circular regions of interest are shown on the angiogram, 2 reside within the AAo, 3 within the arch and 2 within the DAo. Velocity vectors of aortic blood flow (speed is represented by colour and length), were generated at each region of interest at peak systole (the 3rd cardiac phase). Velocity vectors are then shown in order of location along the aorta, with the left of each image corresponding to the left of the infant. aii-aiii: flow within the AAo appears slightly chaotic. aiv-avi: a clockwise helical flow pattern is visible within the aortic arch. avii-aviii: this rotational flow pattern continues to the proximal DAo and then becomes laminar.

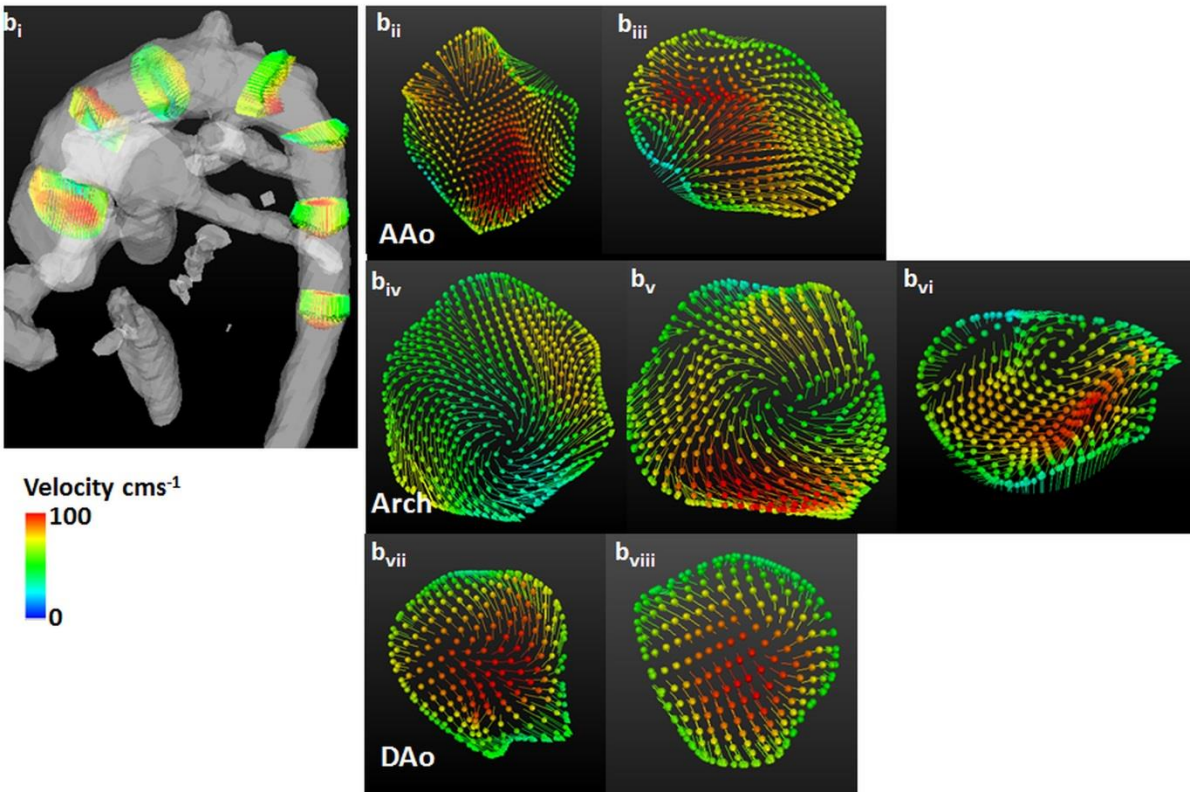

Figure 6.1.8b – Flow patterns within a preterm infant with PDA (P1): bi: the location of the 7 circular regions of interest are shown on the angiogram, again 2 reside within the AAo, 3 within the arch and 2 within the DAo. Velocity vectors of aortic blood flow were generated at each region of interest at peak systole (the 3rd cardiac phase). Velocity vectors are then shown in order of location along the aorta, with the left of each image corresponding to the left of the infant. Velocity vectors appear very similar to those within the aorta of the control infant. bii-biii: flow within the AAo appears faster and more chaotic compared to the control infant. aiv-avi: again a clockwise helical flow pattern is visible within the aortic arch. avii-aviii: this rotational flow becomes laminar within the DAo.

Previously reported adult aortic flow patterns: comparison between adults and neonates

Helical flow within the aorta is an important flow pattern that is considered to be a normal feature in healthy adult subjects (Kilner et al. 1993) (Lorenz et al. 2012) (Morbiducci et al. 2011). It is thought that aortic helical flow is a result of optimized blood flow for efficient perfusion that facilitates left ventricular ejection (Morbiducci et al. 2011). The 3 dimensional curvature of the arch and ventricular twisting and torsion during contraction contribute to generate the aortic helical flow patterns (Baciewiez et al. 1991) (Morbiducci et al. 2009). Aberrant aortic flow patterns are thought to be correlated to cardiovascular disease (Lorentz et al. 2012) (Weigang et al. 2008).

Qualitative studies visualizing particle traces from 4D PC MR acquisitions have shown the presence of helical flow within the aortic arch (Bogren et al. 1999) (Buonocore et al. 1999) (Frydrychowicz et al. 2007). Quantitative studies of global helical flow and helicity quantification in 2D planes orthogonal to the aortic lumen have investigated the extent of helical flow within the healthy aorta (Lorenz et al. 2011) (Morbiducci et al. 2009, 2011). It was shown that helical flow increases in patients with aortic or cardiovascular disease (Lorenz et al. 2012).

In a study of 12 healthy patients Lorentz et al. 2011 showed a consistent direction of rotation over the entire aorta with high clockwise helicity (with respect to direction of flow) within the aortic arch (Lorentz et al. 2011). In both infants a clockwise helical flow pattern is present within the aortic arch at peak systole. Further quantitative analysis is needed to assess the helicity over the entire cardiac cycle and aorta. Yet the initial data suggests that the helical flow patterns within the healthy adult aorta are present in these 2 individual preterm infants.

6.1.4 Discussion

The complex flow patterns within the healthy adult aorta have been visualized and well documented (Kilner et al. 1993) (Markl et al. 2004). Partly due to their size, fragile state and lack of patient cooperation acquiring 4D PC MR data in the preterm cohort is challenging and consequently data does not extend back to this population. 4D PC MRI sequences with adequate spatial and temporal resolution would allow a comprehensive study of the cardiovascular flow patterns present in preterm infants and hemodynamic impact of prematurity and the PDA. A recent 4D PC study to visualize the intra-cardiac flow patterns in preterm and term infants was carried out by Groves *et al.* 2012, however the 2.5mm isotropic acquired spatial resolution was suboptimal to visualize and quantify extra-cardiac flow patterns. This sequence was optimized to provide adequate spatial resolution to assess aortic flow within these small infants in this study. In this initial study 4D PC MRI

data was acquired in 9 preterm infants allowing a group wise comparison with 2D flow methods as well as visualising flow patterns. Data from a control and PDA (P1) preterm infant were presented in detail for a visual comparison between groups. Aortic blood flow patterns were investigated with the visualization of particle traces and velocity vectors from the 3D velocity field information.

Comparison of 2D and 4D flow measurements

Although 4D PC MRI is well documented in adults and to some extent in paediatrics (Markl et al. 2012b) (Roes et al. 2009), (Valverde et al. 2010) validation data does not extend back to the neonatal population. Bland-Altman analysis was therefore carried out to assess agreement between 2D and 4D PC flow measurements in this small challenging cohort. Good agreement was found between 2D and 4D PC LVO flow measurements (normalized loa 13.9%, mean bias 21.5 ml/min and loa -36.7 - +79.7 ml/min). This variability was only marginally higher than that seen in measurements of heart rate during the acquisitions (table 6.1.2), suggesting that a significant proportion of the variability seen in flow quantification may be related to genuine physiological variation as opposed to measurement error.

Reasonably good agreement was found between 2D and 4D DAo flow measurements (normalized loa 19.5%, mean bias -0.8 ml/min and loa -42.1 - +40.6 ml/min). The aortic diameter at the DAo measurement plane is smaller than at the LVO. The reduced agreement between the 2D and 4D DAo flow measurements could indicate the limitations of the 1mm spatial resolution when quantifying flow at this location. However, abdominal flow is known to vary according to food intake (Cranger et al. 1980). The feed and wrap technique used to settle the infants prior to the scan and the time between 2D and 4D PC acquisitions (~20 minutes) may give rise to physiological variation in lower body flow. Studies have shown that DAo blood flow increases by 30% at 20 minutes after feeding (Wieben et al. 2013), this may partly explain the difference in LVO and DAo agreement.

Particle traces: visualization of PDA

The blood flow fields within the aorta of a control and PDA infant were then visualized by generating particle traces, the 3D time resolved trajectories of a fluid element (massless particle) in the blood flow field 40 - 80ms after the R wave. When compared to the control infants, despite the low left to right shunting no disruption of aortic flow during peak systole was observed. Diastolic particle traces revealed fast flow through the duct from the aortic arch. The decrease in right ventricular pressure during diastole maximizes the gradient between pulmonary and systemic pressure across the duct, facilitating ductal blood flow. Particle traces in diastole depicted the blood flowing from the aortic arch into the duct (figure 6.1.7) indicating that preferential steal through the duct is from the arch and not the descending aorta in this particular PDA infant. Faster flow is observed at the superior, outer edge of the proximal arch just before the brachiocephalic artery. Upper and lower body flow measured from 2D PC MRI was within the normal range for this infant. The morphology of the arch and helical flow patterns ensures that the faster flowing blood supplies the upper body. The pressure gradient dependency and aortic location of the duct in this individual infant assists the preservation of upper body flow. Although blood is seen to flow from the arch (no reversal of diastolic flow was observed in the DAo in either 4D or 2D analysis), this steal of systemic blood flow and preferential shunting of faster flowing blood to the upper body may reduce the continuous flow seen during diastole in peripheral lower body vasculature.

Visualization of the duct and ductal flow is possible with 4D PC MRI. However, occasionally the particle traces are unable to depict or follow the entire course of the duct and ductal flow due to the turbulent nature of the blood flow through the PDA. Particle traces were shown to flow from left to right within the duct, yet no traces could be visualized leaving the aorta and entering the duct during systole (figure 6.1.6). The measured velocity within a voxel is the mean of the intravoxel spin velocities. The multiple spin velocities present in turbulent regimes reduces the magnitude of the complex signal and therefore leads to a signal loss (Dyverfeldt et al. 2008) (Oshinski et al. 1995).

Figure 6.1.9 shows the signal loss in the aorta near the insertion of the duct in the PDA infant (P1)presented above, this was also apparent in the analysis of second PDA (P2) infant with shunt volume of 52.7% of LVO (figure 6.1.10/11). This signal loss results in an artefact in the Philips reconstructed phase difference dataset. By increasing spatial resolution this artefact can be minimized. The phase information can be recovered from the raw data; however accurate reconstruction of the phase difference dataset can be problematic. Background phase errors are compensated for within the reconstruction, hence the phase difference image is not just the simple subtraction of the 2 velocity encoded datasets. Consequently although raw data was retained and attempts were made at dedicated reconstructions to recover the flow information in these aorta-PDA branching regions, it did not prove possible to achieve a reliable estimation of the flow.

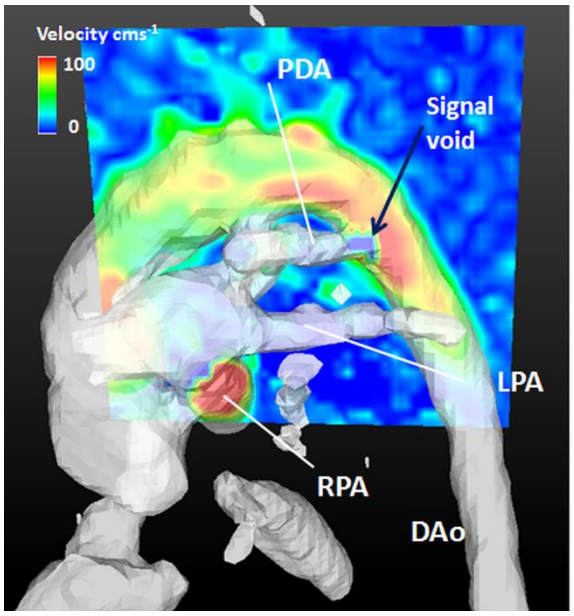

Figure 6.1.9 – Turbulence: The angiogram shows the aorta, duct and pulmonary arteries in the P1 PDA infant. A clip plane dissecting the mid line of the aorta shows the velocity information along the aorta at peak systole. The point of the ductal insertion within the aorta can be seen as a region of zero velocity. Particle traces cannot be visualized leaving the aorta and entering the duct during systole due to this reconstruction artefact.

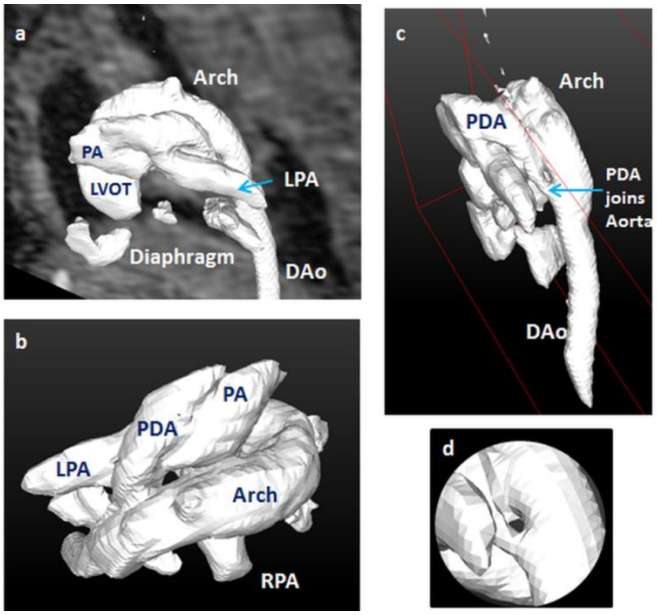

Figure 6.1.10 – Vessel morphology: The PDA and great vessels can be observed from the angiogram in the P2 PDA infant (a, b and c). shunt volume was found to be 52.7% of LVO as determined by 2D PC MRI (chapter 4). Restriction of the duct can be seen at the proximal to the aorta (d).

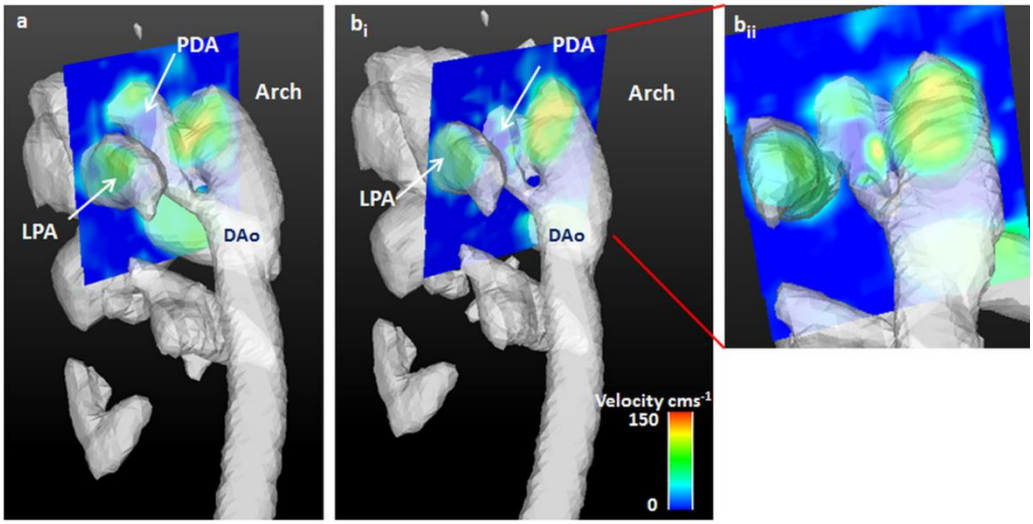

Figure 6.1.11 – Chaotic flow within the duct: The angiogram shows the aorta, duct and LPA in the P2 PDA infant. A clip plane dissecting the duct shows the velocity within the 3 vessels. a: visualization of the velocity within the duct distal to the duct-aorta insertion remains intact. bi: proximal to the junction flow becomes turbulent and bii: regions of zero velocity (dark blue) within the duct are visible.

The 2 infants with large PDA shunt volumes (table 6.1.1, figure 6.1.7/9/10/11) can be depicted. However, it was not possible to visualize the ductus arteriosus vessel and ductal shunting in the 3 infants with low shunt volumes (<16% of LVO). Shunt volume is significantly associated with ductal diameter (chapter 4); all 3 infants had ductal diameter of less than 1mm as determined by echo, higher spatial resolution is required to resolve the PDA infants with low shunt volumes.

Aortic flow patterns in the presence and absence of PDA

From visualization of the velocity vector field within the ascending aorta, arch and descending aorta at peak systole indicated a clockwise helical flow pattern within the arch, developing into laminar flow within the DAo in both the control and PDA infant. It has been suggested that rotational flow within the adult aorta preserves momentum around the arch and leads to more efficient blood flow. It is the 3 dimensional curvature of the arch and ventricular twisting and torsion during contraction that are considered to contribute to the generation of aortic helical flow patterns (Baciewiez et al. 1991) (Morbiducci et al. 2009). Aberrant flow patterns within the aorta have been correlated with cardiovascular pathology and are thought to exacerbate cardiovascular disease. Lorenz et al. 2011, calculated a normalized helicity (equation 6.2) on a pixel wise basis, providing information of direction and intensity of helical flow over the cardiac cycle and showed a consistent direction of rotational flow over the entire aorta with high clockwise helicity within the aortic arch in healthy adults.

$$\text{Normalized helicity} = \frac{\bar{v} \cdot \bar{\omega}}{|\bar{v}| \cdot |\bar{\omega}|} \qquad (6.2)$$

Where $\bar{v}$ is the velocity vector and $\bar{\omega}$ the vorticity vector, resulting in values between -1 (counter clockwise rotation) and +1 (clockwise rotation).

When assessing flow patterns in patients with cardiovascular disease, an increase in helicity was seen (Lorenz et al. 2012) (Morbiducci et al. 2011), the significance of this is still unclear. It is thought that in adults large velocity fluctuations in flow lead to increased wall shear stress and expose endothelial cells and blood constituents to abnormal stresses that increase the risk of hemolysis (Sallam et al. 1984), platelet activation and thrombus formation (Becker et al. 2001) (Dyverfeldt et al. 2008).

Although there is clearly chaotic flow within the aorta at the site of the PDA bifurcation and ductus arteriosus itself (P1 and P2, figure 6.1.9, 6.1.11), this did not appear to disrupt the flow directly above or below the duct (figure 6.1.8b). In both infants a clockwise helical flow pattern was present within the arch at peak systole. However, the nature of this helical flow pattern was not quantified over the cardiac cycle due to the current limitations of the tools available in this study. In addition more work is needed to determine whether the current spatial resolution is adequate to quantify helical flow patterns. Initial data suggests however, that the helical flow patterns within the healthy adult aorta are present in these 2 individual preterm infants. A clockwise helical flow pattern within the arch was visible to varying extents in all infants within this study (appendix 6.1). Whether this rotational flow pattern is present in all preterm and term infants, if the absence of this flow pattern is associated with turbulence, decreased cardiac function and perfusion is unknown and a subject for future work.

A recent study was carried out to calculate the energy loss in the presence of aberrant aortic flow patterns in aortic valve disease patients (Barker et al. 2013). The disruption of aortic flow leads to an increase in left ventricular afterload. The 3 dimensional velocity field was used to calculate the viscous energy loss along particle traces seeded from the AAo, the extra work or left ventricular afterload was then quantified. Abnormal, high helical flow patterns in patients lead to an increase in energy loss when compared to controls, indicating that inefficient flow increases the work load of the left ventricle (Barker et al. 2013). The quantification of energy loss along the aorta in the

presence and absence of PDA would improve understanding of the impact of PDA on cardiac work load. This area of study and possibility of future work is discussed further in chapter 8.

Current limitations

It is thought that the accurate quantification of rotational flow patterns such as helicity and secondary vascular parameters such as wall shear stress require higher spatial resolution than flow measurements (Lorenz et al. 2012) (Markl et al. 2011) (Stalder et al. 2008). The long scan times that arise from this necessity for high spatial resolution to accurately visualize and quantify flow characteristics is problematic in the neonatal population as patient cooperation is not viable. Furthermore the use of acceleration techniques is limited owing to the low SNR due to patient size and inability to use contrast enhancement in these fragile infants. Future progress may include the use of dedicated preterm MR scanners and coils to increase SNR to facilitate acceleration techniques in this cohort.

6.1.5 Conclusion

In this initial study, the feasibility of 4D PC MRI to aid the investigation of cardiovascular hemodynamics in preterm infants was assessed. To the author's knowledge this is the first 4D PC MRI study to visualize the 3 dimensional aortic flow patterns in preterm infants with and without PDA. Although unsurprising, it was reassuring that there was substantial agreement between 2D and volumetric methods and this provided an effective link between this pilot study and the rest of the work in the thesis (chapter 7). Visualization of the particle traces depicting systolic flow did not appear to be disrupted in the presence of a PDA. This was further indicated from the velocity vectors demonstrating that the clockwise helical flow within the aortic arch in the control infant was also present in the PDA infant. The aortic flow regime is further examined in chapter 7. Initial data

suggests that quantification of blood flow volumes and visualization of flow fields from 4D PC MRI is feasible in preterm and term infants. However, higher spatial resolution is potentially required to not only visualize but fully quantify the hemodynamic impact of high and low ductal shunt volumes.

6.2 References

Baker AJ, Bandi KC, Garcia J, Van Ooli P, McCarthy P, Carr J, Malaisrie SC, Markl M. A direct calculation of hemodynamic energy loss in the presence of abnormal aortic flow. Proc ISMRM 2013; 0062.

Becker RC, Eisenberg P, Turpie AG. Pathobiologic features and prevention of thrombotic complications associated with prosthetic heart valves: fundamental principles and the contribution of platelets and thrombin. Am Heart J 2001; 141: 1025–1037.

Baciewiez FA, Penney DG, Marinelli WA, Marinelli R. Torsional ventricular motion and rotary blood flow. What is the clinical significance. Cardiac Chronicle. 1991; 5: 1 – 8.

Bock J, Kreher BW, Hennig J, Markl M. Optimized pre-processing of time-resolved 2D and 3D Phase Contrast MRI data. ISMRM proc 2007.

Bogren HG, Buonocore MH. 4D magnetic resonance velocity mapping of blood flow patterns in the aorta in young vs elderly normal subjects. Econ Lett. 1999; 10: 861 – 869.

Buonocore MH. Visualizing blood flow patterns using streamlines, arrows, and particle paths. Magn Reson Med. 1998; 40: 210–226.

Buonocore MH, Bogren HG. Analysis of flow patterns using MRI. Intt J Card Imaging. 1999; 15: 99 – 103.

Cranger DN, Richardson PDI, Kveitys PR, Mortillaro NA. Intestinal blood flow. Castroenterology 1980; 78: 837-863.

Dyverfeldt P, Kvitting JPE, Sigfridsson A, Engvall J, Bolger AF, MD, Ebbers T. Assessment of fluctuating velocities in disturbed cardiovascular blood flow: In vivo feasibility of generalized phase-contrast MRI. J. Mag Reson Imag. 2008; 28: 655 – 663.

Dyverfeldt P, Gardhagen R, Sigfridsson A, Karlsson M, Ebbers T. On MRI turbulence quantification. Magn Reson Imaging. 2009; 27:913–922.

Firmin DN, Gatehouse PD, Konrad JP, Yang GZ, Kilner PJ, Longmore DB. Rapid 7-dimensional imaging of pulsatile flow. Comput Cardiol IEEE Comput Soc Lond 1993; 14:353–356.

Frydrychowicz A, Stalder AF, Russe MF, et al. Three-dimensional analysis of segmental wall shear stress in the aorta by flow-sensitive four-dimensional-MRI. J Magn Reson Imaging. 2009; 30:77–84.

Gatehouse PG, Keegan J, Crowe LA, Masood S, Mohiaddin RH, Kreitner KF, Firmin DA. Applications of phase-contrast flow and velocity imaging in cardiovascular MRI. Eur Radiol. 2005; 15: 2172–2184.

Groves AM, Durighel G, Finnemore A, Tusor N, Merchant N, Razavi R, Hajnal JV, Edwards AD. Disruption of intracardiac flow patterns in the newborn infant: Pediatr Res. 2012; 71: 380 – 385.

Kilner PJ, Yang GZ, Mohiaddin RH, Firmin DN, Longmore DB. Helical and retrograde secondary flow patterns in the aortic arch studied by three-directional magnetic resonance velocity mapping. Circ. 1993; 88(5 Pt 1):2235–2247.

Lorenz R, Bock J, Korvink JG, Markl M. Normal distribution on blood flow helicity in the healthy aorta. Proc. Intl. Soc. Mag. Reson. Med. 2011; #3412

Lorenz R, Bock J, Barker AJ, Von Knobelsdorff-Brenkenhoff F, Korvink JG, Markl M. 4D flow MRI in aortic valve disease demonstrates altered distribution of aortic blood flow helicity. Proc. Intl. Soc. Mag. Reson. Med. 2012; #0020.

Kilner PJ, Yang GZ, Wilkes AJ, Mohiaddin RH, Firmin DN, Yacoub MH. Asymmetric redirection of flow through the heart. Nature. 2000; 404:759–761.

Markl M, Draney MT, Hope MD, et al. Time-resolved 3-dimensional velocity mapping in the thoracic aorta: visualization of 3- directional blood flow patterns in healthy volunteers and patients. J Comput Assist Tomogr. 2004; 28:459–468.

Markl M, Wallis W, Brendecke S, Simon J, Frydrychowicz A, Harloff A. Estimation of global aortic pulse wave velocity by flow-sensitive 4D MRI. Magn Reson Med. 2010; 63:1575–1582.

Markl M, Wallis W, Harloff A. Reproducibility of flow and wall shear stress analysis using flow-sensitive four-dimensional MRI. J. Magn Reson Imag. 2011; 4: 988 – 994.

Markl M, Frydrychowicz A, Kozerke S, Hope M, Wieben O. 4D flow MRI. J. MRM. 2012a; 36: 1015-1036.

Markl M, Wallis W, Strecker C, Gladstone BP, Vach W, Harloff A. Analysis of pulse wave velocity in the thoracic aorta by flow-sensitive four-dimensional MRI: Reproducibility and correlation with characteristics in patients with aortic atherosclerosis. J. Magn. Reson. Imaging 2012b.

Merchant N, Groves A, Larkman DJ, Counsell SJ, Thomson MA, Doria V, Groppo M, Arichi T, Foreman S, Herlihy DJ, Hajnal JV, Srinivasan L, Foran A, Rutherford M, Edwards AD, Boardman JP. A patient care system for early 3.0Tesla magnetic resonance imaging of very low birth weight infants. Early Hum Dev. 2009; 85: 779-83.

Morbiducci U, Ponzini R, Rizzo G, Cadioli M, Esposito A, De Cobelli F, Del Maschio A, Montevecchi FM, Redaelli A. In vivo quantification of helical blood flow in human aorta by time-resolved three-dimensional cine phase contrast magnetic resonance imaging. Annals of Biomed Eng. 2009; 37: 516 – 531.

Morbiducci U, Ponzini R, Rizzo G, Cadioli M, Esposito A, Montevecchi FM, Redaelli A. Mechanistic insight into the physiological relevance of helical blood flow in the human aorta: an in vivo study. Biomech Model Mechanobiol. 2011; 10: 339 – 355.

Oshinski JN, Ku DN, Pettigrew RI. Turbulent fluctuation velocity: the most significant determinant of signal loss in stenotic vessels. Magn Reson Med. 1995; 33: 193–199.

Roes SD, Hammer S, van der Geest RJ, et al. Flow assessment through four heart valves simultaneously using 3-dimensional 3-directional velocity-encoded magnetic resonance imaging with retrospective valve tracking in healthy volunteers and patients with valvular regurgitation. Invest Radiol. 2009; 44: 669–675.

Sasi A, Deorari A. Patent ductus arteriosus in preterm infants. Indian Pediatr. 2011; 48: 301 – 308.

Skinner J. Diagnosis of Patent Ductus Arteriosus. Semin Neonatol. 2001; 6: 49-61.

Stalder AF, Russe MF, Frydrychowicz A, Bock J. Hennig J, Markl M. Quantitative 2D and 3D Phase Contrast MRI: Optimized analysis of blood flow and vessel wall parameters. Magn Reson Med. 2008; 60: 218–1231.

Valverde I, Simpson J, Schaeffter T, Beerbaum P. 4D phase-contrast flow cardiovascular magnetic resonance: comprehensive quantification and visualization of flow dynamics in atrial septal defect and partial anomalous pulmonary venous return. Pediatr Cardiol. 2010; 31:1244–1248.

Weigang E, Kari FA, Beyersdorf F, Luehr M, Etz CD, Frydrychowicz A, Harloff A, Markl M. Flow-sensitive four-dimensional magnetic resonance imaging: flow patterns in ascending aortic aneurysms. European Journal of Cardio-thoracic Surgery. 2008; 34: 11—16.

Wieben A, Roldan-Alzate A, Reeder SB, Schiebler ML, Nagle SK, Archer CW, Landgraf BR, Grist TM, Francois CJ. 4D flow MRI for non-invasive assessment of mesenteric ischemia. Proc ISMRM 2013; 0063.

Chapter 7

Fluid Dynamic Assessment of the Neonatal Aorta

In chapter 7 the aortic blood flow regime in healthy preterm and term infants is determined. The hemodynamic effect of the ductal shunt and potential presence of turbulence in the aorta is investigated. To begin with the fluid dynamic properties of blood and parameters to quantify them are introduced. A technique to quantify aortic pulse wave velocity (PWV) is then described in preterm and term infants using 4D PC MRI. Initial normative ranges in this population are established to facilitate comparison with adult data. The calculation of Re (Re) from 4D PC MRI data is then described and employed to determine the blood flow regime and if turbulence is present within the aorta in infants with and without PDA. Neonatal data is then compared to previously reported adult data.

7.1 Fluid Dynamic Assessment of Blood Flow

Assessment of blood flow dynamics plays a major role in the understanding of the development and onset of cardiovascular pathologies (Fogel, 2000) (Laurent et al. 2001) (Markl et al. 2012). Both compliance and flow regime within the healthy and diseased aorta have been well documented in adults and paediatrics with multiple techniques (Cheung et al. 2004) (Markl et al. 2012) (Voges et al. 2012). PWV (an inverse measure of vessel compliance and marker for vessel stiffness) and Re (Re) (a measure of the flow regime and marker for turbulence) are two parameters that are increasingly being used as markers for cardiovascular diseases and the development of pathologies in adults and paediatrics. In the following subsections these 2 parameters and their significance are described in more detail.

7.1.1 Pulse Wave Velocity

Compliance

The pulsatile nature of the left ventricular contraction generates a pulse wave that propagates along the aorta and proximal arteries at a velocity proportional to stiffness and inversely proportional to compliance. Changes in aortic stiffness/compliance have a high physiological relevance as they can lead to an increase in aortic pulse pressure and cardiac pressure afterload (Dogui et al. 2011), which can lead to left ventricular hypertrophy (Nussbacher et al. 1999). Compliance, the distensability of an artery and index of vessel elasticity, is described as the change in arterial blood volume per unit length due to a change in pressure as denoted in equation 7.1.

$$C = \frac{\Delta V}{\Delta P} \tag{7.1}$$

Arterial compliance converts pulsatile flow of the central arteries into the steady flow of the peripheral tissues to provide a constant blood supply to organs (Levick, Fifth Edition, 2010, chpt 8). The rapid ejection of blood during systole and high peripheral systemic resistance cause a large proportion of the stroke volume ejected from the left ventricle to be accommodated in the proximal elastic arteries. The increase in blood volume distends the arterial wall. From Laplace's law (chapter 5) the increase in vessel diameter leads to an increase in wall tension causing an increase in arterial blood pressure. Hence changes in pulse pressure are often used to infer stroke volume. As aortic compliance decreases a smaller proportion of the stroke volume is stored in the aorta during systole. A larger blood volume then propagates along the aorta altering the peripheral circulation, pressure and resistance.

Cardiac load and vessel stiffness

Pulse pressure and therefore compliance are considered important due to the relation to cardiac output and load on the heart. The mean load on the heart is determined from the peripheral systemic resistance which governs the average blood flow and pressure (Voges et al. 2012). The peak load on the heart is determined by impedance which governs the pulse pressure. As compliance decreases and therefore impedance increases the pulse pressure increases due to two mechanisms. Firstly vessel compliance is not a fixed quantity, as pressure or volume increases the vessel stretches to accommodate an increased blood volume. Vessel stiffness increases as the vessel wall stretches. Secondly the increased PWV due to increased vessel stiffness results in an earlier return of the reflected wave and augmentation of the pulse pressure. Consequently as vessel compliance decreases cardiac load is increased; the left ventricle must generate more pressure to eject the same volume of blood (Greenwald, 2002) (Levick, Fifth Edition, 2010, chpt 8). As a result increased vessel stiffness is associated with many cardiac risk factors (Bogren et al. 1989) (Franklin et al. 1999) (Laurent et al. 2001).

Pulse Wave propagation

As PWV represents intrinsic arterial stiffness (Sutton-Tyrrell et al. 2005), through this relationship it has been closely associated with atherosclerosis, and is now being used as an indicator of future cardiovascular events (Metafratzi et al. 2002) and vascular impedance (Laurent et al. 2006) (Dogui et al. 2011). PWV has been shown to increase with age in healthy adults as vessels become stiffer and compliance decreases (Mohiaddin et al. 1993). Metafratzi et al. 2002 reported a PWV range from 4 to 10 ms^{-1} in the healthy adult aorta, whilst Vulliemoz et al. 2002 found a mean PWV of 4.4 ms^{-1}. A few studies have assessed aortic compliance in preterm and term neonates from vessel diameter measurements by ultrasound and systemic pressure measurements from pressure cuffs on the limbs

(Mori et al. 2006) (Tauzin et al. 2006). However non-invasive pressure measurements in the neonatal population are prone to inaccuracies and these studies were not validated. Measures of PWV have also been used to investigate the increased risk of cardiac disease seen in preterm infants born at low birth weight. A significant increase in PWV was found in preterm infants and paediatric subjects (~8yrs) born prematurely at low birth weight and may explain the increase in cardiac disease in this population (Barker et al. 1989) (Cheung et al. 2004).

7.1.2 Characterization of Flow Regimes and Re

The Re, originally used to describe laminar flow in a rigid pipe (Reynolds, 1883), has recently been used to define flow regimes and the onset of turbulence within vessels (Stalder et al. 2011). The presence of turbulence is believed to not only decrease the efficiency of blood flow but also play a part in hemolysis, thrombus formation, and in the development of atherosclerosis (Davies et al. 1986) (Stein et al. 1974) (Sutera et al. 1975). Evidence of flow instabilities have been found in the healthy adult ascending and DAo (Stalder et al. 2011). However these models do not extend back to the neonatal and preterm population.

Re and turbulence under physiological conditions

The flow regime of a fluid with a given viscosity, in a vessel with a given diameter is a result of two primary forces, the inertial and viscous, acting on the fluid. The ratio of these two forces the Re is used to determine the onset of turbulence and is defined in equation 7.2. Generally in the scenario of a straight, rigid lumen with constant flow, laminar flow occurs at Re <1200, transitional flow occurs between 1,200 and 2,300 and Re >2300 is considered turbulent flow (Peacock et al. 1998) (Reynolds, 1883).

$$\text{Re} = \frac{inertial\ forces}{viscous\ forces} \quad (7.2)$$

Following from this the Re for flow within a lumen can be calculated from equation 7.3 (Stalder et al. 2011).

$$Re = \frac{4\rho|Q(t)|}{\pi\eta \cdot D(t)} \quad (7.3)$$

Where ρ = blood density, Q(t) = volumetric flow, η = viscosity of blood and D(t) = diameter of blood vessel.

Calculation of turbulence in-vivo

The development of turbulence in-vivo under normal physiological conditions is still not fully understood due to the pulsatile nature of blood flow, the compliance of the vessel walls and the non-Newtonian nature of blood: red blood cells are oval, flexible biconcave disks, the morphology, arrangement, and effective viscosity of these cells are effected by the blood flow field (Eggleton et al. 1998). The development of turbulence is also influenced by the acceleration and deceleration of pulsatile blood flow during systole and diastole as well as the pulse frequency. Acceleration has a stabilizing effect, while turbulence often appears during deceleration. In addition, turbulence needs some time to develop, and depending on the pulse frequency, the deceleration period might not be long enough for turbulence to appear (Peacock et al. 1998).

As a result the traditional assessment of laminar and turbulent flow and corresponding Re needs to be revised when assessing physiological flow. Consequently numerous studies have described a critical Res (Re^c) associated with the presence of flow instabilities and the transition towards a

turbulent regime in-vivo and in-vitro (Nerem et al. 1972) (Peacock et al. 1998) (Stalder et al. 2011). Re^c is the minimum Re that represents turbulence for a given pulsatile flow and lumen. A previous study by Peacock et al (1998) determined the association between Re^c, Re, Womersley (α) and Strouhal (St) numbers with the presence of flow instabilities in vitro for physiologically realistic pulsatile flow (defined in equation 7.4).

$$Re^c = 169\alpha^{0.83} St^{-0.27} \quad (7.4)$$

Wormersley number (α) indicates the transition from Poiseuille flow (parabolic flow) to Womersley flow (plug flow), and the Strauhol number (St) represents the dimensionless stroke volume both defined in equation 7.5 and 7.6.

$$\alpha = \frac{Dm}{2}\sqrt{\frac{\rho \cdot 2\pi f}{\eta}} \quad (7.5)$$

$$St = \frac{Dm}{2}\frac{f}{vp - vm} \quad (7.6)$$

Where Dm = mean diameter over cardiac cycle, f = heart rate, vp = maximum of the mean cross-section velocity over cardiac cycle and vm = mean of the mean cross-section velocity over cardiac cycle.

7.1.3 Fluid Dynamic Assessment of Flow by MRI

Quantification of PWV with MRI

Intra-vascular pressure measurements combined with a distance measurement provide the most accurate PWV measurements (Vulliemoz et al. 2002) but this invasive technique is not suitable for many patients. Non-invasive pressure measurements taken from the pressure cuffs on the limbs are not a direct measure of aortic pressure and can be erroneous in the un-cooperative neonatal population (Konig et al. 2012). In addition echo length and diameter measures are highly user dependent and have poor repeatability (Groves et al. 2008a) (Salvi et al. 2008).

PWV measurements require flow and morphological information. It can be assumed that the pressure wave is unidirectional and reflectionless in the adult aorta between the onset of the blood flow and the time of maximum blood flow (Berger et al. 1994). Hence under these conditions the movement of an infinitesimally thin blood slice in a vessel experiencing a pressure wave can be considered. Consequently from these assumptions 4D PC MRI can provide a non-invasive estimate of PWV based on flow waveform measurements from retrospective analysis planes at almost any anatomical location. Multiple 2D and 4D PC MRI PWV assessments have used this relationship between pulse pressure and blood volume to calculate the pulse wave arrival time from the flow profile at 2 or more locations along the aorta (Markl et al. 2012) and have been validated against in-vivo pressure measurements (Fielden et al. 2008) (Grotenhuis et al. 2009) (Vulliemoz et al. 2002).

MRI quantification of Re and assessment of turbulence

Previous assessments of turbulence in vivo have been based on catheter hot-film anemometry or perivascular Doppler ultrasound in animals and in humans (Nerem et al. 1974) (Stalder et al. 2011) (Stein et al. 1975) (Stein et al. 1976); these studies were limited by their complexity and invasiveness and are not suitable for the neonatal population. A study by Stalder et al (2011) assessed the

presence of turbulence within the adult aorta from 4D PC MRI data. Re was calculated for each cardiac phase (equation 7.3) and then compared to the Re^c for each individual subject to assess the efficiency of the cardiovascular system and onset of pathologies (Stalder et al. 2011).

The method section in the following work has been split into 2 parts; firstly a study to quantify PWV in neonates from 4D PC MRI is presented. Secondly from the same datasets, aortic flow regime is evaluated. The final subsection is a discussion of both studies.

7.2 Fluid Dynamic Assessment of the Neonatal Aorta with 4D PC MRI

7.2.1 Introduction

Using PC MRI the previous chapters have presented data indicating that ductal shunt volumes can be up to 74% of cardiac output (CO), that even in the presence of large shunt volumes total systemic blood flow can be maintained and that it is achieved by a significant increase in CO (chapter 4 and 5). As mentioned previously compliance is not a fixed parameter, vessel stiffness increases as the vessel is stretched. The impact of increased blood volume and pressure associated with PDA on aortic compliance is unknown. Although aortic blood flow fields have been visualized (chapter 6), whether the additional shunt volume, shunt flow pattern and bifurcation of the duct at the inferior wall of the aortic arch creates turbulent flow regimes that disrupt the efficient transport of blood within the aorta is unclear.

Global aortic PWV was originally quantified from two 2D PC MRI sequences (positioned at the level of the aortic valve and in the DAo at the level of the diaphragm) combined with an extra length measurement (Broadhouse et al. 2013) (data not included in this thesis). This was prone to inaccuracies due to erroneous R wave triggering and uncertainty over length measurements. The use

of 4D PC MRI can address both these deficiencies and provide a non-invasive, comprehensive assessment of both aortic PWV and flow regime.

Objective

The aim of this study was to first assess the fluid dynamic parameters, PWV and Re in preterm and term infants using 4D PC MRI. Secondly to establish a normative range in this population and to identify any changes in both PWV and Re associated with the common congenital defect PDA.

7.3 Quantification of PWV in Preterm and Term Infants

7.3.1 Patients and Methods

This study was approved by the North West London Research Ethics Committee (06/Q0406/137) and written informed parental consent was obtained in all cases.

For an initial validation study 4D PC MRI global aortic PWV (PWV-MRI) measurements were compared to PWV values calculated from invasive pressure measurements (PWV-Pres) in the DAo. The 4D PC MRI protocol is described first.

Assessment of PWV via 4D PC MRI

4D PC MRI Study cohort

Cardiac MRI was performed in 9 infants with median (range) GA $26^{+3}(25^{+3} – 32)$ weeks, cGA $32(30^{+4} – 36^{+5})$ weeks, birth weight 895(680 – 1740) grams and weight at scan 1330(875 – 2065) grams, who were inpatients at Queen Charlotte's and Chelsea and St Thomas' Hospital. All infants had an echo

performed within 24 hours of MRI scan by an operator with >10 years of experience (AMG, see glossary for details) in neonatal echocardiography. Four infants had PDA as determined by echo. Shunt volume was determined in PDA infants from PC MRI as described in chapter 4.

All infants were scanned using acoustic ear protection, pulse oximetry, vector ECG monitoring and without sedation or anaesthesia (Merchant et al. 2009). Six infants required low flow supplemental oxygen or nasal continuous positive airway pressure via an MR compatible system but all infants were stable and tolerating full enteral feeds during the scan. None of the infants were mechanically ventilated during the scan.

4D PC MRI Acquisition

Scans were performed on a Philips 3T MR Achieva scanner (Best, Netherlands) using a specialised 8 channel pediatric body receive coil for infants above 2kg and a small extremity receive coil for infants below 2kg. 4D PC retrospective gated sequences (spatial resolution = 1mm isotropic, TR/TE = 5.9/3.1ms, NSA = 1 and cardiac phases = 20) were aligned sagittal oblique providing full coverage of the aortic arch (parameters are shown in table 6.1.1, chapter 6). The 3 directional velocity encoding was calibrated for the range of ±150cms^{-1} and acquisition time ranged between 7 and 15 minutes depending on size of field of view and heart rate of the infant. No undersampling or respiratory compensation techniques were used.

Data processing

To determine aortic PWV multiple data analysis steps were employed. Firstly the freely available pre-processing software velomap_tool (Bock et al. 2007) was used to generate a pseudo angiogram and if present unwrap any aliased pixels. The angiogram was generated from the sum of squares of the velocity map (Bock et al. 2007) and then exported with the 4D PC dataset (chapter 6). An iso-

volume rendering of the aorta was generated from the angiogram using commercially available software (EnSight; CEI, Apex, NC, USA) (figure 7.2.1). Clip planes were then defined orthogonal to the angiogram lumen, at 5 to 8 locations along the arch between the aortic valve and DAo at the level of the diaphragm.

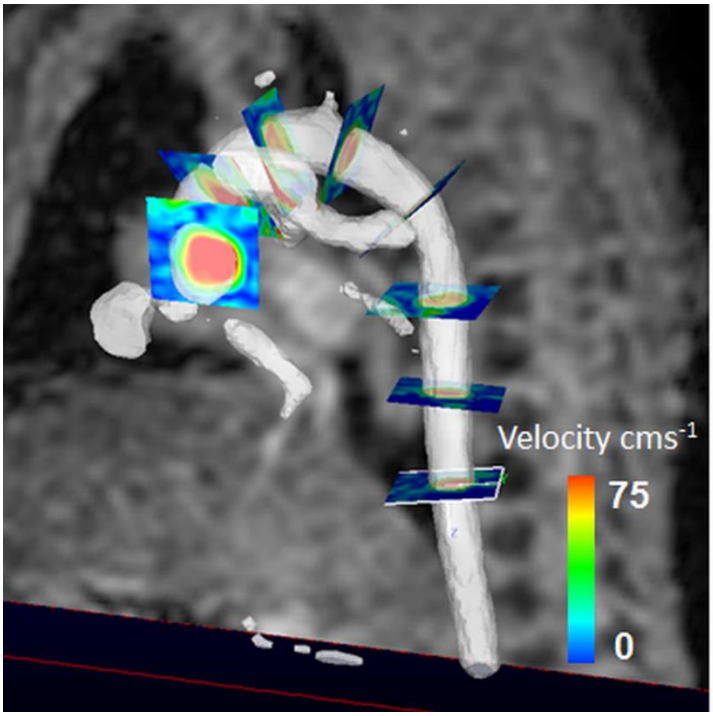

Figure 7.2.1 – Aortic PWV setup: location of 8 clip planes along the aortic arch positioned between the aortic valve and DAo at the level of the diaphragm shown in a 960g infant. The velocity map is shown in each clip plane. The position of the clip planes is determined with the aid of an iso-volume rendering of aorta calculated from the sum of squares of the velocity map. The arch is shown running anterior posterior from left to right of the figure.

The clip planes were exported and flow was then quantified at these locations using a matlab based software tool flow_tool (Stalder et al. 2008), (MathWorks Matlab). The vessel of interest was tracked over all cardiac phases and flow was then calculated at each time point of the cardiac cycle by manual segmentation of the vessel lumen. The time resolved flow was then interpolated and the resultant flow profiles were used to determine the time interval between the arrival of the pulse wave at each plane. The upslope regions of the flow profiles from each location, defined as the time

between 15% and 90% of upstroke flow were then generated (using MathWorks Matlab) (figure 7.2.2a). Often infants with large shunt volumes and therefore elevated left ventricular outputs, have broader peaks to the flow profiles within the AAo (figure 7.2.2b). The range of 15-90% of peak flow was therefore chosen to ensure that this broadening of the peak was excluded so that the upslopes had similar profiles, and did not introduce unnecessary error in the least squares fit registration.

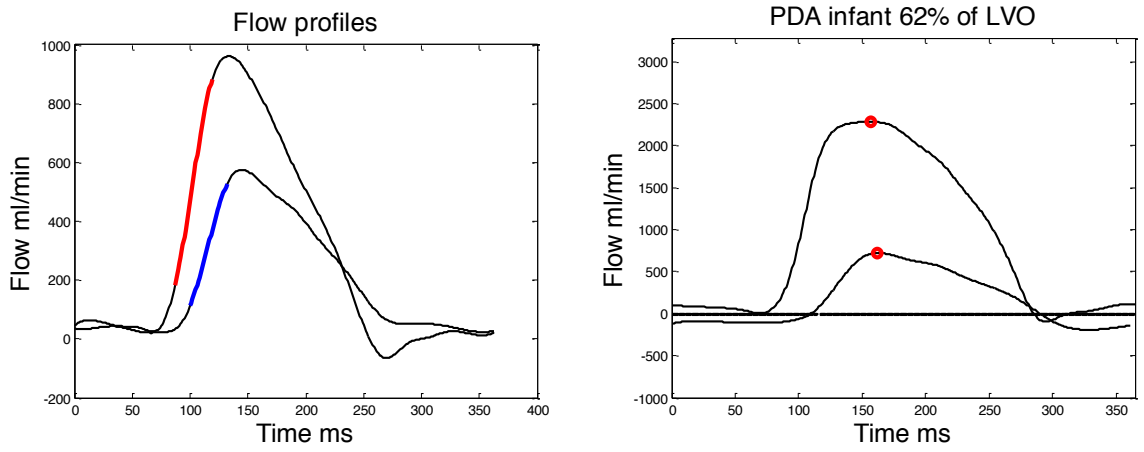

Figure 7.2.2 – Upslope regions: a: upslope regions defined as the time between 15% and 90% of upstroke flow are superimposed onto the flow profiles at the ascending (red) and DAo (blue). The two flow profiles have been shifted along the time axis by 80 ms for clear visualization and analysis of the 2 upslope regions. b:the flow profile in the AAo of an infant with a ductal shunt volume of 62% LVO is shown. The peak of the AAo flow profile is much broader than the in figure a due to the increased blood flow volume associated with the PDA. The red circles denote the maximum peak flow.

The upslope regions were scaled to achieve a set of normalised velocity curves of uniform scale and a least squares fit (using MathWorks Matlab) between 1st and scaled upslope regions of the consecutive planes was performed with time shift as a single free parameter (figure 7.2.3).

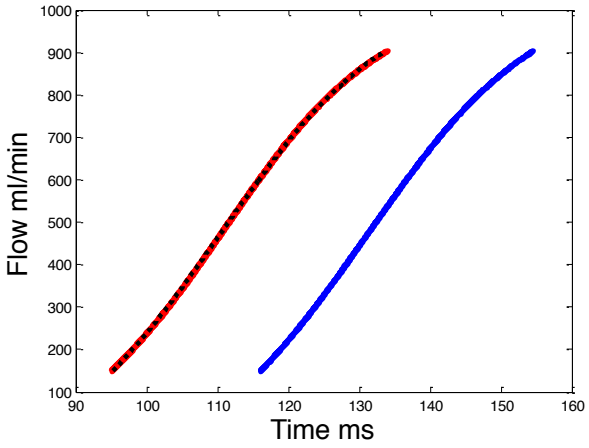

Figure 7.2.3 – Least square fit registration: scaled upslope regions of AAo (red) and DAo (blue) flow profiles and subsequent shifted curve (black) from least squares fit registration.

The aortic length was determined from interpolation between the centre of the lumen's spatial coordinates at each clip plane along the centreline of the aorta (using MathWorks Matlab) (figure 7.2.4a and b). The centre of the lumen was determined by visual analysis. Time delay was plotted against aortic distance between the 1st and consecutive planes. PWV (defined as aortic length/time delay) was then obtained from the gradient of the slope (figure 7.2.5).

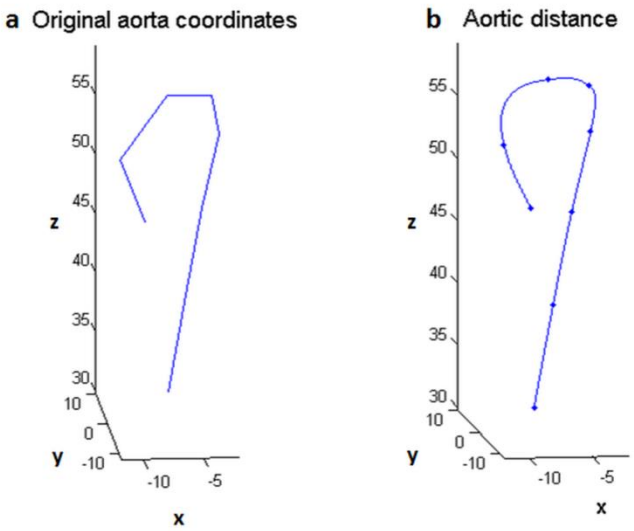

Figure 7.2.4 – Aortic Length: Interpolation a: between the centre of the lumen's spatial coordinates of each plane was performed to obtain, b: aortic length in mm. For the coordinate system shown x is the right left direction, y is the anterior posterior direction and z is the foot head direction.

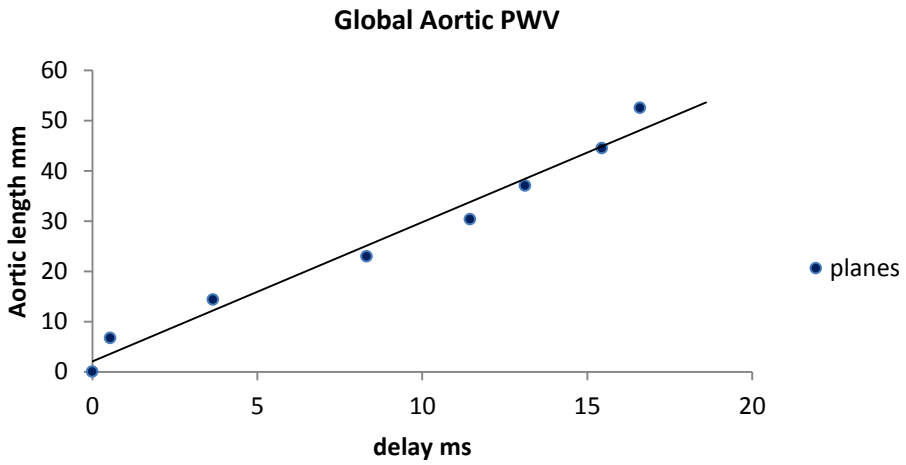

Figure 7.2.5 – PWV: Global aortic PWV determined from the graph of time delay against length.

Assessment of PWV via echocardiography and invasive pressure measures

Echocardiography PWV Study cohort

Invasive pressure measurements and echocardiography assessment data were available from a separate review of a historical cohort of 41 preterm infants with median (range) GA 27(24 – 29) weeks and birth weight 860(510 – 1430) grams. Measurements were taken 12 hours after birth and local PWV was calculated in the DAo using the equations below (equation 7.7 and 7.8). Infants were inpatients at the National Women's Hospital, Auckland, between 1 December 2002 and 1 May 2004. Echocardiography assessment was carried out by one of two investigators (AMG and CAK, see glossary for details), both of whom had more than 2 years' experience in neonatal echocardiography at the start of the recruitment period (Groves et al. 2008a).

The pressure and diameter data was used in a broader study to assess the blood flow volume in the superior vena cava and DAo in the newborn infant and relationship to arterial pressure (Groves et al. 2008a and 2008b), yet was not used for evaluation of PWV. The quantification of PWV from this data was carried out by the author of this thesis and intended to provide a gold standard for the initial assessment of 4D PC MRI PWV feasibility in preterm infants.

Echocardiography protocol

All scans were performed with an ATL 3000 ultrasound scanner (Advanced Technological Laboratories, Bothell, Washington, USA) equipped with a 7 MHz probe. DAo diameter was assessed as close as possible to the plane of the aortic valve when seen in the parasternal short axis view. Systolic and diastolic DAo diameter was assessed by M mode echocardiography using the trailing edge-leading edge technique. DAo diameter was averaged over 5 consecutive cardiac cycles for both end systole and end diastole. All scans were analysed using in-built cardiac analysis software on the ultrasound machine and measurements were performed by a single investigator (AMG) away from the cotside. Full details are given in Groves et al. 2008a.

Invasive pressure measurements

Systolic and diastolic invasive blood pressure values were taken from indwelling arterial lines. Measurements were downloaded every 6 seconds using Marquette Solar 8000 monitors (GE Medical Systems, Wisconsin, USA) and Bedmaster V1.3 software (Excel Medical Electronics Inc, Florida, USA). The downloaded blood pressure value is an average of the blood pressure monitored over the previous 6 seconds. These measurements of blood pressure were then averaged over the precise duration of the echocardiogram (Groves et al. 2008b).

Data processing

To determine PWV from DAo diameter and pressure measurements the following calculations were performed. From an extension of equation 7.1, local compliance can be defined as

$$C = \frac{\Delta A}{\Delta P} \tag{7.7}$$

Where ΔA is the change in lumen area and ΔP is the change in pressure between end systole and end diastole.

Local PWV can then be defined as

$$PWV = \sqrt{\frac{A}{\rho C}} \quad (7.8)$$

Where A is the lumen area at end diastole and ρ is the blood density assumed to be the constant 1055 kgm^{-3} (Stalder et al. 2011). PWV was calculated in this manner in Vulliemoz et al. 2002 and was taken as the gold standard in their validation study.

Data analysis

The invasive pressure and echocardiography based PWV-Pres measurements were used to establish a normative range and to assess the feasibility of 4D PC MRI PWV quantification in preterm infants. Neonatal PWV-MRI values were compared with the PWV-Pres values and previously published adult values. PWV-MRI was plotted against corrected GA to examine the impact of PDA on PWV. Linear regression was carried out to investigate the relationship between birth weight z-score and PWV (graph shown in appendix 7.1).

7.3.2 Results

PDA infants within the PWV-MRI Study cohort

Of the 9 subjects studied, 5 were control infants with no PDA median (range) GA 28(25^{+3}-32) weeks, cGA 34^{+3}(30^{+4} – 36^{+5}) weeks, birth weight 1035(690 – 170) grams and weight at scan 1670(960–2070)

grams were scanned. The remaining 4 infants with median (range) GA 26(25^{+3} – 27^{+2}) weeks, cGA 31^{+6}(30^{+4} – 32) weeks, birth weight 875(680 - 1000) grams and weight at scan 1170(875 - 1430) grams had PDA demonstrated on echo and quantified with PC MRI (chapter 4). Shunt volumes, shown in table 7.2.1 ranged from 12.1 – 52.7% of LVO. As a side note most of the infants within the echo cohort would have had a PDA at the time of scan (12 hours after birth).

GA weeks	cGA weeks	BW g	Wt at scan g	PDA shunt volume %
27^{+2}	31^{+6}	895	1215	12.1
25^{+3}	30^{+4}	850	875	15.4
26^{+3}	32	1000	1430	15.9
25^{+4}	31^{+6}	680	1125	52.7

Table 7.2.1 – Shunt Volumes: GA, cGA, birth weight (BW), weight at scan (Wt) and shunt volume for 4 infants with PDA.

PWV-MRI values

Mean (range) PWV was found to be 3.2(2.3-5.1)ms^{-1}. A strong linear relationship was found between upslope and aortic distance in all of the infants, R^2 ranged from 0.89 – 0.98 (figure 7.2.6).

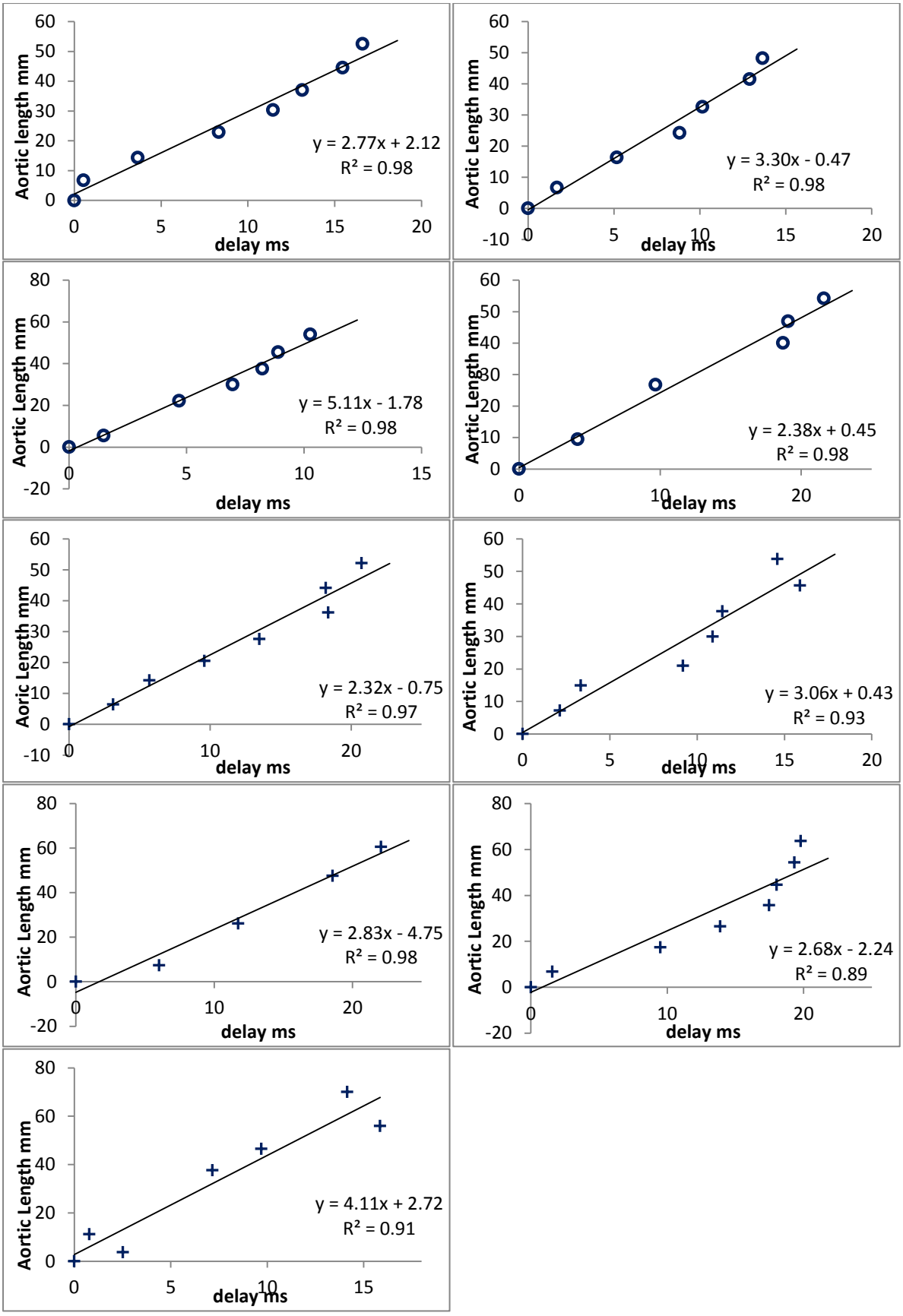

Figure 7.2.6 – PWV: Time delay (ms) plotted against aortic length (mm) for PDA (○) and control (+) infants. Global PWV is derived from the gradient of the line.

Comparison of PWV-MRI, PWV-Pres and previously reported adult measures

PWV determined by echocardiography and invasive pressure measurements was found to have a mean (range) of 2.6(1.8 – 4.2) ms^{-1}. Both echo and MRI cohorts were plotted against cGA (figure 7.2.7). A trend line was fitted to establish a normative range from the PWV-Pres measurements. This trendline and its 95% upper and lower confidence limits were projected forward to include the PWV-MRI cohort. The trendline from the PWV-Pres data indicated an increase in PWV with cGA. From visual assessment the PWV-MRI measurements appeared in general to fit within this trend. Both PWV-Pres and PWV-MRI measurements were found to be lower than the previously reported adult range of 4 to 10 ms^{-1} (Metafratzi et al. 2002).

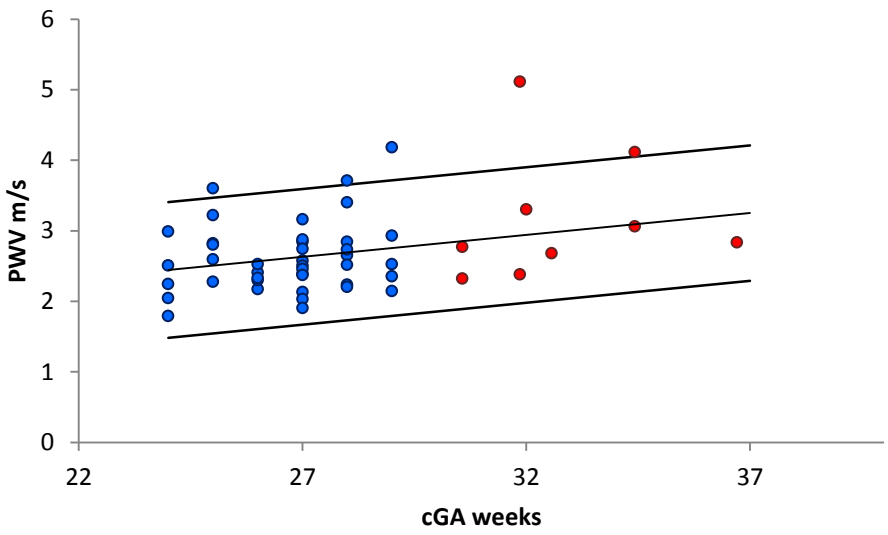

Figure 7.2.7 – Aortic PWV in preterm infants: PWV values determined from invasive pressure and echo measurements (●) and PC MRI (●) plotted against cGA. Trendline and confidence limits from the PWV-Pres cohort have been projected forward to aid in the comparison between PWV-MRI measures.

Impact of PDA: Initial assessment

The normative range from the initial PWV-MRI data showed that 1 PDA infant was above the upper 95% confidence limit. This infant had the smallest ductal shunt volume of the 4 infants (12.4% of LVO).

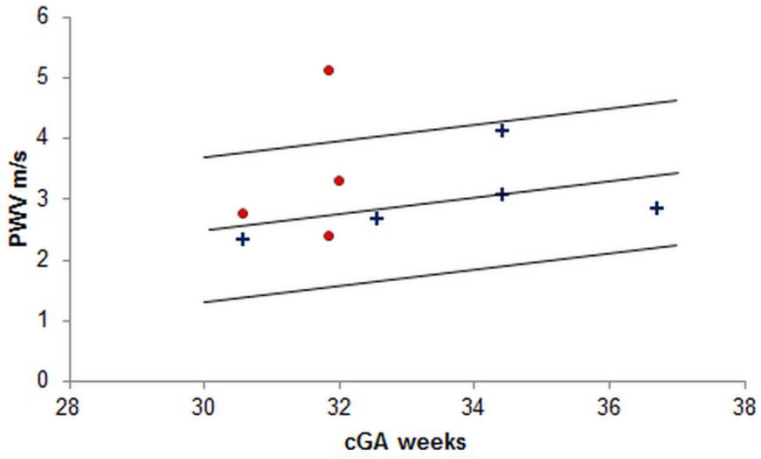

Figure 7.2.8 – Normative range: cGA plotted against PWV for infants with (●) and without (+) PDA. Initial data in 9 infants.

7.4 Quantification of Neonatal Aortic Flow Regime

7.4.1 Methods

Data processing

The method presented in Stalder et al (2011) has been adopted in this chapter to investigate the flow regime along the neonatal aorta. Blood flow was calculated at each clip plane from the 4D PC MRI data using the matlab based software tool flow_tool (Stalder et al. 2008), as in the previous PWV method. Flow and lumen diameter at each cardiac phase were used to determine a time

resolved Re (equation 7.3) at numerous locations within the AAo, arch and DAo. Mean vessel lumen diameter, averaged heart rate over the scan, mean and maximum of the mean cross-section velocity over cardiac cycle were then used to calculate Re^c for each individual infant (equation 7.4-7.6). Calculation of Re and Re^c was carried out in matlab (Matlab, Mathworks). Although small numbers the calculation of Re and Re^c from 4D PC MRI data provided a preliminary assessment of the flow regime along the neonatal aorta.

Re and Re^c were also calculated in the same manner in 22 control and 7 PDA infants from the LVO and DAo 2D PC sequences used in the initial 2D PC PWV study mentioned above. The accurate calculation of Re and Re^c is not dependent on equivalent R wave triggering between sequences. The 22 control preterm and term infants had median(range) GA $32^{+2}(24^{+5} – 38)$ weeks, cGA $33^{+6}(27^{+5} – 38+^{6})$ weeks, birth weight 1580(610 – 3760) grams and weight at scan 1660(745 – 3780) grams were scanned. Seven infants with median(range) GA $26^{+3}(25^{+3} – 28^{+4})$ weeks, cGA $30(27^{+4} – 34^{+2})$ weeks, birth weight 1090(790 – 1400) grams and weight at scan 1270(1040 – 1430) grams were scanned and had PDA determined by echo. Shunt volume ranged between 10.4 - 62.4% of LVO as determined by 2D PC MRI (chapter 4). Results are included in this section to provide a statistical comparison of the flow regime at the LVO and DAo aortic locations between control and PDA infants.

Calculation of blood properties in preterm infants

The viscosity of blood can be determined by the haematocrit level; adult blood viscosity has a linear relationship to Hct for values below 65% (Eckmann et al. 2000). The Hct is the proportion, by volume, of the blood that consists of red blood cells and is often expressed as a percentage of blood volume. In healthy adult subjects the Hct is fairly constant and is general assumed to be 4.6 cp (centipoise) (Stalder et al. 2011). However, Hct levels, and consequently blood viscosity can vary greatly in neonates. Neonatal blood has the same viscoelastic properties as adult blood despite the

larger red blood cells and higher hemoglobin count (Mackintosh et al. 1973), hence below an Hct level of 65% the relationship to viscosity can be considered linear. A study by Merchant et al (Merchant et al. 1992) investigating the relationship between Hct and viscosity in preterm, and term infants and found the following association (equation 7.8). Blood viscosity was therefore calculated on an individual basis from Hct taken from routine blood tests within 24 hours of the scan as this can vary significantly in newborns (Linderkamp et al. 1984). Hct were taken as the percentage volume of the blood sample after being placed in a Hematocrit centrifuge. Blood density was again assumed as the constant $\rho = 1055\ kgm^{-3}$ (Stalder et al. 2011).

$$\eta = 0.73Hct + 0.32 \quad (7.8)$$

Where η = blood viscosity. From the above calculation viscosity has units of millipoise. One poise P = $0.1 kgm^{-1}s^{-1}$, the analogous units in the international system (SI) of units is the Pascal second (Pa·s), 1Pa·s = 10P. Hct was converted to these SI units for the evaluation of Re and Re^c.

Regional assessment of aortic flow regime

To determine regional Re values, the location of each clip plane was defined as either within the AAo (AAo), arch or DAo via visual analysis of the position along the aorta as shown in figure 7.2.9. The Re were then compared to Re^c (equation 7.3) calculated at each plane in each individual.

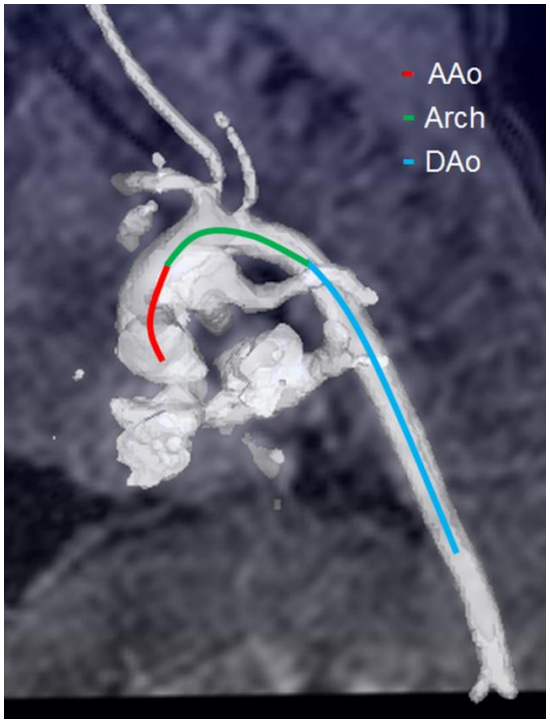

Figure 7.2.9 – Regions along the aorta: AAo (red), arch (green) and DAo (blue) regions of the aorta are visually defined from the isosurface-volume rendering of the sum of squares of the velocity data in a 1.6kg infant. The aorta is shown against the anatomical magnitude data where the diaphragm and spine can clearly been depicted.

Statistical analysis

From 4D PC MRI data the average peak RE was found for AAo, arch and DAo regions, the peak Re in the 3 aortic regions during the cardiac cycle was also normalized by the critical Re calculated for each individual subject (Re/Re^c) and the flow regime along the neonatal aorta was then compared with previously reported adult data. Re/Re^c at the LVO and DAo was also calculated from the 2D PC MRI data and unpaired t-test was carried out to compare control and PDA groups.

7.4.2 Results

Average peak Re and Re/Re^c for the AAo, Arch and DAo regions (from 4D PC MRI) for individual infants are shown in table 7.2.2. Mean values for control and PDA infants are also displayed. From

2D PC MRI analysis the mean peak Re, Re^c and Re/Re^c for control and PDA infants are shown in table 7.2.3. Unpaired t-test analysis of the 2D PC MRI cohort showed that there was no significant difference in Re/Re^c at the LVO or DAo slice location between the control and PDA groups in this cohort (p = 0.14 and 0.57 respectively). Although the cohort is small this is also indicated in the preliminary 4D PC MRI Re data below.

	Wt at scan kg	cGA wks	AAo		Arch		DAo	
			Re	Re/Re^c %	Re	Re/Re^c %	Re	Re/Re^c %
control	0.96	30^{+4}	601	33	528	29	469	29
	1.73	34^{+3}	1062	44	805	37	694	37
	1.6	34^{+3}	622	30	488	28	437	28
	2.07	36^{+5}	727	33	592	31	542	32
	1.33	32^{+4}	554	28	460	26	400	27
PDA	0.88	30^{+4}	594	31	538	31	430	27
	1.22	31^{+6}	658	34	445	25	382	23
	1.43	32	1043	43	800	39	767	37
	1.13	31^{+6}	863	39	670	38	532	31
Mean Control	**1600**	**34**	**713**	**34**	**574**	**30**	**508**	**30**
Mean PDA	**1170**	**32**	**790**	**37**	**613**	**33**	**528**	**30**
Mean Total	**1330**	**32**	**747**	**35**	**592**	**32**	**517**	**30**

Table 7.2.2 – Aortic flow regime: Weight at scan, cGA, mean Re and Re/Re^c for AAo, Arch and DAo regions are shown for all individuals. Mean of above values for control and PDA infants are shown in the bottom 2 rows.

	LVO			DAo		
	Re	Re^c	Re/Re^c %	Re	Re^c	Re/Re^c %
Controls	583	2005	29	489	1595	30
PDA	775	2207	35	590	1715	34

Table 7.2.3 - Flow regime: mean Re, Re^c and Re/Re^c are shown for the analysis of flow regime at the LVO and DAo 2D PC MRI acquisition planes between control and PDA infants.

Comparison of neonatal and adult aortic flow regimes

In their assessment of the healthy adult aorta, Stalder et al. (2011) found that the peak Re was higher in the ascending than DAo (≈4500 and ≈4200 respectively). From the 4D PC MRI neonatal data peak Re was also found to be higher at AAo than DAo (747 and 517 respectively). Stalder et al also found that flow instabilities were present in the ascending and DAo during systole, this was not found in neonates. In all infants, blood flow in the AAo, Arch and DAo was well below the turbulent regime.

7.5 Discussion

Invasive techniques such as catheter hot-film anemometry or perivascular Doppler ultrasound to measure both PWV and Re are still the most accurate methods to evaluate PWV and presence of turbulence, but are not ideal in the neonatal population. Another consideration is that the presence of these measuring devices affects the flow regime within the vessel of interest. In addition non-invasive PC MRI PWV measures have been compared to invasive techniques in adults and found to correlate closely (Grotenhuis et al. 2009) (Vulliemoz et al. 2002). The successful translation of 4D PC MRI to the neonatal population would provide a non-invasive, accurate, comprehensive assessment of not only the visualization of cardiovascular morphology and flow fields within (chapter 6), but quantitative analysis of the hemodynamic impact of prematurity.

From the previous chapters a significant relationship has been shown between ductal shunt volume and increased LVO. This increase in volume is associated with an increase in pressure (Levick, Fifth Edition, 2010, chpt 8), yet it is unknown how this increase in stroke volume and peak pressure effect aortic compliance and turbulence, but it could be expected that this leads to reduction in vessel compliance and an increase towards the turbulent regime in PDA infants. The first part of this study quantified PWV in preterm and term infants with and without PDA using 4D PC MRI: firstly to assess

the feasibility of PWV measurements and secondly to establish a normative range in this cohort and assess impact of PDA. The second part of this study utilized 4D PC MRI flow data to investigate the flow regime within the aorta in neonates with and without PDA based on a method first laid out by Stalder et al (2011). The flow data, heart rate and vessel diameter were used to calculate a Womersley, Strauhol and Re number. These were used to calculate a Re^c according to the work by Peacock et al (1998) to assess the existence of aortic flow instabilities in the neonatal population with and without PDA.

Existing methods of PWV quantification

Ultrasound-based carotid-to-femoral artery PWV is a standard clinical procedure in both adults (Wentland et al. 2013) and somewhat in neonates. However, distance measurements between these two locations are inaccurate as the tortuous path of the vessel is not taken into account; this can lead to differences in PWV values of up to 30% (Salvi et al. 2008). A few previous studies in preterm infants studies have assessed aortic compliance from ultrasound based vessel diameter measurements and systemic pressure measurements from pressure cuffs on the limbs (Mori et al. 2006) (Tauzin et al. 2006). In addition to the low repeatability of echo measures non-invasive pressure measurements in the neonatal population are prone to inaccuracies and these studies were not validated. For this study it was decided that for accurate quantification of PWV in preterms a more robust technique was needed.

There have been multiple validated methods to quantify PWV from PC MR data in adults. The most common method is the transit time method and uses the foot of the flow curve as a marker for the arrival time of the pulse wave at specific locations along the vessel (Dogui et al. 2011) (Grotenhuis et al. 2009) (Mohiaddin et al. 1993) (Wentland et al. 2013). The half maximum and peak flow of the upslope has also been used (Wentland et al. 2013). 2D PC multisite methods using a para-sagittal

slice down the length of the aorta to obtain flow waveforms at multiple locations along the length of the aorta have also been employed (Fielden et al. 2008). Velocity data is acquired in two directions (anterior posterior and foot head) and the centreline of the lumen is determined. The cross-correlation function applies a time shift to the waveforms at multiple locations to the first location until the highest correlation between the two values is obtained. This effectively returns a time shift relative to the first location. The change in arterial lumen diameter coupled with flow measurements have also been used to infer PWV (Vulliemoz et al. 2002).

More recently Markl et al (2012) presented a technique that uses the time-to peak flow that estimates PWV by fitting a plane to the upslope region in a least square sense. The slope of the plane as a function of analysis plane position measured changes in waveform delays across all analysis planes and thus resembled global aortic PWV (Markl et al. 2012). The technique presented in the subsection above is based on this design. Unlike the time to foot or peak methods above the registration of the entire upslope region meant that the calculated time delay did not rely on a single point to be defined from the flow profiles, reducing the error in time delay calculation between planes.

PWV measurements from 2D PC MRI

Initially neonatal PWV values were determined from two 2D PC MRI sequences at the aortic valve and in the DAo at the level of the diaphragm (this work was not included in this thesis). This was then combined with a separate length measurement taken from a pilot sequence aligned sagittal oblique along the arch (Broadhouse et al. 2012). This method gave rise to inaccuracies in the pulse wave arrival time at each location from erroneous R wave triggering and the tortuous arch and 2D pilot sequence lead to inaccurate aortic length measurements. PWV calculation from 4D PC MRI

eliminates the ECG temporal misregistration and the pseudo angiogram reduces the error in the aortic length measurement.

4D PC MRI datasets were then acquired and PWV and Re were assessed in 9 infants. The discussion presented here aims to consider the observations and possible significance seen from these preliminary data, and deliberate areas of future study.

Comparison between PWV-MRI and PWV-Pres

The comparison between the PWV-Pres and PWV-MRI measures was to provide an initial assessment of the feasibility of 4D PC MRI aortic PWV measurements in preterm infants. Accurate validation of this technique is discussed in chapter 8, future work. Consequently there are a few considerations when comparing the PWV-Pres and PWV-MRI measures. Firstly the PWV-Pres is a regional measure of PWV in the DAo at the level of the aortic valve plane; the PWV-MRI is a measure of global aortic PWV. The aortic compliance could change over the length of the aorta (Laurent et al. 2006) however, the high R^2 values of the 4D PC MRI measurements indicate that PWV does not vary considerably from aortic valve to DAo at the level of the diaphragm in preterm infants. Consequently the comparison between global and regional PWV is practical.

Secondly the measures were taken in 2 different cohorts with respect to GA and post natal age. The PWV-Pres group had lower GA (24-29 weeks) and all were scanned at 12 hours after birth. In comparison infants within the PWV-MRI group were all older in gestation at birth and scanned outside the transitional period (between 3 - 6^{+3} weeks after birth). It is unclear how prematurity and postnatal age effect aortic compliance. The extra-uterine circulatory demands on the preterm vasculature that is still developing may lead to abnormal vessel compliance and is an area of study worth investigating (chapter 8).

Considering the above limitations the PWV-Pres normative range with PWV-MRI values superimposed gave encouraging results, indicating that 4D PC MRI PWV measurements are feasible in the preterm population. The majority of the 9 infants assessed with 4D PC MRI lay within the normative range and followed the same linear trend of slightly increasing stiffness with GA. Metafratzi et al. 2002 reported a PWV range from 4 to 10 ms^{-1} in the healthy adult aorta, whilst Vulliemoz et al. 2002 found a mean PWV of 4.4 ms^{-1}. Both PWV measurements in infants were found to be lower than the reported adult ranges. As the multiple studies carried out across different age ranges have been performed with various methods it is difficult to perceive whether there is a progressive increase in vessel stiffness from preterm to term to pediatrics to adulthood and finally to old age, however the data suggests that this is the case.

As an additional point of interest, previous studies in pediatrics and neonates have shown an association between preterm infants born at low birth weight and increased aortic stiffness (Cheung et al. 2004) (Mori et al. 2006) (Norman et al. 2008) (Tauzin et al. 2006) and this may explain the increased risk of heart disease in adulthood seen in this population. Yet the inception of this increased stiffness in this population is still unclear. Linear regression analysis was carried out on the PWV-Pres cohort to assess if any significant association existed between decreased birth weight z-scores and increase in PWV and was found to be close to significant ($p = 0.06$) (graph show in appendix 7.1). This suggests that this difference in aortic stiffness may be apparent very shortly after birth (PWV-Pres measurements were taken 12 hours after birth). 4D PC MRI could be implemented in longitudinal studies to investigate the development/progression of this increase in aortic stiffness in low birth weight preterm infants where long term arterial lines and therefore invasive arterial pressure measurements are not ideal.

Impact of PDA on vessel compliance

All but 1 PDA infant remained within the normative range derived from both the PWV-Pres and initial 9 PWV-MRI values (figure 7.2.8/9). In addition this infant had the lowest ductal shunt volume of the group with 12.4% of LVO as determined by PC (chapter 4). This may suggest that the significant increase in stroke volume and pressure associated with high shunt volumes does not stretch the aorta so much that aortic compliance is significantly decreased. However, in high ductal shunt infants with significantly increased LVO, the low impedance pathway through the duct to the pulmonary circulation may play an important role to reduce blood flow and pressure in the DAo (chapter 4) downstream of the duct and maintain PWV.

Protocol considerations

Although the PWV-Pres measurements were seen as the gold standard in this study the echo measurements of DAo diameter are observer dependent. Vessel diameter assessment by M mode in the parasternal short axis view can lead to inaccuracies in the diameter and therefore area calculations if the true centreline of the lumen is not imaged. Bland-Altman repeatability analysis of the mean DAo diameter from echo measurements gave a repeatability index (RI) of 19% (Groves et al. 2008a). Invasive pressure measurements combined with lumen area values from MRI with adequate spatial and temporal resolution may provide a more accurate PWV measure. The validation of 4D PC MRI PWV measurements is discussed in more detail in chapter 8.

To obtain PWV from the 4D PC MRI data the least square fit registration was performed on upslope regions obtained from interpolated time resolved flow data at 20 time intervals in the cardiac cycle. The average heart rate in this neonatal population was 160bpm. This gave rise to a temporal resolution of 19ms. In adult PWV quantification 20 cardiac phases is considered at the limit to accurately quantify arrival time of the pulse wave. However the systolic period in adults is around

30% of the entire cardiac cycle in neonates it is around 45-50% due to the high heart rate and reduced diastolic function. Consequently the upslope region is a larger proportion of the cardiac cycle, sampled at more time points comparable to 30 cardiac phases in an adult dataset and initial data suggests that this is adequate. However, as mentioned above the validation of this technique in a neonatal regime is discussed in chapter 8.

Re calculation and assessment of aortic flow regime

Analysis of aortic flow regime

According to the comprehensive study carried out by Stalder et al (2011) in healthy adults, flow instabilities but not fully evolved turbulent flow were found to occur in the ascending and DAo. In the AAo, arch and DAo Re was << Re^c in all infants in this study, even in those with large shunt volumes (mean Re and Re^c for AAo – 790, 1700, for Arch – 613, 1840 and for DAo – 528, 1649)). There was no evidence to suggest the presence of turbulent flow in the aorta except at the highly localised site of the bifurcation of the PDA (as seen in chapter 6) where the assumptions for the calculation of Re analysis does not hold. The significant increase in heart rate and the decrease in flow volume and diameter (which is of an order of magnitude) between the adults and neonates are the prominent factors in the Womersley and Strauhol numbers that act to stabilize flow. Hence for blood flows with comparable velocity (both adult and neonatal aortic blood velocity are of similar magnitude), flow instabilities will occur at higher Re in smaller vessels relative to vessels of larger diameter. Likewise acceleration stabilizes flow and turbulence takes time to develop, the higher heart rates seen in infants also acts to stabilize flow. Consequently a turbulent aortic flow regime is very unlikely in neonates.

Although from the discussion above, a fully evolved turbulent flow regime was not expected in the PDA infants, it was at first surprising that there was no noticeable increase in Re/Re^c in PDA infants

(table 7.2.2 and 7.2.3) considering the significantly elevated cardiac outputs (chapter 4 and 5). However, when considering the influence of each variable (vessel diameter (Dm), flow volume (Q), peak mean (v_p) and mean (V_m) cross sectional velocity, heart rate (f) and viscosity (η) on the flow regime and the critical Re this can be explained (blood density, ρ was assumed a constant). From sensitivity analysis both diameter and flow are the dominant factors in the calculation of Re and both diameter and heart rate are the dominant factors in the calculation of Re^c. Considering the Re calculation (equation 7.3), although flow volume is significantly increased in PDA infants, this is somewhat compensated for by the fact that the aortic diameter in PDA infants was shown to be at the upper end of the range. When considering the calculation of Re^c (equation 7.4 – 7.6), the large aortic diameters, significantly increased heart rates in PDA infants and the fact that there is no significant difference in v_p and v_m in control and PDA infants acts to increase Re^c; flow becomes turbulent at higher Re in PDA infants. Hence although flow is significantly increased in the PDA infants the increase in heart rate acts to stabilize flow, it appears that flow remains below the transitional regime even in PDA infants as turbulent flow does not have time to develop. These results and the visualization of flow field in chapter 6 indicate that the presence of the PDA and additional stoke volume is unlikely to cause a fully developed turbulent regime.

The work in this thesis has predominantly been focused on the systemic hemodynamic impact of the PDA. Yet during Doppler echocardiographic assessment of the PDA a jet of blood from the PDA into the pulmonary artery is often observed. Presumably this will cause a degree of disrupted, chaotic flow within the pulmonary trunk and arteries. Quantification of flow in the pulmonary vessel was not feasible with the current 2D PC MRI protocol presented in chapter 4. In addition the sagittal oblique aligned 4D PC sequence and VENC optimized for aortic flow velocities meant that often the pulmonary trunk was outside the acquired volume and flow within the left and right pulmonary arteries was aliased. Hence evaluation of Re and also PWV from 2D and 4D PC MRI data presented in this thesis was not possible. However with an optimized acquisition the calculation of PWV, Re and

assessment of flow regime within these vessels could provide insight into the association between PDA and respiratory status, this is discussed in more detail in chapter 8.

Re study considerations

In-vivo, non-invasive assessment of flow regimes remains difficult and this study is limited by a number of assumptions made about the physiological system by the definition of Re. The Re was originally defined from observations of laminar flow of a Newtonian fluid in a straight rigid pipe, not pulsatile flow through compliant vessels. However the aorta can be assumed to be a straight vessel as the major diameter of the arch is much greater than the minor diameter of the aorta. Vessel compliance may act to increase flow instabilities in systole, however as the flow regime in neonates is below the transitional regime it is unlikely to cause turbulence.

In addition the calculation of Re and Re^c in the DAo does not take into account the presence of a PDA, in this situation the aorta and shunt vasculature can be modelled as a T junction. This will increase flow instabilities (act to decrease Re^c) downstream of the PDA for a certain length determined by the vessel and flow parameters. This is very difficult to model. Yet as stated above Re in the AAo and DAo is well below the turbulent regime even in significant PDA infants. However, as shown in chapter 6 there may be some highly localized turbulence around the bifurcation of the PDA.

Another limitation arises from the properties of blood. Blood is a shear-thinning, non-Newtonian fluid (Eckmann et al. 2000), the viscosity decreases as the shear stress increases; this is partly due to the alignment of red blood cells at high velocities (Eggleton et al. 1998). However above a shear rate of $100s^{-1}$ typically found in the major arteries and more specifically the aorta, viscosity can be assumed as constant (Eckmann et al. 2009).

Hct levels taken within 24 hours of the scan were used to derive the individual blood viscosity (mean (range) was found to be 3.6(2.2 – 6.1)cp). However Hct level in neonates can vary over a few days and may be a source of error when deriving the viscosity. Density is also taken as a constant ρ = 1055 kgm^{-3} when in reality this may vary from individual, yet without data on plasma volume (which was not available) this is difficult to calculate accurately. However the viscosity and density terms will tend to compensate in evaluation of Re/Re^{c} and there is a relatively low dependency on both Hct and ρ which will reduce errors. As an additional point of interest a multiple linear regression revealed a significant association between increase in Hct and decrease in LVO normalised by weight at scan when correcting for postnatal age, p = 0.014 (figure 7. 5.1). This was not taken into account when considering PWV analysis, PWV may vary in individual infants as η fluctuates; periods of low Hct may lead to increased PWV due to decreased vessel compliance as the aorta is stretched to accommodate the increased LVO.

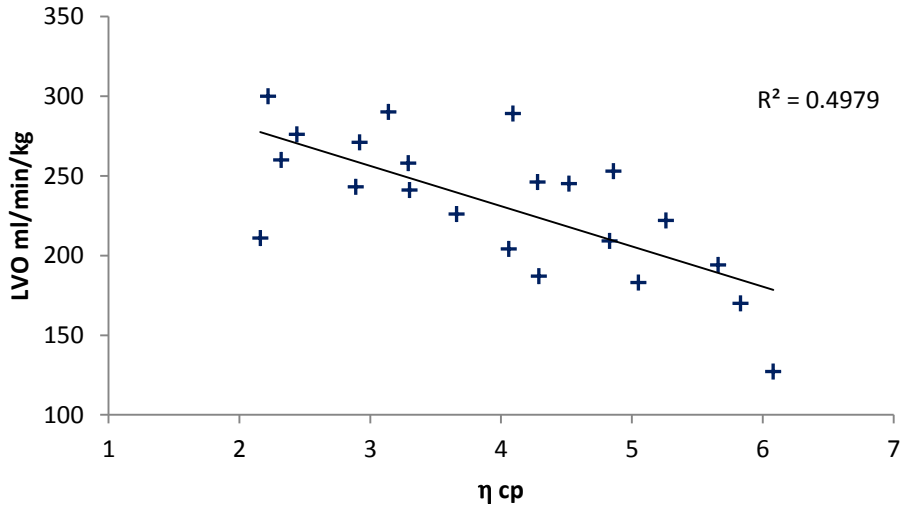

Figure 7.5.1 – Hct and LVO: LVO plotted against Hct in 22 preterm infants without PDA depicts an inverse relationship between the two.

7.6 Conclusion

In summary the feasibility of using 4D PC MRI flow data to determine PWV and Re in the neonatal population has been demonstrated. The common congenital defect PDA was also studied to investigate the hemodynamic impact of the duct. In this initial study aortic PWV was found to be lower than previously reported healthy adult ranges. Data suggests that the increasing linear trend of PWV with age seen in adults can be extrapolated back to the preterm cohort.

It is a common clinical belief that large shunt volumes disrupt normal aortic flow. However, calculations of Re and Re^c revealed that flow regimes at the aortic valve and in the DAo were well below the turbulent regime in infants with and without PDA. The increased heart rate is the prominent factor and acts to stabilize flow; for this reason even with elevated flow volumes and pressure seen in PDA infants, flow is not turbulent.

Previous echo analysis of the PDA is unable to evaluate the full hemodynamic and cardiovascular impact of the duct. The application of 4D PC MRI not only allows the visualization of blood flow patterns (chapter 6) but also the quantification of cardiovascular parameters. With the further implementation of 4D PC MRI a comprehensive assessment of the vasculature and corresponding hemodynamics seen in preterm infants to assess the impact of prematurity and the presence of a PDA can be achieved.

7.7 References

Barker DJP, Winter PD, Osmond C, et al. Weight in infancy and death from ischaemic heart disease. Lancet. 1989; ii: 577–580.

Berger DS, Li JK, Noordergraaf A. Differential effects of wave reflections and peripheral resistance on aortic blood pressure: a model-based study. Am J Physiol. 1994; 266: H1626–H1642.

Bock J, Kreher BW, Hennig J, Markl M. Optimized pre-processing of time-resolved 2D and 3D Phase Contrast MRI data. ISMRM proc 2007.

Bogren HG, Mohiaddin RH, Klipstein RK, Firmin DN, Underwood RS, Rees SR, Longmore DB. The function of the aorta in ischemic heart disease: a magnetic resonance and angiographic study of aortic compliance and blood flow patterns. Am Heart J 1989; 118: 234–247.

Broadhouse K, Price AN, Durighel G, Finnemore AE, Cox DJ, Edwards AD, Hajnal JV, Groves AM. Quantification of aortic pulse wave velocity in neonates to assess impact of PDA. SCMR 2013. Proc.

Cheung YF, Wong KY, Lam BCC, Tsoi NS. Relation of arterial stiffness with gestational age and birth weight. Arch Dis Child 2004; 89: 217–221.

Dogui A, Kachenoura N, Frouin F, Lefort M, De Cesare A, Mousseaux E, Herment A. Consistency of aortic distensibility and pulse wave velocity estimates with respect to the Bramwell-Hill theoretical model: a cardiovascular magnetic resonance study. J. Cardio Magn Reson. 2011; doi:10.1186/1532-429X-13-11.

Eckmann DM, Bowers S, Stecker M, Cheung AT. Hematocrit, volume expander, temperature, and shear rate effects on blood viscosity. Anesth Analg 2000; 91: 539–545.

Eggleton CD, Popel AS. Large deformation of red blood cell ghosts in a simple shear flow. Phys. Fluids. 1998; 10: 1834 – 1845.

Fielden SW, Fornwalt BK, Jerosch-Herold Michael Eisner RL, Stillman AE, Oshinski JN. A new method for the determination of aortic pulse wave velocity using cross-correlation on 2D PCMR velocity data. J. MRM. 2008; 27: 1382 – 1387.

Fogel MA. Assessment of cardiac function by magnetic resonance imaging. Pediatr Cardiol. 2000; 21: 59–69.

Greenwald SE. Pulse pressure and arterial elasticity. 2002; 95: 107 – 112.

Grotenhuis HB, Westenberg JJM, Steendijk P, Van der Geest RJ, Ottenkamp J, Bax JJ, Wouter Jukema J, de Roos A. Validation and reproducibility of aortic pulse wave velocity as assessed with velocity-encoded MRI. J. Magn. Reson. Imaging 2009; 30: 521–526.

Groves AM, Kuschel CA, Knight DB, Skinner JR. Echocardiographic assessment of blood flow volume in the superior vena cava and descending aorta in the newborn infant. Arch Dis Child Fetal Neonatal Ed. 2008a; 93: F24–F28.

Groves AM, Kuschel CA, Knight DB, Skinner JR. Relationship between blood pressure and blood flow in newborn preterm infants. Arch Dis Child Fetal Neonatal Ed. 2008b; 93: F29-F32

Konig K, Casalaz DM, Burke EJ, Watkins A. Accuracy of non-invasive blood pressure monitoring in very preterm infants. Pediatr. 2012; 38: 670 – 676.

Laurent S, Boutouyrie P, Asmar R, Gautier I, Laloux B, Guize L, Ducimetiere P, Benetos A: Aortic stiffness is an independent predictor of all-cause and cardiovascular mortality in hypertensive patients. Hypertension 2001, 37:1236-1241.

Laurent S, Cockcroft J, Van Bortel L, Boutouyrie P, Giannattasio C, Hayoz D, Pannier B, Vlachopoulos C, Wilkinson I, Struijker-Boudier H. Expert consensus document on arterial stiffness: methodological issues and clinical applications. Europ. Heart. Journal. 2006; 27: 2588 – 2605.

Levick JR. An introduction to cardiovascular physiology. Fifth Edition, 2010.

Linderkamp O, Versmold HT, Riegel KP, Betke K. Contributions of red cells and plasma to blood viscosity in preterm and full-term infants and adults. Pediatrics. 1984; 74; 45 – 51.

Markl M, Wallis W, Strecker C, Gladstone BP, Vach W, Harloff A. Analysis of pulse wave velocity in the thoracic aorta by flow-sensitive four-dimensional MRI: Reproducibility and correlation with characteristics in patients with aortic atherosclerosis. J. Magn. Reson. Imaging 2012.

Mackintosh TF, Walker CHM. Blood viscosity in the newborn. Arch Dis Child. 1973; 48: 547 – 553.

Merchant RH, Phadke SD, Sakhalkar VS, Agashe VS, Puniyani RR. Hematocit and whole blood viscosity in newborns: analysis of 100 cases. Indian Pediatrics. 1992; 555- 561.

Merchant N, Groves A, Larkman DJ, Counsell SJ, Thomson MA, Doria V, Groppo M, Arichi T, Foreman S, Herlihy DJ, Hajnal JV, Srinivasan L, Foran A, Rutherford M, Edwards AD, Boardman JP. A patient care system for early 3.0Tesla magnetic resonance imaging of very low birth weight infants. Early Hum Dev. 2009; 85: 779-83.

Metafratzi ZM, Efremidis SC, Skopelitou AS, De Roos A. The clinical significance of aortic compliance and its assessment with magnetic resonance imaging. J. Cardio. Magn. Reson. 2002; 4: 481 - 491.

Mohiaddin RH, Firmin DN, Longmore DB. Age-related changes of human aortic flow wave velocity measured noninvasively by magnetic resonance imaging. J Appl Physiol. 1993; 74: 492–497.

Mori A, Uchida N, Inomo A, Izumi S. Stiffness of Systemic Arteries in appropriate and small-for-gestational-age newborn infants. Pediatr. 2006; 118: 1035 – 1041.

Nerem RM, Seed WA. An in vivo study of aortic flow disturbances. Cardiovasc Res 1972; 6: 1–14.

Nerem RM, Rumberger JA Jr, Gross DR, Hamlin RL, Geiger GL. Hot-film anemometer velocity measurements of arterial blood flow horses. Circ Res 1974; 34: 193–203.

Norman M. Low birth weight and the developing vascular tree: a systematic review. Acta Pædiatrica. 2008; 97: 1165–1172.

Nussbacher A, Gerstenblith G, O'Connor FC, Becker LC, Kass DA, Schulman SP, Fleg JL, Lakatta EG: Hemodynamic effects of unloading the old heart. Am J Physiol. 1999; 277: H1863-1871.

O'Rourke MF, Blazek JV, Morreels CL Jr, Krovetz LJ. Pressure Wave Transmission along the Human Aorta: Changes with age and in arterial degenerative disease. Circulation Research 1968; 23: 567-579.

Peacock J, Jones T, Tock c, Lutz R. The onset of turbulence in physiological pulsatile flow in a straight tube. Experiments in Fluids. 1998; 24: 1- 9.

Reynolds O. An experimental investigation of the circumstances which determine whether the motion of water shall be direct or sinuous and the law of resistance in parallel channels. Proceedings of the Royal Society of London. 1883; 84 – 99.

Salvi P, Magnani E, Valbusa F, et al. Comparative study of methodologies for pulse wave velocity estimation. J Hum Hypertens 2008;22:669–677.

Sutton-Tyrrell K, Najjar SS, Boudreau RM, et al. Elevated aortic pulse wave velocity, a marker of arterial stiffness, predicts cardiovascular events in well-functioning older adults. Circulation. 2005; 111: 3384–3390.

Stalder AF, Russe MF, Frydrychowicz A, Bock J. Hennig J, Markl M. Quantitative 2D and 3D Phase Contrast MRI: Optimized analysis of blood flow and vessel wall parameters. Magn Reson Med. 2008; 60: 218–1231.

Stalder AF, Frydrychowicz A, Russe MF, Korvink JG, Hennig J, Li K, Markl M. Assessment of flow instabilities in the healthy aorta using flow-sensitive MRI. Journal of Magnetic Resonance Imaging. 2011; 33: 839-846.

Stein PD, Sabbah HN. Measured turbulence and its effect on thrombus formation. Circ Res 1974; 35: 608–614.

Stein PD, Sabbah HN. Turbulent blood flow in the ascending aorta of humans with normal and diseased aortic valves. Circ Res 1976; 39: 58–65.

Sutera SP, Mehrjardi MH. Deformation and fragmentation of human red blood cells in turbulent shear flow. Biophys J 1975; 15: 1–10.

Tauzin L, Rossi P, Giusano B, Gaudart J, Boussuges A, Fraisse A, Simeoni U. Characteristics of arterial stiffness in very low birth weight premature infants. Pediatr. 2006; 60: 592 – 596.

Voges I, Jerosch-Herold M, Hedderich J, Pardun E, Hart C, Gabbert DD, Petko C, Kramer HH, Rickers C. Normal values of aortic dimensions, distensibility, and pulse wave velocity in children and young adults: a cross-sectional study. J. Cardio. Magn. Reson. 2012; 14: 77 –

Vulliemoz S, Stergiopulos N, Meuli R. Estimation of local aortic elastic properties with MR. Magn. Reson. Med. 2002; 47: 649 – 654.

Wentland AL, Wieben O, Francois CJ, Boncyk C, Munoz Del Rio A, Johnson KM, Grist TM, Frydrychowicz A. Aortic Pulse Wave Velocity Measurements With Undersampled 4D Flow-Sensitive MRI: Comparison With 2D and Algorithm Determination. J. MRM. 2013; 37: 853 – 859.

Chapter 8

Thesis Conclusion

8.1 Thesis conclusion

The incidence of premature birth is increasing in absolute number and as a proportion of all births around the world (Yeaney et al. 2007). The survival rates in preterm and extremely preterm infants are increasing due to advances in perinatal care, yet these infants are more likely to have long term morbidities and adverse neurodevelopmental outcome compared to their term born peers. The premature transformation from fetal to extra uterine life leads to abrupt alterations in the circulatory system, as to maintain adequate blood flow to the developing organs in the two extreme environments requires very different circulation and cardiovascular function. As a result the persistent patency of the extra cardiac shunt, the ductus arteriosus is common. This delay in circulatory adaption, a prolonged PDA, is thought to contribute to abnormal hemodynamics and potential deficits in organ perfusion in preterm infants. However the resultant effects of the immature circulatory system are numerous, complex and poorly understood as both the body tissues and the circulation supplying them are immature.

Cardiac MRI has contributed greatly to the understanding of many cardiovascular diseases and congenital defects in paediatric and adult patients. Translating these imaging techniques to assess the preterm cardiovascular system requires careful optimization due to their condition, size and significantly increased heart rate. The work presented in this thesis employed multiple functional MRI techniques to investigate the immature preterm cardiovascular system and the resultant cardiac function, blood flow distribution and flow regime in the presence and absence of a PDA.

Determining whether a PDA is clinically significant is challenging. This is highlighted in the controversy over degree of assessment, appropriate indications for treatment and treatment approaches. In addition multiple randomized controlled trials to assess optimal treatment for PDA have shown no improvements in mortality or significant long-term morbidity (Wyllie, 2003). The studies presented in this thesis aim to investigate the preterm cardiovascular system and impact of PDA with scope to better understand the development and effects of certain pathologies seen in this cohort.

Firstly a PC MRI protocol to quantify ductal shunt volume, global upper and lower body flow volumes and distribution of global systemic blood flow in the presence of PDA in neonates was presented (chapter 4). To the author's knowledge this is the first study of any kind that has accurately quantified ductal shunt volume and the resultant systemic flow in preterm infants. The protocol presented here has been shown to have good repeatability and can easily be implemented on standard MRI systems, hence could potential be employed to facilitate trials of targeted intervention to close a PDA.

Initial data suggested that despite large shunt volumes (up to 74% of cardiac output), total systemic circulation for the majority of infants was maintained and was achieved by significantly increased LVO. The preservation of upper body blood flow supports the suggestion that forced closure of the duct with the aim of maintaining cerebral perfusion may be unfounded (Shimada et al. 1994). Initial data to quantify regional abdominal blood flow and impact of a PDA indicated that intestinal blood flow may potentially be maintained even in the presence of a large shunt volume. This study provides valuable insight into the hemodynamic impact of the PDA and suggests that many preterm infants outside the transition period are able to increase stroke volume to compensate for the systemic steal of blood flow through the duct.

In addition to the significantly increased left ventricular output, the left ventricle appeared enlarged in PDA infants. The common clinical belief that large ductal shunt volumes are associated with

congestive heart failure (Agarwal et al. 2007) (Baylen et al. 1977) (Schmitz et al. 2003) is partly due to the idea that systemic blood flow is reduced in these infants as well as the notable increase in cardiac dimensions. In chapter 5 the assessment of left ventricular dimension and function in preterm and term infants with and without PDA was presented. Quantification of LVO, end diastolic volume and LV mass confirmed observation and were found to be significantly increased in PDA infants. Moreover a significant association was found between increased LV mass and ductal shunt volume. Data also suggested that these hearts may be disproportionately hypertrophic. However, EF and LV fractional thickening remained within the normal range and no association was found between EF and ductal shunt volume. In addition when plotting the Frank Starling curve, all control and PDA subjects were consistent with a single linear trend with no evidence of a decline that may indicate heart failure. This suggests that left ventricular function (global contractility) was generally maintained in these enlarged hearts.

This protocol provided good agreement with PC output measures and offers a non-invasive method to quantify cardiac dimension and function that is more reliable and repeatable than echo based methods. Additional left ventricular volumetric and functional analysis in 5 infants post PDA treatment highlight the need for further investigation to aid targeted treatment approach. Further implementation of the protocol presented here would provide valuable information into the cardiac function of preterm infants in general and of the effect of different treatment approaches in PDA infants.

4D PC MRI data is a valuable tool in adult cardiac assessment and the complex flow patterns within the healthy adult aorta have been visualized and well documented. Partly due to their size, fragile state and lack of patient cooperation acquiring 4D PC MR data in the preterm cohort is challenging and consequently data does not extend back to this population. The visualization of the 3 dimensional aortic flow patterns in preterm infants with and without PDA has not been carried out before. A 4D PC MRI sequences with adequate spatial and temporal resolution would allow a

comprehensive study of the cardiovascular flow patterns present in preterm infants and hemodynamic impact of prematurity and the PDA. In chapter 6 4D PC MRI datasets in a preliminary preterm cohort to investigate the aortic blood flow patterns in the presence and absence of PDA was presented. The initial data suggests that quantification of blood flow volumes and visualization of flow fields from 4D PC MRI is feasible in preterm and term infants. The comparison of the aortic blood flow patterns in a control and PDA infant suggested that systolic flow was not disrupted in the presence of a large ductal shunt volume.

In the final work chapter, chapter 7 the 4D PC sequences were employed to evaluate PWV and flow regime within the preterm aorta. Previous assessment of aortic compliance measurements in neonates have involved ultrasound based vessel diameter and non-invasive pressure measurements, both of which are unreliable. To the author's knowledge the assessment of aortic flow regime has not been carried out in the preterm population. Aortic PWV was found to be lower than previously reported healthy adult ranges and flow regimes along the aorta were well below the turbulent regime in infants with and without PDA. The comparable aortic flow regimes found within PDA and healthy preterm term infants suggests that any association with pathology is multifaceted. Further implementation of 4D PC MRI sequences in this cohort can provide a non-invasive, accurate, comprehensive assessment of not only the visualization of cardiovascular morphology and flow fields within, but quantitative analysis of the hemodynamic impact of prematurity.

In summary the impact of the abrupt cardiovascular alterations seen in preterm infants as a response to the extreme changes in circulatory requirements is complex and poorly understood. The correlation of PDA to multiple pathologies, differing diagnostic criteria for ductal patency or significance and the controversy over appropriate treatment is a reflection of this. The work in this thesis demonstrates the feasibility of utilizing multiple CMR techniques to assess the immature preterm cardiovascular system and the resultant cardiac function, blood flow distribution and flow regime in the presence and absence of a PDA. All 4 work chapters have provided valuable insight

into the hemodynamic impact of the PDA and suggest that despite significantly increased shunt volumes and cardiac dimensions systemic blood flow, LV function and aortic compliance and blood flow regime can be relatively maintained in PDA infants outside the transitional period. However, respiratory problems are closely associated with PDA and impact of the shunt volume on the pulmonary circulation was not evaluated in this thesis. Although systemic blood flow was largely maintained, the extra blood volume through the lungs is another aspect of the PDA that needs investigating. Findings support the suggestion that treatment should be carried out on an individual basis and the CMR protocols presented in this thesis can aid future studies to investigate the association between PDA and pathologies seen in this cohort.

8.2 Future work

The following subsection provides considerations and discussion for future work resulting from each work chapter in this thesis.

Regional flow quantification

The protocol presented in chapter 4 provides a highly repeatable method to indirectly quantify ductal shunt volume and distribution of systemic flow. Previous clinical trials to determine appropriate treatment of the PDA have all been weakened by the limited ability to quantify PDA shunt volume and the impact on systemic and pulmonary blood flow with accuracy. This PC MRI technique could be used in the future to facilitate trials of targeted intervention to close a PDA.

The results presented in chapter 4 indicate that a large shunt volume may not be a determinant of aberrant global systemic blood flow or pathology. Quantification of regional blood flow and the resultant impact of the PDA presented in this thesis was limited. In the first study upper body flow is

assumed to be indicative of cerebral flow. Although this assumption is reasonable, further work to quantify cerebral flow in the presence of PDA via PC MRI may provide insight into the association between PDA and adverse neurodevelopmental outcome. Similarly the volume of ductal shunt can be used to infer that pulmonary flow is increased yet the quantification of pulmonary flow and correlation to respiratory status may provide additional understanding into the association with PDA and pulmonary pathology. A PC MRI protocol to investigate regional blood flow in the presence of a PDA would in order to explore possible associations between ductal shunt volumes, treatment and outcome would be valuable.

Initial results from the quantification of abdominal flow suggested that flow within the superior mesenteric artery may be maintained, yet the current spatial resolution would limit flow quantification in the very small infants. Necrotising enterocolitis (NEC) is a known concern in preterm infants and is associated with PDA. A longitudinal study of abdominal flow (with adequate spatial resolution) in infants at high risk of NEC acquired at the same time after feeds may provide insight into the onset and development of the pathology and determine key risk factors. .

Cardiac structure and function

The work in chapter 5 presented data assessing the impact of PDA on cardiac function. This study provided information on the global contractility parameters such as ejection fraction and fractional myocardial wall thickening. Although global function was seen to be maintained in the majority of PDA infants, temporal changes in function were not investigated. In addition it appeared that heart rate variability was decreased in these infants (chapter 5). Whether this indicates cardiac and autonomic stress is unclear. Diastolic function, and more specifically relaxation and compliance are known to be decreased in preterm infants (Kozak-Barany et al. 2001). Investigation of regional myocardial strain, stress and torsion would provide a comprehensive assessment of cardiac function.

A study considering the left ventricular diastolic passive and active filling periods will provide understanding into the added workload imposed on the heart due to the additional blood volume and increase in arterial pressure and give insight into the effect of the observed decrease in heart rate variability in these infants.

The second study presented in chapter 5 provided evidence of LV remodelling in PDA infants and the indication that treatment of the PDA may alter LV dimension and function. This emphasizes the need for further investigation and understanding of the resultant effect of treatment. The techniques and work presented in this thesis could be employed to perform a longitudinal study to quantify ductal shunt volume and resultant left ventricular function prior to and after treatment to further investigate and aid targeted treatment approach.

Recent diffusion MRI tractography studies of the structure and orientation of myofibres in preterm, neonatal and adult bovine and human hearts have demonstrated the plasticity of the neonatal heart (Chen et al. 2013) (Mekkaoui et al. 2013). The arrangement of myofiber structure into the helical pattern seen in adults occurs early in the second trimester and the dense sheet arrangement only begins after this, consequently the myocardium is still developing after term (Mekkaoui et al. 2013). The preterm heart undergoes significant structural and functional changes shortly after birth to provide the circulation sufficient for extra-uterine life. Further in-vivo longitudinal studies to investigate the development of the myofibers structure and orientation in preterm and term infants would aid in the understanding the impact of prematurity and PDA (more specifically the increased preload and arterial pressure).

Finally work in this chapter provided data on the impact of PDA on left ventricular dimensions and function. However a large shunt volume will lead to pulmonary hyper-perfusion causing increased right ventricular afterload. Assessment of the right ventricle (RV) from the current 2D SSFP stacks presented in this work would be suboptimal due to crescent shape of the RV and misalignment of the atrioventricular valves: in general the tricuspid valve resides more distal from the base of the

heart and oblique to the mitral valve. To assess the entire cardiac function in the presence of a PDA 3D SSFP imaging could be utilized.

Aortic hemodynamics in preterm infants

From the 4D PC data presented in chapter 6 visual analysis of velocity vectors along the aorta revealed a clockwise helical flow pattern in the aortic arch in both a "healthy" and PDA infant. The significance of this and the association with efficient flow is unknown. Further data acquisition to quantify the helicity of blood flow within the aorta and association with upper body and cerebral flow may provide insight into neurological outcome in the preterm cohort.

A recent study by Barker et al (2013) calculated the energy loss in the presence of aberrant aortic flow patterns in aortic valve disease patients. The disruption of aortic flow leads to an increase in left ventricular afterload. The 3 dimensional velocity field was used to calculate the viscous energy loss along particle traces seeded from the AAo, the extra work or left ventricular afterload was then quantified. Abnormal, high helical flow patterns in patients lead to an increase in energy loss when compared to controls, indicating that inefficient flow increases the work load of the left ventricle. The quantification of energy loss along the aorta in the presence and absence of PDA would improve understanding of the impact of PDA on cardiac work load and may be correlated to myocardial hypertrophy observed in chapter 5.

Aortic flow regime

At present the most reliable PWV calculations in preterm infants consists of an invasive pressure measurement, which is unfavourable in this population (particularly for longitudinal studies) and ultrasound based vessel diameter measurements, which can be inaccurate. Although the

quantification of PWV from 4D PC MRI has been well documented in the adult population, this technique has not been validated in the preterm cohort. A validation study in a silicon model aorta phantom with pulsatile flow generating equivalent physiological conditions of the preterm cardiovascular system (aorta dimensions and compliance, pulse wave pressure and upslope shape) could be used to compare the 4D PC MRI protocol and invasive pressure based measurements of PWV. Such a study is planned and it is hoped that invasive pressure based PWV and 4D PC MRI PWV measurements will have good correlation.

Previous studies in pediatrics and neonates have shown an association between preterm infants born at low birth weight and increased aortic stiffness (Cheung et al. 2004) (Mori et al. 2006) (Norman et al. 2008) (Tauzin et al. 2006), (the association found between birth weight z-scores and PWV in the preliminary study presented in chapter 7 was near significant, $p = 0.06$). This may partly explain the increased risk of heart disease in adulthood seen in this population. 4D PC MRI could be implemented in longitudinal studies to investigate the development/progression of this increase in aortic stiffness in low birth weight preterm infants where long term arterial lines and therefore invasive arterial pressure measurements are not ideal. In addition, the extra-uterine circulatory demands on the preterm vasculature that is still developing may lead to abnormal vessel compliance. There is a lack of consensus as to whether prematurity and postnatal age are associated in alterations in aortic compliance. This is partly due to the multiple assessment methods used and inaccuracies in ultrasound based protocols for calculating vessel length and diameter. The continuation of PWV analysis in preterm infants may provide understanding into the inception of increased wall stiffness in pediatrics born premature at low birth weight and if there is a general association between prematurity and increased PWV.

Assessment of pulmonary circulation and right ventricular function

The presence of a PDA is associated with pulmonary pathology such as respiratory distress syndrome and pulmonary haemorrhage (Sankar et al. 2008) (Sasi et al. 2011). Yet the work in this thesis has looked predominantly at the impact of PDA on the systemic cardio vasculature hemodynamics and function. Although an increase in pulmonary blood flow can be inferred from the increase in left ventricular output and ductal shunt volume in PDA infants, or indirectly calculated from the right ventricular output and shunt volume (chapter 5), the true impact of the duct on pulmonary function and the right side of the heart were not investigated.

Direct quantification of the blood flow through the pulmonary trunk and left and right arteries was found to be difficult in theses infants due to the small size, and curvature of the vessels (chapter 4). From 4D PC MRI analysis (chapter 6), due to the orientation of the acquisition volume, often the pulmonary trunk was not included, the spatial resolution was often too low to accurately quantify flow in the right and left pulmonary arteries in the smaller infants and there was often considerable aliasing which meant that quantification of the pulmonary flow from these datasets was not feasible.

An initial evaluation to assess total pulmonary flow was carried out from segmentation of the RV (chapter 5) and showed as expected that pulmonary flow was dramatically increased in infants with large shunt volumes. However there is still some disagreement over the correct MR imaging orientation and segmentation protocol when quantifying RV dimension and function due to its concave profile (Schulz-Menger et al. 2013). The accuracy of RV segmentation carried out in this work was not assessed against the pseudo gold standard of PC MRI in neonates. From Bland-Altman analysis between left and right output values derived from ventricular segmentation volumes a somewhat low correlation was found (chapter 5). In addition the RV myocardium-tissue boarder contrast was not adequate to allow semi-automated or manual segmentation of the epicardial boarder with confidence, therefore functional analysis of the RV myocardium was not performed. It was felt that higher spatial resolution is needed to accurately quantify the RV dimension and

function. Three dimensional SSFP acquisitions with appropriate spatial and temporal resolution providing full coverage of the heart would allow segmentation of the RV and LV and would be an interesting area of future work.

Right ventricular function

In left to right shunt PDA infants the extra blood volume overloads the immature lungs and leads to pulmonary hyper-tension; the RV is then required to generate more pressure to eject blood into the pulmonary circulation increasing workload on the side of the heart that at term is within the low pressure system. In the case of right to left shunting the RV will experience increased preload instead of the LV, cardiac function in this scenario will potentially be very different. Furthermore in principle, in preterm infants the transition of ventricular dominance from right to left is incomplete (smolich et al. 1995), how the presence of the PDA and associated increase in pulmonary pressure impacts this transition warrants investigation. Following on from the discussion above, an accurate protocol to evaluate RV and LV function would provide insight into the consequent pulmonary hyper-perfusion in the presence of a PDA and the influence of the increased afterload as well and the result systemic impact. The correlation between RV functional data and pulmonary status, as well as the LV function and systemic perfusion information would provide a comprehensive analysis of the PDA. Evaluation of the extent and temporal nature of the possible RV hypertrophy caused by this increased afterload in PDA infants would be a valuable area of future work and provide further insight into appropriate and targeted treatment.

Flow regime within the pulmonary arteries

During Doppler echocardiographic assessment of the PDA a jet of blood from the PDA into the pulmonary artery is often observed (figure 8.2.1). Presumably this will cause a degree of disrupted

flow within the pulmonary trunk and arteries. The extra blood volume entering the pulmonary vasculature via the duct will cause an increase in pressure and therefore RV afterload and vessel compliance may be decreased. The addition of turbulent flow will act to increase this already overloaded pulmonary system and decrease the efficiency of blood transport. It was not feasible to quantify pulmonary blood flow from 2D or existing 4D PC MRI data (chapter 4 and 7). An optimized axial 4D PC sequence providing coverage of the pulmonary vessels with appropriate spatial resolution and VENC would allow assessment of the PWV, Reynolds number and flow regime within these vessels. Correlation of pulmonary hemodynamics to respiratory status and RV function would again provide insight into the full impact of the PDA and association with respiratory pathology.

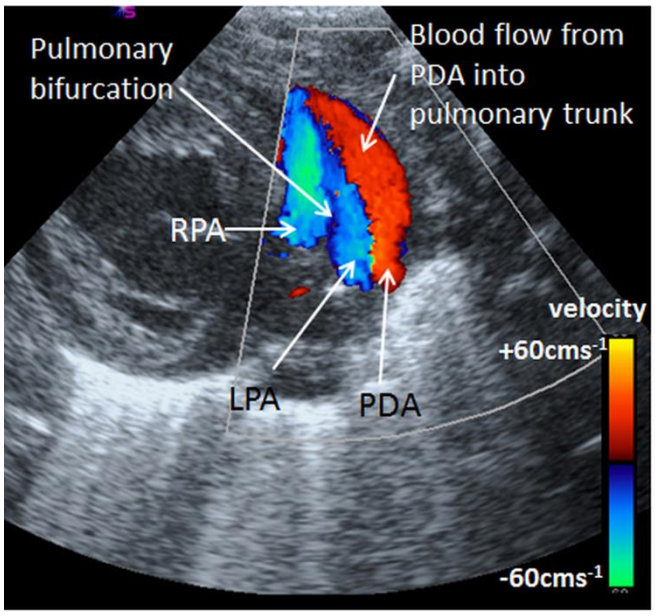

Figure 8.2.1 – Visualization of pulmonary blood flow: Doppler echocardiographic assessment of the pulmonary arteries and PDA blood flow at peak systole. Red represents blood flowing towards the transducer at the top of the image; blue represents blood flow away from the transducer probe. Blood flow from the PDA can be seen leaving the duct (red) and flowing into the LPA and trunk, meeting blood flowing in the opposite direction (blue). This will presumably causes chaotic, disruptive flow within the pulmonary arteries, whether this flow regime approaches turbulent is unclear. However this jet of blood flow will lead to aberrant flow patterns and decrease the efficiency of blood flow in the pulmonary circulation.

Summary

Neonatal cardiac MRI has been demonstrated to be highly feasible by this and other studies. It appears to offer advantages over echo in terms of an ability to systematically study the cardiovascular system with lower variability than echo, although it is of course both more expensive and less widely available, particularly in a form suitable for application to very sick infants. It is hoped that the current study has provided some valuable methods and initial data to provide normative ranges and assess the impact of PDA. However, many more areas of investigation persist and this remains an exciting area to develop not only for diagnosis of individuals and treatment monitoring, but potentially for the next generation of clinical trials designed to create the evidence base for future rational treatments.

8.3 References

Agarwal R, Deorari AK, Paul VK. Patent Ductus Arteriosus in Preterm Neonates. AIIMS-NICU protocols 2007.

Baylen BG, Meyer RA, Kaplan S, Ringenburg WE, Korfhagen J. The critically ill premature infant with patent ductus arteriosus and pulmonary disease – an echocardiographic assessment. J. Pediatr. 1975; 3: 423-432.

Barker AJ, Bandi KC, Garcia J, Van Ooli P, McCarthy P, Carr J, Malaisrie SC, Markl M. A direct calculation of hemodynamic energy loss in the presence of abnormal aortic flow. Proc ISMRM 2013; #0062.

Chen J, Zhang L, Allen JS, Hu L, Caruthers SD, Lanza GM, Wickline SA. Diffusion tensor MRI revealed developmental changes of cardiomyocyte architecture in pig hearts. Proc ISMRM 2013; 0483.

Cheung YF, Wong KY, Lam BCC, Tsoi NS. Relation of arterial stiffness with gestational age and birth weight. Arch Dis Child 2004; 89: 217–221.

Kozak-Barany A, Jokinen E, Saraste M, Tuominen J, Valimaki I. Development of left ventricular systolic and diastolic function in preterm infants during the first month of life: A prospective follow-up study. J. Pediatr. 2001; 139: 539 – 545.

Mekkaoui C, Porayette P, Jackowski MP, Kostis W, Dai G, Sanders S, Sosnovik DE. Diffusion MRI tractography of the developing human fetal heart. Proc ISMRM 2013; #0481.

Metafratzi ZM, Efremidis SC, Skopelitou AS, De Roos A. The clinical significance of aortic compliance and its assessment with magnetic resonance imaging. J. Cardio. Magn. Reson. 2002; 4: 481 - 491.

Mori A, Uchida N, Inomo A, Izumi S. Stiffness of Systemic Arteries in appropriate and small-for-gestational-age newborn infants. Pediatr. 2006; 118: 1035 – 1041.

Norman M. Low birth weight and the developing vascular tree: a systematic review. Acta Pædiatrica. 2008; 97: 1165–1172.

Sankar MJ, Agarwal R, Deorari AK, Paul VK. Chronic lung disease in newborns. AIIMS-NICU protocols. 2008

Sasi A, Deorari A. Patent ductus arteriosus in preterm infants. Indian Pediatr. 2011; 48: 301 – 308.

Schmitz L, Stiller B, Koch H, Koehne P, Lange P. Diastolic left ventricular function in preterm infants with a patent ductus arteriosus: a serial Doppler echocardiography study. Early Hum Dev. 2004; 76: 91-100.

Schulz-Menger J, Bluemke DA, Bremerich J, Flamm SD, Fogel MA, Friedich MG, Kim RJ, Von Knobelsdorff-Brenkenhoff F, Kramer CM, Pennell DJ, Plein S, Nagel E. Standardized image interpretation and post processing in cardiovascular magnetic resonance: Society for Cardiovascular

Magnetic Resonance (SCMR) Board of Trustees Task Force on Standardized Post Processing. J. Cardiovas Magn Reson. 2013; doi:10.1186/1532-429X-15-35-15-35.

Shimada S, Kasai T, Konishi M, Fujiwara T. Effects of patent ductus arteriosus on left ventricular output and organ blood flows in preterm infants with respiratory distress syndrome treated with surfactant. J. Pediatr. 1994; 125(2): 270-277.

Tauzin L, Rossi P, Giusano B, Gaudart J, Boussuges A, Fraisse A, Simeoni U. Characteristics of arterial stiffness in very low birth weight premature infants. Pediatr. 2006; 60: 592 – 596.

Wyllie J. Treatment of patent ductus arteriosus. Semin Neonatol. 2003; 8:425-432.

Yeaney NK, Murdoch EM, Lees CC. The extremely premature neonate: anticipating and managing care. BMJ 2009; 338: b2325.

Appendix

A.4.1 – Multiple Linear Regression Analysis – Impact of Ductal Shunt Volume on Systemic Blood Flow Distribution

Multiple linear regressions was carried out to investigate the association between upper, lower body flow and upper/lower body flow ratio and ductal shunt volume when correcting for gestational age. The graphs are shown below.

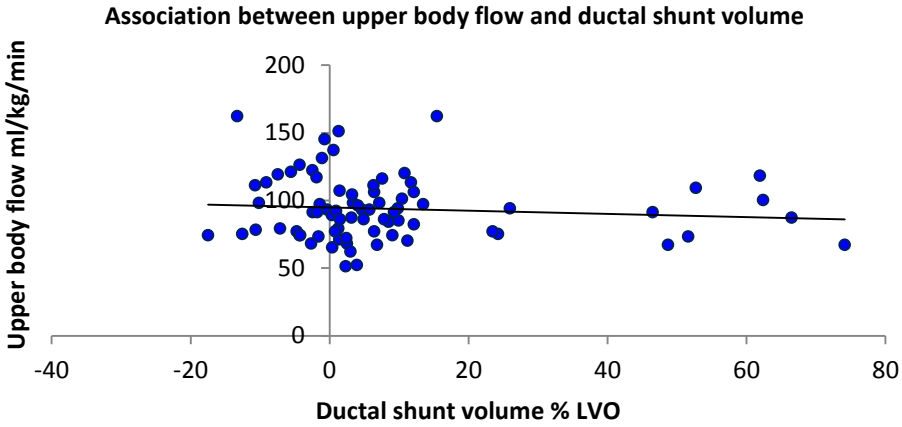

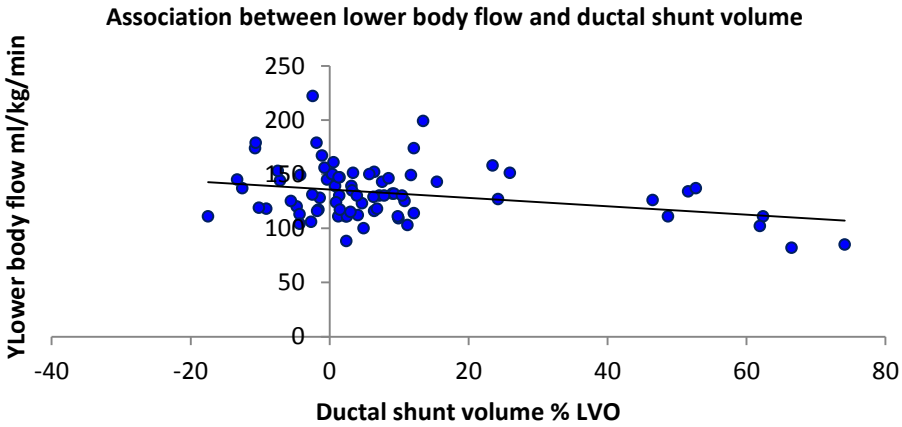

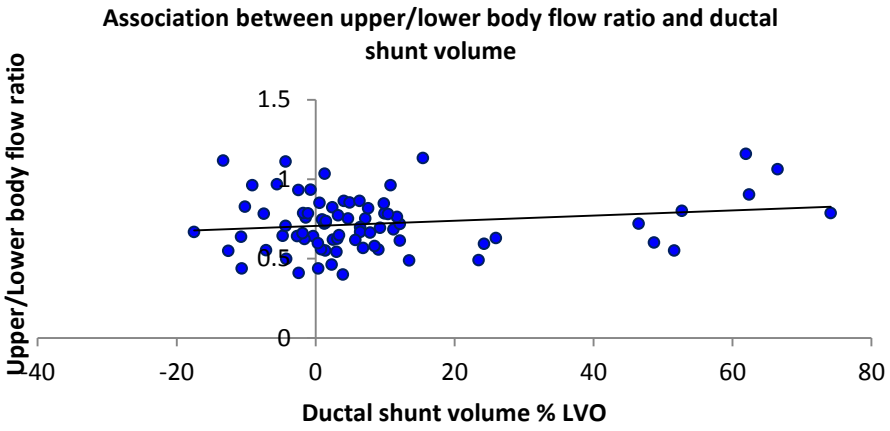

Figure A.4.1 – multiple linear regression graphs: association between ductal shunt volume and systemic blood flow distribution.

A.5.1 – Linear and Multiple Linear Regression Analysis – Impact of Ductal Shunt Volume on LV volumetrics

Linear regression was carried out to investigate the relationship between EF and LVmass and EDV in control infants, the graphs are shown below.

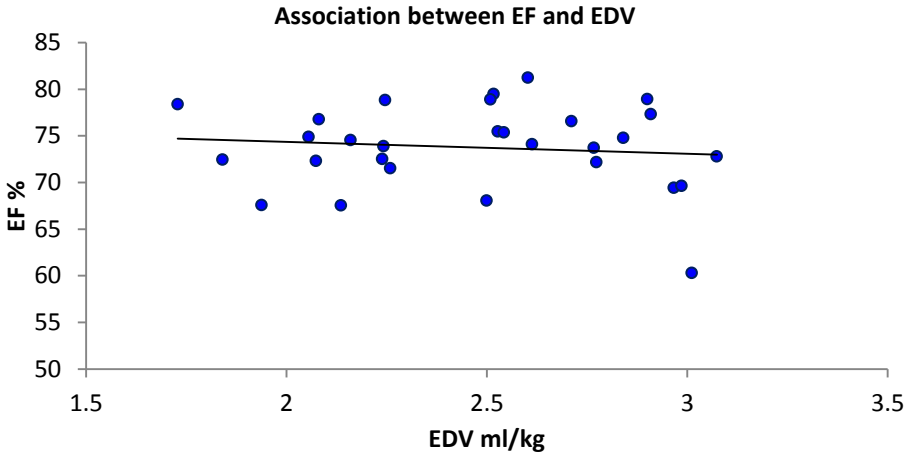

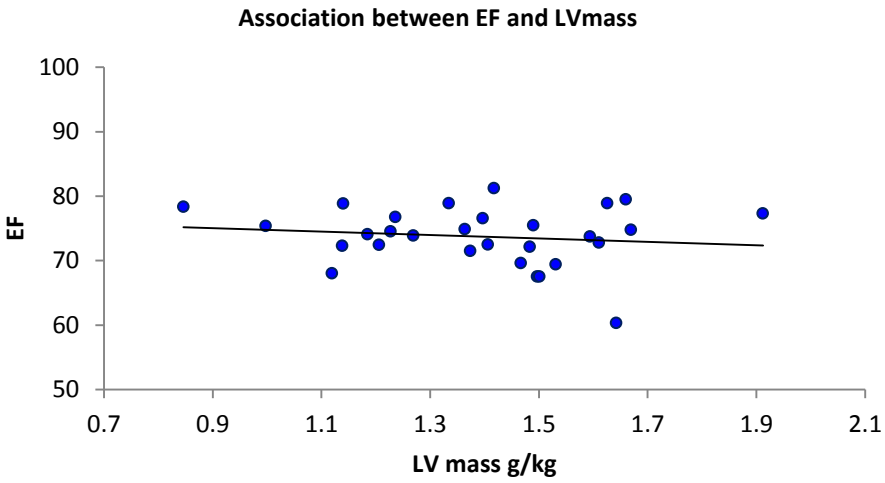

A.5.1 linear regression: association between EF and LVmass and EDV in control infants.

Linear regression was then carried out to investigate the relationship between EF and LVmass, EDV and ductal shunt volume as % LVO in PDA infants.

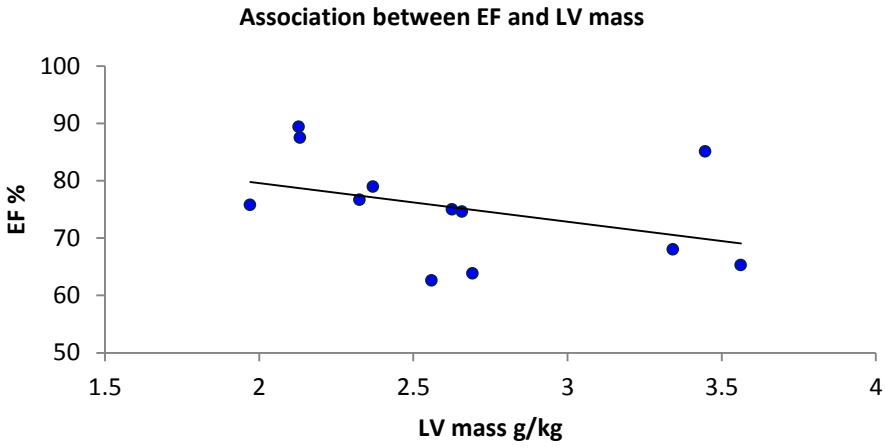

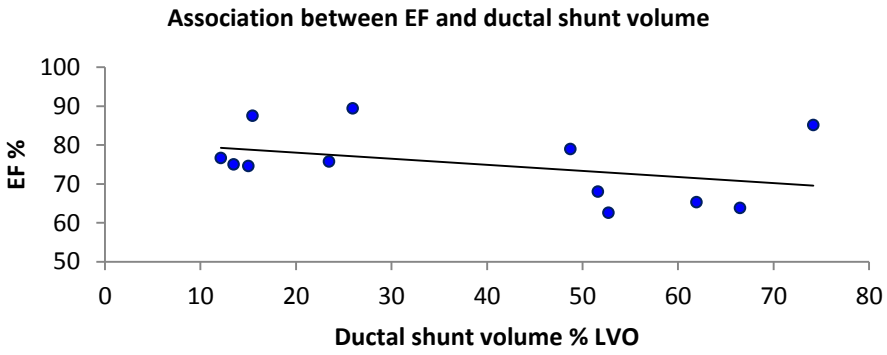

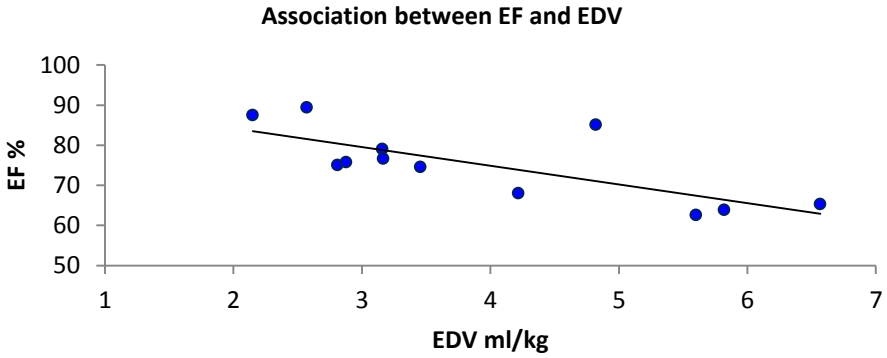

A.5.2 Linear regression: association between EF and LVmass, ductal shunt volume and EDV in PDA infants.

Multiple linear regressions were then used to assess the relationship between LVmass, EDV and MyoV/EDV and ductal shunt volume when correcting for postnatal age and cGA. The relationship between LVmass and respiratory support correcting for cGA, postnatal age and ductal shunt volume was then investigated with multiple linear regression.

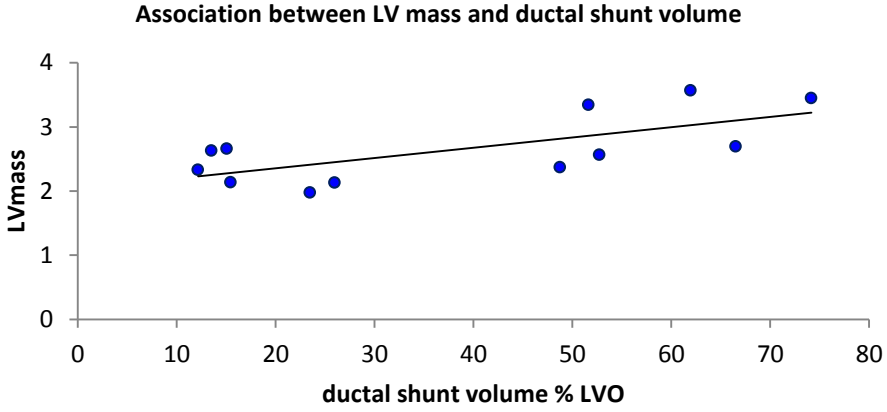

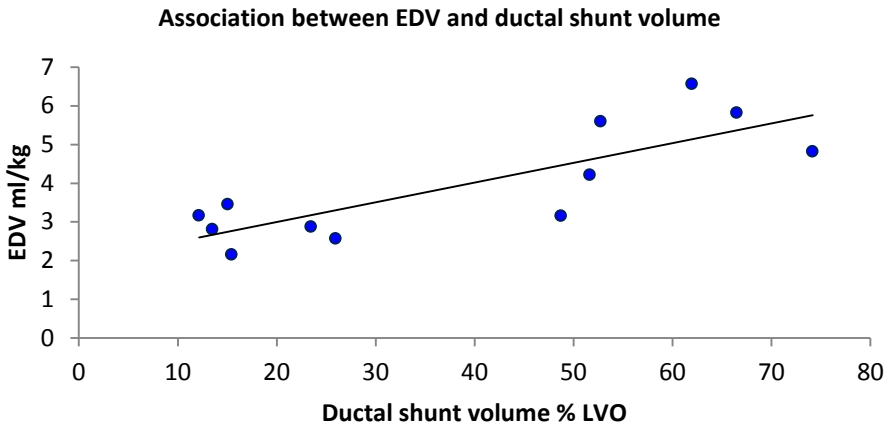

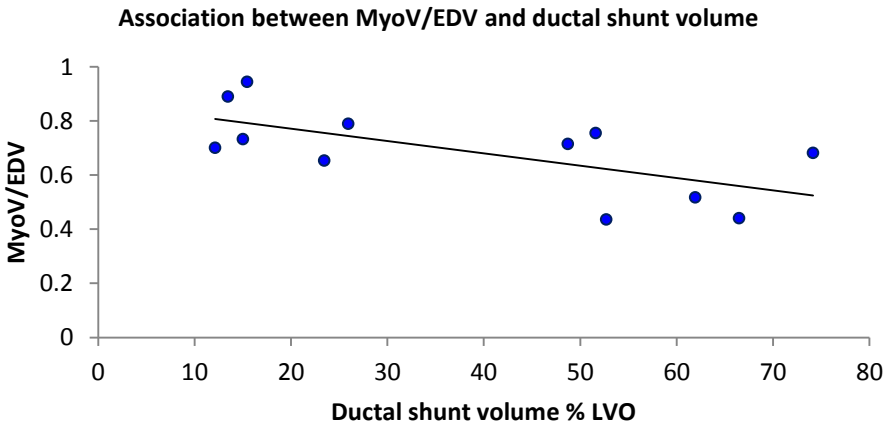

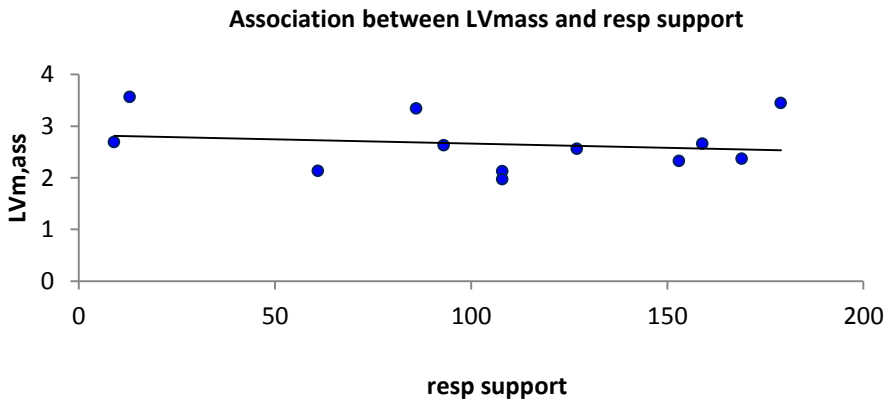

Figure A.5.3 Multiple linear regression: association between LV volumetrics and ductal shunt volume and respiratory support.

A.6.1 – Velocity Vectors and Helical Flow

Velocity vectors depicting the nature of blood flow along the aorta in the additional 7 infants in chapter 6 are shown below. Varying degrees of helical flow can be seen within the aortic arch in all infants.

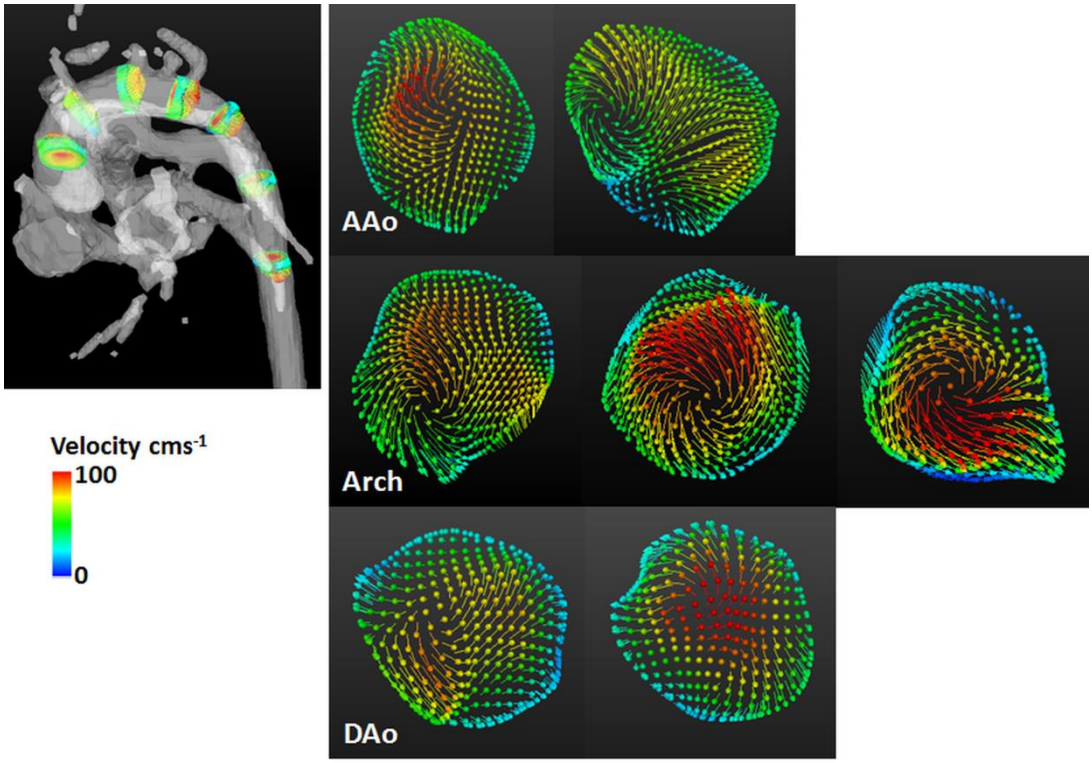

Figure A.6.1a Velocity vectors: Flow patterns within the aorta of a preterm infant with a low ductal shunt volume of 15.0% of LVO. GA 25^{+3} weeks, cGA 30^{+4} weeks, birth weight 850 grams and weight at scan 875 grams.

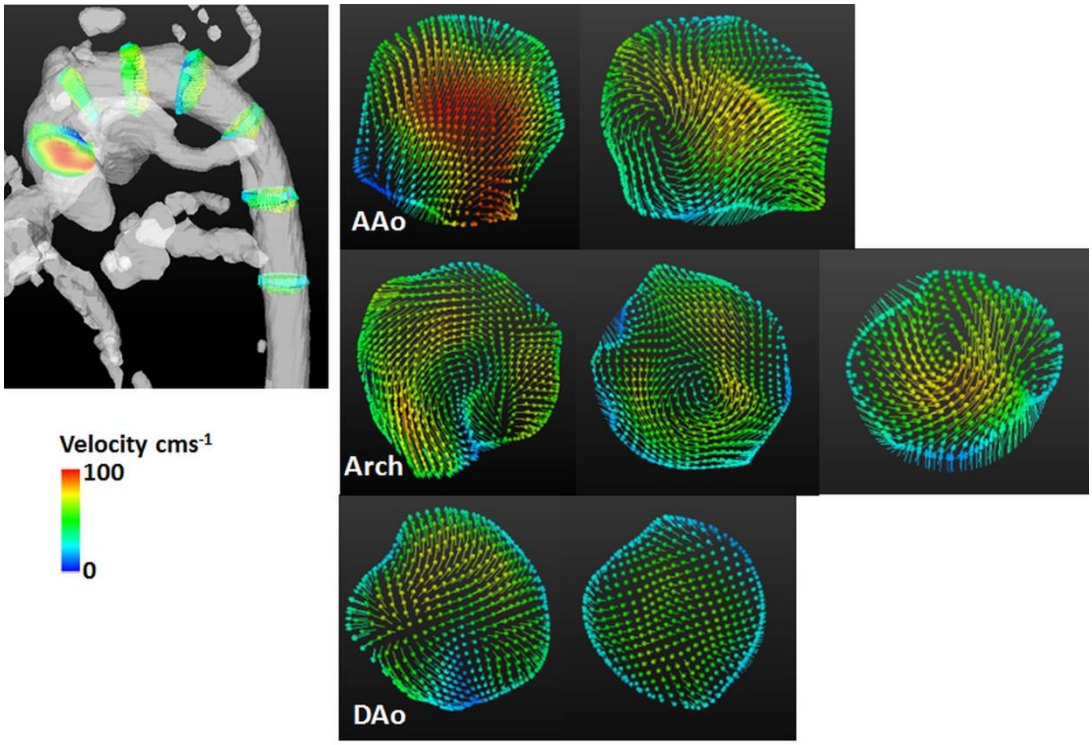

Figure A.6.1b Velocity vectors: Flow patterns within the aorta of a preterm infant with a low ductal shunt volume of 12.1% of LVO. GA 27^{+2} weeks, cGA 31^{+6} weeks, birth weight 895 grams and weight at scan 1220 grams.

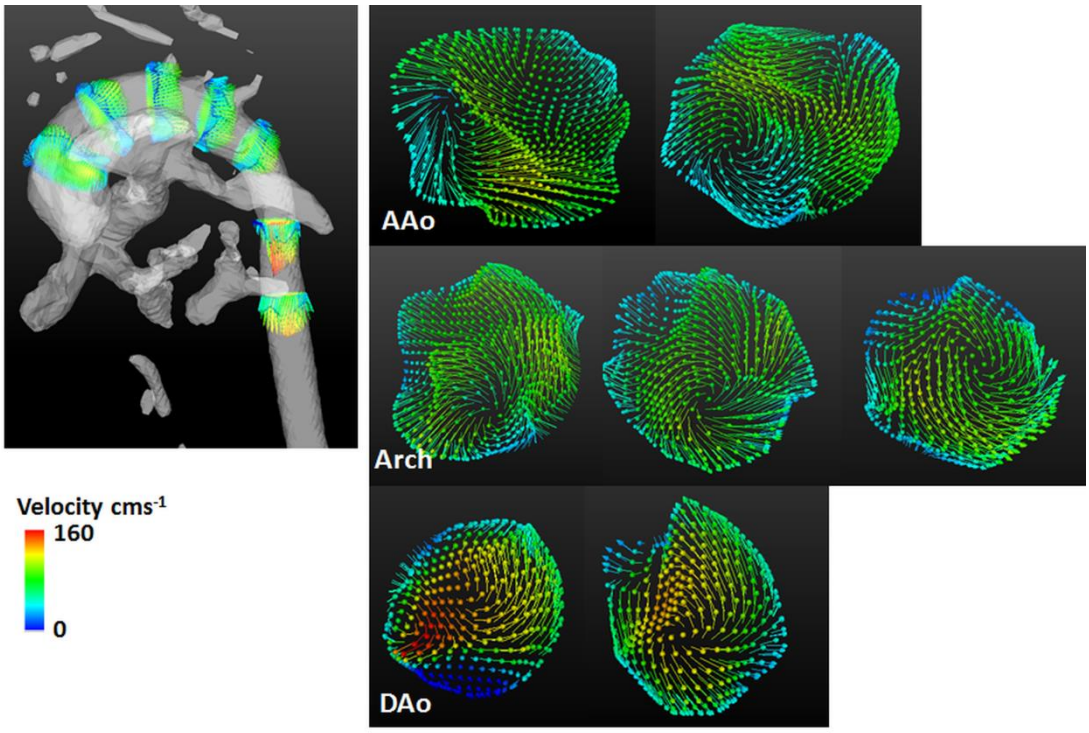

Figure A.6.1c Velocity vectors: Flow patterns within the aorta of a preterm infant with a low ductal shunt volume of 15.5% of LVO. GA 26^{+3} weeks, cGA 32 weeks, birth weight 1000 grams and weight at scan 1400 grams.

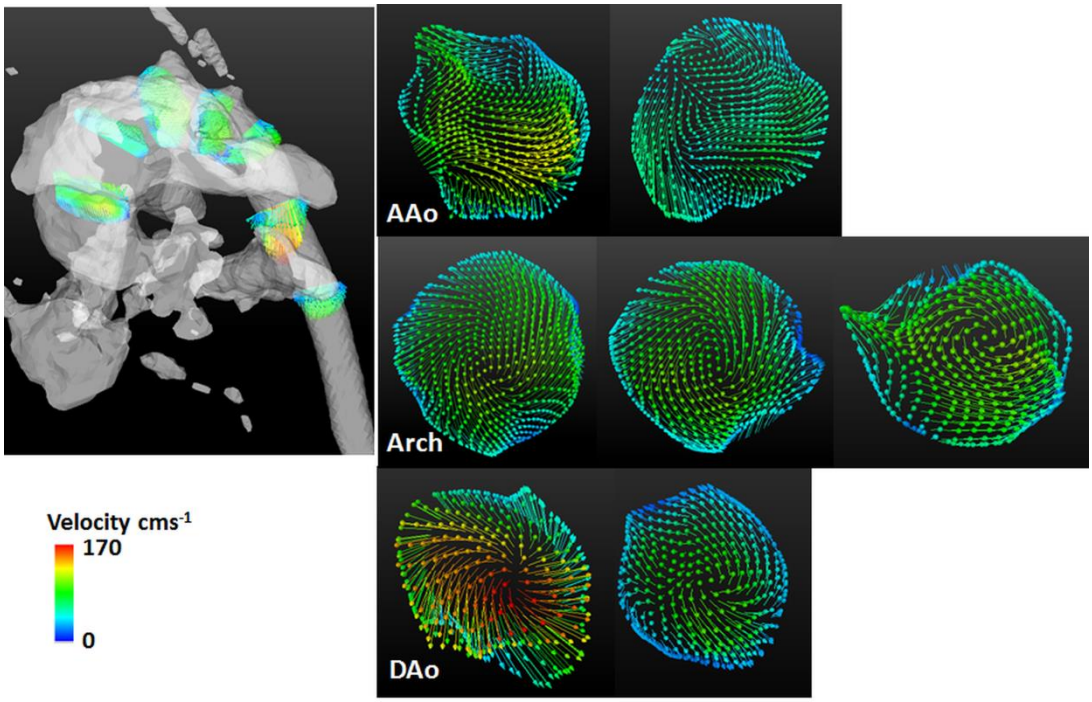

Figure A.6.1d Velocity vectors: Flow patterns within the aorta of a preterm infant with a high ductal shunt volume of 52.7% of LVO. GA 25^{+4} weeks, cGA 31^{+6} weeks, birth weight 680 grams and weight at scan 1130 grams.

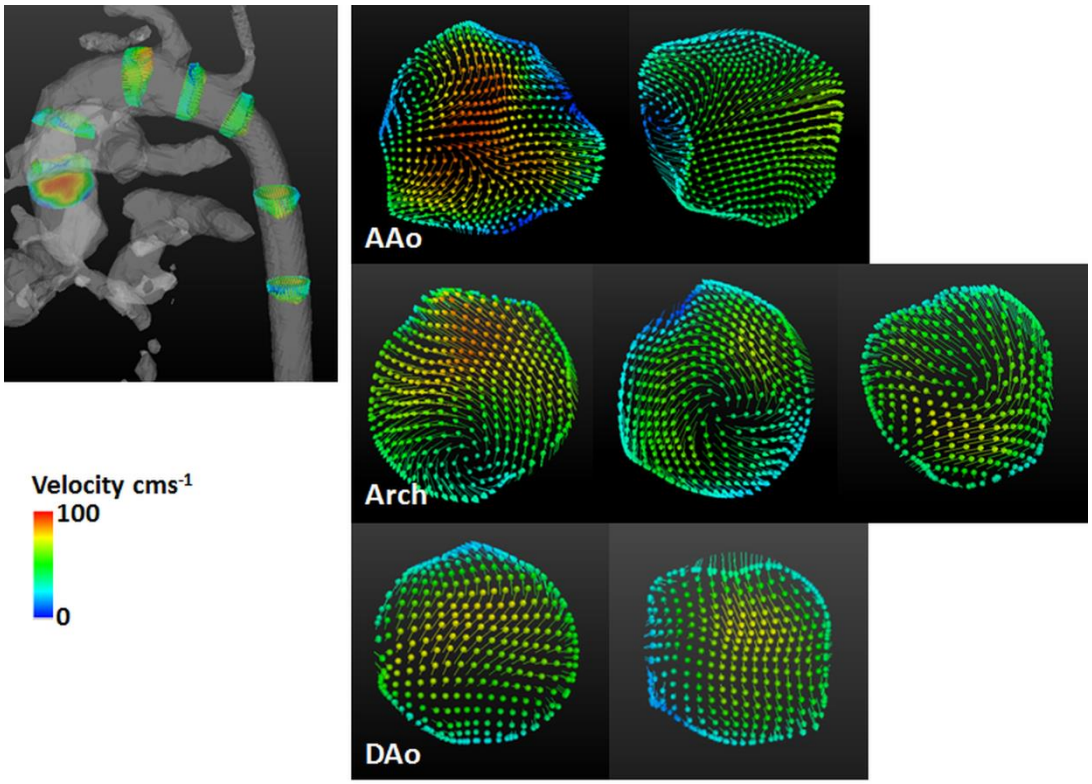

Figure A.6.1e Velocity vectors: Flow patterns within the aorta of a preterm infant. GA 25^{+4} weeks, cGA 32^{+4} weeks, birth weight 690 grams and weight at scan 1330 grams.

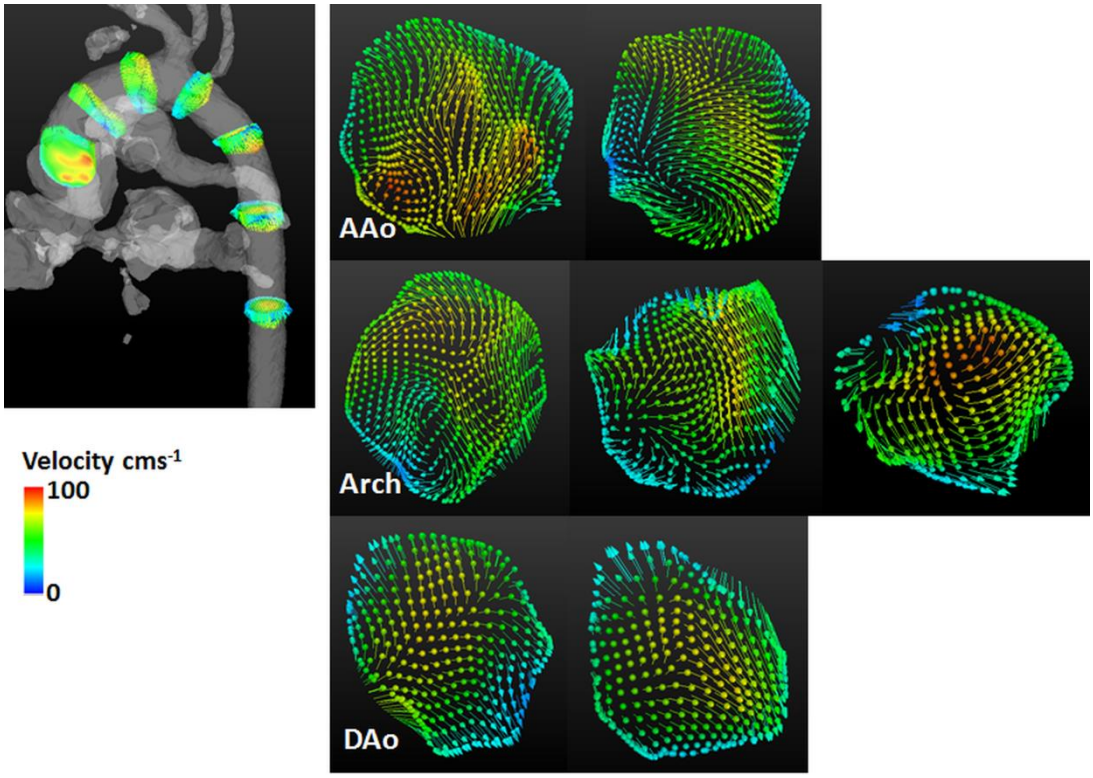

Figure A.6.1f Velocity vectors: Flow patterns within the aorta of a preterm infant. GA 31^{+4} weeks, cGA 34^{+3} weeks, birth weight 1450 grams and weight at scan 1600 grams.

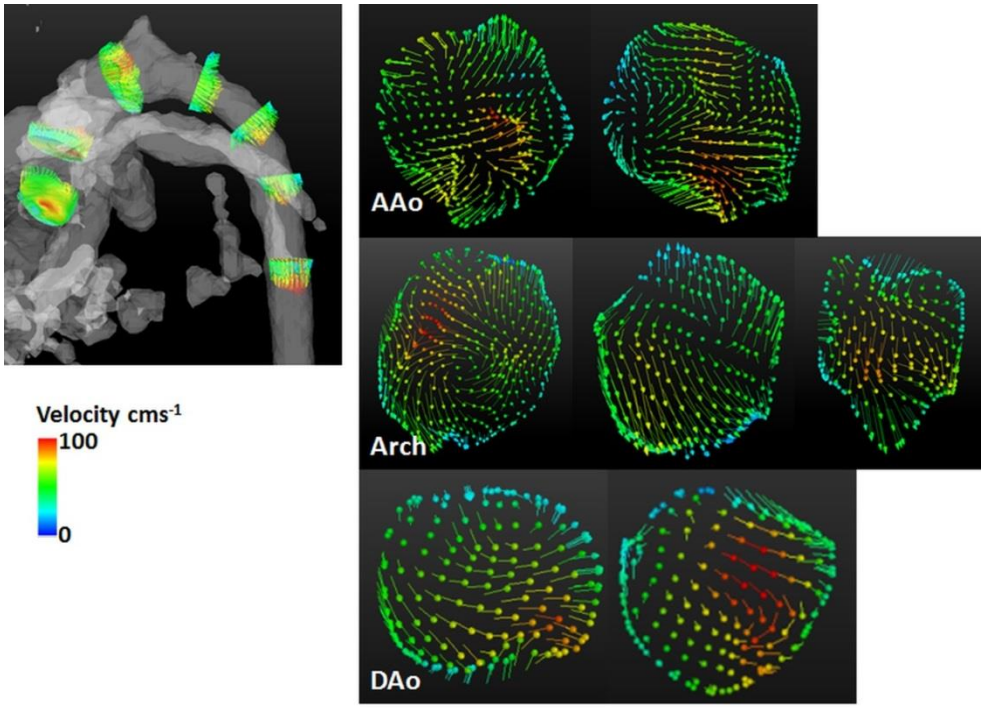

Figure A.6.1g Velocity vectors: Flow patterns within the aorta of a preterm infant. GA 32 weeks, cGA 36^{+5} weeks, birth weight 1740 grams and weight at scan 2070 grams.

7.1 – Linear Regression Analysis- Impact of Birth Weight z-scores on PWV

inear regression shows the relationship between PWV-Pres and birth weight z-scores.

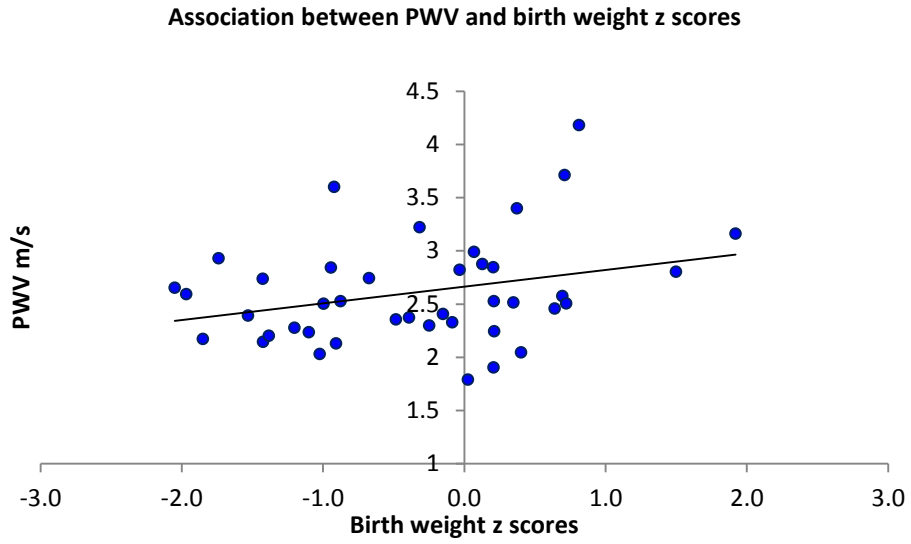

Figure A.7.1 – linear regression: association between PWV and birth weight z-scores.